RPTU Rheinland-Pfälzische Technische Universität Kaiserslautern Landau

UFPR UNIVERSIDADE FEDERAL DO PARANÁ

INTERNAL SEICHE FIELD IN THERMALLY STRATIFIED LAKES

By

Rafael de Carvalho Bueno

A thesis submitted for the degree of Doctor of Philosophy in

Environmental Engineering
at the Federal University of Paraná

•

Natural Sciences
at University of Kaiserslautern-Landau

Curitiba, June 2023

RAFAEL DE CARVALHO BUENO

INTERNAL SEICHE FIELD IN THERMALLY STRATIFIED LAKES

Dissertation thesis for the partial fulfillment of the requirements for a Doctor of Natural Sciences (University of Kaiserslautern-Landau, Faculty of Natural and Environmental Sciences) and Doctor of Environmental Engineering (Federal Univesity of Paraná)

Supervisor:
Dr.-Ing Tobias Bleninger
Federal University of Paraná

Supervisor:
Dr. Andreas Lorke
University of Kaiserslautern-Landau

CURITIBA
2023

Approval

RAFAEL DE CARVALHO BUENO

INTERNAL SEICHE FIELD IN THERMALLY STRATIFIED LAKES

Dissertation thesis for the partial fulfillment of the requirements for a Doctor of Natural Sciences (University of Kaiserslautern-Landau, Faculty of Natural and Environmental Sciences) and Doctor of Environmental Engineering (Federal Univesity of Paraná)

Dr. Leon Boegman
Queen's University

Dr. Damien Bouffard
Eidgenössische Anstalt für Wasserversorgung,
Abwasserreinigung und Gewässerschutz

Dr. Maurício Felga Gobbi
Federal University of Paraná

February 2023

For my extraordinary mother, who selflessly gave everything to raise me single-handedly, and for my beloved father, whose presence lives on in my heart

Acknowledgements

This thesis could not have been written without the unwavering support, encouragement, and expertise of my supervisor, mentor, and friend, Dr.-Ing Professor Tobias Bleninger. He has been instrumental in helping me reach my full potential, serving as a constant source of enthusiasm that has fueled me throughout these years. I am immensely grateful to him for not only fostering my growth as a scientist but also providing me with invaluable experience in managing a research team. Your remarkable qualities as a person shine brightly. My mother often reminds me that while I may have lost my father, I have gained many other cherished people in my life, and I am sure you are one of them.

I also extend my heartfelt gratitude to my other adviser, Dr. Andreas Lorke, for his invaluable insights and profound discussions that have been guiding me throughout these years. Our frequent meetings, even after my time in Germany, have played a pivotal role in shaping the overall direction of my research and propelling me along the right path. The experiences I gained during my stay in Germany and our ongoing interactions continue to be a tremendous source of inspiration. It is an honor and privilege to work with Lorke, a world-renowned researcher in my field of study. I remember the initial years during my master's studies when I merely acquainted myself with his name through the papers I perused. Working with him after all these years is an honor and a privilege. I am deeply grateful for the enlightening experience I had in his group, where I worked with a talented team of researchers.

I want to express my heartfelt gratitude to every single person from the Andreas group, with whom I had the privilege of spending six months during my Ph.D. study. My time in Germany was truly special, filled with unforgettable moments like conducting fieldwork in the rain, the hilarious nights building the floating chambers, engaging lunch meetings, coffee breaks, ice creams, beers, and wines, as well as my farewell party and the memorable barbecue at Andreas' house.

I would like to extend special thanks to Lediane Marcon for our countless scientific discussions, but also for the enjoyable times we spent together, sharing beers, and discussing the bubble dynamics in a beer glass. Your friendship and insight have been invaluable to me.

I am also deeply grateful to Mayra Ishikawa for her indispensable assistance with all the bureaucratic aspects of Landau. Your kindness and warm support made the experience so much better. I especially cherish our trip to Berlin with Ledi and Luzi, where we had a fantastic time together.

To each member of the Andreas group, thank you for the camaraderie, the knowledge shared, and the warm welcome I received. Your support and companionship have made a great impact on my Ph.D. journey.

I would like to extend my heartfelt thanks to Huaxia Yao and James Rusak from the Dorset Environmental Science Centre, Ontario Ministry of Environment, Conservation and Parks, for their invaluable support in providing the data from Harp Lake and assisting with the first manuscript of this thesis. Their contributions have been instrumental in shaping the foundation of this research.

I am also deeply grateful to Bertram Boehrer for engaging in insightful discussions about mode decomposition and internal waves, which have significantly enriched the depth and understanding of my work.

I extend my sincere appreciation to all anonymous reviewers who generously provided feedback and offered the most interesting suggestions for all the articles published in this thesis. Your constructive input has been invaluable in improving the quality and rigor of this research.

Furthermore, I express my gratitude to the editorial boards of Environmental Fluid Mechanics (Springer) and Environmental Modelling and Software (Elsevier) for their valuable contributions in the publication process, enabling this work to reach a broader audience.

I express my sincere gratitude to Dr. Mauricio Gobbi, who has been a committed member of my journey since my final year project. Over the past seven years, your guidance has played a vital role in shaping my growth as a researcher. I am deeply grateful for your continuous support and belief in my potential.

A special thanks goes to my other esteemed committee members, Dr. Leon Boegman and Dr. Damien Bouffard. Having you both on my committee is an honor and a privilege. Your expertise and contributions in my research field have been invaluable and I am immensely grateful for your presence.

I would also like to extend my thanks to Dr. Michael Mannich, who served as a committee member during my qualification. Your valuable insights and feedback have been crucial in shaping the direction of my research.

I extend my sincere thanks to Sofya Guseva for her invaluable help in testing the Interwave Analyzer and the insightful discussions we had about its results during my time in Germany. Your contributions were instrumental in improving the tool's functionality and accuracy. I also express my gratitude to all those who tested the earlier version of the Interwave Analyzer, especially Nathan Streisky da Silva. Your feedback and input were crucial in identifying and resolving issues, helping to refine the tool to its current state.

I also acknowledge financial support provided by CAPES – Brazilian Federal Agency for Support and Evaluation of Graduate Education within the Ministry of Education of Brazil, including financial support during my period in Germany. In addition, I would like to express my sincere appreciation to all from REsMA (Network on Environmental Monitoring and Modeling) and CAPES/UFPR-PRINT that kind supported my period in Germany, which definitely contributed significantly to my scientific and personal development on international level.

I am deeply grateful to the many other individuals who have supported me along this journey, especially my colleagues in the Graduate Program of Environmental Engineering (PPGEA) and the Water Resources and Environmental Engineering (PPGEHA) of the Federal University of Paraná (UFPR). Your camaraderie and encouragement have been invaluable in making this academic path more fulfilling.

A special thanks goes out to all my friends from academia, with special recognition to Dr. Andre Luís Diniz dos Santos, Camila Goulart, and Diego Casas. Your unwavering support, insightful discussions, and shared experiences have made this academic journey even more meaningful.

I also express my gratitude to Professor Cristovao Vicente Scapulatempo Fernandes. Your kindness and mentorship have been an inspiration to me. You exemplify the qualities of an exceptional professor and a remarkable human being.

I am sincerely grateful to all the undergraduate students (initiation scientific and final-year project students) who have chosen to work with me as co-advisors. Your belief in these projects and your active participation in our regular lunch meetings, which were inspired by Andreas, have been instrumental in shaping the progress and success of our research. Your dedication and enthusiasm have brought a fresh perspective and valuable contributions to our work, and I am truly honored to have had the opportunity to mentor such talented and motivated students.

I would like to express my heartfelt gratitude to those outside academia who have provided continuous support and after-hour entertainment during my academic journey. Their presence and friendship have been a source of strength and joy. In particular, I am deeply grateful to Marcelo Kamei, Willian Kamei, Filipi Mello, and Caio Sugi. Your unwavering support, laughter, and camaraderie have been invaluable in balancing the challenges of academic life. I express my heartfelt gratitude to my ex-girlfriend Milena Hofmann. Your unwavering support during my master's and PhD studies has been invaluable to me. Although our paths have evolved, your friendship and encouragement remain deeply important. Thank you for being a significant part of my journey.

I want to express my special and heartfelt thanks to my dear mother. Words cannot fully convey the depth of love and support she has shown me throughout this journey. Her unwavering encouragement and strength have been a guiding light, especially during difficult times. Her resilience and love have been the foundation of my growth. Thank you, Mom, for being my rock, my inspiration and my greatest source of love and encouragement. This journey would not have been possible without you and your influence will forever shape the person I am becoming.

I want to express my heartfelt thanks to my father, who I believe watches over me from the sky above. Knowing that you are with me in spirit provides comfort and empowers me to overcome any challenges that come my way. Your memory is a guiding light and I carry your love and support in my heart every step of this journey. Thank you, Dad, for being my strength source, even in your absence. Your presence, though intangible, is a powerful force that drives me to succeed.

Curitiba, July 2023

Do not fear that their ships are winged with a hundred oars:
their fleet rides an unwilling sea.
– Propertius, Elegies (16 BC)

Resumo

As ondas internas são oscilações que ocorrem no interior um fluido estável estratificado. Em lagos e reservatórios, essas ondas têm sido detectadas e apontadas como um dos processos mais importantes para a dinâmica e mistura vertical que occorem nestes ambientes. Uma fração do momento e da energia do vento que atravessa a superfície da água é responsável por gerar seichas internas. Apesar do grande número de publicações descrevendo diferentes mecanismos que podem influenciar as taxas de dissipação e acelerar o amortecimento das ondas internas em lagos e reservatórios termicamente estratificados, muitos detalhes de sua aplicação em observações de campo são específicos de locais e não buscam avaliar os efeitos de forma combinada. Esta pesquisa tem como objetivo avaliar alguns mecanismos que podem contribuir para inibir a geração de seichas internas através de medições de campo e simulações numéricas. Os resultados destacam a importância da batimetria na dissipação de energia cinética turbulenta, indicando que o fundo inclinado atua como um mecanismo principal para inibir a formação de seichas internas. A morfologia dos lagos e reservatórios e a mistura autoinduzida atuam como mecanismos secundários para extrair energia de eventos de ressurgência, que são responsáveis por desencadear a formação e evolução de seichas internas em lagos termicamente estratificados. Simulações numéricas indicam que uma maior quantidade de energia é transferida do vento para a seicha interna à medida que a estratificação foge de uma estrutura de duas camadas, sugerindo que o perfil de estratificação não é responsável por inibir a ocorrência de seichas internas, mas pode modificar sua estrutura, favorecendo a formação de ondas internas com modos verticais superiores. O resultado deste estudo pode ser de grande relevância na descrição do ciclo biogeoquímico em lagos e reservatórios, uma vez que cada mecanismo pode ter diferentes efeitos desencadeadores no ciclo de nutrientes e outros elementos em lagos termicamente estratificados.

Palavras-chaves: Seicha interna. Classificação de lagos. Número de Wedderburn. Modelagem de lagos.

Abstract

Internal waves are oscillating disturbances within a stable density-stratified fluid. In stratified water basins, these waves have been detected and pointed out as one of the most important processes of water movement and vertical mixing. A fraction of the wind momentum and energy that cross the water surface are responsible for generating large standing internal waves, also called basin-scale internal seiches, in stratified basins. Despite the huge number of publications describing different mechanisms that can influence the dissipation rates and accelerate the wave damping of internal seiche in thermally stratified lakes and reservoirs, many details of their application to field observations are site specific and do not evaluate the effects in a combined way. This research paid particular attention to some mechanisms that may contribute in inhibiting the generation of internal seiche through field measurements and numerical simulations. Our results underline the importance of bathymetry on energy dissipation, indicating that the gentle sloping bottom may act as a primary mechanism to inhibit the formation of internal seiches. The basin shapes (reservoir bends) and self-induced mixing near the wave crest act as secondary mechanisms to extract energy from upwelling events, which is responsible for triggering internal seiches in thermally stratified lakes. Numerical simulations indicate that a higher amount of energy is transferred from the wind to the internal seiche for an increasing deviation of the stratification from a two-layer structure, suggesting that the stratification profile is not responsible for inhibiting the occurrence of basin-scale internal waves, but only for modifying its structure, favoring the formation of internal waves with higher vertical modes. The outcome of this study may be of great relevance in describing the biogeochemical cycle in lakes and reservoirs, since each mechanism may have different trigger effects on the cycle of nutrients and other elements in thermally stratified lakes.

Key-words: Internal Seiche. Lake Classification. Wedderburn number. Lake modeling.

List of Figures

Figure 1 – Schematic overview of internal seiche and high-frequency internal waves. Different shades of blue denote layer of different density, in which $\rho_2 > \rho_1$. Silver layers indicate the solid bathymetry of the lake. . . . 35

Figure 2 – Summary of the main mechanisms investigated that can contribute to inhibit the generation of internal seiche or accelerate the internal wave damping. . . . 39

Figure 3 – Illustration of the heat flux (monthly mean) estimation based on measurements from Lake Zurich (which is located in the northern hemisphere) by Imboden and Wüest (1995). x-axis indicates the time (season) variation. y-axis shows the amount of monthly mean heat flux between water and atmosphere, in which negative values indicate that heat is being lost by the lake to the atmosphere (y-axis does not indicate the energy absorbed along water depth, only the heat energy that crosses the water surface). The red line represents the total balance of heat. . . . 42

Figure 4 – The water density profile and the Thorpe displacement obtained from temperature measurements along the water column. The solid black line indicates the water density associated with water temperature along the water column. The dashed line illustrates the monotonic profile of the density values (black solid line). D_T is the distance between the density measured and its monotonic form, and indicates the billow size that is generated by overturns. . . . 46

Figure 5 – Spectrum of the internal wave field. N is the buoyancy frequency defined by equation 2.9 and ω is the angular frequency. . . . 51

Figure 6 – Schematic overview of a fundamental internal seiche in a lake. Different shades of blue denote layers of different temperatures (density, in which $\rho_2 > \rho_1$). Brown and silver layers indicate the sediment layer and the solid bathymetry of the lake, respectively. . . . 53

Figure 7 – Schematic view of various vertical internal wave modes in a closed lake. a) V0H1, b) V1H1, C) V2H1. The mode for $n = 0$ is related to the pure surface (barotropic) mode. The black dots ($\cdot$) represent nodal points. Arrows illustrate the flow of water direction associated with different layers. . . . 53

Figure 8 – Large Kelvin internal wave modulated by internal surges and high-frequency internal waves measured in Onego Bay. Assembled from Hutter (2011). Isotherms variation at station ST3, measured near the lakeshore at the north portion of Lake Onego during 9 days of field campaign. The isotherms show one wave cycle of Kelvin internal wave, modulated by 24 h internal surges. The power spectral density of 16 °C isotherm shows that the modulation just occurs during the downwelling part of the Kelvin internal wave. 55

Figure 9 – Schematic representation of the instability mechanism caused by propagating internal waves on a flat bottom near the unstable boundary layer. Assembled from Bogucki, Dickey and Redekopp (1997), Stastna and Lamb (2008), Boegman and Stastna (2019). . . . 57

Figure 10 – Portable flux profile of background temperature and velocity structure. The white lines represent isotherms, whilst the color map shows the velocity profile along the depth. Assembled from Boegman et al. (2003). . . . 58

Figure 11 – Diagram describing the a) upwelling and b) downwelling events during the evolution of internal seiche near the lakeshore. Different shades of blue denote layers of different temperatures (density). 60

Figure 12 – Stable N-layer system in a rectangular basin ($\rho_1 < \rho_j < \rho_N$). The vertical coordinate is positive above the water surface. H is the equilibrium layer thickness, whilst h is the local layer thickness. ζ describes interfaces between two fluids with different densities (referenced from $z = 0$). Index i indicates the analyzed layer (as an example, we defined the red dot position as our point of interest). Index j represents all layers that are affecting the pressure in layer i, which are all layers above i. 62

Figure 13 – Stable two-layer system ($\rho_2 > \rho_1$) in a rectangular basin. The vertical coordinate is positive above the water surface. H is the equilibrium layer thickness, whilst h is the local layer thickness. ζ describes interfaces between two fluids with different densities (referenced from $z = 0$) 65

Figure 14 – A wind-induced stationary internal wave in a stratified basin. Left: Tilting of surface and interface, due to wind stress. Right: Oscillatory motion of surface and interface after wind stopped at one half of the wave period. Dashed lines indicate surface and interface location right after wind stopped. 74

Figure 15 – Schematic view of various internal wave modes in a closed basin: a) V0H1, b) V1H1, C) V2H1 and d) V1H2. The mode for $n = 0$ is related to the pure surface (barotropic) mode. The black dots ($\cdot$) represent nodal points 75

Figure 16 – Maps of Vossoroca reservoir (left), and Harp Lake (right), with depth contours and locations of observation points (green: meteorological station, red: platform with thermistor chain), and in and outflows (arrows). 77

Figure 17 – a) Sketch of the numerical experiment and b) the wind event responsible to excite a BSIW for all numerical simulations. Red bar indicates the period of homogeneous wind. 78

Figure 18 – Overview of field data from Vossoroca reservoir during September 2012 (Vossoroca reservoir; 01/09 – 29/09). a) Wind speed and direction, b) wind change with time, and c) thermal structure showing temperatures in colors and the thermocline position as a white solid line. The water surface elevation is represented by the blue solid line. 83

Figure 19 – Spectral analyses of Vossoroca reservoir during September 2012: a) Power spectral density of the isotherms of 18.5 °C and 16 °C (Vossoroca reservoir; 15/09 – 25/09). The dashed lines show the mean red noise spectrum for the time series, where spectral peaks above this line are significantly different from noise at a 95% confidence level. Horizontal color boxes indicate the theoretical period for different vertical modes. b) Coherence between 16 °C isotherm and wind speed. 84

Figure 20 – Isotherm, phase, and wavelet analyses of Vossoroca reservoir during September 2012. a) Phase analyses of two pairs of isotherms (phase was just plotted for coherence above the 95% confidence level). b) 16 °C and 18.5 °C isotherm time series. c) Wavelet analyses of the 16 °C isotherm (Vossoroca reservoir; 15/09 – 25/09) 85

Figure 21 – Internal seiche amplitude of the most energetic isotherm versus a) the daily Ri, b) filtered Ri_{duration} using only periods with winds capable to generate internal waves, and c) filtered $Ri_{\text{direction}}$ using only periods with winds in directions capable to generate internal waves. Linear regression was obtained for each basin 86

Figure 22 – Numerical simulations results: Evolution of the generated basin-scale internal waves. a) internal wave amplitude, and b) non-dimensional internal wave amplitude, plotted against the non-dimensional time (using the internal wave period T_{V1H1} for normalization) for different stratification conditions and pycnocline depths. The arrow indicates the anomaly of the run with $h_e/H = 0.13$. The red region in b) indicates the same interval analyzed in a) 87

Figure 23 – Numerical simulations results: Initial displacement of the generated basin-scale internal waves. a) Decay of the non-dimensional internal seiche amplitude (using the initial displacement for normalization) as a function of the non-dimensional time (using the internal wave period T_{V1H1} for normalization). b) $Ri\ h_e/L$ as a function of non-dimensional time in which 80% of internal wave energy is dissipated. 88

Figure 24 – a) Maximum basin-scale internal wave displacement normalized by the thermocline depth h_e at downwind regions, where the initial displacement is characterized by a downward movement. The horizontal dashed black curve indicates the limit boundaries to direct interaction between water surface and internal seiche at upwind region. b) The longitudinal temperature profile during the wind event (3 h of simulation time) showing the strong erosion of thermocline at downwind region (Simulation: Run 23). The white dashed line indicates the unperturbed thermocline depth and the blue dashed line the theoretical displacement according to linear theory. 89

Figure 25 – a) Variation of g as a function of h_e/H for all simulated cases. Black dots represent the empirical parameter defined considering all simulated h_e/H condition. Red curves indicate different functions to describe the variability of $g(h_e/H)$ (linear and a third order polynomial regressions). b) Maximum vertical displacement associated with internal seiche. Solid curve is derived from parametrized equation (Eq. 3.8) for different h_e/H conditions applying the third-order polynomial equation to describe the g function, expressed with distinct colors. The result using the linear equation for g is presented in Appendix B. Marks indicate the simulated results from different h_e/H conditions. 91

Figure 26 – a) Comparison between theoretical (linear and parametrized equation) and internal seiche amplitude detected in simulations. b) Error percentage with respect to h_e/H. 92

Figure 27 – a) Maximum vertical displacement associated with internal seiche normalized by the epilimnion thickness against $Ri\ h_e/L$. Data points include values from simulations, Harp lake, Vossoroca reservoir, and many other lakes from the literature (FLOOD et al., 2020; HOMMA et al., 2016; COSSU et al., 2017; CARMACK et al., 1986; STEVENS; LAWRENCE, 1997; STEVENS et al., 1996; MACDONALD, 1995) b) Normalization of ζ_o/h_e to incorporate the function $f(h_e/H)$ $(2\ f^2)$ against $Ri\ h_e/L$. The black dashed line represents Eq. 3.8 normalized by $2\ f^2$. "Log" is defined in base e, natural logarithm. . . . 93

Figure 28 – Amplitude growth due to resonance effect against a) the peak of the power spectral density of the wind intensity at the internal seiche period and b) the integration of the wind spectrum for wind frequencies between 0.5 to 1.5 of the internal wave period per bandwidth frequency. 94

Figure 29 – Bathymetric maps of Passaúna reservoir and of the hypothetical basins considered in numerical simulations (the color map represents water depth). a) Scenario M2B2: Original shape (morphology, M) and bathymetry (B) of Passaúna reservoir. b) Scenario M1B2: Simplified (straightened) reservoir shape with similar bathymetry as the original reservoir. c) Scenario M2B1: original reservoir shape, but with constant water depth. d) Scenario M1B1: Simplified reservoir shape with constant depth. The black lines in c) and d) show the grid used for the numerical simulations. The red line marks the longitudinal grid positions for which the horizontal flow velocity in the north/south direction is illustrated in Fig. 36. The red, yellow, and green dots in panel a) show the location of the monitoring station, the weather station, and the reservoir intake, respectively. Small triangles show the inflows, and the blue line indicates the location of the reservoir dam. The stations S1 and S2 (blue and white symbols) are used in the discussion of the numerical simulations. 100

Figure 30 – Vertical profiles of density stratification used in the numerical simulations. a) Buoyancy-frequency (N) and b) temperature profiles for different values of σ (the standard deviation describing the Gaussian form of the buoyancy-frequency profile). N refers is the maximum buoyancy frequency of each stratification profile. 103

Figure 31 – Conditions at Passaúna reservoir during the monitoring period. a) 3-h average wind speed measured at the meteorological station near the dam (purple solid line) and temperature difference between the water surface and the bottom (green solid line). b) Wedderburn number (W) calculated with 3-h resolution (black solid line) and averaged over one internal seiche period (red solid line). The red background color marks the range of W, for which internal seiche dominance is predicted by a common classification scheme (Fig. 60). The vertical blue bars indicate the two analysis periods (P1, from June 28 to July 04), and P2 (from January 29 to February 04). 104

Figure 32 – a) Wind speed (purple line) and wind direction (green line) during the analysis period P1. The red shaded area, delimited by vertical black dashed lines, marks a solitary wind event that may favor the generation of internal seiches. b) Measured, and c) simulated horizontal flow velocities in south to north direction at the location of the monitoring station (Fig. 29a) with a temporal resolution of 1 min. 105

Figure 33 – Temporal dynamics of vertical profiles of horizontal flow velocities near the center of the reservoir (station S1, velocity indicated by color) and kinetic energy in internal wave motion for scenario M1B1 for a) nearly two-layer stratification ($\sigma = 0.2$ m) and b) nearly linear stratification ($\sigma = 30$ m). The vertical black dashed lines mark the end of the wind event. The black triangles show the total internal wave energy. The black solid line illustrates the exponential decay of wave energy (see labels for decay rate, in which the time t has the unit days). 107

Figure 34 – Parameters related to wave generation and dissipation. a) Time averaged energy in internal seiches in response to a solitary wind event as a function of the initial density stratification (thermocline width σ, cf. Fig. 30) for the four simulated scenarios: M1B1, M2B1, M1B2, and M2B2. The line shows the initial wave energy computing assuming the energy from the first wave cycle. The internal seiche energy is normalized by the wind energy input. b) Wave damping coefficient obtained assuming an exponential decay of the total wave energy. Wave dampening of case M2B2 is not shown because the wave is rapidly dissipated right after the end of the wind event. 108

Figure 35 – The influence of morphological characteristics on the internal seiche dynamics. Panels a) to c) show power spectral density (PSD) of vertical velocity: b) M1B1 and $\sigma = 0.2$ m, c) M2B1 and $\sigma = 0.2$ m, and d) M2B1 and $\sigma = 30$ m. The dashed lines show the 95 % confidence limit of the mean red noise spectrum for the time series. The red shaded area marks the frequency band of elevated spectral energy in scenario M2B1 compared to the rectangular basin considered in scenario M1B1. d) The spatial distribution of the spectral variance of the band-pass filtered vertical velocity with cutoff frequencies of 4 h and 6 h for scenario M2B1 and $\sigma = 0.2$. 109

Figure 36 – The influence of bathymetry on internal seiches analyzed in scenario M1B2 for nearly two-layer stratification ($\sigma = 0.2$ m): a) Temperature distribution along the longitudinal cross section of the reservoir during the wind set-up ($t = 0.3$ d). b) North-south velocity component along the longitudinal transect at $t \approx 1$ d. c) Temporal dynamics of the vertical distribution of horizontal flow velocity at the center of the basin. The colored solid lines illustrate the exponential decay of total energy in internal seiches for nearly two-layer stratification (purple color, $\sigma = 0.2$ m) and for nearly continuous stratification (green color, $\sigma = 30$ m). Text labels show decay rates, in which t is defined in days. 110

Figure 37 – Schematic overview of currents and mixing process in lakes and reservoirs. Different shades of blue denote layer of different temperature (density). Brown and silver layers indicate the sediment layer and the solid bathymetry of the lake, respectively. Basin-scale internal waves and high-frequency internal waves can occur at density interfaces. Billows (black arrows) illustrate turbulent mixing. 117

Figure 38 – Illustration of the modal structure of basin-scale (standing) internal waves in an idealized (rectangular) basin. Vertical density stratification is approximated by five vertical layers,(different shades of blue), each having a constant density ρ and thickness (at equilibrium position h). The equilibrium position of the layer interfaces is shown as black dashed lines. The blue shading illustrates the layer displacement (ζ) of a horizontal mode 1 and vertical mode four wave (V4H1). η_0 denotes the displacement of the water surface. 118

Figure 39 – a) Regime diagram for generation and degeneration of internal waves for a hypothetical reservoir with a basin length of $L = 4$ km. Different colors separate three mixing regimes based on Wedderburn number W_{V1} and the epilimnion thickness (h_e) normalized by the lake depth H. The two regimes proposed by Spigel and Imberger (1980), which result in complete vertical mixing are combined in the *severe vertical mixing*. Dashed lines show regime boundaries according to Spigel and Imberger (1980). Solid lines separate regimes of wave degeneration, as proposed by Horn, Imberger and Ivey (2001). b) The theoretical relationship between W_{V1} and the vertical displacement of the thermocline ζ_o normalized by the epilimnion thickness (h_e). Solid lines show theoretical results from Spigel and Imberger (1980) and the dashed line shows the empirical formulation proposed by Bueno et al. (2020). The latter takes an additional contribution of the epilimnion thickness and the interaction of the internal seiche with the lake boundaries into account. 120

Figure 40 – Results of the numerical simulation of water temperature in an idealized (rectangular) basin in response to a single wind event. a) Time series of wind speed (blue solid line) and wind direction (gray solid line). The dark and light vertical red box indicates the period of maximum and the total duration of the wind event, respectively. The inset figure shows a sketch of the two-layer rectangular tank of $H = 15$ m and $L = 4.5$ km with the initial temperature distribution. ST is the location where temperature time series were analyzed. b) Contour plot of water temperature at station ST. The solid blue and white line represent the water level ($H = 15$ m) and the thermocline, respectively. 127

Figure 41 – a) Time series of selected isothermal depths at the sampling point ST in the numerical simulations. b) Temporarily averaged vertical temperature profiles /red line) and the two (black line) and three-layer (blue line) approximation of the temperature profiles used for modal internal wave analysis. 128

Figure 42 – a) Power spectral density (PSD) of isotherm displacements for the three isotherms shown in Figure 41a. The vertical red, green, and blue bars in the spectrum mark the frequencies of basin-scale internal waves estimated by the multi-layer model for first, second, third vertical mode, respectively. The width of the colored boxes indicate the variability of the estimated internal wave periods based on variations of the basin length that was aligned with the mean wind direction. The dashed lines indicate the mean red noise spectrum for the time series at a 95% confidence level. b) Sensitivity analysis of the multi-layer hydrostatic model to variations in density stratification. ρ_1 and ρ_2 are the mean density in the hypolimnion and epilimnion, respectively, whereas $\Delta\rho = \rho_2 - \rho_1$. The green horizontal bar corresponds to the width of the green bare in a) (caused by variability of wind direction). The gray vertical bar indicates the variability of the density gradient during the analyzed period. Blue and red dots show the average internal wave periods predicted by the internal wave model and estimated from spectral analysis, respectively. 129

Figure 43 – a) Normalized internal wave amplitude (normalized by the epilimnion thickness (ζ_o/h_e)) versus Wedderburn number W. The blue solid line represents the theoretical formulation defined by Spigel and Imberger (1980), whilst green and yellow represent the empirical parameterization described by equation 5.10. The red dot indicates the maximum observed for the modeled wind event. b) Regime diagram characterizing the degeneration of basin-scale internal waves according to the theoretical classification (HORN; IMBERGER; IVEY, 2001). The variability of h_e/H and W marked by the red arrow refers to the first two days of simulation, which may characterize the degeneration regime of internal wave. The blue region indicates conditions when internal seiche are more susceptible to be damped by viscosity. The range colored in gray indicates a regime where internal waves degenerate into a propagating waves. The red and yellow region characterize regime of degeneration with formation of supercritical flow, and bore and billows, respectively. . . 130

Figure 44 – Overview of the water temperature distribution along the centerline of the rectangular basin for three selected times: a) right after the wind event (t=0), b) $t = T_{V1H1}/4$, and c) $t = T_{V1H1}/2$, in which T_{V1H1} is the theoretical period of the fundamental basin-scale internal wave. The vertical (v) and horizontal (u) velocity profiles are shown at different locations near the basin shore and in the center of the reservoir ($x \approx 2000$ m), respectively.131

Figure 45 – Measurements at Vossoroca reservoir: a) Wind speed and direction. b) Water temperature measured by a thermistor chain. The solid blue line represents the water surface. black and red lines represent the isotherms of 22 °C and 17.5 °C, respectively. The altitude of reference for reservoir bottom is 799 m. c) Temperature profile estimated by the software for a two- and three-layer approximations. The blue dots show the mean temperature measured by the 7 thermistors deployed in the reservoir. 132

Figure 46 – Time series of wind direction at Vossoroca reservoir (grey line). The blue bars above the graph indicates periods of constant wind directions according to three different angles of wind direction contribution: A: ± 20°, B: ± 40°, and C: ± 5°. Periods marked by green and red color correspond to criteria suggesting internal wave generation. The green line represents the more flexible criteria often described by mathematical results from Spigel and Imberger (1980). The red line indicates a more restrictive result, which fall into regime of internal wave described by Spigel and Imberger (1980) and often observed from field data reported in the wide literature. The value of W_{V1} displayed in the label indicates an average for the entire period, and just illustrates the mean value of the adopted criteria. The vertical red bar indicates the period in which the internal wave was generated. . . . 133

Figure 47 – Power spectral density (PSD) of isotherm displacements for three different segment sizes for the Fourier transform: a) 4 days (Flattop window function), b) 4 days (Hamming window function), and c) 1.5 days (Hamming window function). The theoretical period of internal waves are marked by horizontal bars: mode V1H1 (green), V2H1 (red), and V3H1 (blue). The theoretical period threshold (height of the horizontal bars) are plotted for three different wind direction contribution parameter, which are estimated through the maximum and minimum length of the lake that is aligned with the wind direction: a) ± 40°, b) ± 20°, and c) ± 10°. The black horizontal solid lines indicate the inertial frequency and the dashed lines shows the mean red noise spectrum for each time series at a 95% confidence level. 134

Figure 48 – Coherence (solid line) and phase-shift (cross symbols) of two selected isotherms (17.5 °C and 21 °C) during the period April 9 to 12 (2012).The vertical black dashed line indicates the period of the internal wave detected by spectral analysis (Fig 47). The embedded graph shows the opposing displacement of both isotherms in response to a wind event. The time series of isothermal depth were band-pass filtered with cutoff frequencies of 1/10 and 1/9 h^{-1}. 135

Figure 49 – Summary of the main findings related to the mechanism of wave dissipation observed during upwelling events and internal seiche activity. Explanations are provided in the text. 137

Figure 50 – Internal bore generated as a result of the degeneration process of basin-scale internal wave (Simulation: Run 23) 166

Figure 51 – Thermal and wind speed condition in Harp Lake. a) Wind speed time series (Harp Lake; 25/09 – 04/10). b) Isotherms time-series in height above the bottom (h.a.b.) 169

Figure 52 – a) Power spectral density of the isotherms of 12 °C and 8 °C. Dashed lines show the mean red noise spectrum for the time series, indicating significant peaks at a 95% confidence level. b) spectral phase analyses considering just coherence higher than 80% (Harp Lake; 25/09 – 05/10), c) Vertical temperature profile obtained from Harp Lake in 2nd of October 2013 at 5 a.m., d) Zoom-in view of the temperature profile with a second profile 2 h late, which is approximately half of the internal seiche period. At 22 m above the bottom the water becomes warmer, which leads to an erosion of the 12 °C isotherm due to internal seiche passage. However, 2 m bellow that point, the water becomes colder due to the elevation of the 8 °C isotherm, that was caused by the oscillation of the second interface, clearly out-of-phase with the 12 °C isotherm. e) a sketch of the V2 mode that is presented in item (d). 170

Figure 53 – Longitudinal sections of water temperature and horizontal flow velocity in Passauna Reservoir in response to an idealized 8-h wind episode (scenario M2B2) and with observed wind forcing. a) Water temperature and b) longitudinal flow velocity for scenario M2B2. c) Water temperature and d) longitudinal flow velocity simulated with observed wind dynamics and measured initial water temperature profile. The temperature distribution was obtained at the end of the wind episode, which was at $t = 8$ h in a), while for the measured data the end of the wind episode was characterized by the end of a strong wind event measured on 29 June at 21 h 20 min (cf. Fig. 31 in the main text). The horizontal velocities are shown at the end of the wind event, during the initial seiche excitation. The solid black lines in a) and c) mark isothermal depth with 1.0 °C increment. 181

Figure 54 – Hydrodynamic characterization of the analyzed period P1. a) Simulated horizontal flow velocity during the upwelling event on June 29 (2018) at 17 : 00 h. The black arrows illustrate the horizontal velocity direction and magnitude near the water surface (2 m depth). The color scaling shows opposing (northward) flow in the hypolimnion (8 m above the deepest part of the reservoir). Power spectral density of b) observed, and c) simulated time series of horizontal flow velocity at two different depths at the monitoring station (red dot in Fig. 29a in the main text). For low-frequencies (10^{-6} to 10^{-4} Hz), the spectra were calculated with a window size of 3 d, while in the high-frequency range (up to 10^{-4} Hz), we used a window size of 12 h. The dashed lines show the 95% confidence limit of the mean red noise spectrum estimated for each time series. The vertical black dashed line marks the buoyancy frequency ($N = 0.02$ Hz), and the vertical solid black line shows a 24-h period. 183

Figure 55 – The influence of bathymetry on internal seiches analyzed in scenario M1B2 (straight channel with sloping water depth) for nearly two-layer stratification ($\sigma = 0.2$ m) in response to a wind event from southern direction (from the left towards the dam). a) Temperature distribution along the longitudinal cross section of the reservoir during the wind set-up ($t = 0.3$ d) and b) the longitudinal flow velocity distribution at $t \approx 38.5$ h. c) Time series of horizontal velocity profiles at the basin center. The solid lines illustrate the exponential wave energy decay (see labels for decay rates, in which t is defined in days). 185

Figure 56 – Temporal dynamics of the vertical profiles of horizontal flow velocities near the center of the reservoir (station S1, velocity indicated by color) for scenario a) M1B1 $\sigma = 0.2$ m, b) M1B1 $\sigma = 30$ m, c) M2B1 $\sigma = 0.2$ m, d) M2B1 $\sigma = 30$ m, e) M1B2 $\sigma = 0.2$ m, f) M1B2 $\sigma = 30$ m, g) M2B2 $\sigma = 0.2$ m, and h) M2B2 $\sigma = 30$ m. The vertical black dashed lines mark the end of the wind event. 187

Figure 57 – Simulated water temperature, horizontal flow velocity, bed shear stress, and depth-integrated energy dissipation rates at the center line of Passaúna reservoir for scenario M1B2. a) Longitudinal cross section of water temperature (at $t = 7$ h 12 min) and b) horizontal velocity (at $t = 7$ h 12 min). Light and dark red lines show time series of integrated turbulent energy dissipation rates during the first interaction with the lakeshore for scenario M1B1 with $\sigma = 0.2$ m and $\sigma = 30$ m, respectively. Bed shear stress for c) $\sigma = 0.2$ m and d) $\sigma = 30$ m at the center line of Passaúna reservoir. High shear stress observed after the wind event (above the dashed white line) at the center of the basin (4500 m from the dam) indicates the response of internal seiche, since higher horizontal velocity are observed near the wave node (seiche response). Right after the end of the wind event high shear stress is observed near the shore, where the current shear across the density interface interacts with the bottom slope, at 6200 m from the dam (wave interaction). This occurs due to the acceleration of the flow near the sloping bottom, causing a up sloping current. This event persists for more wave periods (wave interaction) but promoting lower shear stresses since most part of the energy has been dissipated during the first interaction. 189

Figure 58 – Vertical stratification during the analysis periods at the sampling site near the intake station (Fig. 29a in the main text): a) P1 (from June 28 to July 04, 2018) and b) P2 (from January 29 to February 04, 2019). Both panels show the mean vertical profiles of simulated (blue dots) and measured (red solid line) temperature, with their standard deviations marked by the blue and red shaded areas. The purple dashed lines show the root mean square difference between simulations and observations. 195

Figure 59 – Comparison of measured and simulated horizontal flow velocities for period P1 (weaker stratification) and P2 (stronger stratification). a) Normalized root mean square difference (NRMSD) of the horizontal velocity difference between measured and simulated data for different velocity classes for period P1 (black) and P2 (red). The boxes extend over the 25th and 75th quartiles, whilst the horizontal line indicates the median value. The whiskers extend to the minimum and maximum values neglecting outliers, which are represented by gray dots. b) Period of time (in percentage) that the direction of simulated horizontal velocities agreed with measured data for both periods and for different velocity classes. Crosses and triangles represent data from near the reservoir bottom (2.5 m above the bottom) and near the water surface (9 m above the bottom), respectively. c) Power spectral density of horizontal velocity variations at approximately 2.5 m above the bottom for measured (purple) and two simulations (blue and green). The solid blue line represents the spectral density of simulations using the standard grid size of our scenario analyses, whilst the solid green line represents PSD obtained from a coarser numerical grid. The colored shaded area shows the 95% confidence interval. 196

Figure 60 – Regime diagram for the classification of mixing dynamics in a stratified basin in response to wind forcing. Different color separate four mixing regimes based on the Wedderburn number (W) and the epilimnion thickness (h) normalized by the total water depth H (considering a rectangular-shaped basin). Solid lines shows regime boundaries according to the classification scheme of Spigel and Imberger (1980), text labels show the respective equations. The diagram presented here assumes $H/L = 0.01$, but even for other value the variation is relatively small, keeping the same order of magnitude of W. 200

Figure 61 – Time-series of internal wave energy (E_{wave}) and the procedure to remove the background flow from the basin-integrated kinetic energy (Eq. 4.2 in the main text). Red and blue dots represent the identified maximum and minimum values from the time-series of basin-integrated kinetic energy, respectively. Red solid and blue dashed lines represent the total energy decay and the background flow decay, respectively. Green blue dot is the internal wave energy obtained from the difference between the basin-integrated kinetic energy (red dots) and the function of the background flow energy (blue dashed line), in which the first green dot (red arrow) describes the initial energy of the internal wave ($E_{\mathrm{wave}}^{\mathrm{max}}$). k is the internal wave damping coefficient (Eq. 4.3 in the main text). 201

List of Tables

Table 1 – Output parameters provided by Interwave Analyzer. 125
Table 2 – Description of Interwave Analyzer subprograms (modules). 126

Table 3 – Summary of collected data from simulated cases. h_e and H indicate the epilimnion and total water depth, respectively. $E_{\text{dissipation}}$ represents the internal wave energy that is dissipated in the first wave cycle. ζ_o is the measured initial vertical displacement.$Ri_{\text{min}}\ h_e/L$ and $Ri_{\text{max}}\ h_e/L$ are the minimum and maximum values from theoretical results in which internal wave activity should be dominant in the lake interior, respectively. $Ri\ h_e/L$ was obtained from numerical results. 166
Table 4 – Summary of processed results from simulated cases. Linear theory indicates the ζ_o/h_e obtained from linear theory (SPIGEL; IMBERGER, 1980). $g(h_e/H)_{\text{lin}}$ and $g(h_e/H)_{\text{pol}}$ represents the ζ_o/h_e estimated by the parametrized equation (Eq. 3.8) using the linear and polynomial expression of g-function, respectively. *Obs. regime* indicates the observed regime of lake mixing, whilst the *Degeneration* describes, according to theoretical results derived from Horn, Imberger and Ivey (1998), the regimes for internal seiches degeneration. 167

Table 5 – List of physical and numerical parameters used in numerical simulations of the baseline and hypothetical scenarios with Delft3D. *10 days have been simulated for baseline and hypothetical scenarios, however, for baseline simulations (validation simulations) the first 4 days have been used for model spin-up and were discarded from further analysis. **Heat flux model has been applied only for the baseline scenario, and neglected for hypothetical scenarios. 192

Table 6 – Damping coefficients for all hypothetical scenarios. σ is the standard deviation describing the Gaussian form of the buoyancy-frequency profile, in which $\sigma = 0.2$ m indicates that the basin approximates to a two-layer stratification and $\sigma = 30$ m indicates that the basin presents a linear stratification condition from surface to bottom. 193

List of symbols

ρ_a	Air density
ω	Angular frequency
N	Buoyancy frequency
Ri	Bulk Richardson number
Ri_{filtered}	Bulk Richardson filtered by wind duration and/or wind duration
Ri_{V1}	Bulk Richardson number for a two-layer system
Bu	Burger number
σ	Characterize the stratification profile
k_1	Constant for minimum energy
Ri_{crit}	Critical bulk Richardson number
ρ	Density
$\Delta\rho$	Density gradient
T_{wind}	Duration of wind event
k_3	Empirical constant
ρ_e	Epilimnion density
h_e	Epilimnion thickness
g	Gravitational acceleration
u	Horizontal flow velocity
ρ_h	Hypolimnion density
h_h	Hypolimnion thickness
ζ	Interfacial displacement
ν	Kinematic eddy viscosity coefficient
E	Kinetic energy
Δh	Metalimnion thickness
c	Phase speed
g'	Reduced gravity
L	Reservoir length
B	Reservoir width
ΔT	Temperature gradient

D_T	Thorpe length scale
H	Total water depth
k_2	Universal constant
κ_v	Von Kármán constant
a	Wave amplitude
k	Wave damping coefficient
E_{wave}	Wave energy per half wave cycle
k_j	Wave number for layer j
T_{VnHm}	Wave period for specific mode (VnHm)
λ	Wavelength
W	Wedderburn number
W_{V1}	Wedderburn number for a two-layer system
C_D	Wind drag coefficient
f_{dur}	Wind duration factor
$u_{wind}*$	Wind friction velocity
U_{10}	Wind speed 10 meters above the surface
τ	Wind stress

Contents

Preface 33

1 Introduction 35

1.1 Research question and hypothesis 38

1.2 Outline 39

1.2.1 An empirical parametrization of internal seiche amplitude including secondary effects 40

1.2.2 Physical mechanisms of internal seiche attenuation for non-ideal stratification and basin topography 40

1.2.3 Internal wave analyzer for thermally stratified lakes 40

2 Literature Review 41

2.1 Dynamic of stratified lakes 41

2.1.1 Surface Boundary Layer 42

2.1.1.1 Surface heat flux 42

2.1.1.2 Turbulent Kinetic Energy 43

2.1.1.3 Heat-induced in the surface boundary layer 44

2.1.1.4 Wind-induced in the surface boundary layer 47

2.1.2 Mixing in the lake interior 48

2.1.3 Stable interior layer 50

2.1.3.1 Basin-scale internal wave 52

2.1.3.2 High-frequency internal waves 55

2.1.3.3 Mixing on the stable interior 57

2.1.4 Bottom Boundary Layer 58

2.1.4.1 Mixing on the bed boundary layer 59

2.2 Mathematical description 61

2.2.1 Internal wave model 61

2.2.1.1 Hydrostatic multi-layer model 62

2.2.1.2 Continuous stratification model 63

2.2.1.3 Internal seiche amplitude 65

2.2.2 Modeling of heat transport: Delft3D-FLOW 67

2.2.2.1 Governing equations 67

2.2.2.2 Heat flux model 69

2.2.2.3 Turbulence model 70

2.2.2.4 Numerical aspects 71

3 An empirical parametrization of internal seiche amplitude including secondary effects 73

3.1 Introduction 74

3.2 Methods 76

3.2.1 Site description and Data collection 76

3.2.2 Data treatment 78

3.2.3 Numerical simulation 78
3.2.4 Spectral Analysis 79
3.2.5 Internal Seiche Model 80
3.2.6 Characteristic parameters 81
3.3 Results and discussions 81
3.3.1 Spectral Analysis and seiche model 81
3.3.2 General comparison 83
3.3.3 Numerical simulations and spatial variations 86
3.3.4 Parametrization 90
3.4 Conclusion 95

4 Physical mechanisms of internal seiche attenuation 97
4.1 Introduction 98
4.2 Materials and Methods 99
4.2.1 Site description 99
4.2.2 Data collection 100
4.2.3 Numerical model 101
4.2.4 Baseline scenario 101
4.2.5 Hypothetical scenarios 102
4.2.6 Internal seiche energy 103
4.3 Results 104
4.3.1 Reservoir hydrodynamics during field monitoring 104
4.3.2 Response to a wind event 105
4.3.3 Identification of factors influencing attenuation 106
4.3.3.1 Effects of density stratification 106
4.3.3.2 Effect of reservoir morphology 107
4.3.3.3 Effect of bathymetry 108
4.3.3.4 Combined effects of morphology and bathymetry 109
4.4 Discussion 109
4.4.1 Model validation and internal seiches in Passaúna Reservoir 109
4.4.2 Generation of internal seiches 111
4.4.3 Mechanisms of internal seiche damping 111
4.4.4 Physical and ecological implications 112

5 Internal wave analyzer for thermally stratified lakes 115
5.1 Introduction 116
5.2 Internal wave dynamics and mixing classification 118
5.2.1 Modal model for basin-scale internal waves 118
5.2.2 Wave generation and mixing 119
5.3 Methods 122
5.3.1 Input data processing 122
5.3.2 Input data and configuration 125
5.3.3 Overview and program structure 125
5.4 Results and discussions 126
5.4.1 Case Studies 126

5.4.1.1 Rectangular-shaped box 126
5.4.1.2 Vossoroca Reservoir 131
5.4.2 Software availability and performance 135
5.5 Conclusion 136

6 Discussion 137
6.1 Internal seiche generation and detection 137
6.1.1 Internal seiche destabilization due to wave interaction on slopping boundaries . . . 138
6.1.2 Self-induced mixing during upwelling event 139
6.1.3 Internal wave disintegration due to reservoir bends 140
6.1.4 Effects of stratification profile on the internal seiche generation 140
6.1.5 Effect of the interaction between internal seiche and water surface on internal seiche generation 141
6.2 Research Limitation and recommendation for future investigations 141

7 Conclusion 145

References 147

APPENDIX A Linearization 163

APPENDIX B Rectangular shaped-box simulations 165

APPENDIX C Harp Lake 169

APPENDIX D Additional calculation 173
D.1 wind parameters 173
D.2 Thermocline depth and metalimnion boundaries 173
D.3 Mean wind direction 174
D.4 Equation of state 174
D.5 Multi-layer internal wave model 175
D.6 Decomposition model 176
D.7 Spectral analysis 176

APPENDIX E Running Interwave Analyzer in a python interpreter 179

APPENDIX F Longitudinal cross sections 181

APPENDIX G Hydrodynamic characterization (Period P1) 183

APPENDIX H Downwelling at sloping bottom 185

APPENDIX I Horizontal flow velocity of hypothetical scenarios 187

APPENDIX J Effects of sloping boundary 189

APPENDIX K Numerical parameters 191

APPENDIX L Damping Coefficients **193**

APPENDIX M Model validation **195**

APPENDIX N Lake classification **199**

APPENDIX O Internal wave energy **201**

ANNEX A Author contributions **203**

A.1 Internal seiche parameterization 203
A.2 Physical mechanisms of internal seiche attenuation 203
A.3 Internal wave analyzer 203

Preface

This document is an extended version, with a literature review, of the thesis submitted to University of Kaiserslautern-Landau, Faculty of Natural and Environmental Sciences and to Federal Univesity of Paraná for the partial fulfillment of requirements for a Doctor of Natural Sciences and Doctor of Environemntal Engineering, respectivelly. The original version can be found at https://kluedo.ub.rptu.de/frontdoor/index/index/docId/7389

This thesis is presented in a manuscript-based format and is composed of three original manuscripts, each containing a succinct introduction with a relevant literature review, methods, results and discussion, including a general conclusion. A general introduction (Chapter 1) is used to motivate the overall study.

The first manuscript, available in chapter 3, is published in *Environmental Fluid Mechanics* under the title **An empirical parametrization of internal seiche amplitude including secondary effects** by de Carvalho Bueno, Bleninger, Yao, and Rusak (doi: 10.1007/s10652-020-09767-1). Original, modeling and pre-processed data to support the findings are available at https://github.com/buenorc/empaper.git (DOI: 10.5281/zenodo.4264546).

The second manuscript, available in chapter 4, is published in *Environmental Fluid Mechanics* under the title **Physical mechanisms of internal seiche attenuation for non-ideal stratification and basin topography** by de Carvalho Bueno, Bleninger, Boehrer, and Lorke (doi: 10.1007/s10652-023-09928-y). The pre-processed data to support the findings are available at https://github.com/buenorc/wepaper (DOI: 10.5281/zenodo.5708040).

The third manuscript, available in chapter 5, is published in *Environmental Modelling and Software* under the title **Internal wave analyzer for thermally stratified lakes** by de Carvalho Bueno, Bleninger, and Lorke (doi: 10.1016/j.envsoft.2020.104950). The manuscript describes a software developed to analyze internal waves in lakes and reservoirs. Interwave Analyzer version 1.00.3 and the input data to support the results of this manuscript are available at https://github.com/buenorc/espaper.git (DOI: 10.5281/zenodo.4264546).

The Interwave Analyzer codes are available at https://github.com/buenorc/interwaveanalyzer.git. The complete documentation can be found at https://sites.google.com/view/interwaveanalyzer/manual. For more information, see https://sites.google.com/view/interwaveanalyzer/interwave-analyzer

Chapter 6 brings together the insights from each of the three manuscripts. Chapter 7 provides an answer to the main research question.

The work contained in this thesis is wholly my own, although carried out under the supervision of Professors Tobias Blenninger and Andreas Lorke. Huaxia Yao and James A. Rusak from the Dorset Environmental Science Centre (Ontario, Canada) provided Harp Lake data and helped in general discussions related to Harp Lake and general aspects of lake mixing. Bertram Boehrer has help on the discussion of the wave dissipation and how these data could be applied into a mode decomposition to explain how the seiche energy is distributed into different vertical modes.

PS: Symbols may differ from the published version to maintain consistency between the variables presented in different chapters of this document.

1 Introduction

> *"The present investigation of "Dead-Water" was occasioned by a letter in November 1898 from Prof. NANSEN asking my opinion on the subject. In my reply to Prof. NANSEN, I remarked that in the case of a layer of fresh water resting on the top of salt water, a ship will not only produce ordinary visible waves at the boundary between the water and the air, but will also generate invisible waves in the salt-water fresh-water boundary below; I suggested that the great resistance experienced by the ship was due to the work done in generating these invisible waves."*
>
> Vagn Walfrid Ekman (1904)

Internal gravity waves are an ubiquitous oscillatory response of thermal stratified lakes to wind forcing (MORTIMER, 1952), which can persist for hours to days even after the wind stops (MÜNNICH; WÜEST; IMBODEN, 1992; ROGET; SALVADÉ; ZAMBONI, 1997). Studies have shown that large-scale internal waves are the main source of kinetic energy in the stable interior (LORKE, 2007; LORKE; UMLAUF; MOHRHOLZ, 2008) and in the bottom boundary layer of lakes and reservoirs (WÜEST; LORKE, 2009).

The wind that blows over the lake acts as a primary source of momentum. Although most are used to accelerate the upper layer, favoring surface tilt (BOEGMAN, 2009) and dissipation by mixing in the surface boundary layer (WÜEST; PIEPKE; SENDEN, 2000), a significant fraction that is carried to the stable interior is used to energize the field of internal seiches (WETZEL, 2001; WÜEST; LORKE, 2003; BOUFFARD; BOEGMAN, 2012). Part of the wind energy that crosses the surface boundary layer pushes down the thermocline, creating a vertical displacement in which one side of the lake experiences an upwelling, while the opposite side experiences a downwelling event (Figure 1). Depending on the stratification condition, different internal wave modes may be excited due to the unbalanced pressure distribution in each layer interior, creating an out-of-phase response between interfacial layers (LAZERTE, 1980; MÜNNICH; WÜEST; IMBODEN, 1992; VIDAL et al., 2005; ROGET; SALVADÉ; ZAMBONI, 1997).

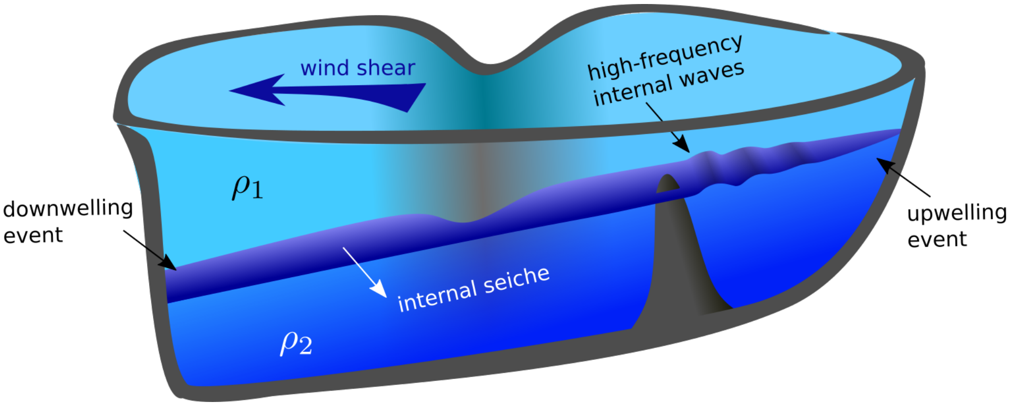

Figure 1 – Schematic overview of internal seiche and high-frequency internal waves. Different shades of blue denote layer of different density, in which $\rho_2 > \rho_1$. Silver layers indicate the solid bathymetry of the lake.

Large-scale internal waves play a crucial role in the dynamic of lakes and reservoirs, affecting the biogeochemical cycle. Strong turbulence induced by internal waves promotes mixing (OSTROVSKY et al., 1996; LOZOVATSKY; ROGET; FERNADO, 2005) and accelerates vertical and horizontal transport

(ANTENUCCI; IMBERGER; SAGGIO, 2000) in lake interior. The break of the internal wave (ETEMAD-SHAHIDI; IMBERGER, 2006; LORKE, 2007) and self-induced shear caused by the internal wave (PREUSSE; PEETERS; LORKE, 2010) are the predominant source of turbulence and mixing in the stable interior.

In the bottom boundary layer (BBL), internal waves induce a turbulence level 30 times higher than the magnitude found in the stable layer (WÜEST; LORKE, 2009). Turbulence in BBL is often induced by baroclininc activities (BOUFFARD; LEMMIN, 2013) and their interactions on slopes, which promote local convective turbulence due to instabilities (IVEY; WINTERS; SILVA, 2000; LORKE; PEETERS; WÜEST, 2005; LORKE; UMLAUF; MOHRHOLZ, 2008). The turbulence induced by internal seiche can contribute to the mixing between hypolimnetic and metalimnetic volumes, improving the transport and resuspension of sediment, nutrients, and chemical components. Recently, observations have also identified that turbulence convection is also generated by large internal seiches (HAREN; DIJKSTRA, 2021).

Studies have identified that, combined with surface waves, large-scale internal waves play an important role in photosynthetic activity (EVANS; MACINTYRE; KLING, 2008). Observations have suggested that the biomass of cyanobacterial and phytoplankton is strongly affected by internal seiche (MORTIMER; HORN, 1982; RINKE et al., 2007; PANNARD; BORMANS; LAGADEUC, 2008; PANNARD et al., 2011; CUYPERS et al., 2011; HINGSAMER; PEETERS; HOFMANN, 2014).

Studies have revealed that sediment resuspension events can be induced by propagating internal waves (STASTNA; LAMB, 2008) and internal seiches (FRINDTE et al., 2013; SAKAI et al., 2002), which may also facilitate the penetration of oxygen into the deeper sediment layer, which favors microbial activities (FRINDTE et al., 2013). Furthermore, an increase in turbidity due to the resuspension of sediments induced by internal waves can amplify the concentration of dissolved methane near thermocline regions (SAKAI et al., 2002). New evidence has suggested that internal seiche plays a pivotal role in the dynamics of greenhouse gases in lakes (STEPANENKO et al., 2016).

Most mathematical formulations that predict the magnitude of the upwelling events and the maintenance of internal seiche activity are based on idealized conditions, which take into account the stratification condition, the length of the basin and the speed of the wind (SPIGEL; IMBERGER, 1980; SHINTANI et al., 2010; PATTERSON; HAMBLIN; IMBERGER, 1984). The Wedderburn number (W) and the derived W-based classification scheme have been used to predict persistent upwelling events and internal seiche activity (SPIGEL; IMBERGER, 1980):

$$W = \frac{g' \ h_e^2}{u_*^2 \ L}, \tag{1.1}$$

in which h_e is the thickness of the epilimnion, L is the lake length, g' is the reduced gravity, and u_* is the wind stress.

Although this theoretical framework is based on idealized conditions; e.g., two-layer system, rectangular basin, regular wind events, and no turbulence production near lake boundaries (SPIGEL; IMBERGER, 1980; PATTERSON; HAMBLIN; IMBERGER, 1984; SHINTANI et al., 2010), studies suggest that simplified mathematical formulations are reasonable predictors of upwelling events and subsequent energy relaxation (VALBUENA et al., 2022; ANTENUCCI; IMBERGER; SAGGIO, 2000; MACINTYRE et al., 2009; ROBERTS et al., 2021). However, the generation of internal seiche may be influenced by many factors. Observations have suggested that the higher horizontal (BOEGMAN; IVEY, 2012) and vertical (VIDAL; RUEDA; CASAMITJANA, 2007) modes may be affected by the wind forcing frequency. Evidence has identified that wind resonance amplifies internal seiche (ARNON et al., 2019). The bathymetry of the lake and the slope of the lakeshore may also influence the formation and evolution of internal seiches (FRICKER; NEPF, 2000;

IMAM et al., 2020). Based on the baroclinic moment about the central volume of the lake, studies have proposed an integral form of the Wedderburn number, the Lake Number, to analyze the occurrence of internal seiche and lake mixing regimes, incorporating the basin shape and the effects of water column stratification (IMBERGER; PATTERSON, 1989; STEVENS; IMBERGER, 1996). The Lake number has been extensively investigated by many researchers (MACINTYRE et al., 1999). Although this dimensionless quantity incorporates bathymetry and continuous stratification, the effect is limited to the balance of moments around the central volume of the lake, neglecting the mixing effects caused by the interaction between the internal seiche and the sloping bathymetry.

Despite the huge number of publications that describe different mechanisms that can contribute to the increase of dissipation rates and accelerate the wave damping of internal seiches in thermally stratified lakes, many details of their application to field observations are site-specific and do not evaluate the effect of combining different mechanisms of wave dissipation. A unified framework to show the influence of these complexities in wide-range applications is currently lacking, which could help to identify when upwelling events and subsequent energy relaxation could be predicted by simplified mathematical formulations and when we should be aware of the limitations.

In addition, most of the time, the analysis of internal waves in lakes requires a costly and time-consuming effort to process and analyze the results of the numerical model and field observation. There is a lack of adequate tools to provide a unique framework for analyzing internal waves, combining a consistent and universal technique with theoretical results from the wide literature.

1.1 Research question and hypothesis

This study aims to provide a consistent and universal technique for describing the internal wave field in a wide range of lakes and reservoirs, quantifying the effect of different mechanisms that can contribute to inhibiting or accelerating the dissipation of basin-scale internal waves, highlighting which analyzed mechanisms influence more the W-based classification often used to predict upwelling events and internal seiche occurrence in thermally stratified lakes with non-ideal stratification and basin topography.

In light of the foregoing discussion, we work toward answering one main question:

QUESTION: How bathymetry, morphology, continuous stratification, shear layer mixing, and interaction between the internal seiche and the water surface can inhibit the formation of basin-scale internal waves in lakes and reservoirs with non-ideal stratification and basin topography?

HYPOTHESIS 1: A sloped reservoir bed contributes to wave dissipation by wave destabilization and breaking mechanisms. Destabilization of the bottom boundary layer induced by wave break may not only have consequences for local diapycnal diffusivity (LORKE, 2007; COSSU; WELLS, 2013), but could contribute to extract significant energy from basin-scale internal waves, inhibiting the formation of internal seiches in thermally stratified lakes with a gentle slope bed.

HYPOTHESIS 2: Basin bends from complex morphology reservoirs promote shear instability along meander bends near the thermocline region, promoting an increase in dissipation rates caused by the interaction between the internal seiche and lateral boundaries. Although strong meander bends can promote the formation of internal seiches of higher horizontal modes (VIDAL et al., 2013), when a fundamental internal seiche is generated, the lateral shear stress can contribute to an increase in energy dissipation, extracting energy from the mean flow (SILVA; BUIJSMAN; MAGALHAES, 2015).

HYPOTHESIS 3: Self-induced mixing generated by basin-scale internal waves in a miscible two-layer system may promote attenuation of the internal seiche amplitude. Although shear instability is expected when the Richardson number falls below 0.25 (YEATES; GÓMEZ-GIRALDO; IMBERGER, 2013), isotherms can be strongly disturbed, inducing irreversibly mixing in the vicinity of this critical value, favoring the mixing processes and the transference of energy from basin-scale internal waves to small scale of turbulence, a process that would result in attenuation of internal seiche amplitude.

HYPOTHESIS 4: Continuous stratification (e.g. linear stratification) may inhibit the formation of basin-scale internal waves that would be predicted under favorable meteorological conditions by model schemes based on a two-layer system. Observations from Passaúna reservoir suggested that one of the reasons that wind-induced flows did not cause internal seiches was due to a more continuous vertical density gradient (ISHIKAWA; BLENINGER; LORKE, 2021).

HYPOTHESIS 5: Upwelling events in lakes with a shallow epilimnion are susceptible to strong surface temperature drops due to the thermocline breaking the surface, promoting mixing and contributing in inhibiting the generation of internal seiche. Since surface buoyancy flux and wind are a source of turbulent kinetic energy (TKE) in the surface boundary layer (SBL), which can lead to increased mixing in this layer (WÜEST; LORKE, 2003), the interaction between internal waves and the higher level of TKE promoted in the SBL can contribute to extracting energy from the basin-scale internal wave, inhibiting its evolution.

1.2 Outline

Field measurements and numerical simulations were performed and analysed to test the hypothesis that could explain the inhibition and strong internal seiche damp observed in field measurements. The water temperature and the wind characteristics were monitored in three medium to small basins for at least one year. In one of the reservoirs studied, the flow velocity was monitored using an acoustic Doppler current profiler with high temporal and spatial resolution. Three-dimensional hydrodynamic simulations were carried out to investigate the mechanism associated with each hypothesis (Figure 2). Hydrodynamic models were set up to reproduce the mechanisms in simplified systems, in order to investigate deeply the physical processes behind each mechanism and how they could influence the generation and evolution of internal seiche in thermally stratified lakes even under meteorological conditions in which lake classification model schemes based on rectangular shaped-box tank predict the dominance of internal seiche activity.

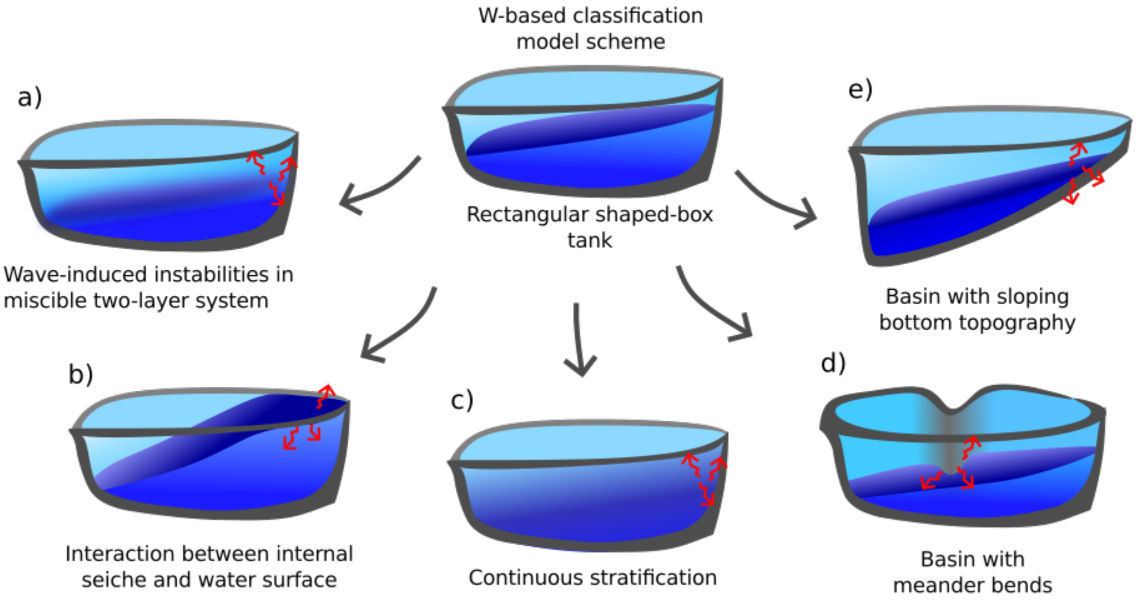
W-based classification model scheme
Rectangular shaped-box tank
a)
Wave-induced instabilities in miscible two-layer system
e)
Basin with sloping bottom topography
b)
Interaction between internal seiche and water surface
c)
Continuous stratification
d)
Basin with meander bends

Figure 2 – Summary of the main mechanisms investigated that can contribute to inhibit the generation of internal seiche or accelerate the internal wave damping.

The thesis consists of three original manuscripts (Chapters 3 - 5), which contain the main findings to answer the main research question of this study.

1.2.1 An empirical parametrization of internal seiche amplitude including secondary effects

de Carvalho Bueno, R., Bleninger, T., Yao, H., and Rusak, J. A. (2021). An empirical parametrization of internal seiche amplitude including secondary effects. *Environmental Fluid Mechanics*, 21(1), 209-237. doi: 10.1007/s10652-020-09767-1 (Chapter 3)

The analysis of the influence of the mixing mechanism generated on the wave crest due to the destabilisation of the miscible layers (**H.3**) and the interaction of the internal seiche with turbulent surface water (**H.5**) on the internal seiche amplitude was performed using underwater temperature data obtained from a numerical simulation set up in a rectangular shaped-box tank. The results were compared with the temperature and meteorological data obtained from the Vossoroca reservoir and Harp Lake.

1.2.2 Physical mechanisms of internal seiche attenuation for non-ideal stratification and basin topography

de Carvalho Bueno, R., Bleninger, T., Boehrer, B., and Lorke, A. (2022). Physical mechanisms of internal seiche attenuation for non-ideal stratification and basin topography. Submitted to *Journal of Limnology and Oceanography* (Chapter 4)

Expanding the potential effect of the real basin on the internal seiche field, non-ideal stratification, and basin topography were investigated through numerical simulations and field measurements performed in the Passaúna reservoir. Hypothetical scenarios were created and simulated to investigate the influence of reservoir bends (**H.2**), sloping bottom (**H.1**), and non-ideal stratification profile (**H.4**) on the magnitude of energy transferred from the wind to the internal seiche and the influence of these mechanisms on internal seiche damping. The results have been compared with the physical effects observed through field measurements, which were also correlated with numerical simulations performed to reproduce the hydrodynamics of the Passaúna reservoir.

1.2.3 Internal wave analyzer for thermally stratified lakes

de Carvalho Bueno, R., Bleninger, T., and Lorke, A. (2021). Internal wave analyzer for thermally stratified lakes. *Environmental Modelling and Software*, 136, 104950. doi: 10.1016/j.envsoft.2020.104950 (Chapter 5)

More than 45 numerical simulations were performed to answer the main research question of this thesis. To test the hypothesis **H.1**, **H.2**, **H.3**, **H.4**, and **H.5**, facilitate the interpretation of each simulation, and facilitate the analysis of internal seiches for those without special knowledge in fluid dynamics, an open source software has been implemented in Python scripting language to provide an in-depth analysis of internal seiches and lake mixing regimes. The software requires time series of water temperature from various depths and meteorological data (wind speed and direction), performing analysis of temperature fluctuations by Fourier and Wavelet transforms, wave periods by multilayer models, and also derives indices to describe and characterize the excitation of internal waves and lake mixing regimes.

2 Literature Review

"Do not fear that their ships are winged with a hundred oars:
their fleet rides an unwilling sea."
Propertius, Elegies (16 BC)

This chapter is divided into two main sections. A general description of the physical processes that contribute to the lake dynamic is provided in section 2.1, whilst the modeling aspects are discussed in section 2.2. The processes involved in the hydrodynamics of lakes are discussed individually for each layer, which includes a characterization of the surface boundary layer, stable interior, and bottom boundary layer. Additional subsections are included to describe the mechanical interaction between different layers and potential physical processes that could lead to a different configuration of these three distinct layers. Section 2.2 is also divided into two subsections: internal wave models and 3D hydrodynamic models suited to investigate the hydrodynamics of stratified lakes.

2.1 Dynamic of stratified lakes

Vertical density stratification is one of the most important processes in determining the hydrodynamics of lakes and reservoirs. Thermal stratification controls the dynamic and mixing of thermally stratified lakes and thereby drives biogeochemical fluxes along the system. The gradient of water density is generated mostly as a result of solar radiation activity, which strikes the water surface and part penetrates the water column. Combined with the convection process, the wind-induced energy flux also plays an important role in the hydrodynamic of lakes [1]. Hence, understanding the hydrodynamics of thermally stratified lakes requires a good understanding of the atmosphere-water interaction, including the processes of momentum and mechanical energy transference from air to water (WÜEST; PIEPKE; SENDEN, 2000).

Stratified lakes are characterized by a wide range of fluxes acting at different temporal and spatial scales generated by different sources of instability. Fluxes and mixing are driven by external forces, such as shear-driven mixing as a result of the wind stress acting on the water surface, or by molecular diffusion, such as double-diffusive and shear-induced convection.

In the thermal-stratified basin, mixing and transport phenomena are directly associated with thermal and mechanical energy. Energy is not evenly distributed in the water column. With respect to the hydrodynamic processes and turbulence patterns, the vertical extent may be divided into three distinct regions, in which each of them presents an individual characterization of turbulence. The system can be divided into the surface boundary layer (SBL), stable interior, and bottom boundary layer (BBL). In the next sections, we present some details, defining the energy fluxes path for each layer. We start our analysis by looking at the closest layer to the water's surface.

---

[1] In this work we often use the word *lakes* to refer to all types of thermally stratified basins, including lakes, reservoirs, and ponds

2.1.1 Surface Boundary Layer

In lakes, the upper layer called the surface boundary layer (SBL) is a region of constant heat, gases, and momentum fluxes and consequently is a highly turbulent region with an average thickness of 5 m, which may vary according to local temperature stratification, wind field, and among others. The SBL is the most complex region due to the constant physical quantities that exchange between water and air (BOUFFARD; WUEST, 2018). In addition, the surface wave plays an additional complexity in the interaction between the atmosphere and SBL.

The SBL is located in the upper layer of the epilimnion, a warmer oxygen-rich region that provides favorable conditions for microorganisms at the base of the aquatic food web, and consequently is important to the biodiversity of lakes.

2.1.1.1 Surface heat flux

Short-wave radiation is not the only source of heat flux between water and the atmosphere. Total heat flux at the water surface is a combination of long-wave radiation (infrared and water surface radiation), evaporation, precipitation, heat convection, and fluxes from inflows and outflows. Figure 3 illustrates the importance of some components for the heat balance of the lake in different seasons of the year. When the heat balance is positive, heat is stored in the lake, which often occurs during the summer season. During winter, the lake loses heat and, consequently, most of the heat energy is transferred to the atmosphere. Heat flux may also present a component of daily variation, which is created by the difference in heat flux during daytime and nighttime.

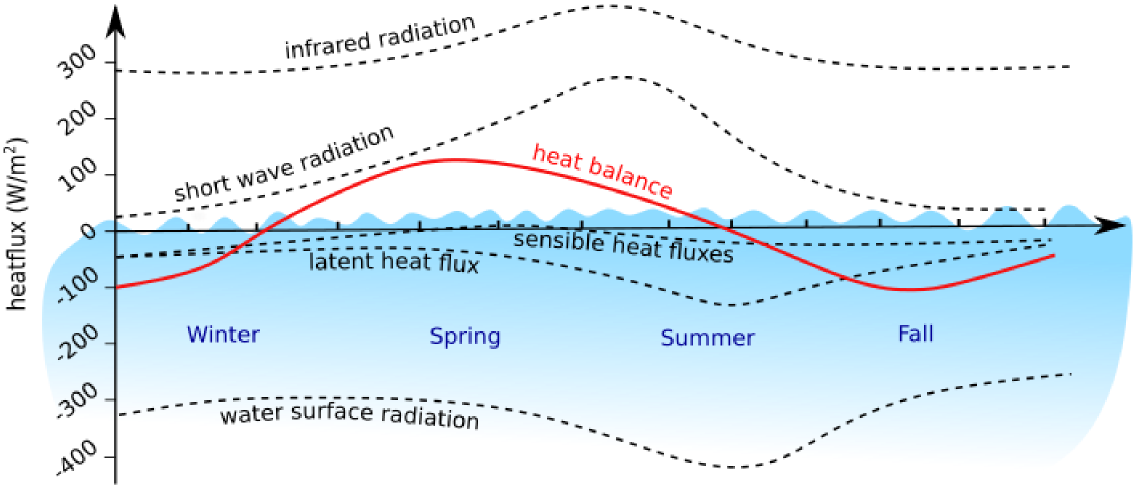

Figure 3 – Illustration of the heat flux (monthly mean) estimation based on measurements from Lake Zurich (which is located in the northern hemisphere) by Imboden and Wüest (1995). x-axis indicates the time (season) variation. y-axis shows the amount of monthly mean heat flux between water and atmosphere, in which negative values indicate that heat is being lost by the lake to the atmosphere (y-axis does not indicate the energy absorbed along water depth, only the heat energy that crosses the water surface). The red line represents the total balance of heat.

Due to the low heat conduction, the amount of absorbed heat decreases with depth, leading to the formation of a vertical thermal gradient, resulting in a thermally stratified system. The accumulation of heat energy in the surface layer creates a warmer upper layer, which is called the epilimnion. Often most of the heat remains in the surface boundary layer (SBL) and is transferred to deeper regions just by turbulence processes.

2.1.1.2 Turbulent Kinetic Energy

The wide range of eddies and billows present in a turbulent flow creates an additional space and time fluctuation, increasing mixing and energy dissipation. The fluctuation of a generic quantity in a turbulent flow may vary over space and time. Although the small-scale turbulence observed in lakes can be treated in most cases as isotropic (IMBODEN, 2003), numerical observations have observed the generation of anisotropic turbulence due to Kelvin-Helmholtz instabilities in stable stratified shear flow (SMYTH; MOUM, 2000). The flow can be divided based on Reynolds decomposition into two components: the contribution of the mean flow ($\overline{J}$) and the contribution of turbulent fluctuation (J'), in which J represents any generic quantity under the influence of turbulence (e.g., field velocity components, pressure, and density).

Assuming an incompressible flow under the Boussinesq approximation ($\rho \approx \varrho_o$), the momentum equation can be partitioned using the Reynolds decomposition to obtain the turbulence kinetic energy (κ) balance,

$$\begin{aligned} \underbrace{\frac{\partial \kappa}{\partial t}}_{(a)} + \underbrace{\overline{u_j}\,\frac{\partial \kappa}{\partial x_j}}_{(b)} + \underbrace{\overline{u_i' u_j'}\frac{\partial \overline{u_i}}{\partial x_j}}_{(c)} + \underbrace{\frac{1}{2}\frac{\partial}{\partial x_j}\overline{\left(u_i' u_i' u_j'\right)}}_{(d)} = \\ -\underbrace{\frac{1}{\varrho_o}\frac{\partial \overline{u_i' P'}}{\partial x_i}}_{(e)} - \underbrace{\frac{\overline{\rho' w' g}}{\varrho_o}}_{(f)} + \underbrace{\nu \frac{\partial^2 \kappa}{\partial x_j^2}}_{(g)} - \underbrace{\nu \overline{\frac{\partial u_i'}{\partial x_j}\frac{\partial u_i'}{\partial x_j}}}_{(h)}, \end{aligned} \tag{2.1}$$

in which term (a) is the change rate of turbulence kinetic energy (κ), (b) is the flux of κ in space, (c) is the rate of κ production due to interaction of the Reynolds stress and mean flow. Terms (d), (e), (f), and (g) are the transport of κ by Reynolds stress, due to gradient of pressure fluctuations, due to density change (turbulent buoyancy flux), and due to viscous stress, respectively. The last term (h) is the turbulence kinetic energy dissipation ε.

Under homogeneous conditions, neglecting the contribution of pressure and Reynolds stress on the transport of κ and considering an unsteady horizontal flow, the balance of the turbulence kinetic energy is given by

$$\underbrace{-\overline{u' w'}\,\frac{\partial \overline{u}}{\partial z}}_{\text{production}} = \underbrace{\overline{\rho' w'}\,\frac{g}{\varrho_o}}_{\text{buoyancy flux}} + \underbrace{\varepsilon}_{\text{dissipation}}, \tag{2.2}$$

in which the production is equal to the dissipated energy plus the energy stored to the buoyancy flux. Studies have suggested that the buoyancy flux varies from 5% to 20% compared to the kinetic energy dissipation (BOUFFARD; WUEST, 2018). The estimation of energy dissipation is a function of background stratification and turbulence strength. The mixing efficiency is estimated by the ratio between the total buoyancy flux and the dissipated energy:

$$\gamma_{\text{mix}} = \frac{B}{\varepsilon}, \tag{2.3}$$

in which under strong shear-mixing conditions, the mixing efficiency is $\ll 1$. Studies have indicated a typical range between 0.05 and 0.25 (WÜEST; LORKE, 2003).

Although the dissipation energy ε represents the majority of the TKE production, and consequently ε is often used to estimate the turbulence intensity, the buoyancy flux may consume a small part of the TKE production. However, when the water is unstratified, the production of turbulence is equal to the dissipation. Mathematically, from equation 2.2, this implies that

$$\varepsilon = -\overline{u'w'}\,\frac{\partial \overline{u}}{\partial z}, \tag{2.4}$$

in which u and w are the horizontal and vertical velocity components, respectively.

2.1.1.3 Heat-induced in the surface boundary layer

The convection process is a crucial physical mechanism to control the dynamic of thermally stratified lakes, which normally results from the action of gravity on an unstable density stratified system (BOUFFARD; WÜEST, 2019).

To understand the mixing and convection processes that occur within a thermally stratified lake, it is crucial to quantify the turbulent buoyancy flux (IVEY; IMBERGER; KOSEFF, 1998), which describes the amount of kinetic energy from the heat flux that is transferred from the water surface to the entire SBL when the system is stratified. The buoyancy flux per unit of area can be defined in $\mathrm{m}^2/\mathrm{s}^3$ as

$$B(z) = \frac{g}{\varrho} B_\rho = \frac{g}{\varrho}\left(\overline{\rho' w'}(z) + B_{\text{molecular}}\right), \tag{2.5}$$

in which B_ρ is the density flux.

The density flux (B_ρ) depends on the covariance of the vertical velocity and the components of the fluctuation of the water density ($\overline{\rho' w'}$). Furthermore, the density flux may also be influenced by the flux of molecular diffusion ($B_{\text{molecular}}$). However, since molecular diffusion is much smaller than the turbulent component, $B_{\text{molecular}}$ can often be neglected.

One of the most important sources of turbulent kinetic energy is the buoyancy forcing at the water's surface. This production may be computed through the surface buoyancy flux, $B(z = 0) = B_o$, which accounts for the effect of heat and evaporation [2] and is given by the energy flux divided by the water mass per unit of area. Assuming a freshwater lake, where evaporation does not produce buoyancy flux and neglects the contribution of salinity and suspended particles, surface buoyancy flux may be expressed as a function of total turbulent boundary fluxes of heat (IMBODEN; WÜEST, 1995). Mathematically, the surface buoyancy flux (density energy production) per unit of area is defined as

$$B_o = h_{\text{mix}} \frac{g}{\varrho}\frac{\partial \rho}{\partial t} \approx -\frac{g}{\varrho}\frac{\alpha\; Q{*}_{\text{total}}}{cp_{\text{water}}}, \tag{2.6}$$

where h_{mix} is the depth of the homogeneous layer with water density ρ, $cp_{\text{water}} = 4.186$ J/(g°C) is the specific heat of water, α is the thermal expansion coefficient of the water, which has a typical value equal to 10^{-4} K^{-1} for a water temperature of 11 °C. $Q{*}_{\text{total}}$ is the total net flux at the water surface, which takes into account the infrared radiation, and the latent and sensible heat fluxes, but does not consider the contribution of short-wave solar radiation, as it penetrates the water column as a volumetric source of heat instead of a boundary flux (BOUFFARD; WÜEST, 2019). Surface buoyancy flux B_o has a typical value equal to 2.4 10^{-8} W/kg (IMBODEN, 2003).

---

[2] In deep lakes, the surface buoyancy flux can be produced also by inlets, which due to the vertical extension of the lake, maybe the only mechanism to facilitate the vertical exchange of the hypolimnetic volume, providing a buoyancy flux that may vary from 10^{-9} to 10^{-7} W/kg .

Equation 2.6 is also valid to describe the buoyancy flux along the water column, the only difference is that $Q *_{\text{total}} (z)$ should be a function of the water depth.

The surface buoyancy flux (B_o) is positive when the water temperature is decreasing on the surface of the water due to thermal energy loss. This heat flux creates a downward convective plume that travels vertically, resulting in an increase in mixing efficiency, which leads to an expansion of the convective mixed layer (h_{mix}). Additionally, the downward flux increases the temperature fluctuation at the bottom of the surface boundary layer. According to Townsend (1964), this phenomenon results in a transference of kinetic energy from the vertical flux to internal wave fields.

The density flux $B_\rho \approx \overline{\rho' w'}$ (from equation 2.5) may be written through the gradient-transport (eddy diffusivity) formulation:

$$\overline{\rho' w'} = -K_\rho \frac{\partial \rho}{\partial z}, \tag{2.7}$$

which K_ρ is the diapycnal diffusivity and describes the rate of vertical exchange. K_ρ varies inversely with the stratification strength, presenting typical values between 10^{-4} and 10 m^2/s. Unlike oceans that have universal diapycnal diffusivity (PETERS; GREGG; TOOLE, 1988), in stratified lakes, the diapycnal diffusivity may change abruptly from lake to lake, influenced by internal wave breaking and stratification conditions. Studies have reported an increase in diapycnal diffusivity from 5 10^{-6} m^2/s to 5 10^{-2} m^2/s due to the passage of a shoaling high-frequency internal wave (LORKE, 2007).

Substitution of equation 2.7 into 2.6, and neglecting the molecular diffusion contribution, the buoyancy flux per unit of area is reduced to

$$B(z) = K_\rho \frac{g}{\rho} \frac{\partial \rho}{\partial z} = K_\rho N^2, \tag{2.8}$$

in which N is the buoyancy frequency, also called Brunt-Vaisalla frequency, defined as

$$N = \sqrt{-\frac{g}{\rho} \frac{\partial \rho}{\partial z}}. \tag{2.9}$$

By applying the mixing efficiency (equation 2.3) into equation 2.8, the diapycnal diffusivity (K_ρ) can be defined as

$$K_\rho = \frac{\gamma_{\text{mix}} \varepsilon}{N^2}. \tag{2.10}$$

If diapycnal shear is strong and the stratification is weaker compared to instabilities, it favors the increase of turbulence level and consequently mixing. When the system is strongly stable, the maximum scale of eddies that are deformed by buoyancy, known as the Ozmidov scale, decreases whilst the smallest scale of turbulence (Kolmogorov scale) increases. As a consequence, the inertial subrange of the turbulent spectrum is shortened. On the other hand, when the stratification strength is weaker than the instabilities, the shear stress feeds turbulent fluctuation, and as the turbulence becomes more intense, the Kolmogorov scale becomes smaller. As a result, the inertial subrange of the turbulent spectrum increases, resulting in scales that are not large enough to be deformed by shear stress and small enough to be damped by viscosity.

Although it does not appear to be related to the internal wave, the turbulence pattern is a crucial parameter to define the internal wave field, helping to understand how internal waves may degenerate within the lake interior. This is a key parameter in hydrodynamic models that are used to reproduce the internal wave field in thermally stratified lakes because their capability is limited to large-scale motion.

Eddies larger than the Ozmidov scale L_o have a strong anisotropic characteristic. Between L_o to 10 L_o, the spectrum range is called the buoyancy range and is located between the integral and inertial subrange. The Ozmidov length scale (HOLLOWAY, 1981; GIBSON, 1986) is defined as

$$L_o = \sqrt{\frac{\varepsilon}{N^3}}, \tag{2.11}$$

in which ε is the turbulence kinetic energy dissipation.

Substitution of equation 2.10 into 2.11, gives the Osborn model, a relationship for diapycnal diffusivity as a function of the stratification condition:

$$K_\rho = \frac{\gamma_{\text{mix}}\ \varepsilon}{N^2} = \gamma_{\text{mix}}\ L_o^2\ N. \tag{2.12}$$

Similarly, we may find these physical parameters applying the concepts of the Thorpe scale (THORPE, 1977), which is estimated from high-resolution underwater temperature profiles by the technique illustrated in Figure 4. Observations in stratified lakes and oceans have shown that the Thorpe scale D_T is approximately the Ozmidov length scale L_o ($L_o \approx 0.8\ D_T$) (DILLON, 1982).

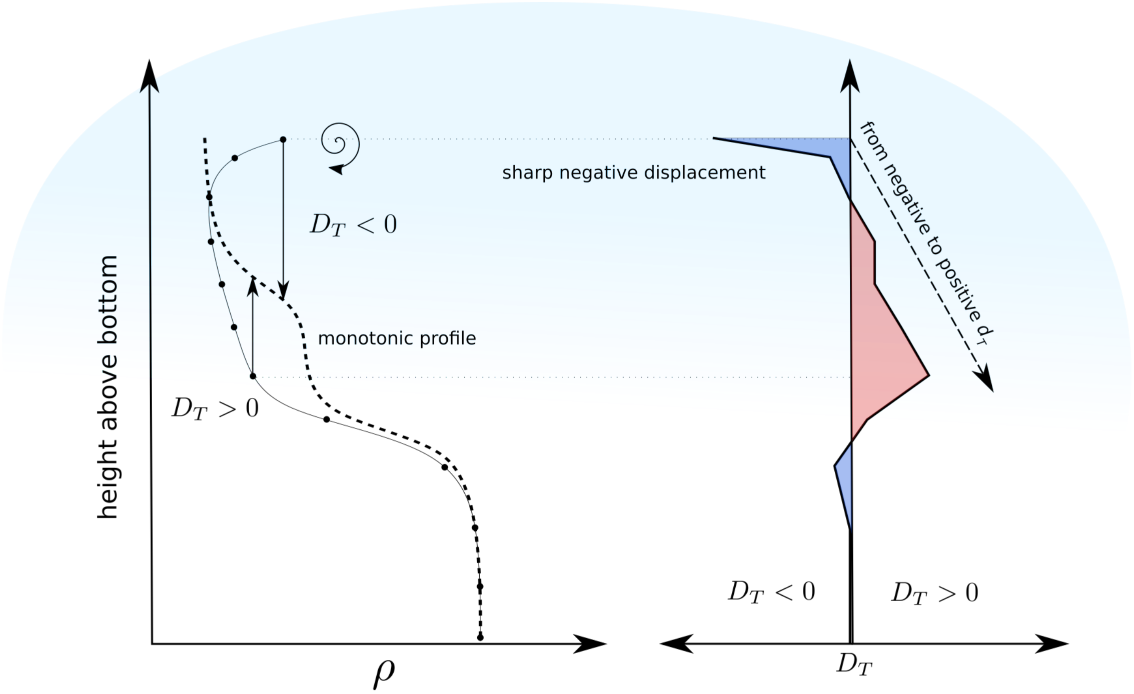

Figure 4 – The water density profile and the Thorpe displacement obtained from temperature measurements along the water column. The solid black line indicates the water density associated with water temperature along the water column. The dashed line illustrates the monotonic profile of the density values (black solid line). D_T is the distance between the density measured and its monotonic form, and indicates the billow size that is generated by overturns.

Substitution of this relation into equation 2.11, gives

$$\varepsilon = 0.64\ D_T^2\ N^3. \tag{2.13}$$

2.1.1.4 Wind-induced in the surface boundary layer

Surface wind-stress controls wind-driven circulation in most lakes, significantly influencing lake mixing in the lake interior. Although the energy associated with heat flux is much larger than the wind energy, the mechanical efficiency to set the water in motion is small (IMBODEN, 2003). The horizontal velocity wind above the lake is described by the *law of the wall*, and the wind-stress is established near the water surface.

Although equation 2.13 shows a direct wind dependence, the Thorpe scale describes inversions that may be strongly correlated to wind intensity. the sharp negative displacement illustrated in Figure 4 is often observed in lakes near the water surface due to the action of the wind. The total incident surface-wind stress (σ_{wind}) is generally parameterized as

$$\sigma_{\text{wind}} = \rho_{\text{atm}} C_D \; U_{10}^2, \tag{2.14}$$

in which ρ_{atm} is the air density, U_{10} is the wind velocity measured at 10 m above the water surface, and C_D is the wind drag coefficient, a dimensionless wind stress coefficient.

The energy flux that describes the momentum transferred from the wind to the water surface is proportional to the shear stress of the wind (Eq. 2.14) and may be described as:

$$P_{\text{wind}} = \sigma_{\text{wind}} \; u_{\text{sur}}, \tag{2.15}$$

in which u_{sur} is the surface horizontal velocity. P_{wind} usually varies from 0.01 to 1 W/m^2 in typical lakes.

The wind stress energy is not completely transferred to the SBL to contribute to the momentum flux; most of it is dissipated in the interface. However, the second-largest part of the energy, approximately 20%, is consumed to accelerate and maintain surface waves (WÜEST; LORKE, 2003; SIMON, 1997). Due to the presence of surface waves, the shear stress is not equally balanced through the water interface. Therefore, the wind stress energy available in the SBL (σ_{sbl}) can only be found through a complete understanding of the surface wave field.

Surface gravity waves increase the roughness of the water surface, increasing the shear stress and enhancing the momentum flux from the air to the water. When the wind blows over the lake surface, the wind transfers energy to the water, and due to the unbalanced pressure caused by the wind, waves are formed on the water surface. However, the wave amplitude is a function of wind speed, wind duration, and wind fetch. Only when all these factors combine together are surface waves susceptible to being excited.

Since σ_{wind} is parametrized by the wind drag coefficient (C_D), the wind intensity directly influences the shear stress available in the SBL. Based on this dependency, C_D assumes different behaviors depending on the speed of the wind (WÜEST; PIEPKE; SENDEN, 2000).

Stronger winds generate waves of higher amplitude, amplifying the roughness of the lake surface and creating waves rapidly developing, which are usually observed in typical oceanic conditions. On the other hand, weak wind events have a lower influence on surface waves, and consequently, the surface roughness of the lake is essentially controlled by surface tension and capillarity waves. The wind drag coefficient increases much faster for weaker winds, indicating additional friction between the wind and the water surface.

Given the size of lakes, the wind drag coefficient (C_D) is strongly influenced by the wind fetch, which depending on the size of the lake, can generate underdeveloped waves (short, steep, and high-frequency waves) (WU, 1994). An underdeveloped wave is an accelerating wave that tends to extract more energy from the wind for its acceleration. Often this kind of wave is much more susceptible to break, appearing rougher and favoring turbulence production, leading to a C_D much larger than observed for developed waves. When surface waves are completely developed, wave energy only extracts wind energy to compensate for wave breaking.

Considering the Prandtl assumption (PRANDTL, 1904), which implies that the wind speed varies according to the distance of the interface and the applied shear stress, we may assume an analog case for wind-induced stress in the SBL. Considering that the total wind stress (σ_{wind}) contributes directly to the density flux (σ_{sbl}), we may assume that

$$\frac{\partial \overline{u}}{\partial z} = -\frac{1}{\kappa_v \; z}\sqrt{\frac{\sigma_{\text{sbl}}}{\rho_{\text{sbl}}}}, \tag{2.16}$$

in which $\kappa_v = 0.4$ is the Von Kármán constant and ρ_{sbl} is the water density in the SBL. Integrating with respect to z, we obtain the velocity profile for the SBL, which is analog to the wind profile:

$$u(z) = U_o - \int_0^z \frac{1}{\kappa_v z}\sqrt{\frac{\sigma_{\text{sbl}}}{\rho_{\text{sbl}}}}\,\mathrm{d}z = U_o - \frac{1}{\kappa}\sqrt{\frac{\sigma_{\text{sbl}}}{\rho_{\text{sbl}}}}\ln\left(\frac{z}{z_o}\right).$$

Substitution of equation 2.16 into the production term of equation 2.2 and considering $\sigma_{\text{sbl}} = \rho_{\text{sbl}}\overline{u'w'}$ and $u_{sbl*} = \sqrt{\sigma_{sbl}/\rho_{\text{sbl}}}$, the production term becomes

$$P = \frac{u_{sbl*}}{\kappa z} \tag{2.17}$$

When the surface boundary layer is not stratified, there is no buoyancy flux into the deeper regions, and consequently, all turbulent production is dissipated within the SBL. Moreover, considering that the wave-induced stress is relatively small, $\sigma_{\text{sbl}} \approx \sigma_{\text{wind}}$ (equation 2.14), which results in the law-of-the-wall scaling of turbulence:

$$\varepsilon = -\overline{u'w'}\,\frac{\partial \overline{u}}{\partial z} = \left(\frac{\sigma_{\text{wind}}}{\rho_{\text{sbl}}}\right)^{3/2}\frac{1}{\kappa z} = \left(\frac{\rho_{\text{atm}} C_D}{\rho_{\text{sbl}}}\right)^{3/2}\frac{U_{10}^2}{\kappa z}. \tag{2.18}$$

Wind-induced turbulence is generally proportional to the wind speed at 10 m above the water surface. Although some evidence has shown that the turbulence production in stratified lakes found consistency in the energy dissipation estimated by equation 2.18 (IMBERGER, 1985), observations during strong wind events have shown that the energy dissipation rates are one to two orders higher than predicted by the law-of-the-wall scaling (DONELAN, 1998). This increase in energy dissipation is due to the additional energy input of wave breaking, which occurs essentially during periods of strong wind events. The consequence of this has been extensively studied, but assuming a simplified framework, we may consider just two different values for C_D, depending on the wind speed only (for more information, see Appendix D.1).

2.1.2 Mixing in the lake interior

Mixing events in lakes may have different temporal and spatial scales, depending on the source of the water disturbance. Even in a strong stratified system, depending on the strength of the disturbed event, the system may not be capable of supporting stratification, favoring mixing events, leading to a stratification break that may appear locally or globally in the lake. To determine whether the perturbation is strong enough to cause mixing, we use often a non-dimensional parameter, called bulk Richardson number, that represents the ratio of buoyancy frequency (equation 2.9) to the field velocity profile:

$$Ri = N^2\left(\frac{\partial u_i}{\partial z}\right)^{-2}, \tag{2.19}$$

in which u_i is the reference velocity field, z is the vertical scale characteristic, and N is the buoyancy frequency (equation 2.9).

Mixing events are often associated with surface wind stress, turbulence, instabilities, gravity currents, internal wave evolution, and wave breaking. In a strong stratification system, turbulence decays over time when the instability energy is too low to balance the losses by buoyancy and viscosity. Observations have identified that the flow becomes unstable in the stratified system when $Ri < 0.25$, favoring turbulent mixing (ROHR et al., 1988).

The mixing efficiency (equation 2.3) can be expressed in terms of flux Richardson number as

$$\gamma_{\text{mix}} = \frac{Ri_{\text{flux}}}{1 - Ri_{\text{flux}}}, \tag{2.20}$$

in which Ri_{flux} (< 0.25) describes the amount of turbulent kinetic energy converted to potential energy (B/P).

Before exploring the stable interior, we devote this section to briefly discussing the response of a stratified lake to a sudden wind shear stress that favors the break of thermal stratification globally in the lake interior. Local mixing in a stratified lake is discussed in section 2.1.3.3.

To determine whether the wind shear stress is strong enough to cause mixing, studies have used the bulk Richardson number for a two-layer system and derived many timescales associated with the mechanisms of stratified lakes, including entertainment, wave damping, and internal seiche formation, among others (SPIGEL; IMBERGER, 1980). The entrainment time was obtained from the turbulent kinetic energy budget, neglecting the influence of the internal wave radiation on the production of shear stress near the thermocline, while the internal seiche period was based on a rectangular-shaped box model. Since the lake mixing regimes is wind-fetch dependent, we may also derive the classification proposed by Spigel and Imberger (1980) in terms of the Wedderburn number W for a two-layer system and lake length L:

$$W_{\text{V1}} = \frac{Ri_{\text{V1}}\ h_e}{L} = \frac{g'\ h_e^2}{u_*^2\ L}, \tag{2.21}$$

in which h_e is the epilimnion thickness, L is the lake length, g' is the reduced gravity, and u_* is the wind stress. Subscription V1 indicates that these quantities are related to a two-layer system. The classification proposed by Spigel and Imberger (1980) was obtained from many simplified conditions. One of these simplifications refers to the geometry of the basin, which considers that the lake is rectangular. New approaches have been proposed to estimate the Wedderburn number (equation 2.21) considering the bathymetric variability of the longitudinal section of a basin (SHINTANI et al., 2010).

Observations have suggested that when $W_{\text{V1}} < h_e/L$ ($Ri_{\text{V1}} < 1$), mixing occurs on a time scale lower than the time it takes to form billows (SPIGEL; IMBERGER, 1980). This regime is often observed during the winter season when thermal stratification is too weak to be maintained after a strong wind event.

However, observation in different lakes has identified complete mixing events even for $W_{\text{V1}} > 1$ (MORTIMER, 1952; MORTIMER, 1955a; THORPE, 1978). Studies have suggested that for

$$\frac{h_e}{L} < W_{\text{V1}} < 0.5\sqrt{\frac{H}{H - h_1}}, \tag{2.22}$$

the system may present persistent large vertical displacement, which favors the appearance of Kelvin-Helmholtz billows and interfacial shear. Due to instabilities generated at the layer boundary interfaces, the lake may be completely mixed during persistent wind events.

Above the upper limit of the criteria 2.22 (SPIGEL; IMBERGER, 1980), wind events do not break the thermal stratification, favoring the formation of internal waves. This formulation and each regime associated with a stable interior are better explored in the next section.

2.1.3 Stable interior layer

Below surface boundary layer (SBL) is located in the most stable region of a thermally stratified lake, which is characterized by a region with the highest temperature gradients. This zone has strong stratification, where turbulence is suppressed, and internal waves are susceptible to being excited. Only 10% of the total wind energy transferred to the stratified lake passes through the SBL and can excite internal seiches in the stable interior (IMBERGER, 2013). The dominance of large internal waves does not occur every time W_{V1} is lower than the upper limit defined by equation 2.22. Observations have suggested that the dominance of internal waves is limited for

$$0.5\sqrt{\frac{H}{h_h}} < W_{\mathrm{V1}} < \frac{L\ H}{4\ h_e\ h_h}, \tag{2.23}$$

in which H is the total water depth, and h_e and h_h are the epilimnion and hypolimnion thicknesses, respectively. Above this upper limit, the system is too stable to support high-amplitude interfacial displacements. When W_{V1} satisfies the criteria 2.23, the lake interior can be dominated by fundamental internal seiches. New techniques used to estimate the Wedderburn number for a non-idealized condition have observed that the Wedderburn number is higher than the value estimated using the standard procedure proposed by Spigel and Imberger (1980) (SHINTANI et al., 2010). This feature is more pronounced in reservoir-shaped basins with the wind blowing from the deep part of the basin toward the shallows. In this case, the thermocline upwelling produces a shorter effective length of the thermocline, resulting in a higher Wedderburn number; as a consequence, stronger winds are needed to generate internal seiche under these conditions.

Unlike surface waves, internal waves have isobars and isopycnals inclined with respect to each other, resulting in a rotational flow that increases the shear in the wake to a level that increases the turbulence intensity. In addition, internal waves can propagate vertically and horizontally through the water system as a result of continuous stratification. Although internal waves may be excited by different sources in thermally stratified lakes and may present varied temporal and spatial scales, due to the low-density difference, internal waves have higher periods compared to surface waves with the same wavelength. Since the wind stress often acts briefly rather than a few periods of fundamental internal seiches, the vast majority of lakes and reservoirs are dominated by internal waves (IMBERGER, 1998).

It should be mentioned here that although this theoretical framework has successfully predicted the formation of internal seiche in some lakes (WEDDERBURN, 1912; MORTIMER, 1952; MORTIMER, 1953; MORTIMER, 1955b; THORPE, 1977), in many others this mathematical description fails (CARMACK et al., 1986; STEVENS; LAWRENCE, 1997). The simplified framework presented by Spigel and Imberger (1980) should be extended to a more realistic scenario, including many effects that could attenuate or amplify the occurrence of internal seiches. Studies have indicated that the Coriolis effect (MORTIMER, 1955a), internal seiche resonance with wind forcing (BOEGMAN; IVEY, 2012), and lake bathymetry (VALERIO et al., 2012) are just some of the important factors that may play a crucial role in the evolution of internal seiches in thermally stratified lakes.

Given the dominance of internal waves, many studies have pointed out the importance of these movements on the biogeochemical fluxes and their implications for the water quality of these ecosystems. There is growing evidence that large internal waves may be associated with large-scale motions in the bottom boundary layer (BRUCE et al., 2008a), which may be responsible for energizing the bottom layer, increasing the mass transport processes in that region (IVEY; WINTERS; SILVA, 2000). Investigation in large lakes has shown that approximately 50% of the hypolimnetic volume may be exchanged after the evolution of the basin-scale motion associated with internal waves (UMLAUF; LEMMIN, 2005). Furthermore, recent observation indicates that wave-induced vertical movements can cause steep displacement in phytoplankton communities (HINGSAMER; PEETERS; HOFMANN, 2014). Internal waves may also influence the light availability for photosynthetic microorganisms (EVANS; MACINTYRE; KLING, 2008), and play a pivotal role in the magnitude of mixing in the lateral boundaries of stratified lakes (WÜEST; LORKE, 2009).

The energy in the internal wave field may be described by the Garrett-Munk spectrum (GARRETT; MUNK, 1972), which reconstructs the complete three-dimensional internal wave spectrum from the observation of one-dimensional underwater temperature. The power spectral density of the isotherms shows the oscillation response at each frequency (THORPE, 2005). The isotherm spectrum suggests the existence of a universal spectrum that describes the decay of energy from basin-scale internal waves to small-scales of turbulence (Figure 5). The energy cascade may characterize internal mixing in thermally stratified lakes and has been widely studied (HORN; IMBERGER; IVEY, 1998; IMBERGER, 2013; HORN; IMBERGER; IVEY, 2001; BOEGMAN; IVEY; IMBERGER, 2005b; BOEGMAN; IVEY; IMBERGER, 2005a).

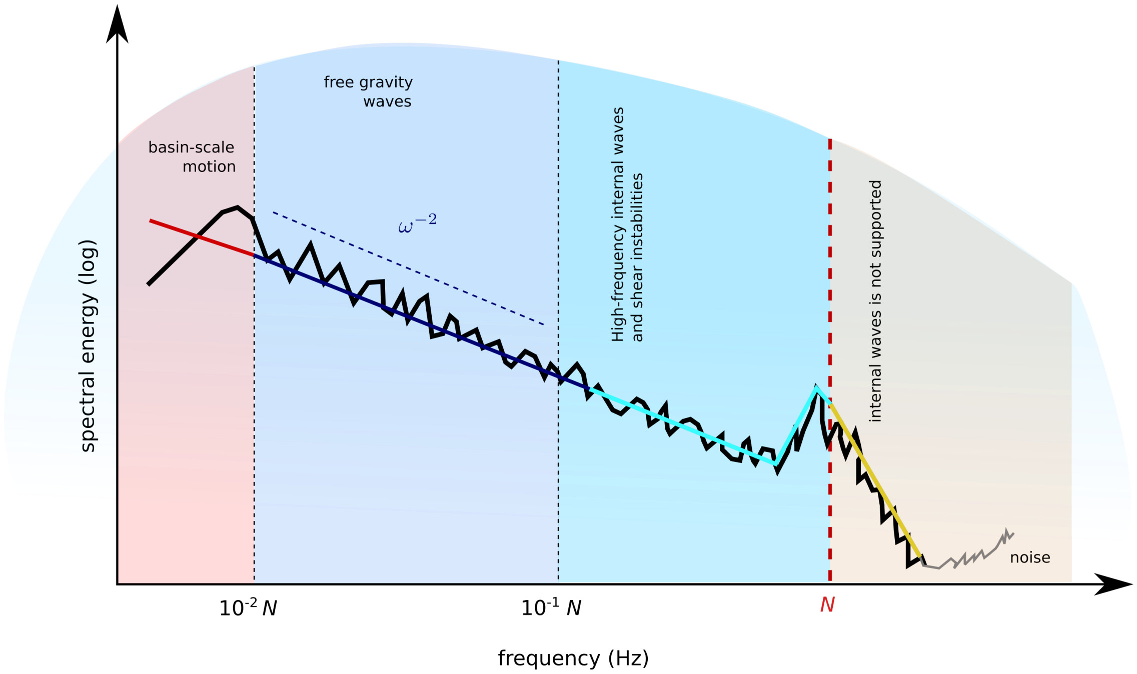

Figure 5 – Spectrum of the internal wave field. N is the buoyancy frequency defined by equation 2.9 and ω is the angular frequency.

The spectrum is divided into four regions. The first one is bounded at the low-frequency band, comprising large-scale motion excited often due to wind stress acting on the water surface. The large-scale motion is often characterized by the evolution of internal seiches (a standing large internal wave) that is discussed in more detail in section 2.1.3.1.

The second part of the internal wave spectrum ($10^{-2}\ N < f < 10^{-1}\ N$) describes a down-scale energy cascade that decays according to the ω^{-2}-power law, where ω is the angular frequency of the internal wave (GARRETT; MUNK, 1972). The energy cascade represents a transference of energy from large-scale motion to small-scale of turbulence, which is characterized by the formation and evolution of high-frequency internal waves (HFIW). High-frequency internal waves can be observed in the third part of the spectrum, where the frequency varies from $10^{-1}\ N$ to N and is characterized by an increase in spectral energy. Often, this pronounced peak is followed by a sharp reduction (BOEGMAN et al., 2003; HUBER; PEETERS; LORKE, 2011). Evidence has also demonstrated through field observations that the HFIW can also be observed in the spectrum as a simple plateau with elevated power spectral density compared to the ω^{-2}-power law (LORKE, 2007). Often the peaks related to high-frequency internal waves are followed by a rapid decay (faster than the -2 slope decay) toward higher frequencies[3].

Research has shown that internal waves with these frequencies are not continuous, they occur in groups (SAGGIO; IMBERGER, 1998). Although it is associated with the vertical advection of high-frequency internal waves and continuous stratification, studies have shown that these waves belong to a complex field of multi-modal internal waves that can be distorted by other waves with different frequencies (SAGGIO; IMBERGER, 1998). These high-frequency internal waves may be generated from many sources, such as the interaction of horizontal flows with lake bathymetry, shear instabilities and, most likely, due to degeneration of the internal seiche (HORN; IMBERGER; IVEY, 1998; BOEGMAN; IVEY; IMBERGER, 2005a). Below the buoyancy frequency (equation 2.9), the system is weakly stable to support the evolution and formation of internal waves.

2.1.3.1 Basin-scale internal wave

A small part of the energy from strong wind events that cross the water surface and the SBL is responsible for the excitation of basin-scale internal waves (IMBERGER, 2013). The wind introduces kinetic energy to the water surface, and the momentum transference pushes a volume of water to the leeward shore, resulting in a surface displacement. If the wind event persists for a sufficient time, part of the momentum and energy crosses the SBL and is used to excite internal wave fields in deeper regions based on mechanisms described in section 2.1.1. The horizontal pressure increases and the hypolimnion layer is accelerated towards the upwind direction (Figure 6). When the wind stops, the inertia of the water returns to equilibrium, creating an oscillatory motion around the nodal points. This oscillation is characterized by the evolution of an internal seiche (BSIW), which might oscillate for long periods, on the order of several hours to weeks depending on the lake size, thermal stratification conditions, lake bathymetry, wind, and among others.

Strong wind events may intensify the formation of internal seiches in stratified lakes, increasing spectral energy in the lowest frequency band (SAGGIO; IMBERGER, 1998). As a result, the spectral energy in the ω^{-2} region may also increase due to the down-scale energy cascade of large-scale motion, which physically implies the formation of internal waves with higher amplitudes.

Internal seiches are often observed in thermally stratified lakes as an interfacial wave that acts near the pycnocline, the region of fastest density changes. The flow is characterized by the motion of the epilimnion in the opposite direction from the hypolimnion layer, with high shear stress in a single intermediate interface. In this case, the wave is known as a fundamental internal wave (also called V1H1 mode). This phenomenon has been widely reported in the literature since the last century (MORTIMER; HORN, 1982; FRICKER; NEPF, 2000; PANNARD et al., 2011).

---

[3] Especially when current velocity components are analyzed through spectral analysis, oscillatory motion can be identified with a frequency higher than the buoyancy frequency. This oscillatory motion is not generated by baroclinic activity and is normally caused by surface waves propagating

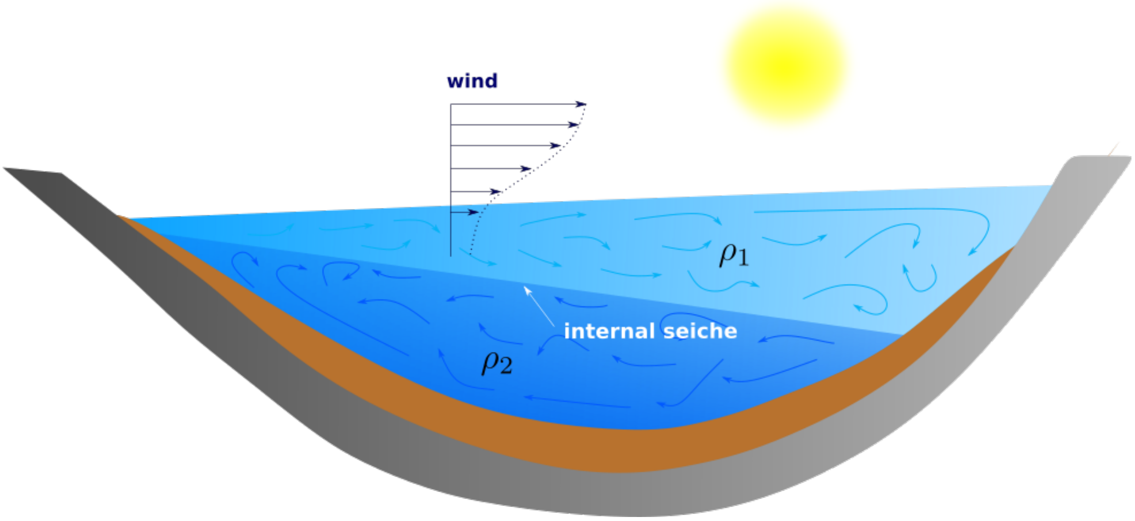

Figure 6 – Schematic overview of a fundamental internal seiche in a lake. Different shades of blue denote layers of different temperatures (density, in which $\rho_2 > \rho_1$). Brown and silver layers indicate the sediment layer and the solid bathymetry of the lake, respectively.

Fundamental internal waves are not the only type of internal seiche that can be exciting in continuous thermally stratified lakes. Due to bathymetry, thermal stratification conditions, wind resonance, and many other effects, many studies have reported the formation of internal seiches with higher vertical and horizontal modes.

The higher vertical internal seiche mode is characterized by oscillation response in different depths with opposite phases (MÜNNICH; WÜEST; IMBODEN, 1992). Although a higher vertical mode has not often been identified (MORTIMER, 1971), nowadays it is accepted that the high vertical mode may be dominant in some thermally stratified lakes due to wind-wave resonance, thermal stratification (HUTTER; WANG; CHUBARENKO, 2011), as well as bathymetric conditions. Higher horizontal modes are characterized by shorter internal seiches, which are generated due to bathymetry and wind field characteristics (IMAM et al., 2020; VALERIO et al., 2012).

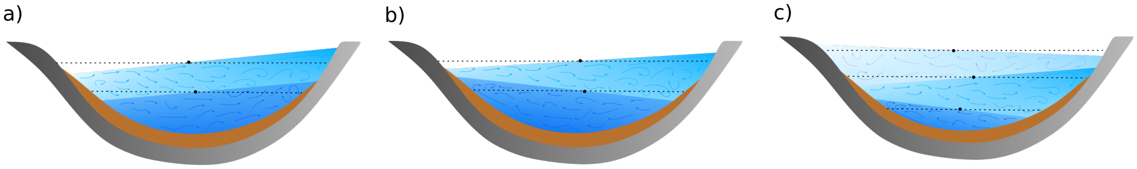

Figure 7 – Schematic view of various vertical internal wave modes in a closed lake. a) V0H1, b) V1H1, C) V2H1. The mode for $n = 0$ is related to the pure surface (barotropic) mode. The black dots $(\cdot)$ represent nodal points. Arrows illustrate the flow of water direction associated with different layers.

The internal seiche of the second vertical mode is characterized by large shear stress across the metalimnion boundaries and a less perturbed hypolimnion, in which both layers move in the same direction whilst the metalimnion flows in the opposite direction.

Evidence has shown that higher vertical modes may be more susceptible to being excited in shallow lakes where the metalimnion takes up a relatively larger proportion of the total water depth (ROGET; SALVADÉ; ZAMBONI, 1997). Evidence has shown that resonance with wind forcing may also favor the excitation of higher vertical (VIDAL et al., 2005) and horizontal modes (BOEGMAN; IVEY, 2012), often resulting in higher amplitude internal waves (MÜNNICH; WÜEST; IMBODEN, 1992). Figure 7 illustrates different internal seiche modes.

The period of internal seiche can be estimated through the mathematical models based on governing equation of motion, which is discussed in detail in Section 2.2. Since usually the total internal seiche energy is equally partitioned, the mean total energy can be estimated from the vertical displacements of isotherms due to internal seiche activity (potential energy) or through the horizontal velocity at the center of the basin due to the evolution of the internal seiche activity (kinetic energy). One approach to compute the total energy deposited into the system is to integrate the velocity field (GOUDSMIT et al., 2002):

$$E(t) = 2\ E_k(t) = \int_{z_0}^{H} \rho(z)\ A(z)\ u(z,t)^2\ \mathrm{d}z, \tag{2.24}$$

in which E_k is the kinetic energy, z_0 is the reference height, H is the total water depth, $u(z)$ is horizontal field velocity along the water depth, A is the layer area, and ρ is the water density. Observation in Lake Alpnach has demonstrated that the integrated total energy associated with one fundamental internal seiche period is of the order 10^8 J (GOUDSMIT et al., 2002). The integrated energy deposited into each mode of internal seiche can be obtained from the model decomposition[4] (BOEHRER; ILMBERGER; MÜNNICH, 2000), which is detailed in section 2.2.

Higher vertical modes create a vertical propagation mechanism, which carries energy from the water surface to the lakebed. This mechanism is characterized by wave groups that propagate downward to the lakebed (HENDERSON; DEEMER, 2012).

In large lakes, internal seiches may present a frequency lower than the inertial frequency of the Earth, leading to the formation of waves that are affected by the Earth's rotation. In this case, the internal Poincaré and Kelvin waves may be formed. Internal Kelvin waves are large-scale waves that have higher amplitude at the boundary, decaying exponentially with distance from the lakeshore, where the wave is trapped. As a result, this motion often presents higher velocities near the shore and smaller ones in the center of the lake. Another general behavior of Kelvin waves is that they can travel along the coast in one direction only. The pressure balances the Coriolis force, driving the wave along the horizontal boundaries, clockwise in the Southern Hemisphere.

Poincaré waves are also large-scale waves, but they are not trapped at boundaries. This type of wave develops from crosswise seiching, which becomes deflected by the Coriolis force. It propagates in the counterclockwise direction in the south hemisphere with greater transverse velocities.

Internal seiche may degenerate due to viscous friction and diapycnal mixing, which often occurs in the bed boundary layer (BBL), a rough turbulent boundary where the flow is strongly influenced by the bed. Field observations have shown that most of the internal seiche energy is lost due to turbulence production in the BBL (SIMPSON; WILES; LINCOLN, 2011a). This region is discussed in section 2.1.4.

Small-amplitude internal seiches are susceptible to being dissipated by viscous friction in the BBL. However, higher-amplitude internal seiches tend to transfer energy to smaller-scale motion, such as high-frequency internal waves, Kelvin-Helmholtz billows, or supercritical flow (HORN; IMBERGER; IVEY, 2001; BOEGMAN; IVEY; IMBERGER, 2005a). The internal seiche degeneration process is classified based on the dimensionless Wedderburn number (equation 2.21) and time-scales associated with internal seiche conditions.

---

[4] This approach also helps to compute the energy only due to internal seiche activity, decoupling this energy from other contributions.

The degeneration of internal seiches into high-frequency waves has been reported in several lakes around the world (THORPE; HALL; CROFTS, 1972; MORTIMER; HORN, 1982; LEMMIN, 1987; SAGGIO; IMBERGER, 1998). Although the internal seiche contains more than 98% of the internal wave energy, the shoaling and breaking are practically restricted to high-frequency internal waves. Observations suggest that more than 80% of the available potential energy of large-scale internal waves is transferred to high-frequency waves or dissipated into heat during the first wave period (STEVENS et al., 1996). However, high-frequency waves are often dissipated because of wave breaking in the first interaction with the basin shore.

Observations of the displacement of the isotherms have identified the degeneration of the Kelvin internal seiche into an internal surge due to wave steepening, as illustrated in Figure 8 (HUTTER et al., 2007). The study detected in the downwelling part of the Kelvin internal seiche, an increase in the thickness of the upper mixed layer, which is accompanied by the formation of a modulated internal surge with a period of ≈ 24 h. Due to the shoaling between ST4 and ST5, observations have identified the generation of higher-frequency internal waves of 10 min. The observation has been confirmed by numerical simulations, which identified that due to the asymmetric topography with respect to the basin center, internal bore has been generated, which was disintegrated into a train of solitary internal waves with amplitude between 5 and 15 m.

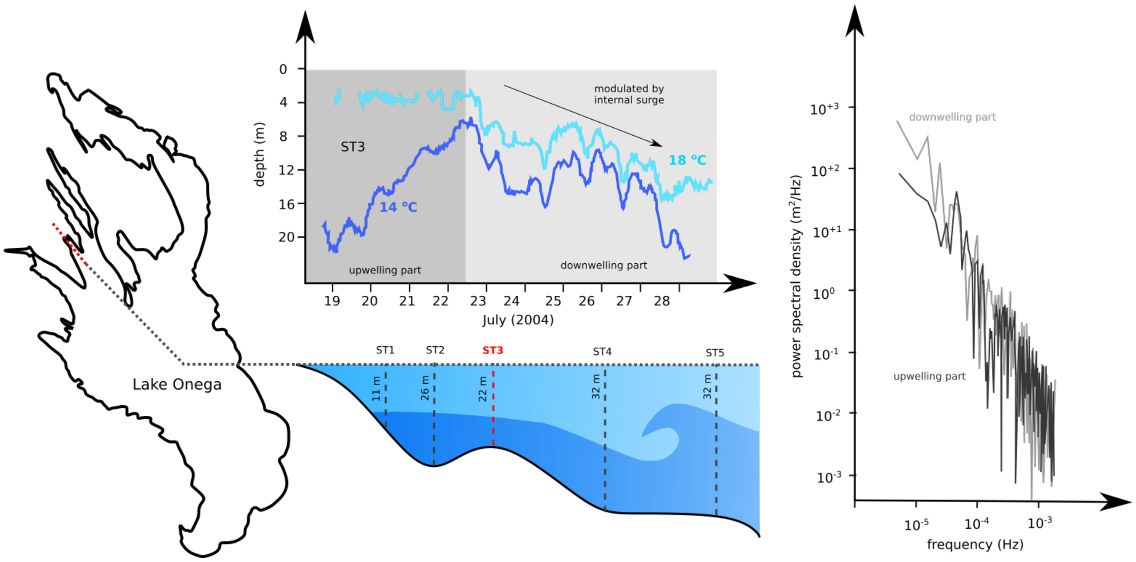

Figure 8 – Large Kelvin internal wave modulated by internal surges and high-frequency internal waves measured in Onego Bay. Assembled from Hutter (2011). Isotherms variation at station ST3, measured near the lakeshore at the north portion of Lake Onego during 9 days of field campaign. The isotherms show one wave cycle of Kelvin internal wave, modulated by 24 h internal surges. The power spectral density of 16 °C isotherm shows that the modulation just occurs during the downwelling part of the Kelvin internal wave.

Other studies have also identified the transference of energy from basin-scale internal waves to internal surges, which, due to shoaling processes, degenerated into high-frequency internal waves (HUTTER et al., 2007).

2.1.3.2 High-frequency internal waves

High-frequency internal waves are characterized as a disturbance about an equilibrium position that travels in the high-frequency band within the interior of a stratified fluid, often from $5\ 10^{-4}$ Hz to $1.5\ 10^{-3}$ Hz (LORKE; PEETERS; BÄUERLE, 2006), which is characterized by a buoyancy frequency that varies between 10 N and N (Figure 5). The most common type of high-frequency internal wave detected in lakes and reservoirs is termed *solitary internal wave*. Although this wave is strongly grouped (SAGGIO; IMBERGER, 1998), often the groups tend to be very isolated.

Solitary internal waves are characterized by a nonsinusoidal propagating wave with a single crest. Due to the balance between weakly non-linear convection and dispersion, the wave retains its shape while traveling at a constant speed. A solitary internal wave is governed by non-linear or weakly non-linear partial differential equations. A solitary internal wave in a two-layer system has been extensively studied using numerical models (WHITHAM; FOWLER, 1975).

Although high-frequency internal waves are often excited as a result of the degeneration of internal seiche (HORN; IMBERGER; IVEY, 2001; BOEGMAN; IVEY; IMBERGER, 2005a), propagating internal waves can also be formed due to other factors, such as flow interactions with topography (THORPE et al., 1996; SAGGIO; IMBERGER, 1998), internal hydraulic jumps (FARMER; ARMI, 1999), mixing result of shear instabilities (BOEGMAN et al., 2003; MAXWORTHY; MONISMITH, 1988), convective motion in the epilimnion (LINDEN, 1975), turbulence generated through Langmuir currents, and gravity currents (WHITE; HELFRICH, 2008; OTTOLENGHI et al., 2020). Analyses of isotherms fluctuation have revealed that nonlinear internal waves, such as internal solitary waves and surges, are a general feature of lakes.

Laboratory and field observations have suggested that the interaction between internal seiches and lake boundaries may favor the occurrence of high-frequency internal waves (CHU; CHOU, 1990; IMBERGER, 2013). Non-uniform bathymetry on the west portion of Lake Kinneret has been noted as one important source to favor the occurrence of high-frequency internal waves in that spot (BOEGMAN et al., 2003; HORN; IMBERGER; IVEY, 2001).

Other studies have identified high-frequency internal waves due to shear instability at the base of the pycnocline during periods of intense wind forcing (ANTENUCCI; IMBERGER, 2001b) and are also associated with internal seiches of higher vertical modes (BOEGMAN et al., 2003). Internal seiches with higher vertical mode may generate a layer jet that flows in the opposite direction compared with the boundary layers, creating a mixing region in the layer interior. Evidence has shown that the mixing region reduces the local potential energy, favoring the formation of high-frequency internal waves of mode-one and -two (MAXWORTHY; MONISMITH, 1988), with no intermediate energy cascade.

Experimentally, observations have suggested that high-frequency internal waves may cause an unstable near-wall jet along the bottom (BOGUCKI; DICKEY; REDEKOPP, 1997). Structural characteristics are attributed to a negative pressure gradient in the case of a single internal wave passage, which creates a jet-like boundary flow, as illustrated in Figure 9. The flow is observed in the same direction as the wave celerity but opposite with respect to the lower layer of the fluid, favoring the development of an unstable boundary layer (CARR; DAVIES, 2006).

Although investigation in laboratory tanks has suggested high-energy dissipation during internal solitary wave propagation, some observations have suggested that the wave attenuation is due to the unrealistic boundary conditions of laboratory tanks (TROY; KOSEFF, 2006). High-frequency internal waves may be capable of propagating for thousands of kilometers in thermally stratified lakes and lose their energy mainly due to mixing and dissipation via breaking upon sloping boundaries.

Since nonlinear internal waves are not sinusoidal in character, the wave shoaling leads to a significant energy flux in the benthic boundary layer and consequently has a great impact on the water mixing, sediment resuspension, and flux of nutrients, chemical compounds, and microorganisms. Turbulence produc-

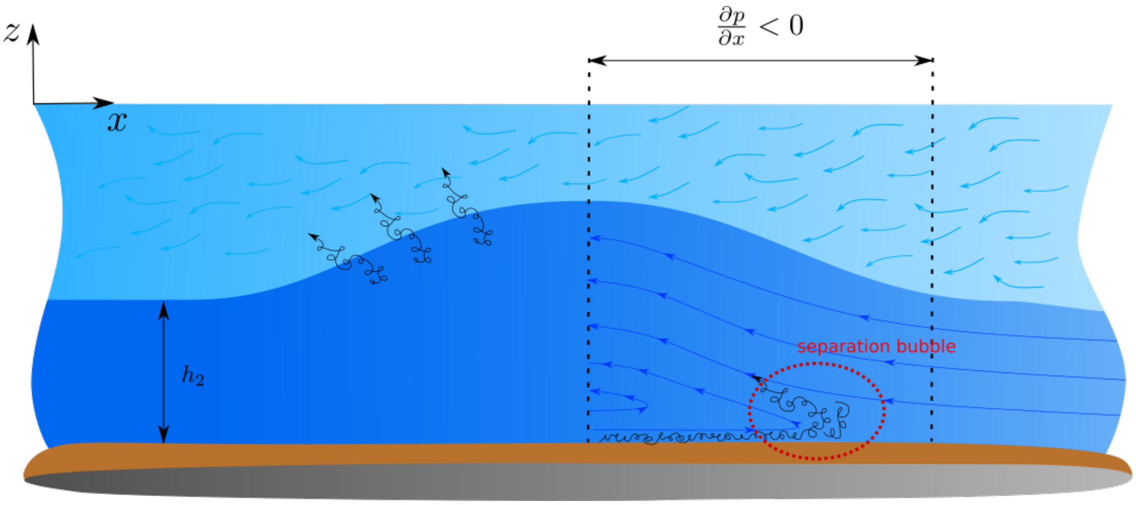

Figure 9 – Schematic representation of the instability mechanism caused by propagating internal waves on a flat bottom near the unstable boundary layer. Assembled from Bogucki, Dickey and Redekopp (1997), Stastna and Lamb (2008), Boegman and Stastna (2019).

tion caused by the shoaling and breaking of high-frequency internal waves has been studied numerically and experimentally (BOEGMAN; IVEY; IMBERGER, 2005a; HELFRICH, 1992). Observations have suggested that this mechanism is one of the most important factors in generating mixing in lakes (GARRETT, 2003). Studies have shown that single internal waves of mode-one can transfer kinetic energy to higher modes of solitary internal waves due to the mixing region caused by shear instabilities (MAXWORTHY; IMBERGER; SAGGIO, 1998).

2.1.3.3 Mixing on the stable interior

Although the stable interior of lakes suppresses turbulence and mixing, there are some mechanisms that favor mixing in these regions, such as the turbulent collapse of density inversion (PREUSSE; PEETERS; LORKE, 2010). Overturn generates turbulence and mixing often associated with shear flow between layers (MACINTYRE et al., 1999), which can be characterized by the formation of Kelvin-Helmholtz billows. Although shear stress between stable layers can cause mixing events or disturbances in the lake interior, the diapycnal diffusivity in BBL is usually an order of magnitude higher than in the stable lake interior (GOUDSMIT et al., 1997; WÜEST; PIEPKE; SENDEN, 2000; LORKE; UMLAUF; MOHRHOLZ, 2008). The mixing in BBL is better explored in Section 2.1.4.

Observations have shown that the turbulent kinetic energy dissipation (ε) in the stable lake interior can be estimated through the buoyancy frequency and the available potential energy of overturns, which is obtained from the available potential energy of unstable density fluctuations (DILLON, 1984):

$$\varepsilon = C_{\text{prop}}\ N\ \text{APEF}, \tag{2.25}$$

in which N is the buoyancy frequency, $C_{\text{prop}} = 4.8$ is the proportionality constant (DILLON; PARK, 1987), and APEF is the energy that is released due to a collapse of density inversion (DILLON, 1984).

The shear between layers favors interior mixing and is an important piece in a study of the formation of different modes of high-frequency internal waves. Studies have indicated that disturbances caused by the evolution of large-scale internal waves of higher vertical modes can be associated with high-frequency internal waves of higher vertical modes (BOEGMAN et al., 2003), where the metalimnion creates a jet flowing in the opposite direction to the upper and lower layers (Figure 10). Turbulence in the interior generates mixing and high-frequency waves, which are susceptible to propagating and breaking near the lakeshore.

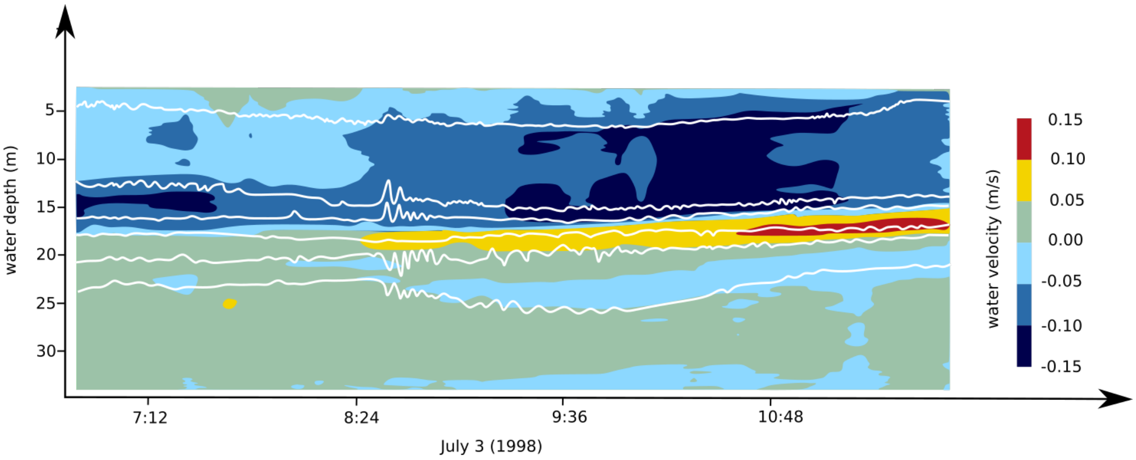

Figure 10 – Portable flux profile of background temperature and velocity structure. The white lines represent isotherms, whilst the color map shows the velocity profile along the depth. Assembled from Boegman et al. (2003).

The mixing caused by this interaction may be computed through the bulk Richardson number Ri_{jet}, similar to equation 2.19, but with a different parameterization,

$$Ri_{\mathrm{jet}} = \frac{g\alpha\Delta\tau_{\mathrm{uns}}\Delta H_{\mathrm{uns}}}{\Delta U^2}, \tag{2.26}$$

where g is the gravitational acceleration, $\Delta\tau_{\mathrm{uns}}$ is the temperature difference of the unstable layer thickness ΔH_{uns}, ΔU is the intermediate layer velocity, and α is the thermal expansion coefficient of the water as a function of temperature.

It is well known that when $Ri_{\mathrm{jet}} \leq 0.8$, the interior layer is susceptible to mixing events (MAXWORTHY; IMBERGER; SAGGIO, 1998). Although the internal wave field occurs along the stable interior of the lake and shear instabilities may be generated by flows in opposite directions, turbulence, and mixing are suppressed by stratification. The mixing induced by internal waves plays a more critical consequence in the bottom boundary layer (BBL), the deepest region of the lake.

2.1.4 Bottom Boundary Layer

The bottom boundary layer, also called the benthic boundary layer, is a well-mixed layer right above the sediment surface, with a thickness of a few meters (up to 3 m above the sediment). Unlike the SBL, which is located in an open upper boundary layer, the bottom boundary layer (BBL) is defined by friction between water flow and lake bathymetry (WÜEST; LORKE, 2009). The mixed layer is maintained by a strong turbulent kinetic energy dissipation from large-scale currents (LEMCKERT; IMBERGER, 1998; WÜEST; PIEPKE; SENDEN, 2000; FRICKER; NEPF, 2000), internal seiche impinging on the lakeshore (LORKE; PEETERS; WÜEST, 2005; COSSU; WELLS, 2013), breaking and reflection of high-frequency internal waves (THORPE, 1997; MICHALLET; IVEY, 1999; LORKE, 2007), and interaction of large-scale currents with topography (RUDNICK et al., 2003), leading to temperature gradients smaller than 0.03 °C (LORKE; PEETERS; WÜEST, 2005).

The bottom boundary structure can be defined similarly to the SBL, assuming the law-of-the-wall. Studies have demonstrated through high-resolution Acoustic Doppler Current Profile (ADCP) measurements in lakes that the law-of-the-wall is valid at the interface between water and sediment (WÜEST; PIEPKE; SENDEN, 2000; RAVENS et al., 2000; LORKE et al., 2002). From equations 2.16 and 2.18, but assuming the bottom boundary layer components, the kinematic turbulent energy dissipation in the BBL can be estimated as

$$\varepsilon = \frac{u_{\mathrm{bbl}_*}}{\kappa_v \ z_h}, \tag{2.27}$$

in which $\kappa_v = 0.4$ is the Von Kármán's constant, z_h is the length scale from the lake bottom, and $u_{\mathrm{bbl}_*} = \sqrt{\sigma_{\mathrm{bbl}}/\rho_{\mathrm{bbl}}}$ is the BBL friction velocity, where σ_{bbl} is bottom shear stress and, similar to the SBL, is relatively constant.

Assuming a well-mixed bottom boundary layer, the law-of-the-wall leads to a diapycnal diffusivity (equation 2.10) that is not a function of buoyancy frequency and is described by the distance from the bottom only:

$$K_\rho = \kappa_v \ z_h \ u_{\mathrm{bbl}_*}, \tag{2.28}$$

which indicates that as far as the fluid is from the bottom, the higher will be the diapycnal diffusivity, leading to higher eddies and more efficient mixing.

However, for weakly forced lakes, the level of turbulence can be much lower, preventing the formation of a well-mixed BBL. In this case, the diapycnal diffusivity is defined, from equation 2.10, as:

$$K_\rho = \frac{\gamma_{\mathrm{mix}} \ u_{\mathrm{bbl}_*}}{N^2 \ \kappa_v \ z_h}. \tag{2.29}$$

2.1.4.1 Mixing on the bed boundary layer

Similarly to a stable interior, the mixing in the BBL is accompanied by an overturn mechanism. However, since the stratification is weaker, the turbulence kinetic energy dissipation is much stronger than the stable interior. Additionally, differently from the lake interior, mixing in the BBL is often associated with the interaction between the internal waves and the lakebed, which may include the breaking of shoaling internal waves and the differential advection of the stratified layer during the propagation of internal seiche near the lake boundaries.

Often, the up- and downwelling motion of the internal seiche interacts with the lakebed, resulting in an increase in the level of turbulence in the BBL. Observations have shown that the temperature inversion may extend across the entire BBL (LORKE; PEETERS; WÜEST, 2005). Field observations have shown that there is a strong asymmetry between downslope and upslope flows from internal seiche, which is consistent with the description of shear-induced convection (COSSU; WELLS, 2013; LORKE; PEETERS; WÜEST, 2005; LORKE, 2007). The upwelling of colder water leads to mixing events that promote BBL destabilization. The wave front propagates upslope at a constant speed, similar to a gravity current (non-linear bore), with a Froude number of unity

$$U_d = \sqrt{g' \ h_{\mathrm{bore}}}, \tag{2.30}$$

in which U_d is the mean velocity of the internal bore, g' is the reduced gravity, and h_{bore} is the height of the bore head.

Since the lower layer feels a resistance force due to shear stress with the lakebed, the front interface near the lake bottom propagates slower than the upper interface that does not feel the resistance from the boundary, favoring the formation of overturns, which leads to mixing events (Figure 11a). Studies have suggested that the maximum unstable stratification occurs when the internal seiche reaches the maximum amplitude, but thermal inversions persist even during the downslope current until the maximum horizontal velocity when the interface reaches the equilibrium position (LORKE; PEETERS; WÜEST, 2005).

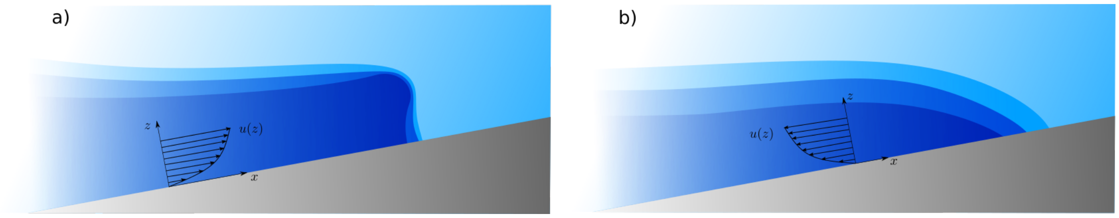

Figure 11 – Diagram describing the a) upwelling and b) downwelling events during the evolution of internal seiche near the lakeshore. Different shades of blue denote layers of different temperatures (density).

Although strong asymmetry has been reported near the lakeshore, evidence has shown no difference between up- and downwelling offshore (COSSU; WELLS, 2013), indicating that the flow is only influenced near the lakeshore. We should mention here that due to strong turbulence dissipation, the internal wave amplitude is attenuated due to the energy dissipation. Clearly, there is a physical consequence of this dissipation in the whole internal seiche field, including offshore. However, the mixing observed in the awash zone does not directly influence the flow offshore.

Field observations have demonstrated that overturns can reach 1 m, presenting a maximum diapycnal diffusivity of $K_\rho = 2 \times 10^{-5}$ m^2/s. Studies have shown that the mean value of K_ρ during the upwelling phase varies from 1×10^{-6} m^2/s to 2×10^{-3} m^2/s, while 2.35×10^{-7} m^2/s to 5×10^{-4} m^2/s for the downwelling phase (COSSU; WELLS, 2013; BOUFFARD; BOEGMAN; RAO, 2012; LORKE; UMLAUF; MOHRHOLZ, 2008; MACINTYRE et al., 1999). When the thermocline propagates downward, turbulence production is limited and stratification is maintained, with no mixing events, resulting in lower diapycnal diffusivity. The difference between the values obtained from the studies can be correlated with secondary effects, such as differences on the bottom slope, the bed roughness, and the high-frequency internal wave field (BOUFFARD; BOEGMAN; RAO, 2012).

The variation of energy dissipation can also be related to the bed slope angle. A larger awash zone is expected for milder bed slopes, which typically indicate higher dissipation conditions. On the other hand, higher bed slopes suggest reflective zones in which lower energy from internal waves is dissipated.

Although there are few field observations in lakes that show the relative importance of shear-induced convection versus the breaking of high-frequency internal waves in the production of turbulence near boundaries (COSSU; WELLS, 2013), new techniques to estimate the turbulence dissipation rates of ADCPs have helped to understand the contribution of high-frequency internal wave breaking to enhanced bottom boundary layer turbulence (LORKE et al., 2002; LORKE; WÜEST, 2005; WILES et al., 2006; LORKE, 2007).

The rapid increase in the dissipation rate nearshore has been attributed to the breaking of high-frequency internal waves, since observations have demonstrated a non-correlation with the magnitude of current velocities (LORKE, 2007). The rapid peak, which results in an increase in the dissipation rate from 10^{-9} W/kg to 10^{-5} W/kg, is caused by a gradual reduction of the dissipation rate after passage of the high-frequency internal wave (LORKE, 2007).

Although turbulence production is directly associated with dissipation, studies have demonstrated that at low production rates, the correlation between the produced and dissipated turbulence energy presents a greater variance, suggesting that the local equilibrium between dissipation and production is not a valid assumption (LORKE, 2007).

The bottom slope may also play a crucial role in the production and dissipation of turbulence due to changes in the breaking of the high-frequency internal wave (MACINTYRE et al., 2009).

A large flux Richardson number (equation 2.20), which characterizes a smaller turbulent energy production, can be expected for milder bottom slopes. Ivey, Imberger and Koseff (1998) have shown that the dissipation of turbulence kinetic energy ε at BBL can be estimated as

$$\varepsilon = \frac{3}{4\pi} \; N \; u_{\text{field}}^2 \; \sin 4\beta, \tag{2.31}$$

in which N is the buoyancy frequency, u_{field} is the incident wave field speed, and β is the bottom slope of the lake. Based on equation 2.31, Imberger (2013) estimated that turbulent kinetic energy dissipation in lakes varies from $8 \; 10^{-7}$ m²/s^3 to $1 \; 10^{-5}$ m²/s^3. As mentioned above, the diapycnal diffusivity in BBL is usually on an order of magnitude higher than in the stable lake interior (GOUDSMIT et al., 1997; WÜEST; PIEPKE; SENDEN, 2000; LORKE; UMLAUF; MOHRHOLZ, 2008).

2.2 Mathematical description

Given the complexity of the internal flows field, as well as the difficulty in specializing data measurements to understand in detail the internal wave field, over the last six decades, attempts have been made to model the dynamic of thermally stratified lakes using mathematical models (HODGES et al., 2000; DISSANAYAKE; HOFMANN; PEETERS, 2019). Although these models have several simplifications, when combined with field and experimental data, numerical simulation allows a comprehensive understanding of the physical processes of lakes.

In this section we describe mathematical techniques to characterize the internal wave field in thermally stratified lakes based on governing equations of motion:

$$\left(\frac{\partial \rho \; u_i}{\partial t} + \frac{\partial \rho \; u_i \; u_j}{\partial x_j}\right) = -\frac{\partial p}{\partial x_i} + \varrho\left(g_i - \overline{\omega_o} \; u_k\right) + \frac{\partial}{\partial x_j}\left(\mu \frac{\partial u_i}{\partial x_j}\right), \tag{2.32a}$$

$$\frac{\partial \rho \; u_i}{\partial x_i} = 0, \tag{2.32b}$$

in which p is the total thermodynamic pressure, ρ is the water density, g is the acceleration of gravity, u is the velocity vector, μ is the dynamic viscosity coefficient, and $\overline{\omega_o} = 2 \; \omega_\epsilon \; \sin \phi_\epsilon$ is the inertial frequency, where ω_ϵ is the angular frequency of the earth and ϕ_ϵ is the mean latitude.

We describe the heat transport in lakes and reservoirs through numerical models, with special attention given to numerical techniques that may influence the evolution of internal waves. We discuss here the modeling approaches, indicating some limitations of the numerical simulation, and also providing some connection with the physical processes described in Section 2.1.

2.2.1 Internal wave model

In this section, two internal wave models are derived from governing equations. Both solutions are valid only for linear internal waves (small-amplitude waves) and do not take into account the Coriolis effect. The multilayer hydrostatic model, described in detail in Section 2.2.1.1, assumes the hydrostatic approximation, providing a solution just for shallow water waves, which considers that the horizontal scales are larger compared to the vertical ones. The model solves the N-momentum equations for the N-phases. The second model, derived in Section 2.2.1.2, assumes that the stratification condition is prescribed by the buoyancy frequency $N(z)$, Equation 2.9. The derivation leads to one of the most general partial differential equations to describe the evolution of the Boussinesq internal wave for continuous stratification and can be used to define different internal wave modes. Unlike the first model, the solution is obtained by solving only one momentum equation for the N-phases being transported.

2.2.1.1 Hydrostatic multi-layer model

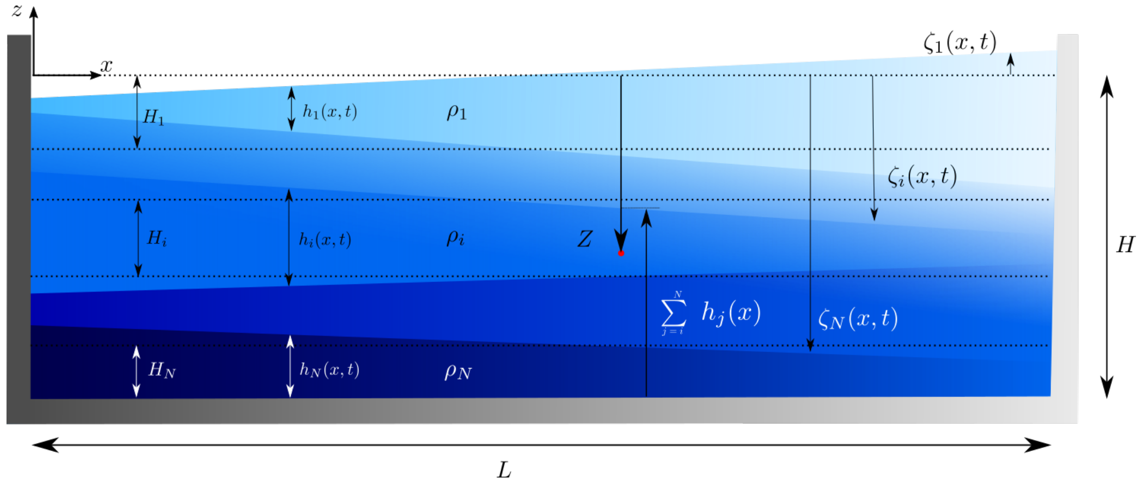

Figure 12 – Stable N-layer system in a rectangular basin ($\rho_1 < \rho_j < \rho_N$). The vertical coordinate is positive above the water surface. H is the equilibrium layer thickness, whilst h is the local layer thickness. ζ describes interfaces between two fluids with different densities (referenced from $z = 0$). Index i indicates the analyzed layer (as an example, we defined the red dot position as our point of interest). Index j represents all layers that are affecting the pressure in layer i, which are all layers above i.

Linearizing[5] the momentum equation 2.32a for x-direction to N-layers and applying the mass conservation equations, assuming a non-rotating and non-viscous shallow water flow, the expression for layer i can be written as

$$\frac{\partial u_i}{\partial t} = -\frac{1}{\rho_i}\frac{\partial p_i}{\partial x}, \tag{2.33}$$

in which the subscript $i = 1, \ldots, N$ describes each layer of the N-layered multi-layer system. It should be mentioned here that i in equation 2.33 just expresses the layer number, completely different from equation 2.32, in which i is used to indicate the components of the coordinate system (index notation).

The hydrostatic pressure p_i is estimated through the density and thickness of the layer, as well as the interfacial waves functions (ζ) as

$$p_i(Z,x,t) = p_o + \underbrace{\boxed{g\sum_{j=1}^{i-1}\rho_j h_j}}_{\text{above layer } i} + \underbrace{\boxed{g\rho_i\left(\left(\sum_{j=i}^{N} h_j\right) - (H+Z)\right)}}_{\text{in layer } i}, \tag{2.34}$$

---

[5] Although the linearization procedure is a simple step to find the dispersion relation by just neglecting non-linear terms, the reason that this approach leads to a small-amplitude solution is not so evident. For clarification see appendix A

in which p_o is the atmospheric pressure, g is the gravitational acceleration, h_j is the j-layer thickness accounting for the boundaries fluctuations (interfacial waves), and H is the total water depth. Note that i-index is fixed (located in the layer that we want to define the pressure), whilst j-index describes the contribution of layers above i. It should be mentioned here that $h_j(\zeta_i, \zeta_{i+1}) = H_j + (\zeta_i - \zeta_{i+1})$, in which H_j is the thickness of the layer j assuming the unperturbed level and ζ is the interfacial wave function.

Substitution of equation 2.34 into 2.33 and assuming that p_o is constant over the entire lake, gives

$$\frac{\partial u_i}{\partial t} = \frac{g}{\rho_i} \sum_{j=1}^{N} \rho_{i,j} \frac{\partial}{\partial x} \left(\zeta_j - \zeta_{j+1} \right). \tag{2.35}$$

Deriving the mass conservation equation 2.32b in x and equation 2.35 in time and combining both equations to eliminate the horizontal velocity, we find

$$\frac{\partial^2}{\partial t^2} \left(\zeta_i - \zeta_{i+1} \right) - \underbrace{\frac{gH_i}{\rho_i} \sum_{j=1}^{N} \rho_{i,j}}_{c} \frac{\partial^2}{\partial x^2} \left(\zeta_j - \zeta_{j+1} \right) = 0, \tag{2.36}$$

in which c is the internal wave phase speed.

The wave equation 2.36 is a system of second-order partial differential equations. By simplification, the system is reduced to second-order linear ordinary differential equations, which is a classical Sturm-Liouville eigenvalue problem. Combining the horizontal eigenvalue problem with the phase speed yields the dispersion relation:

$$\omega_{n,m}^2 = c^2 \frac{4\pi^2}{\lambda_m^2}, \tag{2.37}$$

where ω is the angular frequency of the wave, $c^2 = g\ \beta_n$ is the phase speed of vertical mode n, and the λ_m is the wave length of horizontal mode m.

Considering the lateral boundary condition of a lake, the dispersion relation (equation 2.37) in terms of the internal wave period $T_{n,m}$ is defined as

$$T_{n,m} = \frac{\lambda}{c} = \frac{2L}{m\sqrt{g\beta_n}}, \tag{2.38}$$

in which L is the effective basin length at thermocline depth. For the smooth shoal region, L may generally be less than the full length of the interfacial wave (SIMPSON; WILES; LINCOLN, 2011a). $\lambda = 2\ L/m$ is the wavelength, obtained from the vertical boundary conditions. Each solution of equation 2.38 represents a different vertical n and horizontal m mode.

2.2.1.2 Continuous stratification model

Linearizing[6] equations 2.32 and applying the Reynolds decomposition, the equation of motions for non-rotating and non-viscous flow can be written in Cartesian coordinates as

$$\frac{\partial u_i}{\partial t} = -\frac{1}{\bar{\rho}} \frac{\partial p}{\partial x_i} - g_i \frac{\rho}{\bar{\rho}}, \tag{2.39a}$$

$$\frac{\partial u}{\partial x} + \frac{\partial v}{\partial y} + \frac{\partial w}{\partial z} = 0, \tag{2.39b}$$

---

[6] Although the linearization procedure is a simple step to find the dispersion relation by just neglecting non-linear terms, the reason that this approach leads to small-amplitude solution is not so evident. For clarification see appendix A

in which $u_i = (u, v)$ is the velocity field, p is the pressure, and g is the gravitational acceleration.

Deriving equation 2.39a for x- and y-direction in x and y, respectively, we obtain

$$\overline{\rho}\frac{\partial}{\partial x}\frac{\partial u}{\partial t} = -\frac{\partial^2 p}{\partial x^2}, \tag{2.40a}$$

$$\overline{\rho}\frac{\partial}{\partial y}\frac{\partial v}{\partial t} = -\frac{\partial^2 p}{\partial y^2}. \tag{2.40b}$$

Assuming that u and v are characterized by a smooth function, we may combine equations 2.40a and 2.40b:

$$\overline{\rho}\frac{\partial}{\partial t}\left(\frac{\partial u}{\partial x} + \frac{\partial v}{\partial y}\right) = -\left(\frac{\partial^2 p}{\partial x^2} + \frac{\partial^2 p}{\partial y^2}\right). \tag{2.41}$$

Substitution of mass conservation equation 2.39b into 2.41 and deriving the final expression in z and time gives

$$\overline{\rho}\frac{\partial^2}{\partial t^2}\left(\frac{\partial^2 w}{\partial z^2}\right) = \frac{\partial}{\partial t}\frac{\partial}{\partial z}\left(\frac{\partial^2 p}{\partial x^2} + \frac{\partial^2 p}{\partial y^2}\right). \tag{2.42}$$

A second equation can be found deriving in time the momentum equation in z-direction:

$$\overline{\rho}\frac{\partial^2 w}{\partial t^2} = -\frac{\partial}{\partial t}\frac{\partial p}{\partial z} - g\frac{\partial \rho}{\partial t}. \tag{2.43}$$

Remember that $\overline{\rho}$ is a function of z only, differently from $\rho(\mathbf{x}, t)$. The last term from equation 2.43 can be obtained from the conservation of mass assuming an incompressible flow.

Applying the Reynolds decomposition to split the contribution of density ($\rho(\mathbf{x}, t) = \overline{\rho}(z) + \rho'(\mathbf{x}, t)$), we find

$$\frac{\partial \rho}{\partial t} + u_i\frac{\partial \rho}{\partial x_i} = -w\frac{\partial \overline{\rho}}{\partial z}, \tag{2.44}$$

in which ρ is the water density and $\overline{\rho}$ is the mean component of density.

Linearizing equation 2.44 and substituting the linearized equation into 2.43, we find

$$\frac{\partial^2 w}{\partial t^2} - w\underbrace{\frac{g}{\overline{\rho}}\frac{\partial \overline{\rho}}{\partial z}}_{-N^2} = -\frac{1}{\overline{\rho}}\frac{\partial}{\partial t}\frac{\partial p}{\partial z}, \tag{2.45}$$

in which N is the buoyancy frequency, defined by equation 2.9.

Substitution of equation 2.45 into 2.42 gives us

$$\frac{\partial^2}{\partial t^2}\underbrace{\frac{\partial^2 w}{\partial x_i^2}}_{\text{total laplacian}} + N^2\underbrace{\left(\frac{\partial^2 w}{\partial x^2} + \frac{\partial^2 w}{\partial y^2}\right)}_{\text{horizontal laplacian}} = 0, \tag{2.46}$$

in which $x_i = (x, y, z)$. Note that if the system is not stratified ($N^2 = 0$), the Laplacian $\nabla^2 w = 0$ (irrotational flow) indicates the formation of surface gravity waves only (barotropic waves).

Considering just the $x - z$ plane, we can obtain the bi-dimensional form of the internal wave equation:

$$\frac{\partial^2}{\partial t^2}\frac{\partial^2 w}{\partial x_i^2} + N^2\,\frac{\partial^2 w}{\partial x^2} = 0. \tag{2.47}$$

By assuming that the solution of equation 2.47 is given the form of a plane wave ($w(x, y, t) = W(z)\ \mathrm{e}^{-(kx-\omega t)}$), we can obtain the internal wave ordinary differential equation, also known as Taylor-Goldstein equation:

$$\frac{\partial^2 W}{\partial z^2} + \left(\frac{N^2 - \omega^2}{\omega^2}\right) k^2 W(z) = 0. \tag{2.48}$$

The solution of equation 2.48, which can be obtained from the boundary condition at the lake bottom and surface, can be found analytically just for some special cases, however, for a general solution it needs to be solved numerically.

2.2.1.3 Internal seiche amplitude

The amplitude of the fundamental internal waves has been derived from the governing equations of motion for idealized (rectangular two-layer system) lakes. From the momentum equation in a non-rotating frame of reference and assuming a shallow water system, we can estimate the interfacial tilting of the thermocline. Basically, we should solve the multilayer internal wave model, which is detailed in Section 2.2.1.1, but taking into account surface wind stress applied on the lake surface. For this analysis, we may limit our example to a rectangular basin with two-layer stratification, as illustrated in Figure 13.

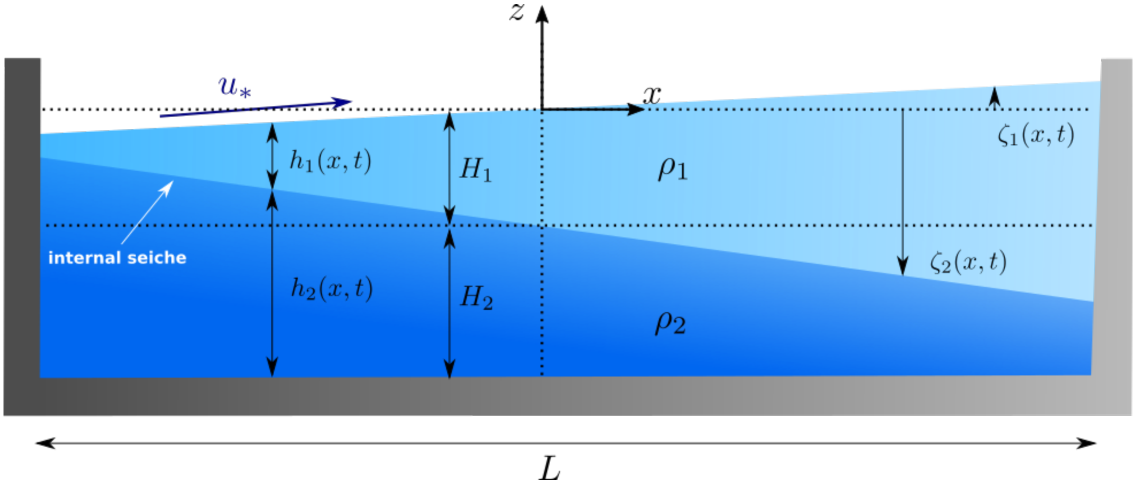

Figure 13 – Stable two-layer system ($\rho_2 > \rho_1$) in a rectangular basin. The vertical coordinate is positive above the water surface. H is the equilibrium layer thickness, whilst h is the local layer thickness. ζ describes interfaces between two fluids with different densities (referenced from $z = 0$)

The hydrostatic pressure distribution along the water column within each layer is defined as

$$p_1 = p_o + \rho_1 g(-Z + \zeta_1), \tag{2.49a}$$

$$p_2 = p_o + \rho_1 g(\zeta_1 - \zeta_2) + \rho_2 g(-Z + \zeta_2), \tag{2.49b}$$

in which p_o is the atmospheric pressure, ρ is the fluid density, g is the acceleration of gravity, and ζ is the interfacial displacement. Subscript 1 describes quantities related to epilimnion (water surface), while subscript 2 describes hypolimnion quantities (interfacial layer).

Substitution of equations 2.49 into the momentum equation for x-direction gives us

$$\frac{\partial u_1}{\partial t} = -g\frac{\partial \zeta_1}{\partial x} + \frac{u_*^2}{H_1}, \tag{2.50a}$$

$$\frac{\partial u_2}{\partial t} = -\frac{\rho_1}{\rho_2}g\frac{\partial \zeta_1}{\partial x} - \frac{\rho_2-\rho_1}{\rho_2}g\frac{\partial \zeta_2}{\partial x}, \tag{2.50b}$$

where u is the horizontal velocity, u_* is the wind stress, and H_1 is the equilibrium upper layer thickness. Unlike 2.33, now we add an additional term on the right-hand side that accounts for the contribution of the wind stress u_* to the upper layer.

Deriving equation 2.50 in x and the mass conservation equation 2.32b in time, and combining both results, we obtain the same partial differential equation presented in 2.36, the only difference is that here we restricted the result for a two-layer stratification. It should be mentioned here that the wind stress term does not modify the internal wave pattern, such as the speed and period of the wave. The only difference is that now the initial amplitude is dependent on wind speed.

Assuming that the horizontal velocity is zero, the expression for the first two layers can be written as:

$$\frac{\partial \zeta_1}{\partial x} = \frac{u_*^2}{g\ H_1}, \tag{2.51a}$$

$$\rho_1\ \frac{\partial \zeta_1}{\partial x} = -(\rho_2-\rho_1)g\frac{\partial \zeta_2}{\partial x}. \tag{2.51b}$$

Combining equations 2.51a and 2.51b, we find

$$\frac{\partial \zeta_2}{\partial x} = -\frac{u_*^2}{g'\ H_1}, \tag{2.52}$$

in which ζ_2 is the internal seiche displacement (assuming V1H1 internal seiche mode), g' is the reduced gravity, u_* is the wind stress, and H_1 is the equilibrium upper layer thickness. Note that the negative sign in equation 2.52 is related to the sign convention.

Integrating equation 2.52 and applying the lateral boundary conditions ($\Delta\zeta(x = L/2) = a_2$ and $\Delta\zeta(x = 0) = 0$), the interfacial displacement is given by

$$\frac{a_2}{H_1} = 0.5\ \frac{u_*^2\ L}{g'\ H_1^2} = \frac{0.5}{W}, \tag{2.53}$$

in which W is the Wedderburn number (equation 2.21), indicating an interesting relation between the Wedderburn number and the internal seiche amplitude.

By comparison we may find that for $W = 1$, $a_2 = H_1/2$, which indicates that metalimnetic water will upwell to the surface. Although this technique has been used to predict the internal seiche amplitude for many lakes (WEDDERBURN, 1912; MORTIMER, 1952; MORTIMER, 1953; MORTIMER, 1955b; THORPE, 1977), observations have identified that this technique does not predict the internal seiche amplitude for many other lakes due to lake complexities (CARMACK et al., 1986; STEVENS; LAWRENCE, 1997; SHINTANI et al., 2010; IMAM et al., 2020; FLOOD et al., 2021).

Observations have shown that asymmetries in basin geometry have a strong influence on the magnitude of thermocline deflection, resulting in a higher vertical displacement on the narrower shore (SHINTANI et al., 2010; FLOOD et al., 2021).

2.2.2 Modeling of heat transport: Delft3D-FLOW

Although unidimensional internal wave models, similar to those described in sections 2.2.1.1 and 2.2.1.2, have been used to describe internal seiche patterns in thermally stratified lakes (LEMMIN; MORTIMER, 1986; MÜNNICH; WÜEST; IMBODEN, 1992; ROGET; SALVADÉ; ZAMBONI, 1997; VIDAL et al., 2005; BUENO; BLENINGER, 2018), they have several simplifications and cannot be used to describe the whole process of heat transport associated with the internal wave field. The simplified multilayer internal wave model neglects horizontal variability, including effects of inflows, outflows, heat transport, mixing, and interaction between internal wave and lake bathymetry. These limitations cause fundamental problems to describe the hydrodynamic of lakes and reservoirs, especially when we are concerned with the internal wave field, which has different spatial and temporal scales, and an intrinsic three-dimensional nature.

With an improvement in computational performance, three-dimensional models of heat transport have gained prominent research interest because they are capable of simulating processes in lakes by solving the full continuity, momentum, and transport equations. As with all numerical approaches, three-dimensional hydrostatic models also have several limitations, mainly related to the turbulence aspect. Due to numerical diffusion and dissipation (HODGES; LAVAL; WADZUK, 2006) and the inability of hydrodynamic models to deal with nonlinear and non-hydrostatic mechanisms, the energy fluxes must be investigated carefully, especially the mechanism of internal seiche damping (SHIMIZU; IMBERGER, 2008). ELCOM and Delft3D are among the most well-known three-dimensional models to simulate the dynamics of shallow-water systems, such as coastal regions, reservoirs, estuaries, lakes, ponds, and rivers. The basin-scale internal wave affected by Earth's rotation has been greatly stimulated by ELCOM (HODGES et al., 2000; VALERIO et al., 2012) and Delft3D (DISSANAYAKE; HOFMANN; PEETERS, 2019; BUENO; BLENINGER, 2019; KRANENBURG et al., 2020; BARACCHINI et al., 2020). Recently, observation has shown that Delft3D and ELCOM are significantly trained in simulated large-scale internal seiches in lakes, which agrees well with field measurements in Upper Lake Constance (DISSANAYAKE; HOFMANN; PEETERS, 2019).

Now we focus on the description of the three-dimensional Delft3D-FLOW model, which is the model used in this thesis to simulate the hydrodynamics of the lake. In the next section, we present the model description, paying special attention to numerical approaches that may limit the applicability of Delft3D to investigate the internal wave field, trying to make the connection with the physical description discussed in section 2.1. A full description of the model is provided by Hydraulics (2003).

Delft3D is a multidimensional hydrodynamic numerical model based on Reynolds-Average Navier-Stokes (RANS) under the Boussinesq approximation and shallow-water assumption. The program calculates the unsteady flow and transport phenomena of heat and matter due to tidal and meteorological forces by solving the equations of mass conservation, transport, and horizontal momentum, using a turbulence closure model (HYDRAULICS, 2003). The vertical velocity field is obtained implicitly from the continuity equation.

2.2.2.1 Governing equations

The depth-averaged mass conservation equation is obtained by integrating the equation 2.32b along the water column, taking into account the boundary conditions at the water surface and lake bottom:

$$\int_{-H}^{\eta} \frac{\partial u_i}{\partial x_i} \mathrm{d}z = \frac{\partial}{\partial x_i} \int_{-H}^{\eta} u_i \mathrm{d}z - u_i(z=\eta)\frac{\partial \eta}{\partial x_i} - u_i(z=-H)\frac{\partial H}{\partial x_i} = 0, \tag{2.54}$$

in which $\eta(x,y,t)$ and $H(x,y,t)$ are the water level (surface function) and bed horizontal plane of reference, respectively.

Assuming that the bathymetry does not vary with time, we may rewrite equation 2.54:

$$\frac{\partial}{\partial x_i}\int_{-H}^{\eta} u_i \mathrm{d}z - u_i(z=\eta)\frac{\partial \eta}{\partial x_i} = 0, \tag{2.55}$$

in which η and H are the water level above and the depth below a horizontal plane of reference, respectively.

The kinematic boundary condition at water surface ($z = \eta(x, y, t)$) is defined as

$$u_i = \left\{ \frac{x_2 - x_1}{\Delta t}, \frac{y_2 - y_1}{\Delta t}, \frac{\eta(x_2, y_2, t_2) - \eta(x_1, y_1, t_1)}{\Delta t} \right\} \tag{2.56}$$

Expanding $\eta(x_2, Y_2, t_2)$ in a Taylor series:

$$\eta(x_2, t_2) \approx \eta(x_1, t_2) + (x_2 - x_1)\frac{\partial \eta(x_1, t_2)}{\partial x} + (y_2 - y_1)\frac{\partial \eta(y_1, t_2)}{\partial y}, \tag{2.57}$$

and substituting equation 2.57 into the vertical component of equation 2.56, we obtain

$$w = \frac{\partial \eta}{\partial t} + u\frac{\partial \eta}{\partial x} + v\frac{\partial \eta}{\partial y}, \tag{2.58}$$

in which $u_i = \Delta x_i/\Delta t$, where Δx_i is the grid size of each component and Δt is the time step.

Finally, substitution of equation 2.58 into equation 2.55 gives

$$\frac{\partial \eta}{\partial t} + \frac{\partial}{\partial x_i}\left(u_i\ (\eta + H)\right) = 0. \tag{2.59}$$

In Delft3D an additional term of source and sink per unit of area is added to equation 2.59 to account for the contribution of inflows and outflows.

Delft3D solves the Reynolds Averaged Navier-Stokes equations (RANS) for an incompressible fluid considering the Boussinesq approximation and the hydrostatic assumption in the vertical direction. Dividing the contribution of vertical and horizontal eddy viscosities from equation 2.32a, and applying the conservation of mass and hydrostatic assumption:

$$\frac{\partial u_i}{\partial t} + u_j\frac{\partial u_i}{\partial x_j} - \overline{\omega_o} u_k = -\frac{1}{\rho}\frac{\partial p}{\partial x_i} + \nu_h\frac{\partial^2 u_i}{\partial x_j^2} + \frac{\partial}{\partial z}\left(\nu_v\frac{\partial u_i}{\partial z}\right), \tag{2.60}$$

in which u_i is the Reynolds' time-averaged velocity field, p is the pressure, $\overline{\omega_o}$ is the inertial frequency, used to account for the contribution of the Coriolis effect. ν_h and ν_v are the horizontal and vertical eddy kinematic viscosity (m^2/s), respectively. Recall that for the shallow water assumption, the momentum equation in z-direction is reduced to the hydrostatic form since the vertical velocity is neglected in the numerical procedure ($w = 0$). Once horizontal velocities have been found, the vertical velocity is estimated by integrating the mass conservation equation 2.59.

The transport of scalars and heat are governed by a multidimensional convection-diffusion equation, which can be defined, in the orthogonal coordinates as

$$\frac{\partial C}{\partial t} + \frac{\partial u_i\ C}{\partial x_i} = \frac{\partial}{\partial x_i}\left(D\frac{\partial C}{\partial x_i}\right) + S, \tag{2.61}$$

in which C is a scalar (e.g. heat, salinity, or constituents), S is sources and sinks due to discharges and withdrawals, and D is the eddy diffusivity coefficient. For the horizontal plane and the vertical direction,

$D = D_h$ and $D = D_v$, respectively. The horizontal eddy diffusivity coefficient (D_h) is anisotropic along the horizontal plane x-y.

In order to solve equations 2.60 and 2.61, Delft3D estimates the eddy viscosity and diffusivity coefficients from the turbulence closure modules, discussed in Section 2.2.2.3.

2.2.2.2 Heat flux model

The total flux of heat energy across the water surface is modeled according to the heat balance illustrated in Figure 3. Delft3D-FLOW offers different heat flux models (HYDRAULICS, 2003) depending on the available meteorological data, such as the Murakami heat flux model (MURAKAMI; OONISHI; KUNISHI, 1985) and the Ocean flux heat model (LANE, 1989; GILL, 2016). Observations in small thermally stratified reservoirs have shown that the Murakami heat flux model underestimates the energy loss by evaporation compared to the Ocean model (POLLI; BLENINGER, 2019). Although this difference has been identified, the Murakami model was capable of detecting Kelvin and Poicaré internal waves in Lake Constance (DISSANAYAKE; HOFMANN; PEETERS, 2019). Ocean heat flux model has been used in the Delft3D model to simulate internal seiches (BUENO; BLENINGER, 2019; KRANENBURG et al., 2020). Since both models have been capable to simulate internal seiches in lakes, here we describe in detail only the Ocean heat flux model, which has been used in this thesis. The Ocean heat flux model takes into account the following components of heat:

$$Q_{\text{total}} = Q_{sw} + Q_{ir} + Q_{la} + Q_{se}, \tag{2.62}$$

in which Q_{sw} is the net heat flux from short wave, Q_{ir} is the infrared (long wave) heat flux, Q_{la} is the latent heat flux (phase change effect; e.g. evaporation), and Q_{se} sensible heat flux (temperature change effect; e.g. convection).

The net incident solar radiation (short wave) is the only term that is entirely prescribed by the Ocean heat flux model [7]. The absorption component of the net incident solar radiation into the water column is computed from the albedo coefficient $Ab_s = 0.06$, which reduces the magnitude of short wave that hits the water surface

$$Q_{sw} = Q_{iw}\ (1 - Ab_s)\ F_{cc}, \tag{2.63}$$

in which Q_{iw} is the incident solar radiation and $F_{cc} = 1 - 0.40\ C_c - 0.38\ C_c^2$ is a function to take into account the influence of absorption of solar radiation by clouds, where C_c is the user-specified fraction of sky covered by clouds. Equation 2.63 describes the balance between *short wave radiation* and *water surface radiation* illustrated in Figure 3.

The infrared radiation (Figure 3) is calculated by Ocean heat flux model as

$$Q_{ir} = 0.985\ K_{sb}\ \tau^2_{\text{water (K)}}(0.39 - 0.05\ \sqrt{e_a})(1 - 0.6\ C_c), \tag{2.64}$$

where $K_{sb} = 5.67\ 10^{-8}$ J/(m^{2}sK^4) is the Stefan-Boltzmann's constant, $\tau_{\text{water (K)}}$ is the water surface temperature in Kelvin units, and e_a is the vapor pressure, which is defined as

$$e_a = RH\ 10^{\frac{0.7859+0.03477\ \tau_{\text{atm(ř}C)}}{1+0.00412\ \tau_{\text{water(ř}C)}}}, \tag{2.65}$$

where τ_{atm} is the air temperature, τ_{water} is the surface water temperature, and RH is the relative humidity (%), which can be specified by the user as a function of time and space.

---

[7] Delft3D also provides an option that estimates the incoming shortwave radiation based on geographical position and the local time of the simulated system

The latent heat flux is calculated by dividing the contribution into two factors: wind-driven and buoyancy forces ($Q_{la} = Q_{la}^{\text{wind}} + Q_{la}^{\text{buoy}}$). The contribution due to wind is calculated through Danton's law of mass transfer (MURAKAMI; OONISHI; KUNISHI, 1985):

$$Q_{la}^{\text{wind}} = L_{\nu}\ \rho_{\text{atm}}\ c_e\ U_{10}\Bigg(q_s - q_a\Bigg), \tag{2.66}$$

in which L_{ν} is the latent heat of vaporization (J/kg), $c_e = 0.0015$ is the Dalton number, U_{10} is the wind speed at 10 m height (m/s), and q_s and q_a are the specific humidity of saturated and remote air, respectively. ρ_{atm} is the user-specified air density $(\text{kg/m})^3$.

The contribution due to buoyancy forces to the evaporation rates Q_{la} is caused essentially by the temperature differences, and is calculated based on the principle of heat and mass transfer:

$$Q_{la}^{\text{buoy}} = \kappa_s L_{\nu} \overline{\rho_{\text{atm}}}\Bigg(q_s - q_a\Bigg), \tag{2.67}$$

where κ_s is the heat transfer coefficient (-) and $\overline{\rho_{\text{atm}}}$ is the average air density (kg/m³).

The sensible heat flux is computed similarly to the latent heat flux, being split into two contributions, wind forcing and buoyancy effect:

$$Q_{se} = cp_{\text{atm}}\Bigg(\tau_{\text{water}} - \tau_{\text{atm}}\Bigg)\Bigg(\rho_{\text{atm}}\ c_h\ U_{10} + \kappa_s\overline{\rho_{\text{atm}}}\Bigg), \tag{2.68}$$

in which $cp_{\text{atm}} = 1004$ J/(kg K) is the specific heat of air at constant pressure, $c_h = 0.00145$ is the Stanton number, κ_s is the heat transfer coefficient (-) and τ_{water} and τ_{atm} are the surface water and air temperature expressed in Kelvin unit, respectively.

2.2.2.3 Turbulence model

Since Delft3D is based on RANS concepts, which average all flow fluctuations, the influence of turbulent fluctuation on mean flow can be modeled through an implemented turbulence closure model, which determines ν_v and D_v. The Delft3D model has four different turbulence closure models, including the κ-ε and $k - L$ models.

The κ-ε model is a second-order turbulence closure scheme that is based on the balance between dissipation and production of turbulent energy, which implies an equilibrium hypothesis under the boundary condition, $P = \varepsilon$. Investigations have shown that the κ-ε turbulence closure model provides good applicability to detect internal seiches in stratified lakes (GOUDSMIT et al., 2002). However, vertical mixing induced by shear and break of high-frequency internal waves is not explicitly taken into account in the κ-ε turbulence closure model implemented in Delft3D (HYDRAULICS, 2003). Furthermore, the energy of BSIW transferred to high-frequency waves through degeneration processes is underestimated by the Delft3D model (BUENO; BLENINGER, 2019).

The vertical eddy viscosity (ν_v) is defined as the combination of the molecular viscosity and the maximum eddy viscosity coefficient comparing the result of the turbulence closure model and the background vertical mixing that accounts for all other forms of unresolved turbulence ν_v^{back}, which must be specified by the user. For a strong stratified system, ν_v is reduced to the molecular viscosity, which neglects the contribution of unresolved internal waves. To model the production of turbulence induced by the internal wave field, the vertical eddy viscosity must be amplified. In Delft3D, propagating internal waves, which are susceptible to being excited and breaking near the lakeshore, may not be explicitly taken into account depending on the wavelength scale. The effect of these internal waves can be taken into account through a constant background vertical eddy viscosity coefficient.

The vertical eddy diffusivity coefficient D_v is obtained similarly to the viscosity coefficient. In addition, for the 3D-turbulent closure model, the influence of internal wave breaking is also taken into account in a strong stratified system by the Ozmidov length scale (equation 2.11):

$$D_v^{wave} = 0.2\ L_o^2\ N \tag{2.69}$$

in which L_o is the Ozmidov length scale and N is the buoyancy frequency (equation 2.9). The vertical eddy diffusivity (D_v) is determined as the maximum of the vertical eddy diffusivity estimated by equation 2.69 and the 3D turbulence closure model (UITTENBOGAARD; KESTER; STELLING, 1992), which is also combined with the molecular contribution. Note that the equation 2.69 defined in Delft3D uses a constant mixing efficiency $\gamma_{\text{mix}} = 0.2$ (equation 2.3).

The horizontal components of the viscosity and diffusivity are calculated based on the contribution of the sub-grid scale horizontal eddy viscosity/diffusivity, background quantity, and the coefficients computed following the κ-ε turbulence closure model.

To find all eddy coefficients, the user must specify the background vertical eddy diffusivity (D_v^{back}) and the background vertical eddy viscosity (ν_v^{back}), which are specified to take into account the contribution of vertical mixing associated with internal wave breaking and shearing, and other mixing effects that are not resolved by the turbulence model. The background coefficient should be of the order of 10^{-4} to 10^{-5} m^2/s for the diffusivity coefficient and 10^{-4} m^2/s for the viscosity coefficient (HYDRAULICS, 2003). For fine grids ($\mathcal{O}(< 100\text{ m})$), $D_h \approx 1$ to 10 m^2/s, while for coarser grids, D_h may vary between 10 and 100 m^2/s.

2.2.2.4 Numerical aspects

The full momentum, continuity, and transport equations in Delft3D are solved based on a finite difference approach with the implicit method in alternating direction (STELLING; DUINMEIJER, 2003) using the Arakawa C-grid type of discretization (ARAKAWA; LAMB, 1977), in which the water level is defined in the center of the cell and the velocity components are specified perpendicular to the faces of the cells. Delft3D follows the Courant-Friedrichs-Lewis (CFL) condition to guarantee the stability of the model (SMITH; SMITH; SMITH, 1985)

$$C_r = 2\Delta t\sqrt{gH\left(\frac{1}{\Delta x^2} + \frac{1}{\Delta y^2}\right)} \leq 1, \tag{2.70}$$

in which g is the acceleration of gravity, H is the total water depth, Δt is the simulation time step, and Δx and Δy are the grid size in x and y direction, respectively. It should be mentioned here that, since Delft3D uses an implicit scheme, even for $C_r > 1$, the simulation is not unstable. The recommended limit to guarantee a stable solution is $C_r < 11$ (HYDRAULICS, 2003).

To keep small numerical diffusion, the horizontal advection term in the multidimensional convection-diffusion equation 2.61 is split into two second-order central discretizations and a third-order upwind scheme (cyclic method).

The horizontal eddy viscosity must be specified by the user under the following condition:

$$\nu_h < \frac{\Delta x^2 \ \Delta y^2}{\Delta t(\Delta x^2 + \Delta y^2)}, \tag{2.71}$$

in which Δt is the time step, and Δx and Δy are the grid size of the simulation in x-direction and y-direction, respectively.

The model also requires a condition for the stability of baroclinic mode (internal wave propagation), which requires that

$$\Delta t \sqrt{\frac{\rho_b - \rho_o}{\rho_o} \frac{gH}{4} \left(\frac{1}{\Delta x^2} + \frac{1}{\Delta y^2} \right)} < 1, \tag{2.72}$$

in which ρ_b and ρ_o are the water density at the lake bottom and surface, respectively.

3 Internal seiche parameterization

The work described in this chapter has been published to *Environmental Fluid Mechanics Journal* under the title 'An empirical parametrization of internal seiche amplitude including secondary effects'.[1]

Abstract

An internal wave is a propagating disturbance within a stable density-stratified fluid. The internal seiche amplitude is often estimated through previously established theories that describe the amplitude growth based on the Bulk Richardson number (Ri). However, most theoretical formulations neglect secondary effects that may influence the evolution of internal seiches. Since these waves have been pointed out as the most important process of vertical mixing, influencing the biogeochemical fluxes in stratified basins, the wrong estimation may have several impacts on the prediction of the system dynamics. This research paid particular attention to the importance of secondary effects that may play a major role on the basin-scale internal wave amplitude, especially related to the interaction between internal waves and lake boundaries, internal wave depth, and mixing processes due to turbulence. Based on a set of methods, which include auto- and cross-correlations, spectral analysis, and mathematical models, we analyzed the effect of total water depth, wind-resonance, and higher vertical modes on the amplitude growth. We based our analysis on underwater temperature measurements and meteorological data obtained from two small thermally-stratified basins, complemented with numerical simulations, which simulated the dynamics of basin-scale internal waves in a hypothetical rectangular tank. We introduce here a new parameterization which takes into account the total water depth (H), lake length (L), epilimnion thickness (h_e), as well as the resonance effect. We observed that the rate of amplitude growth decreases compared to linear theory when $Ri\ h_e/L \leq 1$. In these cases, we suggests that previous theories overestimate the internal seiche amplitude, neglecting the instabilities generated near the wave crest due to weak stability and wave interactions. However, under shallow thermocline conditions, due to extra pressure in the upper layer, the vertical displacement may be higher than that predicted by the linear theory.

---

[1] de Carvalho Bueno, R., Bleninger, T. B., Yao, H. & Rusak, J. A. - An empirical parametrization of internal seiche amplitude including secondary effects. *Environ. Fluid Mech.* (2020) https://doi.org/10.1007/s10652-020-09767-1

3.1 Introduction

Internal gravity waves are a propagating disturbance within a stable density-stratified fluid, and have been observed to have great impact on many stratified ecosystems, such as atmosphere (SUTHERLAND, 2020), ocean (WELLS, 2007), lakes, and reservoirs (HINGSAMER; PEETERS; HOFMANN, 2014). In closed stratified systems, generally called basins, such as lakes and reservoirs, the most common type of waves is the basin-scale internal wave which is often formed due to the wind stress at the water surface (WATSON, 1903). Herein, the wind introduces kinetic energy at the water surface, and the wind stress pushes the surface water to the leeward shore, causing a small surface displacement. If the wind stress is applied for sufficient time, the horizontal pressure gradient rises, and the hypolimnion water is accelerated towards the upwind direction, resulting in an internal tilt of the thermocline (Figure 14). When the wind stops, the tilted layer flows back towards equilibrium. However, as momentum is considerable the equilibrium position can be overshot, resulting in a rocking motion around the nodal point, which characterizes the evolution of a basin-scale internal wave (BSIW), a stationary wave.

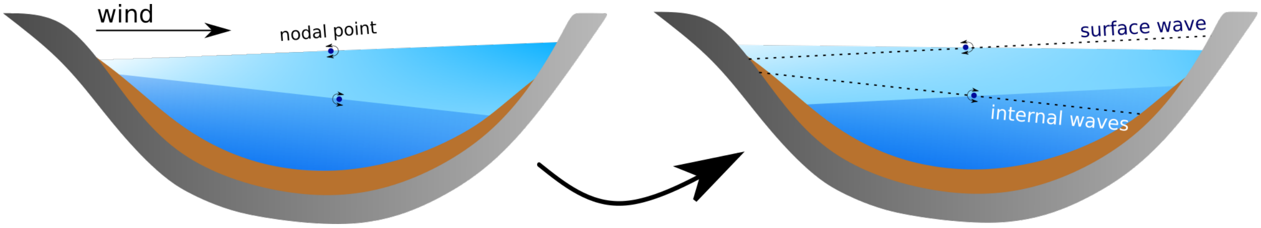

Figure 14 – A wind-induced stationary internal wave in a stratified basin. Left: Tilting of surface and interface, due to wind stress. Right: Oscillatory motion of surface and interface after wind stopped at one half of the wave period. Dashed lines indicate surface and interface location right after wind stopped.

Basin-scale internal waves have been studied extensively since the 20th century. New field and laboratory measurement techniques have provided a better understanding of internal wave patterns, revealing the strong influence on the system dynamics. Studies have pointed out that wind-induced BSIWs are responsible for benthic boundary layer resuspension (BRUCE et al., 2008a). Furthermore, there is evidence that up to 40% of the hypolimnic volume may be exchanged after a passage of a BSIW in stratified lakes (UMLAUF; LEMMIN, 2005). Wind-induced internal seiches are capable of moving back and forth between the reservoir boundaries without appreciable damping. In addition, the energy deposited into such long internal seiches is transformed through a down-scale energy cascade across the spectrum of internal waves (BOEGMAN; IVEY; IMBERGER, 2005b), increasing the system mixing, and consequently, affecting significantly the water quality of these ecosystems. Internal waves produced in stratified systems have direct consequences on nutrients (MACINTYRE; JELLISON, 2001), microorganisms (PANNARD; BORMANS; LAGADEUC, 2008), and chemical substance fluxes (BOUFFARD; ACKERMAN; BOEGMAN, 2013).

Normally, BSIWs are classified by nodal points on the vertical (V) and horizontal (H) components, VnHm, in which n and m are the number of nodes of each component (Figure 15). Higher vertical internal seiche modes were rarely reported for large lakes. However, there is a growing evidence that the formation of higher vertical modes is more evidenced in small lakes where the metalimnion takes up a relatively larger proportion of the total lake depth than in large closed basins (ROGET; SALVADÉ; ZAMBONI, 1997). In addition, there is evidence that the higher vertical modes are also correlated to unequal differences of density between layers, wind resonance, and basin asymmetry (MÜNNICH; WÜEST; IMBODEN, 1992).

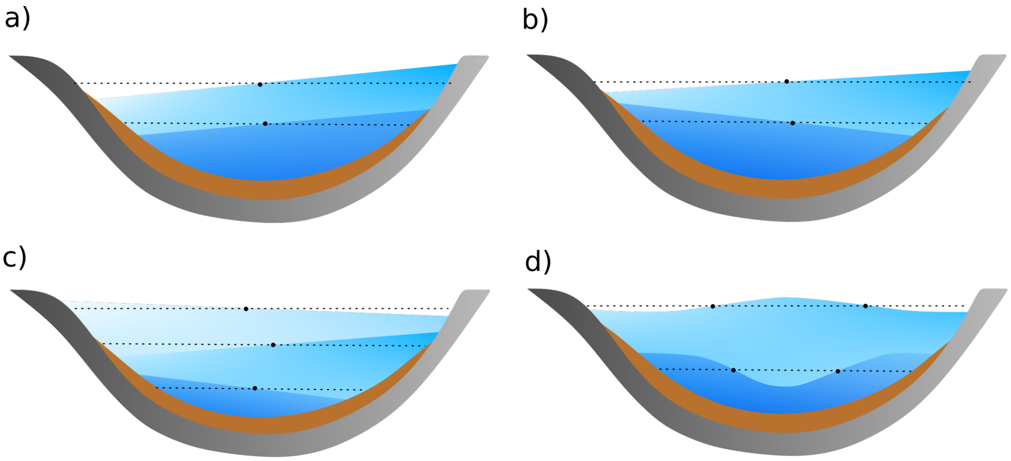

Figure 15 – Schematic view of various internal wave modes in a closed basin: a) V0H1, b) V1H1, C) V2H1 and d) V1H2. The mode for $n = 0$ is related to the pure surface (barotropic) mode. The black dots ($\cdot$) represent nodal points

Previous theories of the dynamics of BSIWs have shown that the internal seiche amplitude is inversely proportional to the ratio of the buoyancy frequency and the vertical wind shear (SPIGEL; IMBERGER, 1980; BOEGMAN et al., 2003; SHINTANI et al., 2010), which is often described by the Bulk Richardson number (Ri),

$$Ri = \frac{g' h_e}{\kappa_v u_{\text{wind}*}^2}, \tag{3.1}$$

in which g' is the reduced gravity ($= g\Delta\rho/\rho$), $\kappa_v \approx 0.4$ is the Von Kármán constant, h_e is the epilimnion thickness at the deepest point, and $u_{\text{wind}*}$ is the friction velocity of the wind. Although many studies have investigated internal seiches excited during summer seasons due to the stratification conditions, higher amplitude internal waves have been detected during periods of weak thermal-stratification (ARNON et al., 2019).

Current theories and descriptions of internal wave dynamics (SPIGEL; IMBERGER, 1980; BOEGMAN et al., 2003; SHINTANI et al., 2010) have shown good agreement with field observations under some conditions, especially for high Bulk Richardson numbers (STEVENS; LAWRENCE, 1997). However, the motion of the basin-scale internal waves is not well understood yet. The theories formulated to describe the evolution of BSIWs just take the thickness and density of an immiscible two-layer system and the wind intensity into account. Based on that, the theories show that the weaker the stratification, the higher will be the internal wave. However, the evolution of BSIWs can be modified by secondary effects, such as the influence of mixing due to higher turbulence production, interaction between internal wave and lake surface and lake bathymetry, wind resonance, and systems with multi-layer or continuous stratification, which may favor the formation of higher vertical modes. Furthermore, only specific case studies analyzed their internal wave characteristics (STEVENS, 1999; VIDAL et al., 2005; ROGET et al., 2017). Studies are missing on analysis of universal features or common processes that cause the excitation of BSIWs and their evolution, and this holds especially for BSIWs generated during periods of low Bulk Richardson number.

This study therefore aimed to compare field observations and numerical simulations with previously established theories that predict the height of BSIWs based on dimensionless variables (SPIGEL; IMBERGER, 1980; SHINTANI et al., 2010). This paper highlights the differences between BSIWs generated in different conditions, and exploring the reasons of these differences. Based on this analysis, we suggest a new empirical parametrization which includes the contribution of internal seiche interaction with lake boundaries. The analysis is based on Ri and internal seiches detected in two real thermally-stratified basins (Vossoroca reservoir and Harp Lake) and additionally generated in a three-dimensional numerical model, considering different meteorological and underwater temperature conditions.

3.2 Methods

To identify internal wave patterns, we used spectral analysis of different isotherms and pycnocline variations. From the governing equation of motion, internal wave periods were estimated. To highlight and observe the universality of BSIWs, internal seiches were analyzed in two different thermally-stratified basins, a dendritic reservoir in the subtropics and a nondendritic lake in a temperate climate. We also simulated the formation of BSIWs in a three-dimensional numerical model under different density stratifications and pycnocline depths. We combined all parameters and stratification structures obtained from Vossoroca Reservoir, Harp Lake, and the numerical simulations, in a single diagram, through a new parametrization.

3.2.1 Site description and Data collection

Vossoroca Reservoir (25° 49’ 31” S, 49° 3’ 60” W) is a small and dendritic-shaped reservoir located 30 km from Curitiba, capital of Paraná state in southern Brazil. The reservoir presents a shoreline development index of 6.2 (ratio of the length of the shoreline to lake area) and has two long narrow arms 300 m wide oriented to the southeast and southwest with length of 3.25 km and 2.72 km, respectively. The reservoir, shown in Figure 16 (left), has a volume of 35.7 10^6 m^3, a maximum depth of 17 m, an average depth of approximately 6 m, and surface area of 510 ha. The wind action over the reservoir is essentially driven by the regional topography to northeast direction with an average magnitude of 3.6 m/s. Winds stronger than 5.5 m/s are rare in the region, lasting only few minutes and never greater than 7.3 m/s.

We compare the results obtained from Vossoroca Reservoir with those obtained from Harp Lake. Harp Lake (45° 22’ 45” N, 79° 08’ 08” W), which has been monitored by Dorset Environmental Science Centre (DESC) (YAN; STRUS, 1980; YAN; PAWSON, 1997; YOUNG; LOEW; YAN, 2009), is a small, square-shaped lake located in south-central Ontario, Canada. The lake, shown in Figure 16 (right), is an oligotrophic lake with an area of 71.38 ha, volume of 9.5 million m^3, maximum depth of 37.5 m, and average depth of approximately 13.3 m. The Harp Lake presents a shoreline development index of 1.7. The wind does not present a dominant direction as observed in Vossoroca Reservoir, presenting wind speed average of 3.0 m/s, with a maximum of 5.4 m/s.

The vertical temperature structure of Vossoroca Reservoir corresponds to a holomictic (i.e. polymictic) lake, whilst Harp lake is a dimictic lake that is covered by ice during the winter. In Vossoroca reservoir, periods with weaker stratification start in autumn (after April), and the system is completely mixed only in July. In summer, around December, the temperature difference between bottom and surface reaches 10 °C. The relatively simple bathymetry of Vossoroca Reservoir and the constant wind direction leads to standing internal wave activities (BUENO; BLENINGER, 2018). This study amplifies the previous study by adding a multi-layer model and a complete analyses along the whole year of 2012 and 2013.

Differently from Vossoroca reservoir, in Harp Lake, the thermal stratification starts after April (spring in the northern hemisphere), and the system is strongly stratified in July with $\Delta\tau = 20$ °C. Between the

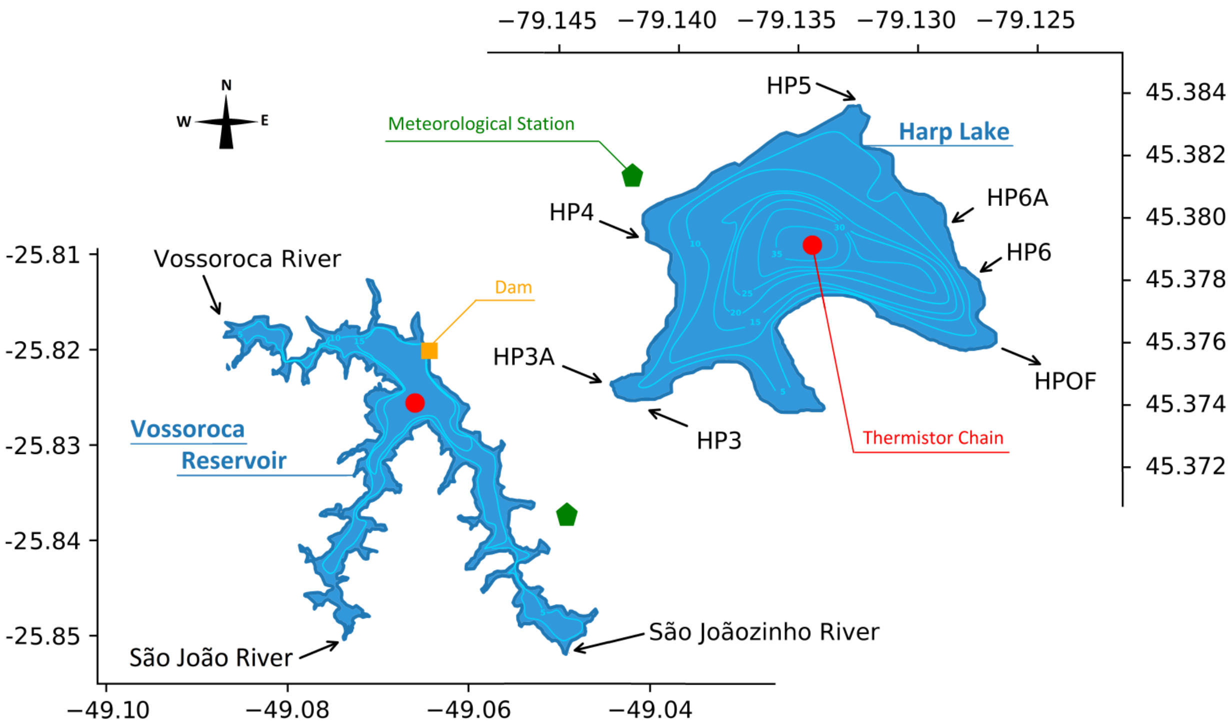
−79.145
−79.140
−79.135
−79.130
−79.125
45.384
45.382
45.380
45.378
45.376
45.374
45.372
N
W
E
Meteorological Station
HP5
Harp Lake
HP6A
HP6
HP4
HPOF
HP3A
HP3
Thermistor Chain
Vossoroca River
Dam
Vossoroca
Reservoir
São João River
São Joãozinho River
-25.81
-25.82
-25.83
-25.84
-25.85
−49.10
−49.08
−49.06
−49.04

Figure 16 – Maps of Vossoroca reservoir (left), and Harp Lake (right), with depth contours and locations of observation points (green: meteorological station, red: platform with thermistor chain), and in and outflows (arrows).

northern winter period, December and March, the lake is ice-covered. Although studies have identified internal waves in ice-covered lakes (BOUFFARD et al., 2016), the excitation mechanism during the winter season is not due to wind forcing on the water surface. As our goals in this study is to compare results between Vossoroca Reservoir and Harp Lake, the consideration of internal waves in ice-covered season was beyond the scope of this study. Thus, we just investigate the internal wave activity during summer and autumn for Harp Lake.

Water temperature, water level, solar radiation, wind speed and direction were recorded during 2010 to 2015. Wind direction and velocity were measured in Vossoroca reservoir and Harp Lake by a Young wind monitor with accuracy of ± 2° and ± 3°, respectively, both with ± 0.3 m/s of speed accuracy. Solar radiation was measured in Vossoroca Reservoir and Harp Lake by a Campbell Scientific CMP3-L Pyranometer with accuracy of ± 1 W/m^2 and a Kipp & Zonen Solar Radiation CMP6 Sensors with accuracy of 5 to 20 μV/W/m^2, respectively. The meteorological station recorded data at 30-min and 10-min interval in Vossoroca and Harp, respectively.

A thermistor chain was deployed at both basins, at the deepest point (Figure 16). The chains were equipped in Vossoroca reservoir and Harp Lake with seven thermistors LM 35 with sampling frequency of 10-min and 28 Campbell Scientific thermistors with a sampling rate of 10-min, respectively. Both thermistor chains have an accuracy of ± 0.1 °C. We analyzed internal seiche formation through water temperature and meteorological data from 2012 to 2015, and we chose different sub-periods to identify baroclinic activity during different seasons and thermal conditions.

3.2.2 Data treatment

We calculated density profiles based on the last version of the equation of state proposed by Intergovernmental Oceanographic Commission and others (2015). We neglected the contribution of salinity to density since salinity levels in those freshwater bodies were insignificant. Moreover, we also ignored the effect of pressure on water density since we considered the flow as incompressible (MORTIMER, 1979). Although, as stated by Wüest and Lorke (2003), dissolved substances may affect water density, however, relevant substance concentrations were insignificant, too.

For the definition of the pycnocline depth and the metalimnion thickness, we used the weight approach proposed by Read et al. (2011). This technique adds a weight to adjacent measurements, improving the initial guess that the pycnocline is located at the midpoint depth between two measurements that present the highest temperature change. In addition, for Vossoroca reservoir, we compared, during sporadic campaigns, once or twice a month, temperature profiles obtained from the thermistor chain with CTD (Conductivity, Temperature, and Density) profiles obtained by a Sontek CastAway probe. The isotherms were obtained through linear interpolations from water temperature data (LEMMIN, 1987).

3.2.3 Numerical simulation

We conduced a total of 32 numerical simulations in a rectangular basin to simulate the formation of a BSIW in a two-layer thermally stratified rectangular tank of 4 km long and 500 m wide with a constant water depth of 15 m (Figure 17a). These dimensions were chosen based on general dimension of Vossoroca reservoir. We covered a range of density differences of $0.04\ \mathrm{kg/m^3} \leq \Delta\rho \leq 2.32\ \mathrm{kg/m^3}$, which correspond to temperature difference of 0.25 °C to 11 °C. The density range used were chosen based on values of Ri. For all simulation, the initial temperature of the lower layer was assumed to be constant and equal to 15 °C. We changed the ratio h_e/H from 0.13 to 0.73, in which h_e is the upper layer thickness and H is the total water depth ($H = 15$ m).

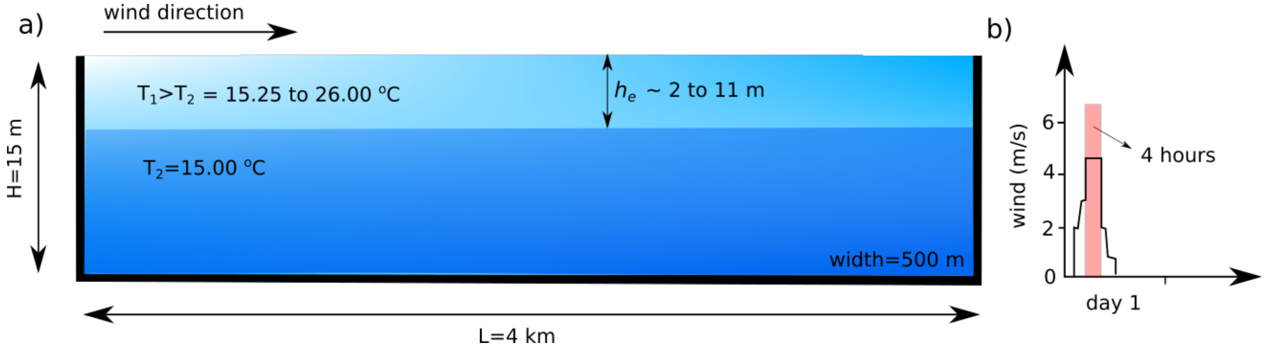

Figure 17 – a) Sketch of the numerical experiment and b) the wind event responsible to excite a BSIW for all numerical simulations. Red bar indicates the period of homogeneous wind.

We used the Delft3D-FLOW model (Deltares, 2014), which is capable of simulating the hydrodynamics of shallow water system, such as coastal waters, rivers, lakes, reservoirs, and estuarine areas, providing a detailed analysis of the spatial and temporal variations of physical mixing and transport processes in water bodies. This model has been widely used to analyze the hydrodynamics of stratified water basins and the biological effects in these ecosystem. Moreover, evidences show that the Delft3D model might successfully reproduce the formation and evolution of basin-scale internal waves in stratified lakes (DISSANAYAKE;

HOFMANN; PEETERS, 2019). The model solves the unsteady Reynolds-averaged Navier-Stokes equations and the hydrostatic assumption for heat and momentum transfer across the tank through a finite difference approach with an ADI numerical scheme. The model uses a multi-directional upwind scheme to solve the horizontal advection equation (STELLING; DUINMEIJER, 2003). For a better analysis of the dynamics of BSIWs, we neglected the heat transfer at the water surface, as well as through internal heating by radiation. Thus, there is no heat energy source or sink considered. In addition, we did not consider the Coriolis effect, which could favor the occurrence of Kelvin and Poicaré internal waves in large lakes or higher vertical baroclinic modes. We used the κ-ε turbulent closure scheme (RODI, 2017), in which turbulent kinetic energy and energy dissipation was estimated by the transport equation.

Simulations were performed on a 90 m × 90 m horizontal grid with 50 fixed layers equally spaced in depth providing a vertical resolution of 30 cm. We used a z-grid in the vertical direction and an orthogonal grid in the horizontal plane. The depth of each layer was defined in the center of each cell, whereas the velocity field was defined in the middle of the cell side. To satisfy the Courant-Friedrichs-Lewy (CFL) stability condition, a time step of 1 minute was used in all simulations. The formation of basin-scale internal waves was obtained through an initial stress boundary condition at the free surface that was kept equal for all simulations. We considered one wind event with maximum peak of 4.5 m/s blowing in the west direction for ≈ 4 h (Figure 17b). No inflows or outflows were considered.

3.2.4 Spectral Analysis

To identify the periodicity and evolution within the measured data, we used Wavelet and Fourier transforms. The spectral analysis of isotherms was used to determine the number of standing wave modes, the depth variation of each mode, and its energy distribution.

The spectral analysis was applied to the time series of wind speed, solar radiation, and the depth of different isotherms. Power spectral densities were applied to overlapping data segments using the Hamming window function. Then, firstly, we obtained the traditional fast Fourier transform (FFT), which provided time-averaged pictures of the frequency distribution. Since we did not know exactly what is the internal wave period range that could be excited in the stratified system, we used four different window sizes (5 days, 1 day, 12 hours, and 1 hour) to analyze the spectrum. This technique was used to improve the confidence interval for the spectral power at short time periods. To analyze more details in frequency spectral variance, we reduce the window size to average more numbers of segments, and tried to balance the frequency resolution and the internal wave peak variance.

We used 50% of overlapping for the Hamming procedure (HEINZEL; RÜDIGER; SCHILLING, 2002). Secondly, through the ratio of sampling frequency and the mean-square power spectrum, which is obtained through the Fourier transform of the auto-covariance function, we obtained the power spectral density (PSD).

We obtained the coherence and phase shift of isotherms and meteorological data to identify energetic peaks in the temperature spectrum that could indicate resonance between wind-forced oscillations and the internal seiche modes, and the excitation of higher vertical baroclinic motions. We compute the coherence between two signals using the mean-square power spectrum of these signals and the cross power spectrum.

Finally, we applied the wavelet technique in different isotherms since this solves the variations of frequency content with time, improving the temporal resolution (TORRENCE; COMPO, 1998). We applied the discrete time continuous wavelet transform (DT-CWT) to the isotherms. We used the Morlet basic wavelet function since it consists of a plane wave modulated by a Gaussian function, improving considerably the temporal resolution.

3.2.5 Internal Seiche Model

All results from the processed field observations and the numerical simulations will be compared also to a simplified seiche model to check its performance and accuracy for the presented multi-scale cases.

We used a multi-layer hydrostatic linear model with free surface and the shallow water assumption ($H \ll \lambda$) based on Mortimer (1952) three-layer model. We computed the wind fetch based on the geographic wind direction and the basin length. As mentioned before, if the wind stress is applied for sufficient time, the setup height at the lake end can increase and, consequently internal waves can develop. Therefore, we compared the wind stress and the direction of the wind to identify the direction and predicted periodicity of internal seiches. We computed the mean internal seiche period by averaging all the fetch vectors within 20 degree from the main wind direction, considering the pycnocline shore for V1H1 mode.

Based on the governing equation of motion for x-direction with N layers and considering a hydrostatic expansion of the total pressure in terms of interfacial displacements, the inviscid, linearized momentum equation becomes

$$\frac{\partial u_j}{\partial t} = -g \sum_{k=1}^{N} \left(\frac{\rho_{k(j)}}{\rho_j} \frac{\partial}{\partial x} (\zeta_k + \zeta_{k+1})(-1)^{k+1} \right), \tag{3.2}$$

where ζ_k is the interfacial displacement of layer k, except for ζ_1 that represents the surface displacement, $\rho_{k(j)}$ is the density of the layer k when $k < j$, whilst for $k > j$, the $\rho_{k(j)}$ assumes the value of j, in which j is just a counter increment.

The linearized mass-conservation equation for layer j can be obtained through the Taylor expansion and the linearization procedure ($a_j \ll \lambda$), which results to

$$\frac{\partial}{\partial t} ((\zeta_j + \zeta_{j+1})(-1)^{k+1}) + H_j \frac{\partial u_j}{\partial x} = 0, \tag{3.3}$$

where H_j is the total depth until layer j.

Combining equations 3.2 and 3.3 to eliminate u, give us the wave equation:

$$\frac{\partial^2}{\partial t^2} (\zeta_j + \zeta_{j+1}) = -g H_j \sum_{k=1}^{N} \left(\frac{\rho_{k(j)}}{\rho_j} \frac{\partial^2}{\partial x^2} (\zeta_k + \zeta_{k+1}) \right). \tag{3.4}$$

Assuming that $\zeta_j + \zeta_{j+1} \equiv f(x,t) = X(x) \cos(\omega\, t)$, equation 3.4 reduces to a second-order linear ordinary differential equation, which is a classical Sturm-Liouville eigenvalue problem for N layers.

Finally, combining the horizontal eigenvalue problem with the phase speed ($c_n = \sqrt{g\beta_n}$) yields the dispersion relation

$$\omega_{n,m}^2 = g \beta_n k^2, \tag{3.5}$$

in which β represents the eigenvalues, k is the wave number, ω is the angular frequency of the internal wave, and n and m are the number of nodes of vertical and horizontal components, respectively.

Finally, since higher vertical modes frequently have frequencies near the inertial frequency, which normally results in the formation of a Poicaré internal seiche, we computed the deviation caused by Earth rotation correcting the angular frequency based on techniques for shallow water influenced by rotation (SUTHERLAND, 2010). Based on recommendations made by Hutter, Wang and Chubarenko (2011), since the higher vertical modes present subjective layer thickness, we also obtained the model sensitivity to evaluate internal wave period changes due to layer thickness change. For numerical simulations, since our system was stratified just in two layers, we only calculated the periodicity for fundamental basin-scale internal waves.

3.2.6 Characteristic parameters

Although many procedures have been proposed to detect the excitation of baroclinic motion, our particular attention was devoted to understand the relationship between basin-scale internal wave amplitude and the thermal stratification stability of the stratified basins. Often this analysis is conducted through the estimation of the dimensionless Richardson number (Ri), which may be expressed through equation 3.1.

We compared the results obtained from Harp Lake, Vossoroca reservoir, and numerical simulations with mathematical theories proposed by Spigel and Imberger (1980) and Shintani et al. (2010). Spigel and Imberger (1980) formulated a linear approach to predict the amplitude of fundamental internal seiches based on the Ri. The linear approach is described by the following expression:

$$Ri_{V1} = \frac{a\ L}{2\ h_e^2}, \tag{3.6}$$

where a is the amplitude of the basin-scale internal wave, h_e is the epilimnion depth, L is the length of the reservoir aligned to the wind at the pycnocline depth,

Recently a nonlinear approach has been proposed by Shintani et al. (2010). The theory presents an upward curvature of the interface due to the nonlinear effects, which tends to deviate from linear theory for small Ri (≈ 3). The nonlinear solution may be estimated by the empirical fitting function,

$$Ri_{V1} = \frac{8L}{9h_e}\left(1 + \tan\left(\frac{\pi}{2}\left(1 - \frac{a}{h_e}\right)^{1/0.57}\right)^{1/0.81}\right), \tag{3.7}$$

in which a is the amplitude of the basin-scale internal wave.

Based on results obtained from Vossoroca reservoir, Harp Lake, and numerical simulations during periods of different meteorological conditions, density profiles, basin morphology, we correlated the spectral energy of internal seiche and amplitude of basin-scale internal wave to Ri, to understand the relationship between the system instability and internal seiche amplitude, highlighting a more complex classification for basin-scale internal seiches. Finally, based on these analyses, we could understand better the condition that favors the excitation of higher amplitude internal waves, and how it affects the internal wave evolution.

3.3 Results and discussions

3.3.1 Spectral Analysis and seiche model

For Vossoroca, the basin-scale internal waves were excited in early spring in the Southern Hemisphere, during the month of September 2012. The selected sub-period is comprised between September 15 and 25, 2012. Although the first half of September has presented a strong oscillation near the thermocline, the system presented higher Ri, with daily wind events < 1 m/s and thermal stratification of $\Delta\tau \approx 4$ °C (Figure 18).

During the selected sub-period the temperature difference increased to $\Delta T \approx 8$ °C, and the mean daily wind speed increased to 1.3 m/s, presenting higher wind changes. Since the increase of the thermal stratification was compensated by the mean daily wind rise, the daily Ri decreased in the sub-period from 10^6 to 10^3. The selected period is likely to excite dominant internal seiches that should be susceptible to a nonlinear degeneration (SPIGEL; IMBERGER, 1980; BOEGMAN; IVEY; IMBERGER, 2005a). During the entire period of analysis the wind presented a small diurnal component that could favor the formation of forced internal seiche (BOEGMAN; IVEY, 2012). However, due to low energy associated with the diurnal wind component, the internal wave of mode two was dominant in the stable interior layer.

The spectral analyses for that period (Figure 19a) shows a significant peak, with spectral energy higher than the mean red noise spectrum for the time series at a 95% confidence level. The peak is observed in the 16 °C isotherm $\approx$ 2 m below the thermocline. Since the coherence between the 16 °C isotherm and the wind intensity is notably low ($<$ 50%), the excited internal wave is not apparently affected by wind resonance effects. Considering that the generated internal wave has higher frequency compared to the diurnal component of the wind (often the most energetic component), diurnal forced internal wave could be excited in the system (BOEGMAN; IVEY, 2012). However, apparently due to the small amount of energy associated to diurnal components of the wind, forced oscillatory motions have not been observed with diurnal period.

The multi-layer hydrostatic linear model with free surface and shallow water assumption was applied to predict the first three vertical internal wave modes (Figure 19a). The model results match with the first two vertical modes, indicating the occurrence of an internal seiche of 16 h 30 period (Figure 19a).

The out-of-phase response between isotherms, a typical characteristic of higher vertical modes, can be evidenced by the phase analysis between the 16 °C and 18.5 °C isotherm time series (Figure 20a). The 16 h 30 period is also observed in 18.5 °C isotherm with spectral energy higher than the mean red noise spectrum for the time series at a 95% confidence level (Figure 19a). The 90° out of phase response between the 16 °C and 18.5 °C isotherm time series suggests that they belong to different layers. This observation corroborates with previous results from Vossoroca reservoir (BUENO; BLENINGER, 2018). Although both isotherms present oscillatory motion compatible with evolution of internal seiches, the deeper interface apparently has more oscillations with higher energy compared to the 18.5 °C isotherm. Since the water density difference is lower in deeper region, the same energy input may generate a higher displacement of the 16 °C isotherm compared to a upper interface (Figure 20b).

The variation due to internal seiche activity presented a total vertical displacement of approximately 1.0 m in the 16 °C isotherm, 6% of the total depth. The wavelet analyses (Figure 20c) shows that the V2H1 internal seiche was generated at the end of September 16. The internal wave action lasted for four days and was completely damped on September 22.

Higher horizontal modes have not been observed to be excited given the small size of Vossoroca reservoir. Often higher vertical modes are more susceptible to be excited in large lakes with irregular bathymetry. In addition, the formation of higher horizontal modes due to wind resonance effects during this period of analysis are unlikely to occur since detected internal seiches in Vossoroca reservoir often have periods lower than the diurnal component of the wind.

For time being this section highlighted only one period of basin-scale internal wave activity, however, other periods are summarized in the supplementary material. In addition, one period from Harp Lake is presented in details in Appendix C, similar to what has been provided here for Vossoroca reservoir.

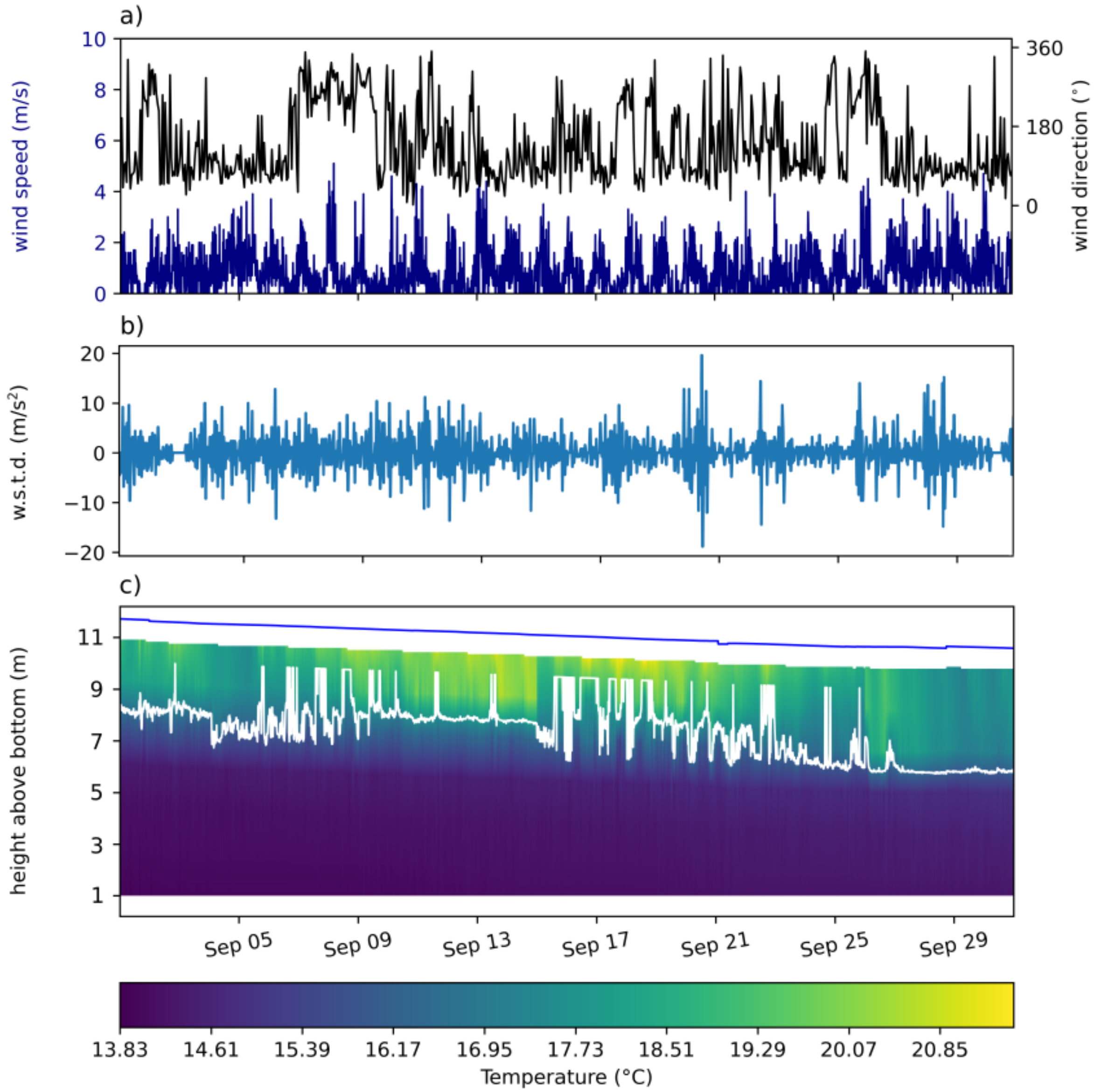

Figure 18 – Overview of field data from Vossoroca reservoir during September 2012 (Vossoroca reservoir; 01/09 – 29/09). a) Wind speed and direction, b) wind change with time, and c) thermal structure showing temperatures in colors and the thermocline position as a white solid line. The water surface elevation is represented by the blue solid line.

3.3.2 General comparison

All data for Vossoroca and Harp were processed in a similar way, and compared to each other with respect to the seiche amplitude for different Ri. Figure 21 illustrates the obtained results for different methods to compute Ri, described as follows.

All isotherms time-series were filtered in terms of spectral analysis to reveal the total vertical dis-

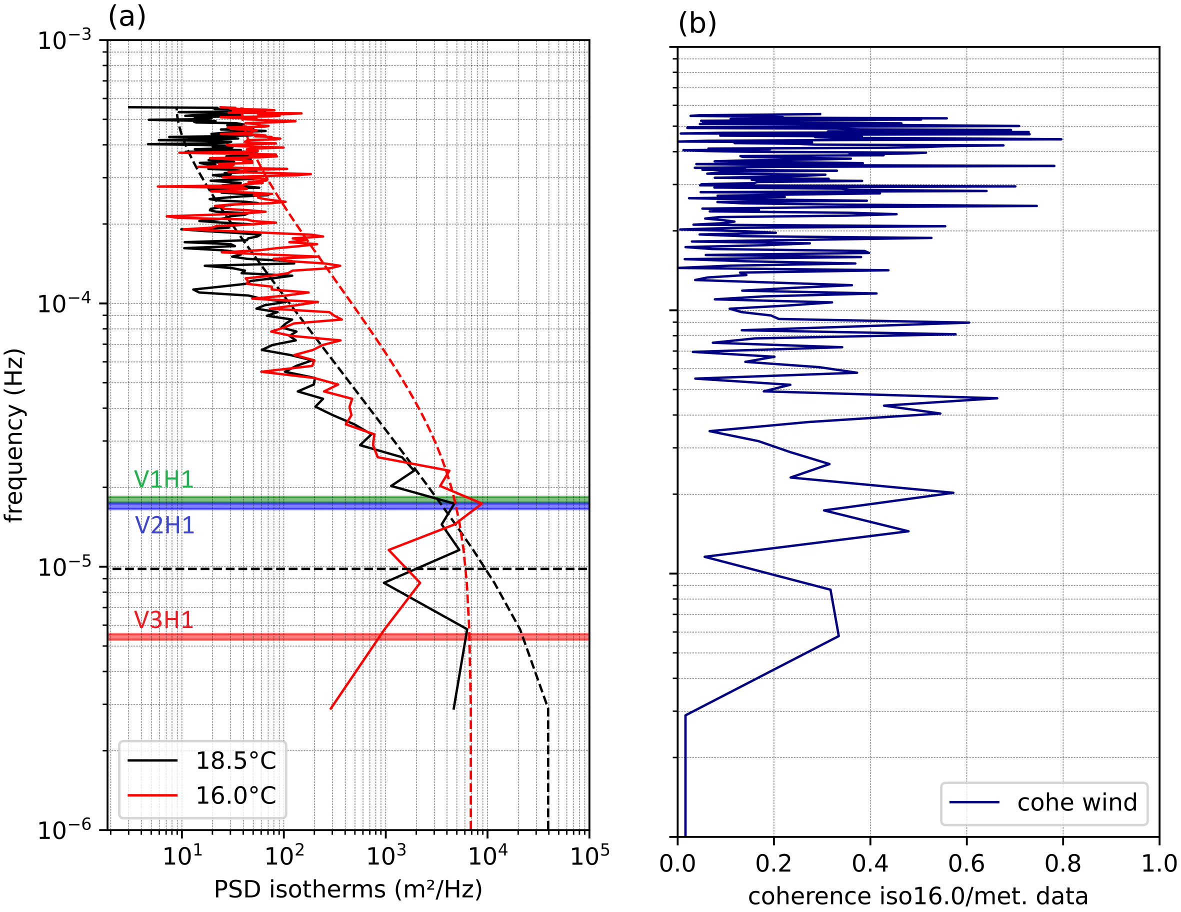

Figure 19 – Spectral analyses of Vossoroca reservoir during September 2012: a) Power spectral density of the isotherms of 18.5 °C and 16 °C (Vossoroca reservoir; 15/09 – 25/09). The dashed lines show the mean red noise spectrum for the time series, where spectral peaks above this line are significantly different from noise at a 95% confidence level. Horizontal color boxes indicate the theoretical period for different vertical modes. b) Coherence between 16 °C isotherm and wind speed.

placement associated to each frequency band. The internal seiche amplitude was estimated through the total vertical displacement in the internal seiche frequency. The internal wave amplitude is directly associated to the daily Ri number of the analyzed period (Figure 21a). The overall result, more clear for V1H1 internal seiche mode observed in Vossoroca reservoir, shows an inversely proportional relationship between internal wave amplitude and Ri number. This suggests, as observed by previous studies (IMBERGER, 1998; SHINTANI et al., 2010) that internal seiche amplitude grows exponentially with the decrease of stability. This is true unless the Ri reaches a critical value, $Ri_{\text{crit}} \sim L/2\ h_e$. In this case, interface shear accompanied by large interface displacements that may cause a complete vertical mixing during a strong wind episode (SPIGEL; IMBERGER, 1980). This type of regime has been observed during the transition between mixed and weakly stratified periods in Vossoroca reservoir, in the beginning of May.

Although we have detected a similar trend in all analyzed periods, data from Harp Lake presented a slight deviation compared to Vossoroca reservoir. Given the lake characteristics, we suggest that the disturbance, mainly observed in Harp Lake, was due to the improper estimation of the mean wind energy available

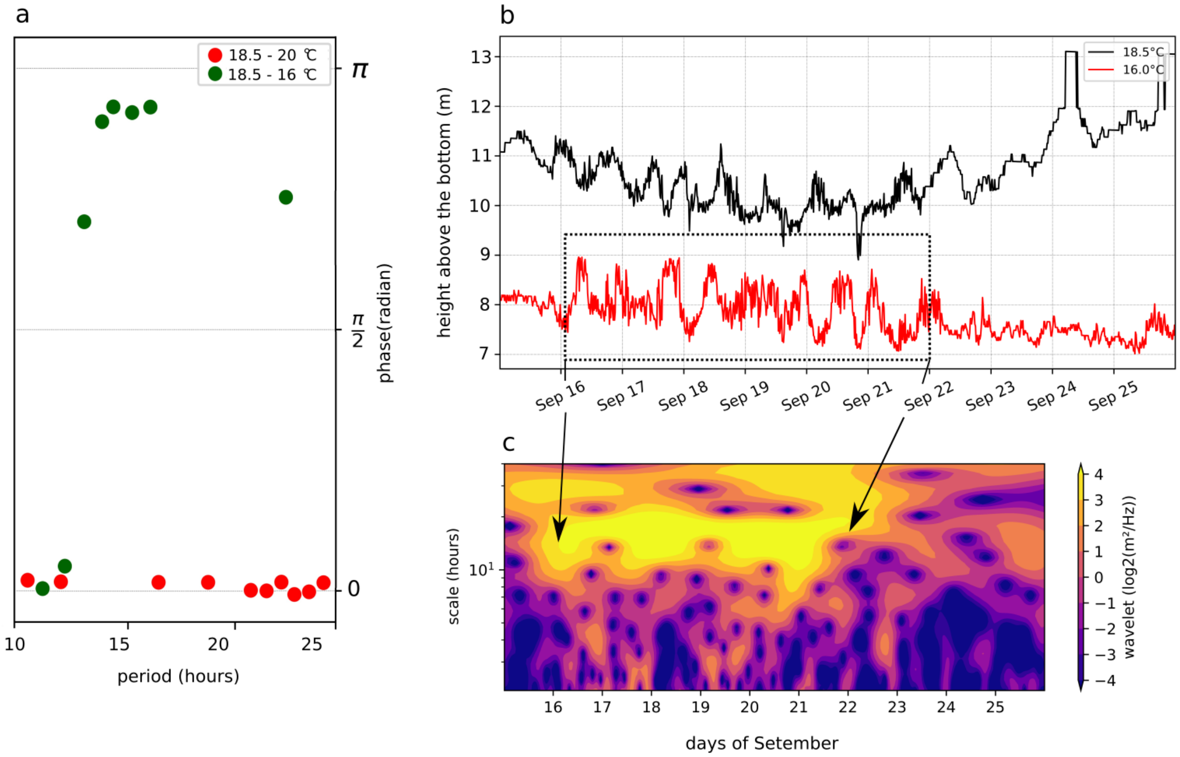

Figure 20 – Isotherm, phase, and wavelet analyses of Vossoroca reservoir during September 2012. a) Phase analyses of two pairs of isotherms (phase was just plotted for coherence above the 95% confidence level). b) 16 °C and 18.5 °C isotherm time series. c) Wavelet analyses of the 16 °C isotherm (Vossoroca reservoir; 15/09 – 25/09)

to excite basin-scale internal waves. As non-homogeneous wind events are predominant in Harp Lake, the mean wind velocity of the period is not a good representation of the wind that contributes to the formation of basin-scale internal waves. Recent studies have pointed out that filtering the friction velocity of the wind, u_*, can improve significantly the accuracy of some numerical models to predict internal seiches in deep lakes (GAUDARD et al., 2017). However, the filtering process is just used to compute the wind energy available to excite internal seiches, and does not represent a reduction of the wind strength.

We filtered the u_* based on the duration of the wind event that could excite basin-scale internal waves (SCHWEFEL et al., 2016). Herefore, we firstly applied a duration filter, which consists of discarding wind events with duration lower than 1/4 of the internal wave period, an essential condition for internal seiche activity (HEAPS; RAMSBOTTOM, 1966). In addition, since heterogeneous direction of wind events may also be incapable to generate internal seiches, we also applied a filter based on wind direction. The Ri was estimated considering the fraction of the time that wind direction was in the same quarter of a circle, considering just events longer than 25% of the wave period. Both processes improved considerably the correlation between Ri and the internal wave displacement (Figure 21b and c). Differences between Harp Lake and Vossoroca reservoir are due to basin length of each basin.

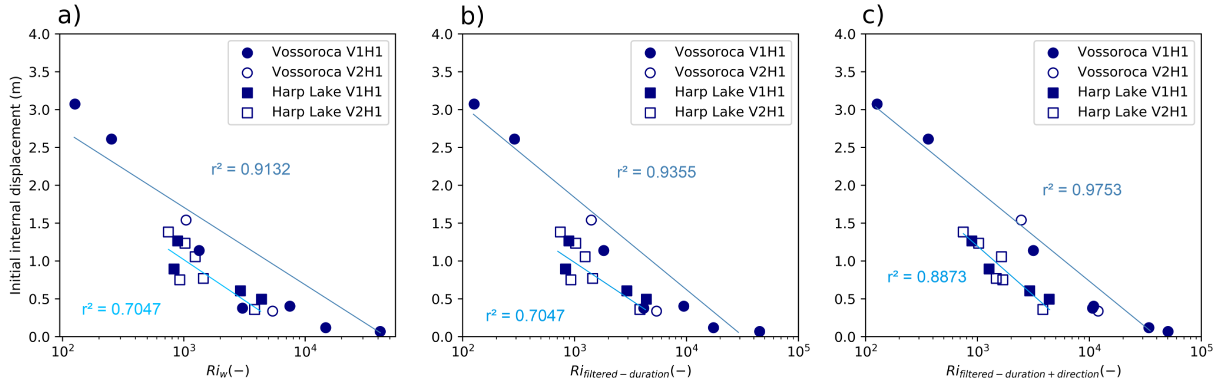

Figure 21 – Internal seiche amplitude of the most energetic isotherm versus a) the daily Ri, b) filtered Ri_{duration} using only periods with winds capable to generate internal waves, and c) filtered $Ri_{\text{direction}}$ using only periods with winds in directions capable to generate internal waves. Linear regression was obtained for each basin

3.3.3 Numerical simulations and spatial variations

Given the innumerable variables that may affect the evolution of basin-scale internal waves in real lakes, the complete description of the generation and evolution of these waves may be difficult considering data from just a pair of thermistor chains deployed in different locations of two different lakes. To overcome the difficulty to describe the evolution of BSIWs in stratified lakes, we firstly provide a detailed description of the dynamics of BSIW simulated through a numerical model. The baroclinic response due to the wind event is easily detected in the numerical results (See Appendix B). To describe the BSIW evolution of all simulations, the results from the numerical model were also processed using spectral analyses and the additional treatment applied to the data from field observations.

Often in thermal-stratified lakes, the Ri is written considering an aspect ratio that takes into account the length of the stratified basin L (SHINTANI et al., 2010). This parametrization preserves the main aspects of the Ri number, including an additional influence of the wind fetch. The non-dimensional parameter is written as $Ri\ h_e/L$, in which h_e is the epilimnion thickness.

The results of the numerical simulations are shown in Figure 22, where the internal wave amplitude (a) or the non-dimensional internal wave amplitude (b) have been plotted against the non-dimensional time (using the internal wave period T_{V1H1} for normalization). The results show good agreement to theoretical results obtained by Spigel and Imberger (1980) and (SHINTANI et al., 2010), which predicted that the vertical displacement due to BSIWs increases as the non-dimensional parameter $Ri\ h_e/L$ becomes lower (Figure 22a). Although this trend is observed in most numerical simulations, we observed a distinct behavior for cases with $h_e/H = 0.13$ (see arrow in Figure 22a).

We suggest that when the pycnocline is too shallow (small h_e/H), the BSIW evolution may be different due to the increase of pressure in the upper layer, which may result in an additional acceleration of the tilted interface when it is returning to the equilibrium position. The faster downward movement is characterized by a temporal displacement of the internal seiche trough, which can be observed in Figure 22a. This phenomenon is similar to wave shoaling, increasing non-linearity aspects, resulting a higher dissipation of energy. The interaction between wave crest and water surface increases energy dissipation of the BSIW resulting in a short-period activity.

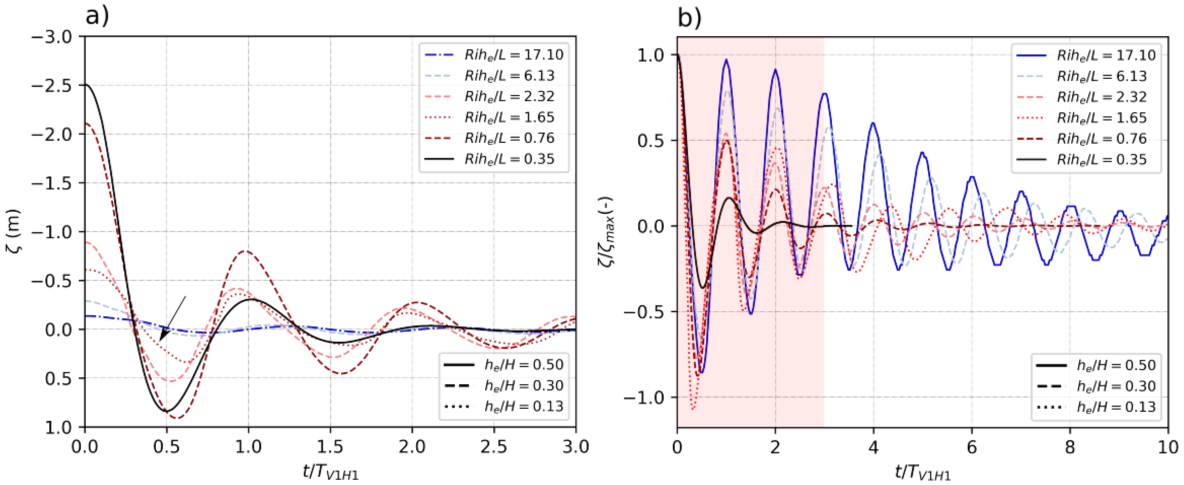

Figure 22 – Numerical simulations results: Evolution of the generated basin-scale internal waves. a) internal wave amplitude, and b) non-dimensional internal wave amplitude, plotted against the non-dimensional time (using the internal wave period T_{V1H1} for normalization) for different stratification conditions and pycnocline depths. The arrow indicates the anomaly of the run with $h_e/H = 0.13$. The red region in b) indicates the same interval analyzed in a)

Internal seiches dissipate energy in the interior of stratified basins by viscous forces or due to a down-scaling energy cascades that transfer energy to high-frequency internal wave fields of various modal structures (ANTENUCCI; IMBERGER, 2001a). The dissipation process reduces the energy of internal seiche, that may be damped after some periods of oscillation. This is evidenced in all numerical simulations, in which some are shown in Figure 22b.

Although the damping of basin-scale internal waves present a substantial contribution of boundary layer dissipation (SIMPSON; WILES; LINCOLN, 2011a), we show a strong influence of the system stability through those numerical results. The rate of energy decay is also a function of the bulk Richardson number. Although the internal seiche amplitude is higher for periods of weaker stability conditions, we observe that the seiche motion decays faster the more energy it contains, which is exemplified in Figure 23a. This conclusion agrees well with observations in Lake Alpnach (GLOOR; WÜEST; IMBODEN, 2000; GOUDSMIT et al., 2002). We observed that for $Ri\ h_e/L = 0.35$, internal seiche of $\approx$ 3 m of amplitude was rapidly dampened, in which more than 80% of its energy was dissipated after the first wave period. On the other hand, considering a more stable system ($Ri\ h_e/L = 2.32$), an 1 m internal seiche was completely dissipated after only 10 wave periods. One reason to the fast energy dissipation can be related to higher turbulent production generated on large amplitude waves and their interaction with boundaries.

The relationship between $Ri\ h_e/L$ and the internal seiche decay is characterized by an exponential function that fits well to our numerical observation with $h_e/H \geq 0.3$. For $h_e/H = 0.13$ (dotted lines in Figure 23a), a disturbance during the internal seiche dissipation may be attributed to the asymmetrical temporal evolution of the excited internal seiche. Although, according to our observations, we may suggest that this interference reduced the energy dissipation, we actually observed a smaller decay rate due to the increase of wave amplitudes due to non-linearity. Eventually, after some periods, this interaction results in a faster energy decay by an increase of local mixing.

Even though the difficulty to analyze the influence of secondary wind events on internal wave evo-

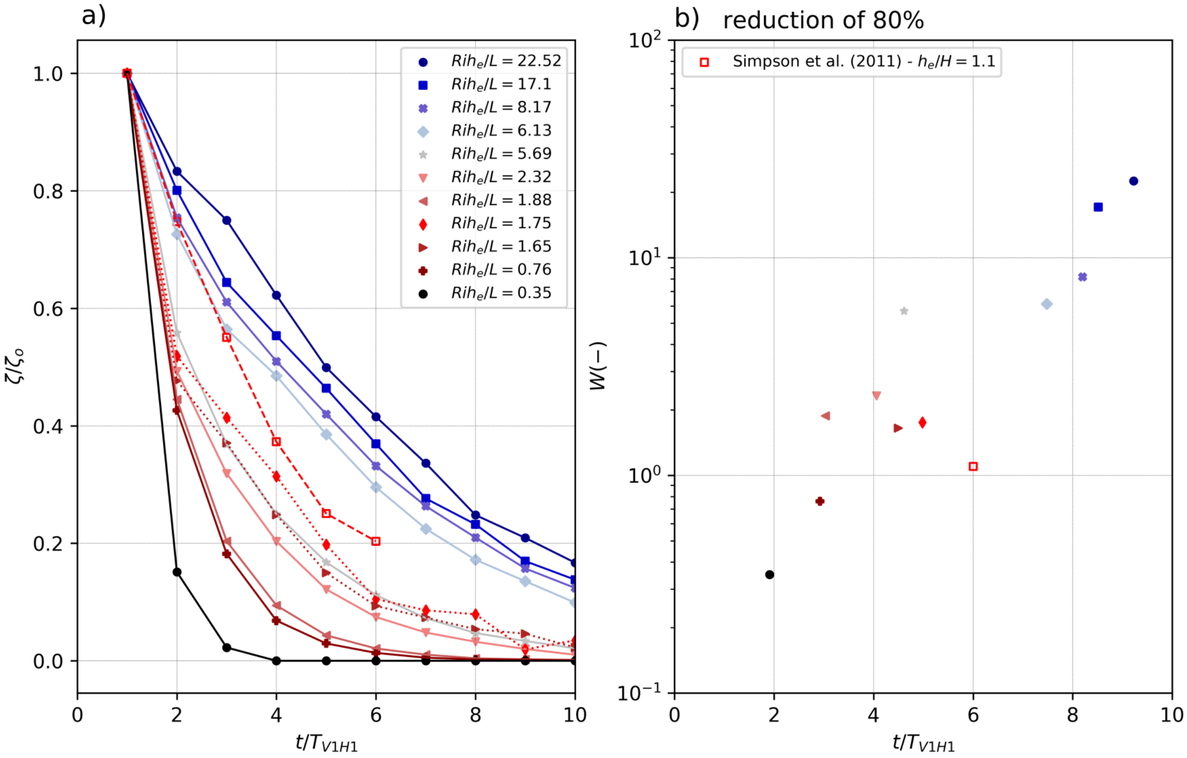

Figure 23 – Numerical simulations results: Initial displacement of the generated basin-scale internal waves. a) Decay of the non-dimensional internal seiche amplitude (using the initial displacement for normalization) as a function of the non-dimensional time (using the internal wave period T_{V1H1} for normalization). b) $Ri\ h_e/L$ as a function of non-dimensional time in which 80% of internal wave energy is dissipated.

lution makes the analysis harder, some field observations have suggested a slower energy decay compared to our numerical results (Figure 23b). We suggest that since real lakes are susceptible to continuous wind events, secondary storms may contribute to energize the internal waves fields, reducing the rate of energy decay. This phenomenon may be correlated to the amplification of internal seiches due to resonance events, typically observed in lakes (MÜNNICH; WÜEST; IMBODEN, 1992; BOEGMAN; IVEY, 2012).

Although field observations are rarely capable to describe in detail the dynamics and evolution of BSIWs in real lakes, the initial responses due to a wind event have been extensively detected in many stratified lakes and reservoirs (MORTIMER, 1952; ANTENUCCI; IMBERGER, 2001a; VALERIO et al., 2012). Even though these field and numerical observations are well represented by theoretical results (STEVENS; LAWRENCE, 1997), those present higher variation for different thermocline depth conditions (Figure 24a). For shallow systems, when the internal seiche displacement is susceptible to reach the lake surface, the variation is completely different from up- and down-wind regions. In the up-wind region, the internal wave growth is limited by the water surface, whilst in down-wind part, the thermocline can erode downward the lake bottom as a strong jet due to an additional pressure at upper layer. As observed, the water surface interaction creates a faster dissipation of energy due to turbulence production, and the displacement oscillates during a shorter period of time. However, the strong jet can potentially intensify the vertical transport of substances, and may also have a strong effect on water quality.

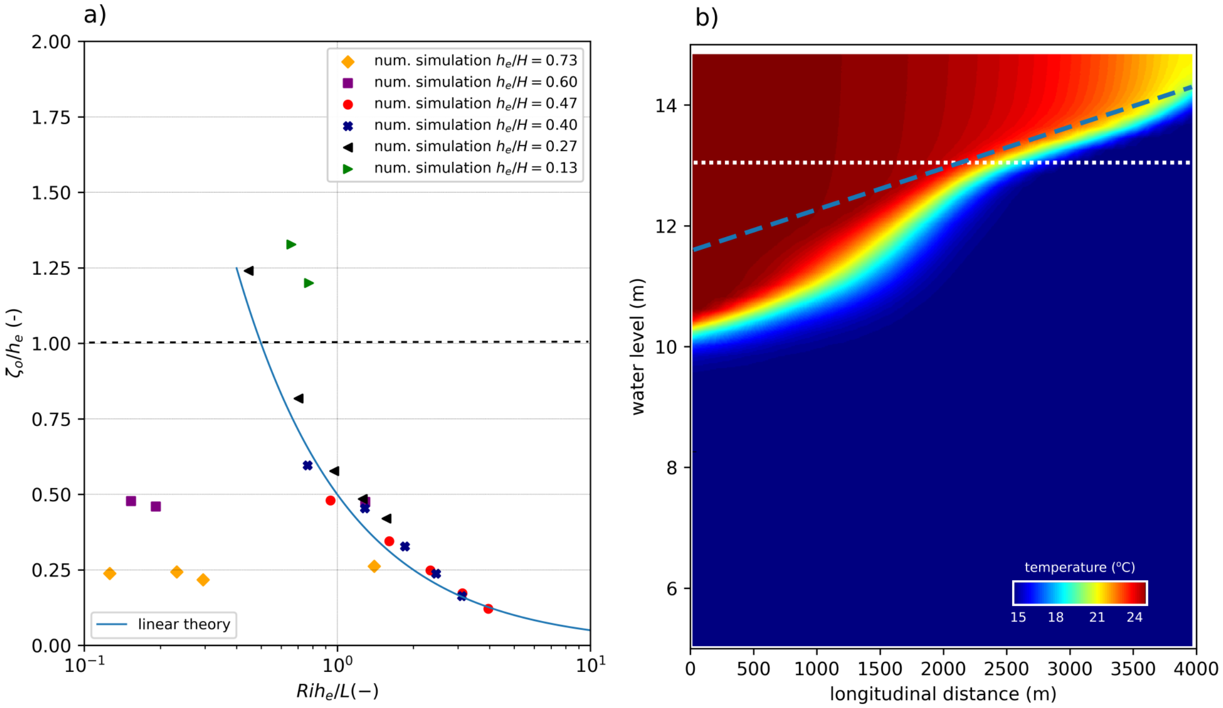

Figure 24 – a) Maximum basin-scale internal wave displacement normalized by the thermocline depth h_e at downwind regions, where the initial displacement is characterized by a downward movement. The horizontal dashed black curve indicates the limit boundaries to direct interaction between water surface and internal seiche at upwind region. b) The longitudinal temperature profile during the wind event (3 h of simulation time) showing the strong erosion of thermocline at downwind region (Simulation: Run 23). The white dashed line indicates the unperturbed thermocline depth and the blue dashed line the theoretical displacement according to linear theory.

As observed in Figure 24, when $Ri\ h_e/L \leq 3$, depending on the h_e/H condition, the internal seiche amplitude does not grow as described by previous theoretical results (SPIGEL; IMBERGER, 1980; STEVENS; LAWRENCE, 1997; SHINTANI et al., 2010). The internal seiche amplitude is higher than predicted by linear theory when the thermocline is near the water surface ($h_e/H \approx 0.2$). The thermocline feels an extra pressure at downwind region due to the interaction of physical barrier imposed by the lake surface and the internal seiche. This increase of pressure pushes the thermocline deeper (Figure 24b). Rapidly after the first wave motion, the BSIW seems to be degenerated into a bore that propagates back and forth (For more detail, see Appendix B). The observation agrees well with the degeneration regime described by Horn, Imberger and Ivey (1998), that falls into the supercritical flow regime.

In the other hand, when the thermocline is located in deeper regions ($h_e/H > 0.6$), the bottom condition may also play an important role on increasing mixing at the wave trough. The linear theory does not include an higher order influence that can be observed in simulated cases due to the extra pressure at the epilimnion layer. Although when the $Ri\ h_e/L$ gets lower nonlinear interactions tend to increase the internal seiche amplitude (SHINTANI et al., 2010) and the extra pressure may also have a relevant contribution depending on the h_e/H condition, mixing activity due to the low thermal stability can have a significant role on the internal seiche growth, reducing their amplitude and accelerating their energy dissipation due to turbulence production.

As observed in Figure 24a and differently from mathematical theories derived by Spigel and Imberger (1980) and Shintani et al. (2010), numerical results show an influence of the total water depth and a higher order contribution of the upper layer thickness. The shallower the interface of the BSIWs, the higher the energy transferred to the internal wave field. However, when $Ri\ h_e/L$ gets really small, the weaker system stability may play an addition role on the internal seiche amplitude. The deeper the tilted interface, the lower will be the energy that will reach the internal wave field. We suggest that part of the energy is lost by mixing and less energy is available to excite basin-scale internal waves. In other words, less energy is transferred to deeper regions.

3.3.4 Parametrization

The parametrization proposed here takes the reservoir depth into consideration and an higher order contribution of Ri, water length and thermocline depth. The parametrization is based on simulation results from $h_e/H = 0.1$ to 0.8 ($h_e = 2$ to 12 m). The parametrized equation that best fits to the numerical observations is given by

$$\frac{\zeta_o}{h_e} = k_1\ \exp\left(\frac{-(Ri\ h_e - k_2\ L)^2}{2\ (L\ f)^2}\right), \tag{3.8}$$

in which Ri is the bulk Richardson number, ζ_o is the initial internal seiche amplitude, h_e is the epilimnion thickness, L is the reservoir length, $k_1 = 0.1$ is the constant that defines the lowest internal wave energy that can be predicted by the parametrization, $k_2 = 6$ is an universal constant obtained empirically, and f is a non-dimensional function of h_e/H, which describes a higher order influence of h_e/H on internal seiche amplitude:

$$f(h_e/H) = g(h_e/H)\ \exp\left(\frac{(h_e/H)^2}{k_3}\right), \tag{3.9}$$

where $k_3 = 0.125$ is an universal constant (obtained empirically) and g is a sub-function of h_e/H. The $g(h_e/H)$ was estimated empirically considering all simulated cases. We applied two best approximations: a linear ($g(h_e/H) = -3.021\ h_e/H + 2.6674$) and a third-order polynomial function ($12.156\ h_e/H^3 - 15.714\ h_e/H^2 + 2.8426\ h_e/H + 2.0846$) (Figure 25).

The k_1 constant limits the minimal energy of the BSIW, which impose that equation 3.8 should be applied just when the wave amplitude is at lest 10% of epilimnion thickness. For small internal wave energy ($\zeta_o/h_e \leq 0.1$), the system should be stable enough and far from the boundaries, that higher order influences of h_e/H and turbulent production at wave crest and trough do not have any additional influence on wave energy. Thus, for $Ri\ h_e/L > 5$, the linear theory is a satisfactory approximation to predict internal wave amplitude.

The universal constants k_1 and k_2, which were determined empirically trough numerical iterations, are independent of h_e/H conditions and apparently valid for all simulated cases.

The parametrization (Equation 3.8) shows a better prediction of internal seiche amplitude compared to linear theory (Figure 26a), suggesting that for most lakes and reservoir that are under $h_e/H = 0.1$ to 0.8 conditions the equation should work well to describe the internal seiche amplitudes. For all tested h_e/H conditions the parametrization showed a better prediction of internal seiche amplitude, mainly for cases when the internal seiche interacts with the lake boundaries (Figure 26b). The observed data suggest a mean error reduction of more than 50% related to the linear theory. In critical h_e/H conditions, the parametrization reduced the error in 90% compared to the linear theory.

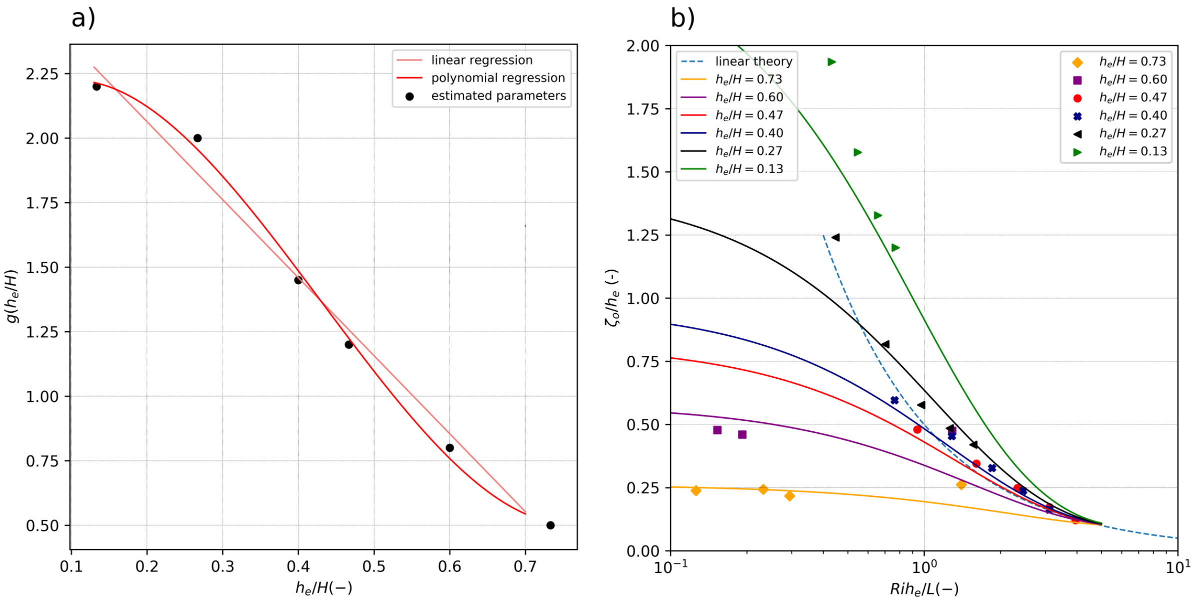

Figure 25 – a) Variation of g as a function of h_e/H for all simulated cases. Black dots represent the empirical parameter defined considering all simulated h_e/H condition. Red curves indicate different functions to describe the variability of $g(h_e/H)$ (linear and a third order polynomial regressions). b) Maximum vertical displacement associated with internal seiche. Solid curve is derived from parametrized equation (Eq. 3.8) for different h_e/H conditions applying the third-order polynomial equation to describe the g function, expressed with distinct colors. The result using the linear equation for g is presented in Appendix B. Marks indicate the simulated results from different h_e/H conditions.

The energy from a wind event that passes the surface boundary layer is susceptible to favor the excitation of basin-scale internal waves in the stable interior layer interior. We suggest that when the thermocline is shallow under low $Ri\ h_e/L$, the wave crest is susceptible to reach the water surface. The change in pressure caused by this phenomenon pushes the wave to deeper regions, which leads to a higher vertical transport at downwind regions. However, when $Ri\ h_e/L$ is lower, the turbulence production at higher vertical displacement and the interaction with lake boundaries start to play a crucial role on the initial internal wave growth, which may result in lower vertical displacement due to turbulence production. This decrease of amplitude may collapse when $Ri\ h_e/L$ is too low so that the vertical displacement may result in turbulent mixing that is not supported by the stratification condition, leading to a complete mixing of the lake. We observed in some simulated cases a rapid stratification break due to high turbulence production. These cases are summarized in Appendix B.

The parametrization equation (Eq. 3.8) describes the distribution of internal wave energy for different values of Ri he/L as a Gaussian function (Figure 25b). However, the higher order contribution of epilimnion layer and the interaction between internal seiche and lake boundaries play a crucial role on describing the maximum internal seiche displacement. The variability observed as a function of h_e/H controls the standard deviation of the Gaussian function, which is parametrized by Eq. 3.9.

Comparing the parametrization with field observations conducted in Vossoroca reservoir and Harp Lake we observe that the linear theory underestimated in the majority of cases the internal wave amplitude for larger Richardson number ($Ri\ h_e/L > 3$) (Figure 27a). The higher vertical displacement may be due to the resonance effect caused by the wind forcing frequency (BERNHARDT; KIRILLIN, 2013). When the forcing

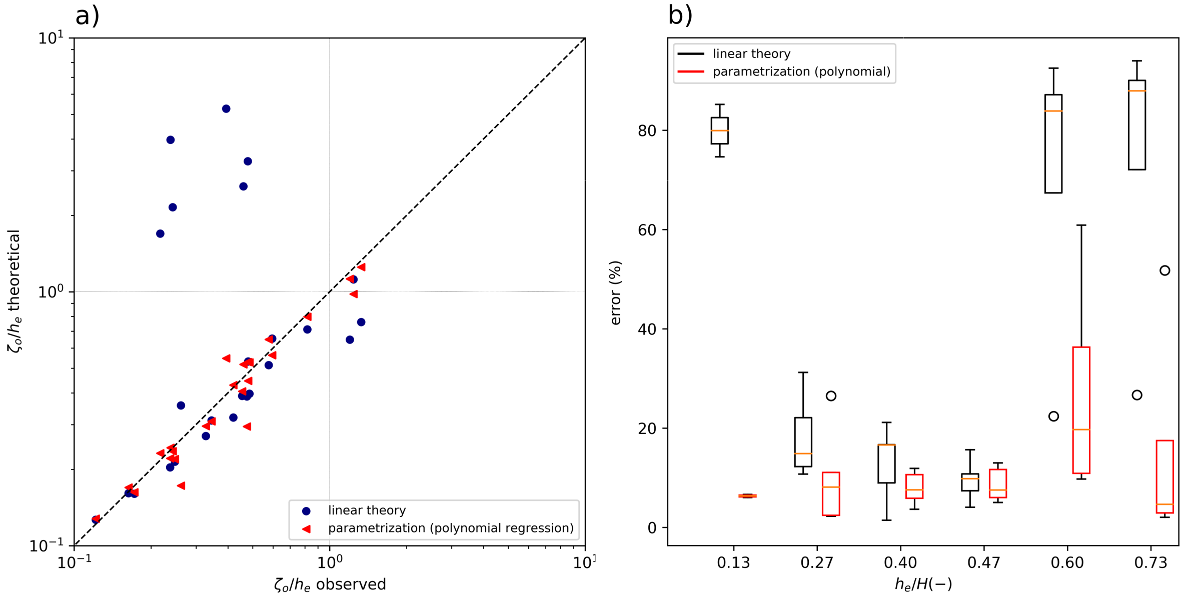

Figure 26 – a) Comparison between theoretical (linear and parametrized equation) and internal seiche amplitude detected in simulations. b) Error percentage with respect to h_e/H.

frequency matches one of the natural frequencies of the basin scale internal wave modes, resonant amplification may occur (BOEGMAN, 2009). For both basins and modes, the initial amplitude was approximately 30% larger than that predicted by the linear theory, except for $Ri\ h_e/L < 5$ that presented different behavior depending on the h_e/H condition, which we suggest to occur due to the mixing and boundary effects discussed previously.

Although field observations suggest that wind resonance apparently affects the internal wave amplitude independently of the $Ri\ h_e/L$ (increasing the wave amplitude by $\approx$ 20%), we observe that for a very stable system ($Ri\ h_e/L > 10$) probably the effect is much less. In this condition, observations suggest that the ξ in equation 3.8 must be a function of other variables based on wind resonance. Physically, this condition may indicate that when the system becomes more stable, wind resonance does not affect strongly the internal seiche amplitude, however a new parametrization is required in order to better predict the growth rate for different $Ri\ h_e/L$.

Another observation is that the proposed parametrization also incorporates the linear theory at $Ri\ h_e/L = 5$, for higher $Ri\ h_e/L$ the linear theory is more adequate to represent the internal seiche amplitude. For $Ri\ h_e/L < 5$ we observe a reduction of the internal seiche amplitude when $Ri\ h_e/L$ gets lower, Figure 27. For different h_e/H condition we may observe an increase of the internal seiche amplitude at downwind region for shallow thermocline, which fits better to the proposed parametrization that takes into account the total water depth of the system and interaction of internal seiche and lake boundaries.

Although we do not observe a clear evidence that resonance occurs exactly when internal seiche periodicity matches a frequency of the wind component, as shown in Figure 28a, we detected good correlation between the total spectral energy of a specific wind frequency bandwidth (0.5 to 1.5 of the internal wave period) with the growth of amplitude due to resonance effects (Figure 28b). This conclusion agrees well with laboratory results conducted by Boegman and Ivey (2012) that showed that wind frequencies between 0.8 and 1.2 of the fundamental basin-scale internal wave period may amplify the internal wave amplitude due to

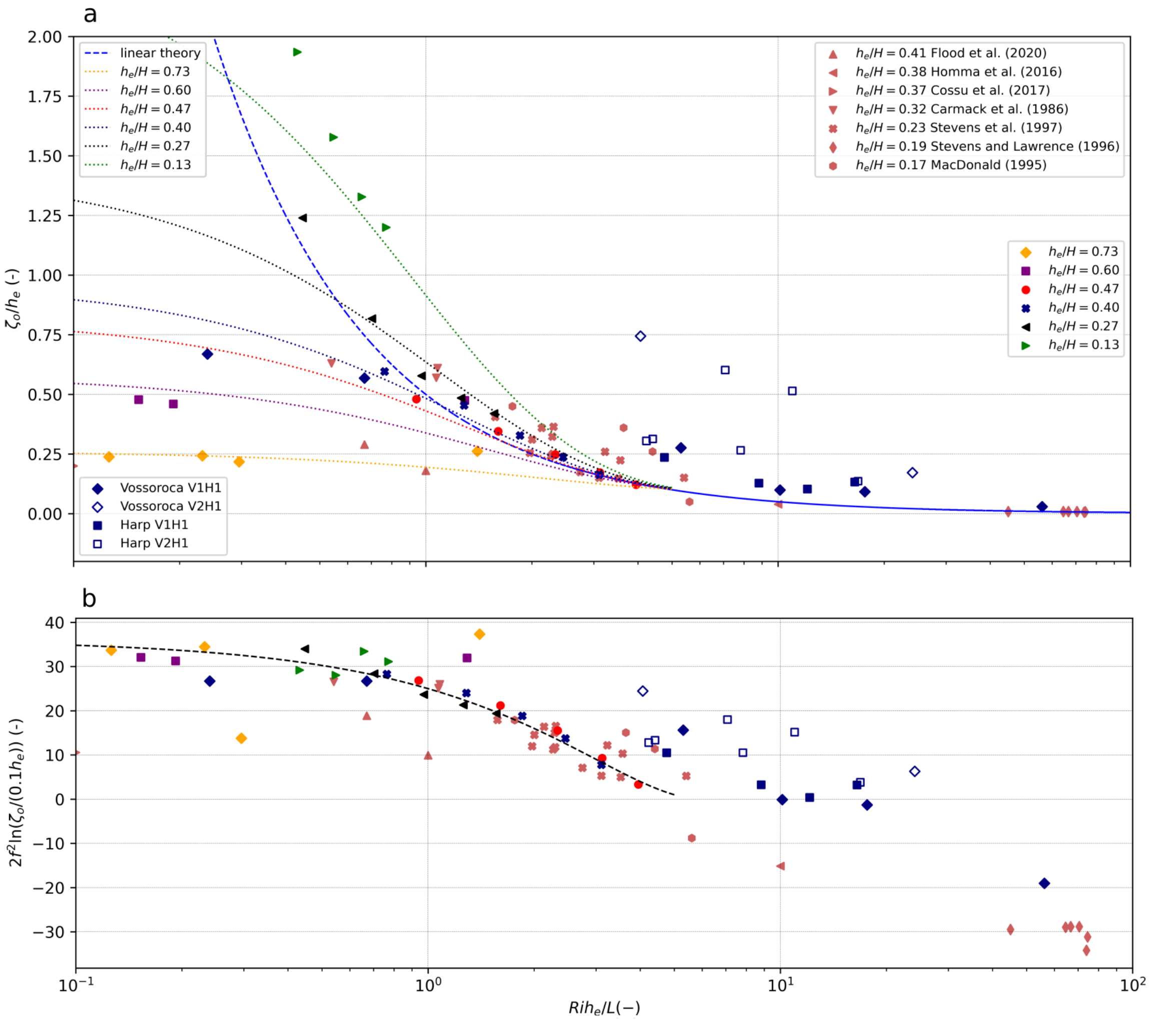

Figure 27 – a) Maximum vertical displacement associated with internal seiche normalized by the epilimnion thickness against $Ri\ h_e/L$. Data points include values from simulations, Harp lake, Vossoroca reservoir, and many other lakes from the literature (FLOOD et al., 2020; HOMMA et al., 2016; COSSU et al., 2017; CARMACK et al., 1986; STEVENS; LAWRENCE, 1997; STEVENS et al., 1996; MACDONALD, 1995) b) Normalization of ζ_o/h_e to incorporate the function $f(h_e/H)$ $(2\ f^2)$ against $Ri\ h_e/L$. The black dashed line represents Eq. 3.8 normalized by $2\ f^2$. "Log" is defined in base e, natural logarithm.

resonance effects.

In addition, our analysis shows that the wind fluctuations with higher spectral energy can also be responsible for generating higher amplitude internal waves and also favor the occurrence of higher vertical modes. This characteristics are also evidenced in Figure 27, in which higher vertical modes detected in Vossoroca reservoir and Harp Lake deviate more from the theoretical results.

As also observed in Figure 28b, the correlations fit well just for a determined basin and internal wave mode. Considering different modes and basins, the correlation patterns are altered. This suggests that the amplification of the internal wave can be directly correlated to resonance effects for data obtained in a same basin for a single mode, but for different modes and basins this correlation differs, probably influenced by basin length and internal wave periodicity. This conclusion indicates that resonance effects may introduce additional

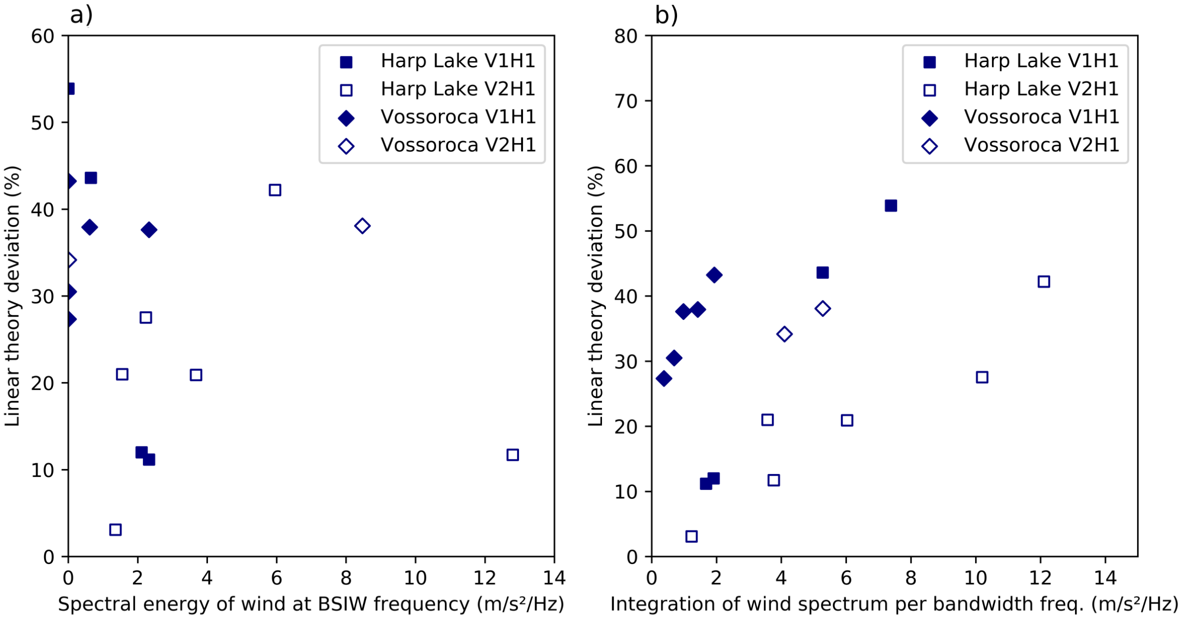

Figure 28 – Amplitude growth due to resonance effect against a) the peak of the power spectral density of the wind intensity at the internal seiche period and b) the integration of the wind spectrum for wind frequencies between 0.5 to 1.5 of the internal wave period per bandwidth frequency.

variables into equation 3.8, which suggests that it should be a function of wave mode and wavelength, characterized by the basin length L. Since L is already incorporated into parametrization $Ri\ h_e/L$, we may assume that L introduces an additional influence on the internal seiche amplitude depending on the resonance efficiency.

In general, this parametrization presents satisfactory results and could be applicable to small to medium lakes under different boundary and meteorological conditions. Some limitations and precautions related to the parametrization are highlighted below:

The parametrization just takes into account linear internal seiches that are not influenced by Coriolis effect, and could not be applied on large lakes where Poicarè and Kelvin internal waves are susceptible to be excited.

The parametrization equation does not take into account the bathymetry irregularity, since the simulation was performed in smooth bed conditions. Although the Vossoroca is a dendritic reservoir, its bathymetry is not much irregular, similar to Harp Lake bathymetry. The comparison between results from simulation and different lakes presented good results. However, the parametrization should be applied with precautions on stratified basin with irregularly bathymetry conditions.

Finally, we did not consider the influence of river discharges in the formation of basin-scale internal waves. This interaction is not well understood yet, but apparently could have only minor effect on the internal wave formation since mixing process just takes place close to rivers. Vossoroca is a dendritic reservoir, its bathymetry is not much irregular, similar to Harp Lake bathymetry and the simulation performed here. The parametrization should be applied with precautions on stratified basin with irregularly bathymetry.

3.4 Conclusion

In the light of recent field observations of basin-scale internal waves, previously established theories often fail to estimate the initial amplitude of internal seiches in thermally-stratified basins during determined conditions. As evidenced by a series of observations, theoretical models (SPIGEL; IMBERGER, 1980; SHINTANI et al., 2010) often fail to describe the BSIW amplitude during periods of $Ri\ h_e/L < 2$. Since basin-scale internal waves have been pointed as one of the most important process of vertical mixing and horizontal transport, the wrong estimation of internal seiche amplitude may have several impacts on the water transport.

The result of this study revealed that secondary effects, which are not incorporated by these theories, play a major role under determined meteorological conditions on the dynamics of basin-scale internal waves. We observed that the interaction of internal seiche with lake boundaries (surface water and lake bathymetry) is an important variable that has been neglected by the previous theories. We have demonstrated through numerical modelling and field observation analysis that the shallower the BSIW, the higher the energy transferred to the internal wave field, exciting higher internal waves. However, simultaneously, when $Ri\ h_e/L$ gets lower, a larger part of the energy is lost by mixing and less energy is available to excite basin-scale internal waves, resulting in a internal seiche with smaller amplitude.

In addition, we observed that wind-resonance effects favor the excitation of higher vertical modes in small lakes and reservoirs since diurnal winds have similar period of higher vertical modes. The resonance effect increases the energy of the BSIW significantly, leading to higher amplitude waves. This may indicate an additional dependence of other variables on the proposed parametrization.

For further analysis we suggested the proposed parametrization should be tested to different conditions of low $Ri\ h_e/L$. Observations here indicate a stratification break which is strongly influenced by both parameters, h_e/H and Richardson number. Although it fitted well to describe the reduction of energy for weakly stable systems, we may observe a critical influence of the wind-resonance. Based on the analysis of resonance efficiency, the parametrization may include new variables related to the wind resonance to better predict the BSIW amplitude. The influence of wind-resonance during period of high stability may also be better tested, to describe more appropriately the low efficiency observed here. In addition, future studies could better explore the influence of modes and basin length on the wind-resonance efficiency.

Finally, although the parametrization has presented positive outcomes for the majority of conditions, we may suggest a deeper investigation on influence of other variables such as: Coriolis effect, lake topography irregularities, and interaction with secondary flows.

4 Physical mechanisms of internal seiche attenuation

The work described in this chapter has been submitted to *Journal of Limnology and Oceanography* under the title 'Physical mechanisms of internal seiche attenuation for non-ideal stratification and basin topography'.[1]

Abstract

The dynamics of vertical mixing and the occurrence of basin-scale internal waves (internal seiches) in lakes and reservoirs are often classified and described based on the force balance of wind shear and horizontal pressure gradients resulting from wind-generated currents (the Wedderburn number). The classification schemes consider specific time scales that are derived from a simplified vertical density distribution, a rectangular basin shape, and a constant water depth. Using field measurements and numerical simulations with a validated hydrodynamic model, we analyzed the transfer of energy from wind to the internal seiche field in a small reservoir. Our results demonstrate that the basin shape has a strong influence on the energy dissipation and on the transfer of energy to high-frequency internal waves, thereby attenuating the generation of basin-scale internal seiches. Most of the energy loss of the internal seiche occurs at the sloping boundary, where the internal seiche is susceptible to shoaling and breaking. These findings suggest that the Wedderburn number can be used to predict the occurrence of internal seiche activity in continuously stratified systems. As the Wedderburn number and derived mixing classifications are widely applied also for the interpretation of observed ecological and biogeochemical processes, its application to basins with sloping bathymetry and complex shape should be critically scrutinized, and deviations from predicted dynamics, including the presence of hotspots of turbulent mixing, should be considered.

---

[1] de Carvalho Bueno, R., Bleninger, T. B., Boehrer, B. & Lorke, A. - Physical mechanisms of internal seiche attenuation for non-ideal stratification and basin topography. *Under review* (2022)

4.1 Introduction

Internal seiches are basin-scale internal waves in density stratified lakes and reservoirs, which are generated by wind shear acting on the water surface (FOREL, 1892; WATSON, 1903; MORTIMER, 1952). Surface shear and the associated momentum transfer from wind to water causes near-surface flow towards the leeward shore and tilting of the water surface. Most of the wind energy that is transferred to water is dissipated in the surface boundary layer by turbulent mixing (SIMON, 1997; WÜEST; PIEPKE; SENDEN, 2000) and used for the generation of propagating surface waves (GUSEVA et al., 2021). However, a small fraction of the wind energy passes through the surface boundary layer, causing a flow of hypolimnetic water towards the windward end of the lake, which leads to a tilt of the thermocline (ROGET; SALVADÉ; ZAMBONI, 1997; LORKE; UMLAUF; MOHRHOLZ, 2008; WÜEST; LORKE, 2009), and to the generation of a horizontal pressure gradient along the basin (IMBODEN, 2003; BOUFFARD; BOEGMAN; RAO, 2012). After the wind has ceased, the pressure gradient acts as a restoring force, which drives a reversal of the flows in both layers and often leads to the generation of basin-scale oscillations of the thermocline (internal seiches), that can have large amplitudes and may persist for many days (MORTIMER, 1953). Observations in Lake Constance, for example, have detected internal seiches with a wave height of 25 m (BOEHRER; ILMBERGER; MÜNNICH, 2000). Depending on the vertical structure of density stratification and wind dynamics, different modes of internal seiches can be excited, with opposing currents in several vertical layers with different density (LAZERTE, 1980; MÜNNICH; WÜEST; IMBODEN, 1992; BOEHRER; ILMBERGER; MÜNNICH, 2000; VIDAL et al., 2005).

Internal seiches play an important role in the transfer of energy to smaller-scale motions and vertical mixing in the basin interior (BOEHRER; ILMBERGER; MÜNNICH, 2000; ETEMAD-SHAHIDI; IMBERGER, 2006; LORKE, 2007; PREUSSE; PEETERS; LORKE, 2010), and in the bottom boundary layer (BBL), where bed friction of wave-induced currents can induce turbulence levels 30 times higher than the magnitude found in the interior of the basin (WÜEST; LORKE, 2009). The vertical displacement of water masses associated with internal seiches also affect the vertical position and distribution of phytoplankton and zooplankton and, consequently, also their productivity and ecological interactions (MORTIMER; HORN, 1982; RINKE et al., 2007; HINGSAMER; PEETERS; HOFMANN, 2014), or can lead to upwelling of anoxic water from deeper layers to the surface (FLOOD et al., 2021). Furthermore, seiche-induced bottom currents enhance oxygen penetration into sediment, favoring microbial organic matter degradation (FRINDTE et al., 2013). Mechanistic understanding and prediction of internal seiche activity is therefore of great importance for understanding the energy flux paths, as well as ecological and biogeochemical processes in stratified lentic ecosystems.

The magnitude of the wind-induced initial tilt of the thermocline can be related to the Wedderburn number, a dimensionless number that describes the force balance between wind shear and horizontal pressure gradients (Appendix N). It forms the basis for a widely applied classification scheme of lake mixing dynamics, which indicates the occurrence of internal seiche activities and vertical mixing in thermally stratified lakes (SPIGEL; IMBERGER, 1980). The Wedderburn number and the derived classification scheme have been used to predict persistent upwelling events (OKELY; IMBERGER, 2007; SIMPSON; WILES; LINCOLN, 2011b; STEVENS; LAWRENCE, 1997), and associated periods of dissolved oxygen depletion in the upper layer (FLOOD et al., 2021), related to the vertical and horizontal transport of nutrients (MACINTYRE et al., 1999), and chlorophyll and nitrate (ROBERTS et al., 2021). Studies have indicated that the Wedderburn-based classification is a reasonable predictor of upwelling events and subsequent energy relaxation (ROBERTS et al., 2021; VALBUENA et al., 2022).

The calculation of the Wedderburn number and the derived classification scheme are based on a few idealized conditions, including a rectangular basin shape, constant water depth, and a vertical density structure that consists of two homogeneous layers of constant density, separated by a single density gradient at the thermocline. The bathymetry and morphology of stratified water bodies may play a crucial role in the formation and dissipation of internal seiches due to the variability of the bed slope and asymmetric distribution of water volume (SHINTANI et al., 2010; BRENNER; LAVAL, 2018; IMAM et al., 2020; FLOOD et al., 2021). In addition, more continuous density stratification, in contrast to the two-layer simplification, may favor the formation of higher vertical modes of internal seiches (MÜNNICH; WÜEST; IMBODEN, 1992; BOEHRER, 2000).

Although many physical mechanisms have been studied in detail to understand their influence on the internal seiche field in stratified water bodies, insufficient attention has been paid to how bathymetry, morphology, and stratification may inhibit upwelling and internal seiche generation and thus influence the transfer of wind energy to internal seiches. Former studies have identified the influence of bathymetry on the structure of internal seiches and have indicated increasing turbulence due to shear-induced convection (MÜNNICH, 1996; FRICKER; NEPF, 2000; SHINTANI et al., 2010; COSSU; WELLS, 2013), yet there is a lack of knowledge about how these mechanisms attenuate the formation of internal seiches and affect the applicability of the Wedderburn-based classification in real lakes and reservoirs. In addition, many studies, which evaluated the effect of bathymetry and stratification on internal seiche dynamics, have used two-dimensional models (MÜNNICH, 1996; FRICKER; NEPF, 2000), neglecting the effect of basin morphology in combination with bathymetry.

The aim of this study is to analyze how basin bathymetry, morphology, and density stratification modify the distribution and dynamics of energy in basin-scale internal seiches and determine which parameter may affect more the applicability of the Wedderburn number for the prediction of upwelling events and internal seiche activity in real lakes and reservoirs. This investigation is based on numerical simulations and field measurements from a small reservoir, where internal seiche activity was predicted by lake classification schemes, but not observed in field measurements. To explore the reasons for this discrepancy and to investigate how deviations of basin geometry and vertical stratification from idealized conditions affect the internal wave energy distribution and eventually suppress internal seiche generation, we performed numerical simulations using a three-dimensional hydrodynamic model. First, we examined the model ability to reproduce the time-series of measured water temperature and horizontal flow velocity. In a second step, we analyzed scenarios with variable morphology (shape), bathymetry (depth), and density stratification for a standardized forcing.

4.2 Materials and Methods

4.2.1 Site description

Passaúna reservoir is a small and shallow reservoir located in Curitiba (Brazil, 25° 31′ S, 49° 23′ W), which is used for drinking water production for approximately 650,000 people. The reservoir has a volume of 96 × 106 m^3, a maximum depth of 16 m, and a surface area of 6.5 km^2 (Fig. 29a). The bathymetry is typical for reservoirs, with a gradual increase in water depth from the main river inflow to the dam.

Passaúna reservoir is classified as a warm-polymictic reservoir (ISHIKAWA et al., 2021), with extended periods of thermal stratification during all seasons. Complete vertical mixing is limited to a few days

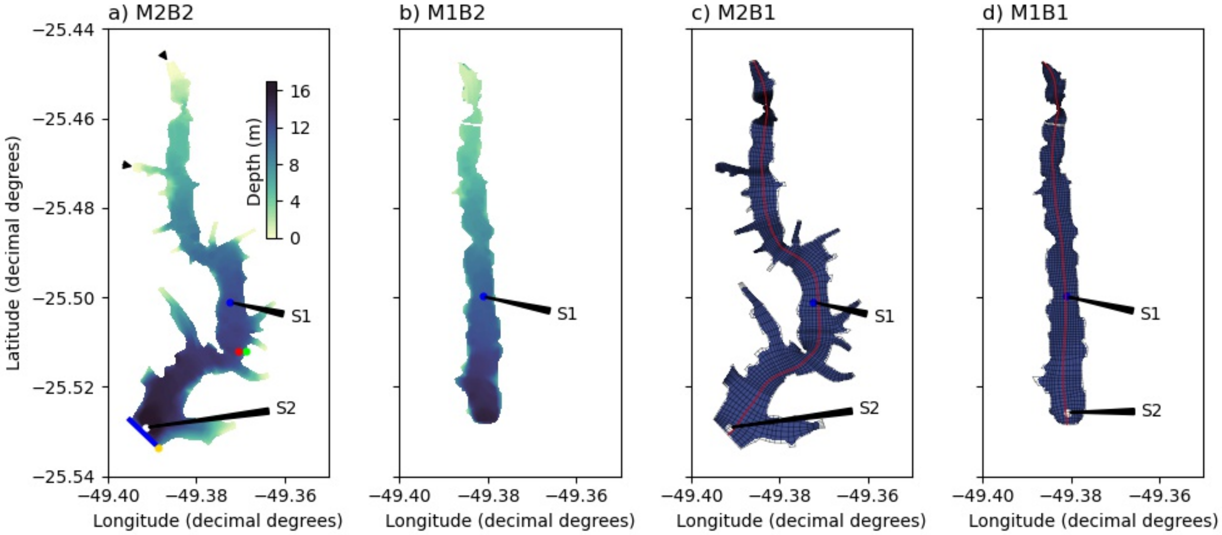

Figure 29 – Bathymetric maps of Passaúna reservoir and of the hypothetical basins considered in numerical simulations (the color map represents water depth). a) Scenario M2B2: Original shape (morphology, M) and bathymetry (B) of Passaúna reservoir. b) Scenario M1B2: Simplified (straightened) reservoir shape with similar bathymetry as the original reservoir. c) Scenario M2B1: original reservoir shape, but with constant water depth. d) Scenario M1B1: Simplified reservoir shape with constant depth. The black lines in c) and d) show the grid used for the numerical simulations. The red line marks the longitudinal grid positions for which the horizontal flow velocity in the north/south direction is illustrated in Fig. 36. The red, yellow, and green dots in panel a) show the location of the monitoring station, the weather station, and the reservoir intake, respectively. Small triangles show the inflows, and the blue line indicates the location of the reservoir dam. The stations S1 and S2 (blue and white symbols) are used in the discussion of the numerical simulations.

during autumn and winter, and weak stratification (≈ 2 °C temperature difference between surface and bottom) may persist for several days even during winter. During summer (December to March), the temperature difference between surface and bottom can reach up to 7 °C, in which the temperature stratification profile is often characterized by a nearly linear temperature decrease from the water surface to the bottom.

4.2.2 Data collection

Passaúna reservoir has been monitored between February 2018 and February 2019 (ISHIKAWA et al., 2021). A vertical thermistor chain equipped with 11 temperature loggers (Minilog-II-T, Vemco, precision 0.01 °C, accuracy ± 0.1 °C) was deployed nearby the intake station in the central part of the reservoir (Fig. 29a). The first thermistor was deployed 1 m above the bed, followed by 10 thermistors, which were vertically spaced 1 m apart with a sampling interval of 1 min. Nearby the thermistor chain, vertical profiles of the three-dimensional flow velocity were measured with an upward-looking acoustic Doppler current profiler (ADCP Signature 1000, Nortek AS) positioned at the reservoir bed. The velocity profiles were measured from 60 cm above the bottom up a depth of 1.5 m below the water surface with a spatial resolution of 0.5 m and a sampling interval of 10 min. Wind direction and wind speed were measured from a weather station positioned near the dam (Fig. 29a) at 10 min intervals.

4.2.3 Numerical model

Internal seiches in thermally stratified lakes have been simulated with three-dimensional numerical models invoking the hydrostatic pressure assumption, such as ELCOM (HODGES et al., 2000; LAVAL et al., 2003) and Delft3D (DISSANAYAKE; HOFMANN; PEETERS, 2019; KRANENBURG et al., 2020) with generally good agreement with observations. We used Delft3D to simulate the hydrodynamics of Passaúna reservoir for different scenarios (see below). The three-dimensional hydrodynamic numerical model is based on the Reynolds averaged Navier-Stokes equations with the Boussinesq approximation and the shallow-water assumption (HYDRAULICS, 2003). The model calculates the unsteady flow velocities and the transport of heat and matter in relation to meteorological forcing by solving the three-dimensional governing equations for conservation of mass, heat, and momentum, using a turbulence closure model. The Coriolis force is taken into account, whilst the compressibility of the water is neglected, as well as the density change, with exception of the buoyancy term.

The numerical models were set up using curvilinear grids with cell sizes varying between 10 m to 100 m in the horizontal domain (mean resolution of 79 m) and 20 fixed vertical layers (vertical resolution of 0.75 m). To ensure numerical stability, all simulations were run with a time step of 6 s. Eddy diffusivity and eddy viscosity were estimated using the $\kappa - \epsilon$ turbulence closure module. All physical and numerical parameters used to run the simulations are summarized in Table 5.

4.2.4 Baseline scenario

As a baseline scenario for model validation, we simulated the hydrodynamics of Passaúna reservoir using the meteorological boundary conditions observed during two periods for which the lake mixing classification (SPIGEL; IMBERGER, 1980) suggested the dominance of internal seiche activity (Appendix N; Eq. N.1 and N.2).

As initial conditions, we used a temperature profile measured by the thermistor chain (Fig. 29a) and assumed horizontal homogeneity. The model was forced by wind velocity and direction measured at the meteorological station. The heat flux at the water surface was estimated as the sum of net longwave and solar radiation, latent and sensible heat, which were calculated from measured time-series of relative humidity, air temperature, fraction of the sky covered by clouds, short wave solar radiation, and Secchi depth. We applied the Ocean model for parameterizing the heat fluxes in Delft3D, which was successfully applied to lakes and reservoirs and presented better results for the energy loss by evaporation compared to Murakami model in former studies (POLLI; BLENINGER, 2019).

The model was run for 10 days, but the analysis started after the fourth day of simulation to account for spin-up of the model since horizontal velocities were set equal to zero in the initial condition. To identify oscillatory patterns due to internal seiche activity, measured and modelled data have been analyzed using power spectral analysis by applying Welch's method (WELCH, 1967). The significance of peaks in power spectral density was evaluated using the mean red noise spectrum at a 95% confidence level (BERNHARDT; KIRILLIN, 2013; BUENO et al., 2020). To reduce random noise and to facilitate the comparison of different confidence limits, spectra were smoothed using a moving average with variable width.

4.2.5 Hypothetical scenarios

To investigate the influence of reservoir shape (morphology), distribution of water depth (bathymetry), and structure of vertical density stratification on internal seiche generation and dynamics, 17 distinct hypothetical scenarios were simulated. For all scenarios, the internal seiche field was excited by a single wind event of 8 h duration with a constant wind speed of 4 m s^{-1} from North. The wind duration can be considered as long enough for internal seiche formation, considering the meteorological and thermal stratification conditions (HEAPS; RAMSBOTTOM, 1966). For the scenarios, a spin-up period was not considered and the system was motionless before the wind event, to ensure that only the wind energy input can contribute to energy content in internal seiches. To control the temperature stratification condition and to quantify the energy distribution in the internal seiche field, we did not incorporate surface heat fluxes into simulations of these hypothetical scenarios. We assumed that the heat flux has a minor impact on the evolution of internal seiches excited by a single wind event. The analysis of the velocity measurements showed that the dominant driver for the reservoir circulation and mixing are wind forcing and baroclinic motions due to stratification (ISHIKAWA et al., 2021). Test runs with the model also showed negligible effect of inflows and outflows on lake circulation during the period of analysis. Given the large water residence time in the reservoir (292 days) compared to the length of the analyzed period, all simulations of hypothetical scenarios were done without consideration of inflows and outflows.

The influence of morphology and bathymetry on internal seiches was analyzed for four different basin configurations (Fig. 29). The first proposed hypothetical scenario (M1B1) is based on the simplest geometry, where the basin was defined as a straight channel that was aligned with the wind direction and a constant depth of 12 m (rectangular reservoir cross-section, Fig. 29d), chose since the mean volume of the hypothetical reservoirs are kept identical with those of Passaúna reservoir.

In a second scenario (M2B1), the basin was defined to have the shape of Passaúna reservoir, but a constant water depth of 12 m (Fig. 29c). The third scenario (M1B2) was defined to have the simplified rectangular-shaped of scenario M1B1, but with an adjusted bathymetry similar to that of Passaúna reservoir (Fig. 29b). The last scenario (M2B2) used the real morphology and bathymetry of Passaúna reservoir, as it was also used for the baseline simulation (Fig. 29a).

To analyze the effect of deviations of vertical stratification from the ideal, two-layer approximation, we used four different temperature profiles in each simulation with different basin shape and bathymetries. The temperature profile was specified according to a modified form of the buoyancy frequency ($N = \sqrt{-g/\rho_o \partial\rho/\partial z}$), where g is the acceleration of gravity, ρ is the water density) profile, which we described by a Gaussian function:

$$N(z) = \frac{0.13}{\sqrt{2\pi\sigma^2}} \ \exp\left(- \frac{(z-h_h)^2}{2\ \sigma^2} \right), \tag{4.1}$$

in which h_h is the elevation of the highest temperature gradient (thermocline) from the deepest point, and σ being the vertical standard deviation, which defines how the stratification profile deviates from the two-layer structure (Fig. 30). We varied σ from 0.2 to 30 m, which characterize a change of the temperature profile from an approximated two-layer structure to a linear stratification profile, respectively. The initial temperature difference between surface and bottom (7 °C) was identical in all scenarios to ensure a Wedderburn number (Appendix N; Eq. N.1) in the order of unity, which, according to theoretical lake classification, indicates strong internal seiche activity (Appendix N; Fig. 60).

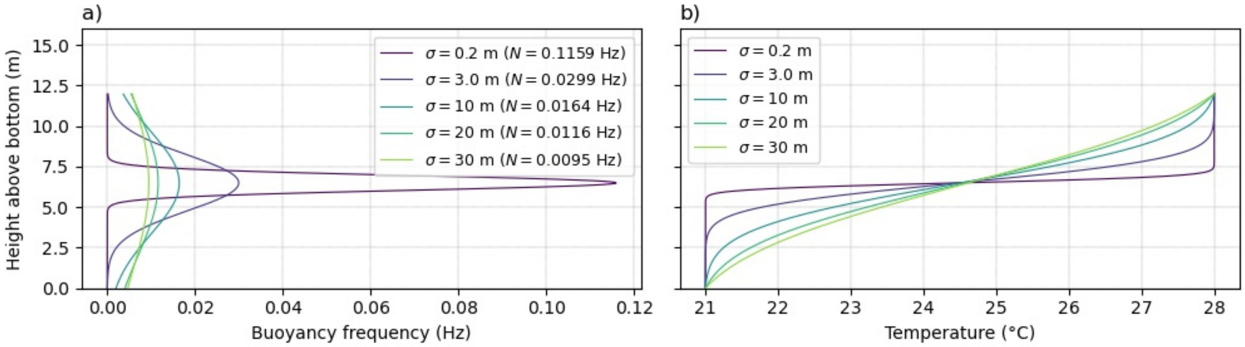

Figure 30 – Vertical profiles of density stratification used in the numerical simulations. a) Buoyancy-frequency (N) and b) temperature profiles for different values of σ (the standard deviation describing the Gaussian form of the buoyancy-frequency profile). N refers is the maximum buoyancy frequency of each stratification profile.

4.2.6 Internal seiche energy

To compare the energy of internal seiches between the scenarios, the mean kinetic energy of the reservoir was computed through the integration of the horizontal velocity field along the basin (GOUDSMIT et al., 2002):

$$E(t) = \int_0^L \int_0^B \int_{z_o}^H \rho(x,y,z)\; u(x,y,z,t)^2 \;\mathrm{d}z\; \mathrm{d}y\; \mathrm{d}x, \tag{4.2}$$

in which z_o is the reference height of the bottom, H is the total water depth, L is the reservoir length, B is the reservoir width, u is horizontal flow velocity in the north/south direction, and ρ is the water density.

The maximum integrated kinetic energy of the basin (E_{max}) was calculated for each half-wave cycle, which has been identified by time between subsequent minima of the wave energy. Adjusting lines to the minimum and maximum of the integrated kinetic energy of the basin was used to separate oscillatory motion from background flows (Appendix O). The fraction of the total kinetic energy that did not exhibit an oscillatory behavior was considered as kinetic energy of background flows, and was removed, retaining only the energy associated with the internal seiche (E_{wave}).

Finally, the maxima in time-series of internal wave energy were used to estimate the damping rate of the wave energy using a first-order decay model (FRICKER; NEPF, 2000):

$$\frac{\mathrm{d}E_{\text{wave}}}{\mathrm{d}t} = -k\; E_{\text{wave}}, \tag{4.3}$$

where k is the damping coefficient and E_{wave} is the wave energy per half wave cycle.

The averaged wave energy was compared to the total rate of work done by the wind stress:

$$E_{\text{wind}} = \tau \int_{\text{wind}}^{T}{}_{0} \int_0^L \int_0^B u_{z=0}(x,y,t)^2 \;\mathrm{d}y\; \mathrm{d}x\; \mathrm{d}t, \tag{4.4}$$

in which $\tau = C_D\; \rho_a\; U_{10}^2$ is the wind stress at the water surface, U_{10} is the wind velocity measured at 10 m above the water surface, L is the basin length, T_{wind} is the duration of the wind event, ρ_a is the air density, $C_D = 1.5 \times 10^{-3}$ is the surface drag coefficient, and $u_{z=0}$ is the horizontal flow velocity at the water surface (uppermost grid cells).

4.3 Results

4.3.1 Reservoir hydrodynamics during field monitoring

During the field monitoring in Passaúna Reservoir, periods of well-mixed conditions were only observed during a few days in the winter season and were interrupted by periods with weak thermal stratification (Fig. 31a). The Wedderburn number (Eq. N.1) indicates that the well-mixed periods were preceded by enhanced interfacial shear, Kelvin-Helmholtz billows, and rapid deepening of the thermocline ($10^{-2} < W < 0.7$, Fig. 31b).

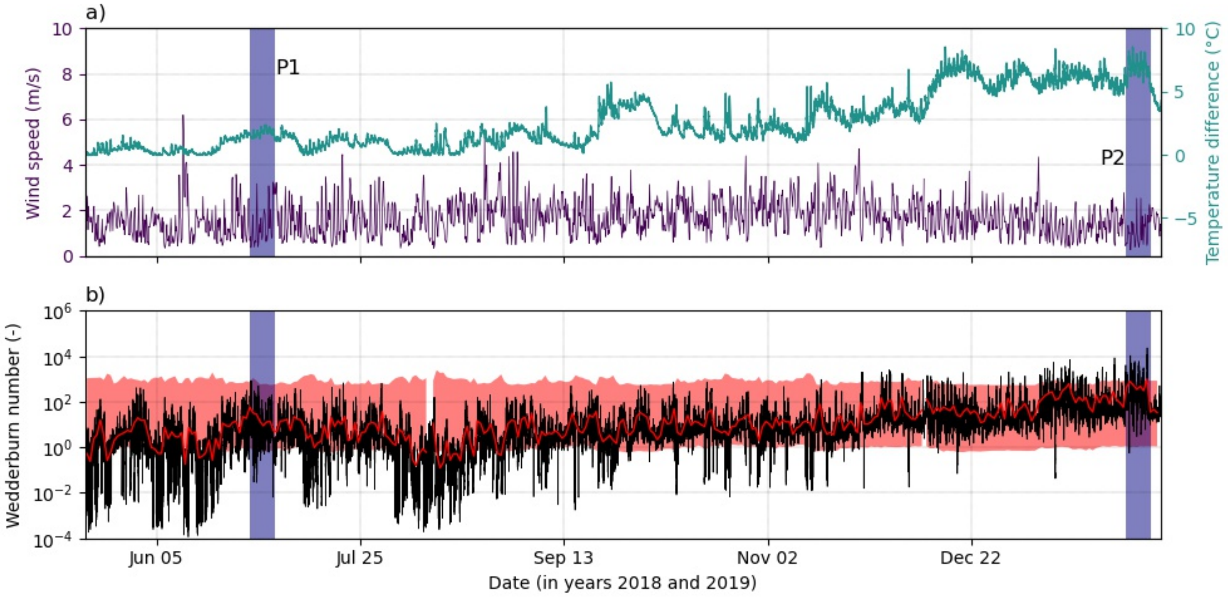

Figure 31 – Conditions at Passaúna reservoir during the monitoring period. a) 3-h average wind speed measured at the meteorological station near the dam (purple solid line) and temperature difference between the water surface and the bottom (green solid line). b) Wedderburn number (W) calculated with 3-h resolution (black solid line) and averaged over one internal seiche period (red solid line). The red background color marks the range of W, for which internal seiche dominance is predicted by a common classification scheme (Fig. 60). The vertical blue bars indicate the two analysis periods (P1, from June 28 to July 04), and P2 (from January 29 to February 04).

Under these conditions, internal seiches are not susceptible to be generated since the entrainment time is shorter than the period of internal seiche formation (SPIGEL; IMBERGER, 1980), i.e. the wind-mixed surface layer deepens to the reservoir bottom during wind excitation (for more details about classification scheme, see Appendix N). However, due to the calm weather condition, with an average wind speed of 1.7 ± 0.9 m s^{-1} (mean ± standard deviation), and a dominant diurnal wind pattern with a maximum wind speed of 8.3 m s^{-1}, theoretical classification of lake mixing suggests the dominance of internal seiches activity during all seasons, including the periods P1 and P2, which were selected for detailed analysis (Fig. 31).

From June 28 to July 04, 2018, a period with weak stratification ($\Delta T = 1.07 \pm 0.54$ °C) was observed (analysis period P1). However, due to weak wind forcing, the mean Wedderburn number during this period was 11.3±35.8, and therewith remained above the threshold for internal seiche dominance ($0.7 < W < 701.3$).

During summer, the thermal stratification became stronger, reaching a temperature difference between the surface and the bottom of the reservoir of 6.61±0.77 °C between January 29 and February 04, 2019 (analysis period P2). This led to an increase of the Wedderburn number during this period ($W = 452 \pm 1245$). Despite the higher Wedderburn number compared to analysis period P1, the mixing classification scheme (SPIGEL; IMBERGER, 1980) indicates that the buoyancy forces did not completely dominate the force balance, favoring the formation of internal seiches ($1.1 < W < 855.0$) (Fig. 31b).

4.3.2 Response to a wind event

In the following, we exemplarily analyze the response of the reservoir to a solitary wind event that occurred during period P1 (June 30 to July 03, 2018). The event started after a prolonged period with calm weather in the morning of June 29, with persistent wind for 8 h from the northeastern direction, reaching a maximum speed of 4.1 m s^{-1} at around noon (Fig. 32a). A detailed model validation is presented in the supplementary information and has also been performed by Ishikawa et al. (2021).

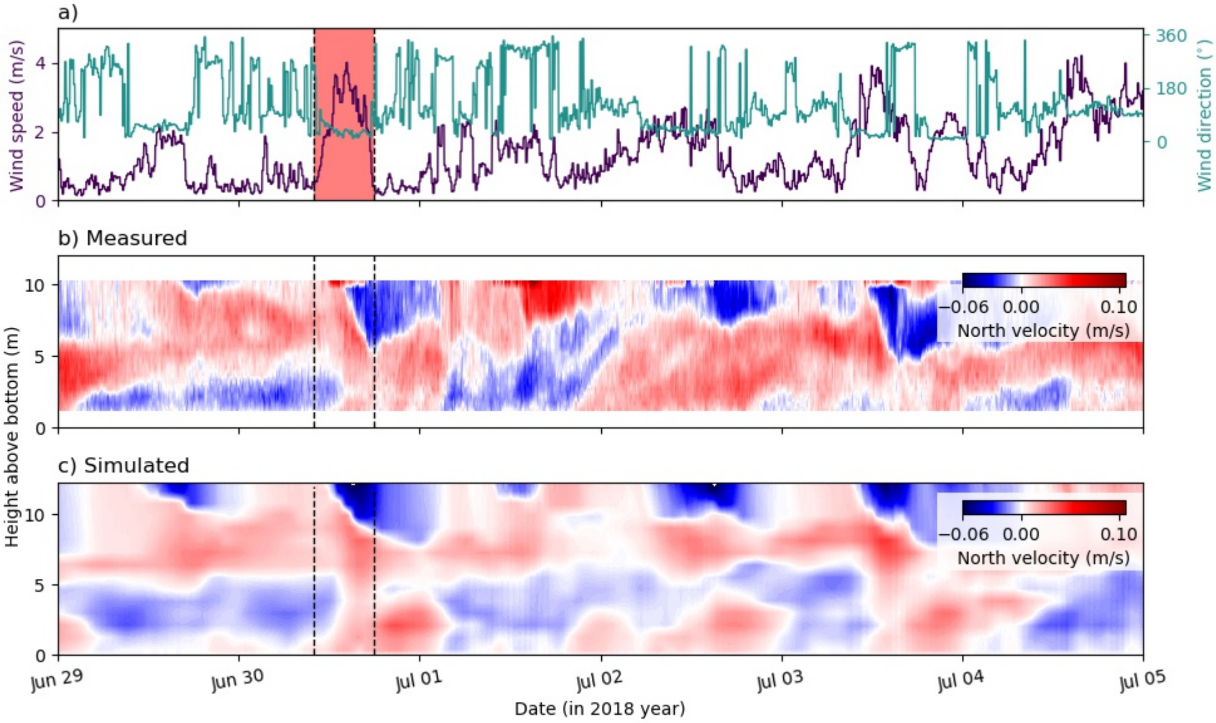

Figure 32 – a) Wind speed (purple line) and wind direction (green line) during the analysis period P1. The red shaded area, delimited by vertical black dashed lines, marks a solitary wind event that may favor the generation of internal seiches. b) Measured, and c) simulated horizontal flow velocities in south to north direction at the location of the monitoring station (Fig. 29a) with a temporal resolution of 1 min.

Both observations and model results show a southward directed flow in the surface layer during the wind event, with horizontal flow velocities reaching 0.063 m s^{-1} (observations) and 0.054 m s^{-1} (model). The wind-driven surface layer gradually deepened to reach a depth of 5.5 m. The water column below the wind-driven surface flow was flowing in the opposing direction with magnitudes reaching 0.026 and 0.030 m s^{-1} in observations and simulations, respectively (Fig. 32b and c). The spatial distribution of the flow field in the model simulations show that the windward-directed flow at the water surface extended to the dam (Fig. 54a). As the upper layer propagated towards the dam, the hypolimnion layer was pushed downward, accelerating the lower layer into the opposite direction (Fig. 54a). The vertical displacement of isothermal depths reached approximately 3 m at the dam (Fig. 53c).

The spatial distribution of the velocity field in the model simulations show that the windward-directed flow at the water surface extended to the dam. As the upper layer propagated towards the dam, the hypolimnion layer was pushed downward, accelerating the lower layer into the opposite direction (Fig. 54a). The vertical displacement of isothermal depths reached approximately 3 m at the dam (Fig. 53c). The flow structure persisted for 9 h after the end of the wind event, before the flow direction in both layers reversed. The flow pattern thus followed the expected dynamics of seiche generation, with wind-generated up- and downwelling at the luv and leeward end of the reservoir, respectively, and flow reversal driven by the resulting longitudinal pressure gradient after the wind has ceased. Given the extension of Passaúna reservoir ($L \approx 7$ km) and the thermal structure during the wind event, the fundamental internal seiche period (first vertical mode, Eq. N.3) was $T_{V1} \approx 20$ h. The 8 h duration of the wind event exceeded one quarter of the fundamental period and can thus be considered favorable for seiche excitation (SPIGEL; IMBERGER, 1980; STEVENS; IMBERGER, 1996). Nevertheless, persistent oscillatory motions after the wind event were neither present in the field observations, nor in the simulations (Fig. 32 and Fig. 54).

4.3.3 Identification of factors influencing attenuation

In the following, we analyze numerical simulations to explore potential reasons for the discrepancy between the internal seiche activity predicted by the classification scheme, and the lack of persistent internal oscillations in the observations. We start with analyzing the response of a most simplified basin shape and bathymetry to a solitary wind event, similar to the one analyzed above, for varying patterns of vertical density stratification. We then stepwise add complexity to basin shape and bathymetry to approach the conditions in Passaúna Reservoir.

4.3.3.1 Effects of density stratification

Scenario M1B1, the simplest basin shape with constant water depth (Fig. 29d), is closest to the assumption of a rectangular basin made in the classification scheme. In this scenario, the longitudinal flow velocity clearly shows indications of internal seiche activity (Fig. 33), thus following the predictions of the classification scheme even for cases when the temperature stratification deviates from a two-layer system. The vertical structure of the flow velocity is characterized by different layers with opposing flow directions.

In case of a two-layer stratification, also two layers of opposing flows develop (Fig. 33a), while for continuous stratification the number of vertical layers increases, indicating the occurrence of internal seiches with higher vertical modes. Interestingly, the simulated velocity structure after the wind event (Fig. 33a) is similar to that found in the baseline scenario for measured and simulated data (Fig. 32). In the scenario with a two-layer stratification (Fig. 33a), the 8 h wind event generated an internal seiche with a period of about 21 h and an amplitude of 1.6 m, corresponding to 13% of the water depth. The theoretical wave period ($T_{\mathrm{V1H1}} = 20$ h) obtained from Merian's equation (Eq. N.3) matches well with the observed period with less than 5% difference. As the stratification profile deviates from a two-layer structure, the internal seiche period increased to 28 h, exciting higher vertical modes (Fig. 33b).

After the wind event, the total kinetic energy in internal waves decreased nearly exponentially with time (Fig. 33). From the time-integrated internal seiche energy (Fig. 34a), we found that only up to 3% of

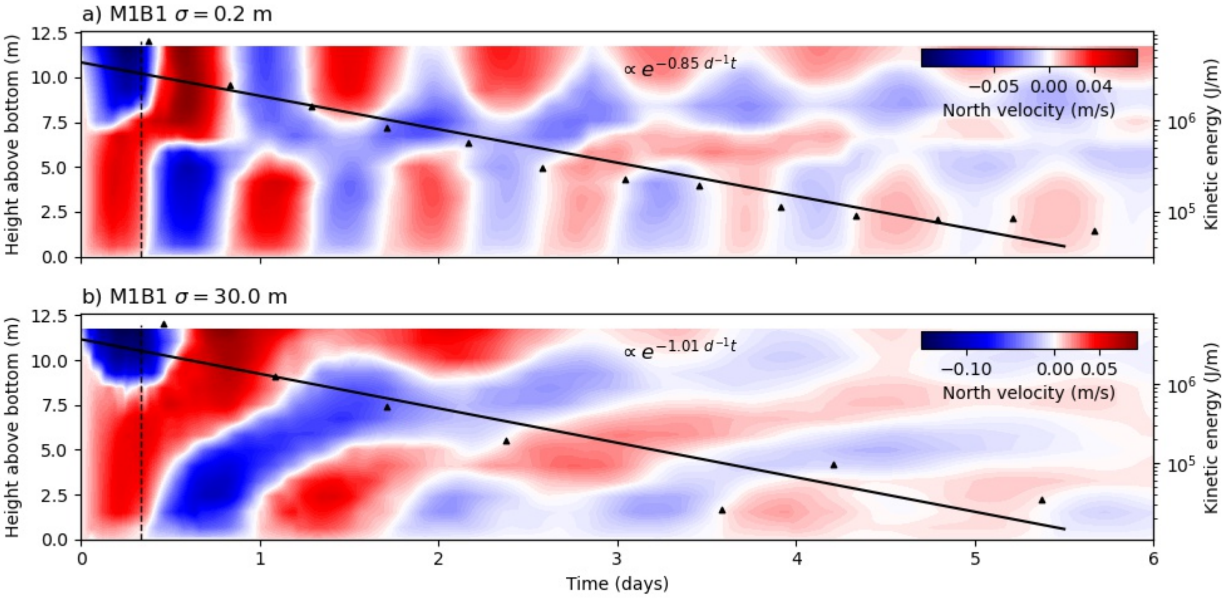

Figure 33 – Temporal dynamics of vertical profiles of horizontal flow velocities near the center of the reservoir (station S1, velocity indicated by color) and kinetic energy in internal wave motion for scenario M1B1 for a) nearly two-layer stratification ($\sigma = 0.2$ m) and b) nearly linear stratification ($\sigma = 30$ m). The vertical black dashed lines mark the end of the wind event. The black triangles show the total internal wave energy. The black solid line illustrates the exponential decay of wave energy (see labels for decay rate, in which the time t has the unit days).

the wind energy input is initially transferred to internal seiches. The total energy in internal seiches increased for an increasing deviation of the stratification from a two-layer structure, i.e. with increasing σ.

4.3.3.2 Effect of reservoir morphology

To analyze the effect of reservoir morphology on the energy content in internal seiches, scenario M2B1 is compared with results from scenario M1B1 (Fig. 34a-b, Fig. 56a-d, and Table 6). The period of the fundamental internal seiche generated in this scenario for a two-layer stratification is approximately 30 h, 32 % higher than the value estimated by Merian's equation (Eq. N.3).

In addition to a reduced initial wave amplitude in comparison to scenario M1B1, the power spectral density of the vertical velocity in the scenario with reservoir morphology shows higher frequency fluctuations (elevated spectral variance between frequencies of 4×10^{-5} and 2×10^{-4} Hz, corresponding to periods from 1.5 to 7 h, Fig. 35b-c), in comparison to the scenario with simplified reservoir morphology.

To explore the spatial distribution of the enhanced spectral variance, we integrated the power spectra of vertical velocity near the thermocline depth within this frequency range. Higher power spectral density was mainly observed near the reservoir bends that were added in scenario M2B1 (Fig. 35d). The enhanced current shear, which is associated with these velocity variations potentially contributes to the energy loss, of the internal seiches. Compared to scenario M1B1, the damping coefficient of the total energy increased by 23 to 30 %, depending on the stratification condition. This interaction with the reservoir bend is also responsible for the lower energy of the internal seiche during generation, reducing the fraction of wind energy that is transferred to internal seiches by approximately 13 % compared to scenario M1B1, with small variation for

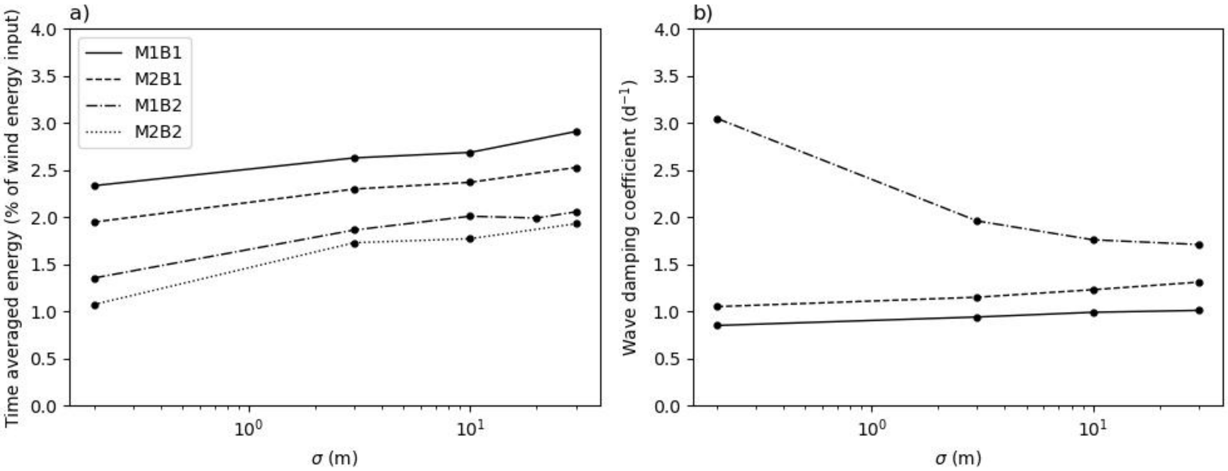

Figure 34 – Parameters related to wave generation and dissipation. a) Time averaged energy in internal seiches in response to a solitary wind event as a function of the initial density stratification (thermocline width σ, cf. Fig. 30) for the four simulated scenarios: M1B1, M2B1, M1B2, and M2B2. The line shows the initial wave energy computing assuming the energy from the first wave cycle. The internal seiche energy is normalized by the wind energy input. b) Wave damping coefficient obtained assuming an exponential decay of the total wave energy. Wave dampening of case M2B2 is not shown because the wave is rapidly dissipated right after the end of the wind event.

different stratification conditions (Fig. 34a).

4.3.3.3 Effect of bathymetry

To compare the effect of bathymetry on the energy transferred from wind to internal seiches, we compared scenario M1B2 with the results from other scenarios (Fig. 34). In M1B2, we observed more complex vertical flow structures with an increasing number of layers with opposing flow direction, suggesting the generation of higher vertical modes for scenario M1B2 (Fig. 34c). The formation of higher vertical modes is clearly observed through the temperature and horizontal velocity profiles when the stratification is continuous (Fig. 53c and d) but can be also observed for nearly two-layer stratification. In this case, the wind-induced mixing causes erosion of the two-layer density distribution (Fig. 36a), promoting the generation of internal seiches with higher vertical modes.

The main difference compared to continuous stratification is that the small density difference associated with the two-layer structure in case of $\sigma = 0.2$ m supports higher-mode internal seiches with larger wave periods compared to simulations with $\sigma \gg 1$ m. The second vertical mode is characterized by enhanced interfacial shear at the metalimnion boundaries, in which the upper and lower layers move in the same direction, whilst the metalimnion flows in the opposite direction (Fig. 36b).

The consideration of basin bathymetry in scenario M1B2 resulted in consistently larger damping coefficients compared to scenarios M1B1 (129%) and M2B1 (84%). In contrast to the other scenarios, the wave damping also decreased with increasing and was 44% lower for nearly continuous stratification ($\sigma = 30$ m) than for the two-layer density structure ($\sigma = 0.2$ m).

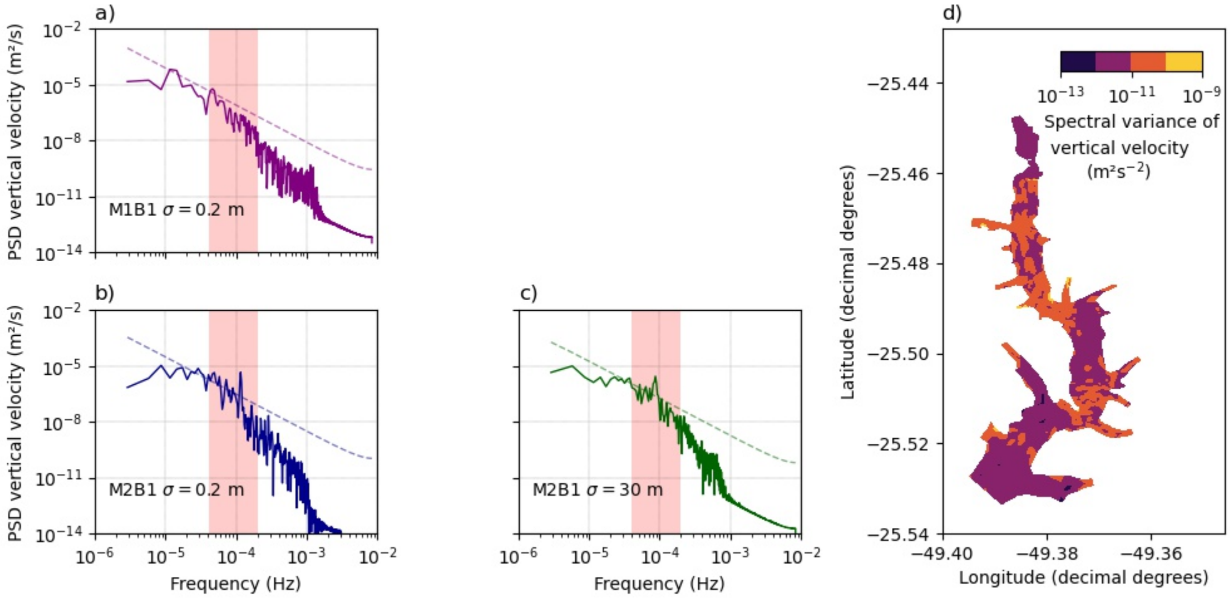

Figure 35 – The influence of morphological characteristics on the internal seiche dynamics. Panels a) to c) show power spectral density (PSD) of vertical velocity: b) M1B1 and $\sigma = 0.2$ m, c) M2B1 and $\sigma = 0.2$ m, and d) M2B1 and $\sigma = 30$ m. The dashed lines show the 95 % confidence limit of the mean red noise spectrum for the time series. The red shaded area marks the frequency band of elevated spectral energy in scenario M2B1 compared to the rectangular basin considered in scenario M1B1. d) The spatial distribution of the spectral variance of the band-pass filtered vertical velocity with cutoff frequencies of 4 h and 6 h for scenario M2B1 and $\sigma = 0.2$.

4.3.3.4 Combined effects of morphology and bathymetry

In the final scenario (M2B2), we considered the morphology and bathymetry of Passaúna Reservoir as in the baseline scenario and analyzed its response to a solitary wind event. The scenario represents a combination of the wave attenuation mechanisms observed in scenarios M2B1 and M1B2, resulting in the lowest energy transfer from wind to internal seiche motions (Fig. 34a). The energy is attenuated during the first wave cycle due to the interactions with the reservoir topography, but particularly due to strong energy dissipation at the sloping reservoir bottom, which is responsible for the strong energy decay that occurs after the initial thermocline displacement (Fig. 57).

4.4 Discussion

4.4.1 Model validation and internal seiches in Passaúna Reservoir

Numerical simulations of the dynamics of the vertical distributions of water temperature and flow velocity in Passaúna Reservoir were in good agreement with measurements (Fig. 32, Fig. 58, and Fig. 59), demonstrating that Delft3D is capable of reproducing heat transport and hydrodynamics of the stratified reservoir. This result confirms previous studies that have successfully applied hydrostatic models to simulate large-scale flow features, including internal seiches in stratified lakes and reservoirs (LAVAL; IMBERGER; FINDIKAKIS, 2005; LEÓN et al., 2005; DISSANAYAKE; HOFMANN; PEETERS, 2019; ISHIKAWA et al., 2021).

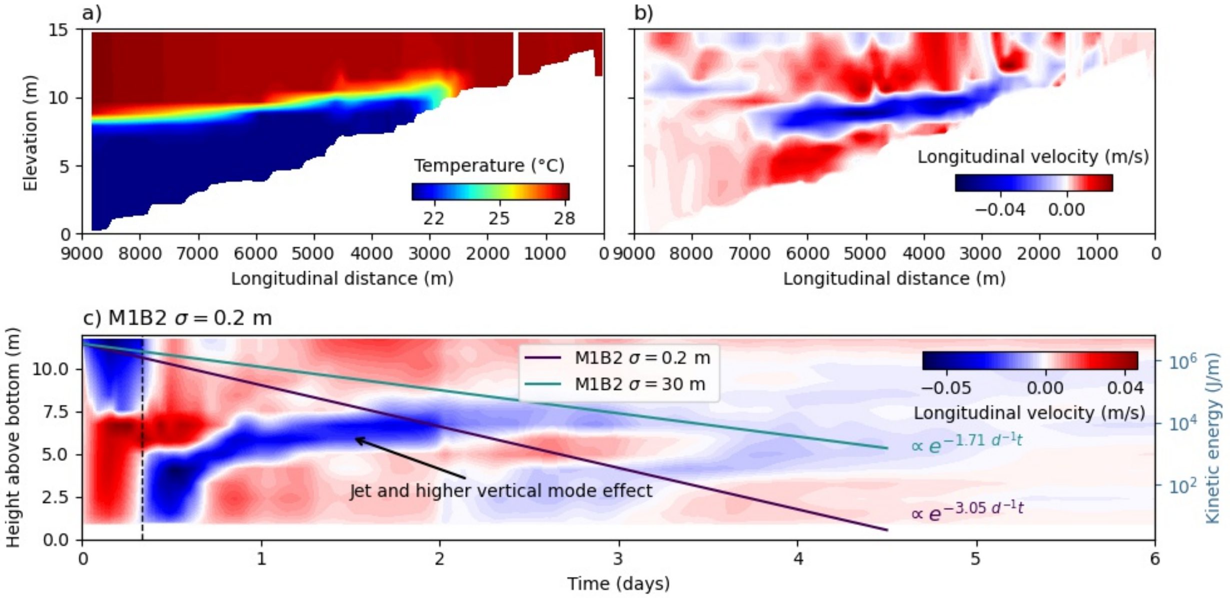

Figure 36 – The influence of bathymetry on internal seiches analyzed in scenario M1B2 for nearly two-layer stratification ($\sigma = 0.2$ m): a) Temperature distribution along the longitudinal cross section of the reservoir during the wind set-up ($t = 0.3$ d). b) North-south velocity component along the longitudinal transect at $t \approx 1$ d. c) Temporal dynamics of the vertical distribution of horizontal flow velocity at the center of the basin. The colored solid lines illustrate the exponential decay of total energy in internal seiches for nearly two-layer stratification (purple color, $\sigma = 0.2$ m) and for nearly continuous stratification (green color, $\sigma = 30$ m). Text labels show decay rates, in which t is defined in days.

Our results further demonstrated that Delft3D is capable of describing the detailed hydrodynamic response of the reservoir to wind forcing. Discrepancies in the spectral distributions of measured and simulated velocity variance occurred at frequencies exceeding 8×10^{-4} Hz (Fig. 59c), i.e. at time scales shorter than ≈ 3 h. Similarly, previous comparisons of power spectra of simulated and measured flow velocities revealed significant differences at frequencies exceeding 10^{-4} Hz (APPT; IMBERGER; KOBUS, 2004; GÓMEZ-GIRALDO; IMBERGER; ANTENUCCI, 2006; VIDAL; CASAMITJANA, 2008). At least partially, this discrepancy could be attributed to the existence of propagating high-frequency internal waves, which can be excited by wind or during the degeneration of internal seiches and tend to break at the sloping boundaries of the basin (BOEGMAN; IVEY; IMBERGER, 2005a). Hydrostatic models can capture the initial nonlinear steepening of internal seiches, but they cannot reproduce the subsequent degeneration into high-frequency internal waves (WADZUK; HODGES, 2009). Although enhanced shear and breaking of high-frequency internal waves was not explicitly reproduced in our simulations, spectral analysis showed that large-scale flow features in Passaúna reservoir were well captured.

Common classification schemes for mixing dynamics in stratified waters based on the Wedderburn number suggest a predominating role of basin scale internal seiches in Passaúna Reservoir (Fig. 31). Even though a set-up of the thermocline and initiation of internal seiches could be identified in the simulation results (Fig. 32), persistent oscillatory flows could not be identified in the power spectra of measured and simulated flow velocities (Fig. 54). A previous study at Passaúna reservoir has described the ubiquitous presence of high-frequency internal waves with periods between 2 and 17 min (ISHIKAWA et al., 2021), but also reported a lack of internal seiches. Our results suggest that, even though wind-induced upwelling and downwelling of the thermocline can occur in Passaúna reservoir, the initial vertical displacement is rapidly damped during its relaxation, without seiche development.

4.4.2 Generation of internal seiches

To explore the reasons for the lack of seiche activity and the discrepancy with predictions of the classification scheme, we analyzed several hypothetical scenarios, in which we simplified shape, bathymetry, and stratification conditions of the reservoir and analyzed its response to a solitary wind event that represents favorable conditions for internal seiche excitation. The scenarios represent stepwise deviations from the ideal conditions of a rectangular basin with two-layer stratification, as it is considered in the classification scheme. The fraction of the total energy input from wind that was attributed to the generation of internal seiches varied between 1.0 and 3.0% among the different scenarios (Fig. 34a). This relatively small percentage of the wind energy flux across the air-water interface is consistent with previous estimates from thermally stratified lakes and reservoir, which suggested that approximately 1% of the wind energy input is transferred to internal seiches (IMBODEN, 2003; GUSEVA et al., 2021). In comparison to a straight, rectangular channel with constant depth (scenario M1B1), the fraction of wind energy transferred to internal seiches was reduced by about 32% and 11% by the consideration of reservoir bathymetry (M1B2) and reservoir morphology (M2B1), respectively. Moreover, both effects were additive, resulting in fourfold reduction of the energy in internal seiches in the combined scenario, representing the morphology and bathymetry of Passaúna Reservoir (M2B2).

In all simulations, the energy increased with increasing deviation of the stratification from a two-layer structure to nearly linear stratification (large values of σ, Fig. 34a). This increase could be related to the increase of energy in higher vertical modes and the decrease of the mixing efficiency in the mixed upper surface layer. Previous studies have suggested that the generation of higher vertical modes is caused by spatial or temporal variations of the of wind energy input, e.g. due to wind sheltering at one end of the basin (MÜNNICH, 1996), or by periodic wind forcing (BERNHARDT; KIRILLIN, 2013). The response to a solitary wind event analyzed in the present study shows that also the lake bathymetry affects the initial distribution of the wind energy input, creating an asymmetric distribution of the wind energy along the basin with sloping water depth, which apparently favors the formation of internal seiches of higher vertical modes (Fig. 36). Even though in the present study the energy from different vertical modes was not quantified, the pattern observed in the horizontal velocity distribution indicates the formation of higher vertical modes in the presence of a sloping bottom.

4.4.3 Mechanisms of internal seiche damping

The deviations of morphology, bathymetry, and stratification from ideal conditions had distinct effects on the damping of the initial wave setup by promoting enhanced energy dissipation. Our results show that basin morphology has a strong influence on the internal seiche period, generating periods 42% higher compared to the scenario with a rectangular cross section (M1B1). However, results show less influence on the internal seiche damping (Fig. 56), presenting damping coefficient only 25% higher than in scenario M1B1. The simulations suggest that the interactions of the internal seiche with the reservoir boundaries leads to the generation of higher frequency flow variations, indicating an energy transfer from basin-scale motion to higher frequency waves, especially in regions where the longitudinal flow direction was deviating from a straight channel (Fig. 35).

The consideration of the sloping reservoir bed (scenario M1B2) resulted in additional interaction between internal seiche with the reservoir boundaries (Fig. 36). Former studies showed that shear induced convection can promote a destabilization of the bottom boundary layer during upslope flow conditions (LORKE; UMLAUF; MOHRHOLZ, 2008). This can be represented by the increase of mixing near the lakeshore, which is observed during the interaction between the internal seiche and the lake bathymetry in our simulations, when the wave propagates upslope (Fig. 36a). The mechanism of shear-induced convection can result in a strong asymmetry of the boundary mixing during downslope and upslope currents (LORKE, 2007), although other studies did not observe significant differences between up- and downwelling events (COSSU; WELLS, 2013). In simulations using two opposite wind directions we found no significant difference of the wave energy decay depending on initial up- or downwelling flows on the reservoir slope (Fig. 55). This result suggested that the wave breaking (COSSU; WELLS, 2013) did not explain the strong attenuation of the internal seiche energy in the simulations with sloping bathymetry. Another mechanism that can strongly contribute to wave dissipation is a trapping process that emerges from the tendency of internal wave energy to propagate vertically along the water column. Depending on angle of wave propagation and the bottom slope, the internal wave may be reflected along lateral boundaries generating an internal wave attractor, a path in which the internal wave may converge or diverge in a confined stratified basin (PILLET; MAAS; DAUXOIS, 2019). This mechanism has been analyzed extensively for propagating internal waves over different bottom slopes (MAAS et al., 1997). Studies have observed that under subcritical bottom topography (gentler slope), the sloping boundary may act as an attractor to internal wave, focusing the wave to the lake shore and reducing its wavelength after each boundary reflection, leading to strong dissipation near the lakeshore. The bottom slope of Passaúna reservoir (0.095°) and the wavevector components angle (0.15°) suggest that most part of the wave energy should be dissipated in the sloping bottom boundary layer. Observation in Lacamas Lake has suggested that high internal seiche damping occurred due to substantial boundary layer absorption of vertically propagating internal waves (HENDERSON; DEEMER, 2012).

The results from the simulated scenarios indicate that during the initial set-up of the thermocline, the sloping bottom caused an attenuation of internal wave energy higher than the effect of reservoir morphology (32% compared to a rectangular-shaped basin). However, stronger wave damping occurred after the set-up in the simulations with sloping bathymetry. The total wave energy decayed 100% faster compared to the scenario with a rectangular cross section (M1B1) and 85% faster compared to the scenario M2B1 (Fig. 36c), which indicates that the seiche interaction with reservoir bathymetry can strongly contribute to the attenuation of internal seiches in stratified basins. We suggest that the rate of wave damping is greater in lakes with more complex topography.

Even though the actual numbers presented in this study are site specific, our analysis demonstrated that both flow-bathymetry interaction is the primary contributor to faster internal seiche damping and must be considered for predicting the occurrence of internal seiches in thermally stratified basins with gentle slopes (0.095°), which cover many small and medium-sized reservoirs that has a gentler slope bathymetry compared to natural lakes.

4.4.4 Physical and ecological implications

Our analysis revealed large variations of the energy that is transferred from wind to internal seiches, despite Wedderburn numbers of the order of unity. This mechanism of internal seiche damping as a function of the sloping boundary may have two important implications on lake dynamics: (1) internal seiches may not persist for long periods of time and (2) almost all energy from upwelling can be transferred to turbulence at the location where the thermocline intersects with the sloping boundary, making this a hot spot of vertical mixing.

Higher dissipation rates near the sloping bottom boundary layer obtained from a numerical simulation of Lake Kinneret (SHIMIZU; IMBERGER, 2008) and observed in field measurements in Lake Erie (LIN; BOEGMAN; RAO, 2021) corroborate the finding that nearshore bathymetry gives rise to higher dissipation rates depending on the bottom slope, where most part of the internal seiche energy may be transferred to turbulence. This mixing mechanisms can contribute to the spatial distribution of contaminated sediments (FORSYTHE; MARVIN, 2005), and to the enhanced nutrient release from the sediment, and higher turbidity in the nearshore regions (MAKAREWICZ et al., 2012). The locally enhanced vertical and horizontal fluxes of nutrients contained in the sediment (IMBERGER; PATTERSON, 1989; MACINTYRE et al., 1999) can favor the abundance of phytoplankton and planktivorous fish in these energetic mixing regions. The internal seiche breaking is therefore likely to have strong implication on the biodiversity and productivity, although more field experiments would need to be carried out to confirm how different sloping boundaries may affect the ecological interactions and biogeochemical fluxes.

We showed that sloping bathymetry not only contributes to the wave damping, but also promotes the generation of internal seiches of higher vertical modes. These findings may explain why internal seiches of higher vertical modes are more dominant in some lakes than others under similar weather and stratification conditions. Higher vertical modes may have strong consequences for the distribution of planktonic organisms. Observations in the Sau Reservoir showed that green algae that were present in two neighboring layers of internal seiche motion were homogenously distributed along the reservoir, whilst diatoms and cryptophyceae, that were present in only one layer, accumulated near the dam (SERRA et al., 2007). In addition, reservoir morphology, such as bends, additionally contributed to the dissipation of seiche energy by favoring the transfer of energy to higher frequency waves, and to the formation of local hotspots of energy dissipation and mixing.

Our findings demonstrate the limitations of the Wedderburn number for predicting internal seiche predominance under non-ideal conditions. Its application in the context of hydrodynamic classification and for the interpretation of observed physical, ecological and biogeochemical dynamics, should therefore critically scrutinize its applicability and consider deviations from predicted dynamics, including the presence of hotspots of turbulent mixing, and the more complex flow patterns associated with higher vertical modes. It remains challenging to express the complex hydrodynamic response of natural basins to wind forcing based on easily accessible bulk characteristics. Future studies may aim at expanding the Wedderburn number approach to water bodies of characteristic shape, such as that of dendritic reservoirs, for which more specific hydrodynamic classification schemes could be developed.

5 Internal wave analyzer

The work described in this chapter has been published to *Environmental Modelling & Software* under the title 'Internal wave analyzer for thermally stratified lakes'.[1]

Abstract

Interwave Analyzer is an open source software that provides detailed characterization of the dynamics of basin-scale internal waves in lakes and reservoirs. It is based on well established theories and empirical knowledge on internal waves and lake mixing and facilitates a general physical classification of lakes and reservoirs. As input data, the program requires time series of water temperature from various depths and meteorological data (wind speed and direction), along with basic characterization of the basin dimensions. These data are typically obtained from measurements or from numerical models. Interwave Analyzer performs an in-depth analysis of periodic motion by Fourier and Wavelet transforms to identify predominant internal wave periods. The software includes a multi-layer model to provide theoretical estimates of internal wave periods, which facilitates the identification of predominant wave modes. The program further derives indices that describe the excitation of internal waves by wind, expected wave amplitudes and the expected regime of wave degeneration. Interwave Analyzer is a powerful, easily accessible, and universal tool, which can be used for obtaining detailed understanding lake hydrodynamics not only in physical sciences, but also in the context of water quality, ecological interactions and biogeochemical fluxes in aquatic ecosystems. linear theory.

---

[1] de Carvalho Bueno, R., Bleninger, T. B., Lorke, A. - Internal wave analyzer for thermally stratified lakes. *Environ. Model. Softw.* (2020) https://doi.org/10.1016/j.envsoft.2020.104950

5.1 Introduction

Although reservoirs and lakes are often classified as standing or stagnant water bodies, the water in these ecosystem is not motionless. There are numerous forces that can generate water motion (MORTIMER, 1974; IMBERGER, 2013; OSBORNE, 2000; WÜEST; LORKE, 2003) (Figure 37). Wind stress at the water surface can excite propagating surface waves and near-surface drift currents. Surface cooling results in convective flows and the inflow of water having a different temperature may promote the formation and propagation of gravity currents. Water currents and mixing processes in lakes and reservoirs interact with vertical density stratification, which may develop in response to surface heating and inflows having different temperature or salinity (BOEHRER; SCHULTZE, 2008). While stable density stratification suppresses vertical turbulent mixing and the exchange of heat and solutes between layers having different density, it gives rise to an additional type of flow. Baroclinic flows, which depend on vertical variations of water density, often occur as internal waves, which cause a periodic displacement of layers with different density (MORTIMER, 1974). Internal waves are generated by wind shear and are among the most important phenomena that drive water currents in the interior of stratified lakes and reservoirs (MORTIMER, 1952; UMLAUF; LEMMIN, 2005; BOUFFARD; BOEGMAN; RAO, 2012). Although just a small fraction of the total wind energy crosses the surface boundary layer (WETZEL, 2001; WÜEST; LORKE, 2003; WÜEST; PIEPKE; SENDEN, 2000), roughly 20% of energy that passes through the surface boundary layer can be found in internal wave motions in closed water bodies (BOUFFARD; BOEGMAN, 2012). These waves are often excited in the form of basin-scale, standing waves, also called internal seiches (SAGGIO; IMBERGER, 1998; WANG; HUTTER; BÄUERLE, 2000). Internal waves have been demonstrated to affect aquatic ecosystems and biogeochemical cycling in stratified lakes and reservoirs, by displacing phytoplankton and zooplankton organisms (MORTIMER; HORN, 1982; RINKE et al., 2007), causing sediment resuspension (SAKAI et al., 2002) and regulating the availability of oxygen in the water column (UMLAUF; LEMMIN, 2005), as well as in the sediment (LORKE et al., 2003; FRINDTE et al., 2013).

Laboratory experiments and field observations revealed that internal wave energy is cascaded to smaller scales of turbulence due to the interaction with the bathymetry and nonlinear steepening of internal seiches, generating trains of nonlinear internal waves (BOEGMAN et al., 2003; BOEGMAN; IVEY; IMBERGER, 2005a). This energy flux path is considered as an important component of mixing processes in stratified lakes. Although basin-scale internal waves can contain more than 98% of the wave energy, shoaling and breaking of internal waves and generation of turbulence is practically restricted to high-frequency waves. Observations in thermally-stratified lakes have suggested that more than 80% of the available potential energy of large-scale internal waves is transferred to high-frequency waves or dissipated into heat during the first wave period (STEVENS et al., 1996).

Water motions in stratified systems are often analyzed in terms of dimensionless numbers, which describe dynamic equilibria between the kinetic energy and inertial forces associated with water currents in relation to the potential energy or the buoyancy forces caused by vertical density stratification (SHINTANI et al., 2010). The required parameters can be obtained in the field using instrumented buoys, such as thermistor chains and meteorological stations, or they are obtained from numerical models. Recent advances in sensor technology and numerical models, lead to more widespread availability of high-frequency data, which can be used to detect internal waves and to estimate or to predict their implications for water quality (LORKE; PEETERS; BÄUERLE, 2006; BOUFFARD; LEMMIN, 2013; SIMPSON; WILES; LINCOLN, 2011a). Although a variety of numbers and parameters describing the baroclinic response of stratified lakes have been formulated based on well established theories and empirical relations, many details of their application to

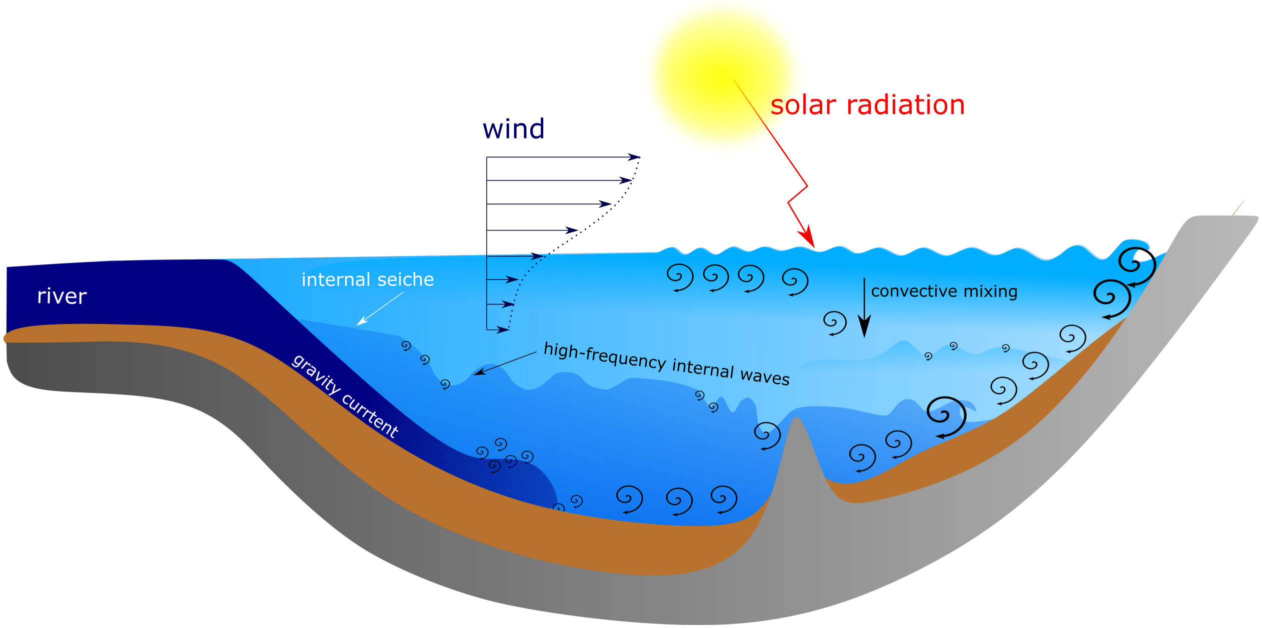

Figure 37 – Schematic overview of currents and mixing process in lakes and reservoirs. Different shades of blue denote layer of different temperature (density). Brown and silver layers indicate the sediment layer and the solid bathymetry of the lake, respectively. Basin-scale internal waves and high-frequency internal waves can occur at density interfaces. Billows (black arrows) illustrate turbulent mixing.

field observations are site-specific. A unified framework for processing field observations and for a quantitative characterization of internal wave activity is currently lacking. Only recently, a powerful open source tool for calculating lake mixing and stratification indices, the Lake Analyzer, has been developed Read et al. (2011). While the Lake Analyzer provides a broad range of different physical parameters, it does not include the characterization of internal waves.

The aim of this paper is to describe and to demonstrate the efficiency of a new open source tool the Interwave Analyzer. The software provides a detailed characterization of lake mixing and internal wave activity by deriving important physical indices and lake classification based on well established theories (HORN; IMBERGER; IVEY, 2001; BOEGMAN; IVEY; IMBERGER, 2005a; SPIGEL; IMBERGER, 1980; BUENO et al., 2020). The Interwave Analyzer facilitates a consistent methodology for analyzing data from lake monitoring buoys and numerical models. Periodic motions are explored by Fourier and Wavelet transforms, which have been widely used in studies on internal waves in lakes (BUENO et al., 2020; HUTTER, 2011; MÜNNICH; WÜEST; IMBODEN, 1992). Interwave Analyzer provides a general classification of lake mixing dynamics (BUENO et al., 2020; SPIGEL; IMBERGER, 1980), which can be used without special knowledge in fluid dynamics, e.g. in interdisciplinary studies analyzing links between internal wave dynamics with water quality and biogeochemical studies. For users specialized in environmental fluid dynamics, the program analyses wind resonance phenomena (MÜNNICH; WÜEST; IMBODEN, 1992; VIDAL; CASAMITJANA, 2008), internal seiche growth, energy distribution in the internal wave spectrum, excitation of higher vertical modes, degeneration of internal seiches (HORN; IMBERGER; IVEY, 2001; BOEGMAN; IVEY; IMBERGER, 2005a), and density inversions.

In section 5.2 we present the theoretical background that is implemented in the software, including details about established theories and internal wave models. We provide information about the program structure, input data, data processing, and output results in section 5.3. The application and the physical interpretation of results provided by the software are described for two case studies in section 5.4. The first case study demonstrates the efficiency of the Interwave Analyzer to describe the evolution of basin-scale internal waves using data from a three-dimensional numerical model, Delft3D-FLOW (HYDRAULICS, 2003). In a second case study, we processed field measurements from a reservoir and provide more detailed explanations of the influence of user-defined parameters on the final results generated by the Interwave Analyzer.

5.2 Internal wave dynamics and mixing classification

5.2.1 Modal model for basin-scale internal waves

Basin-scale internal waves (internal seiches) in a stratified fluid can be approximated by a finite number of eigenvalues having characteristic periods $\mathrm{T}_{n,m}$ (MÜNNICH; WÜEST; IMBODEN, 1992). The different periods belong to different patterns of standing waves, having n nodes in the vertical and m nodes along the horizontal direction of an idealized (rectangular) basin, commonly referred as VnHm internal wave. Vertical density stratification is approximated by a number of layers of thickness h_i with each having a constant density ρ_i, where the number of layers determines the maximum number of vertical modes (38). The possible periods of standing (basin-scale) internal waves in such idealized system can be obtained by numerical solution of the corresponding eigenvalues by further applying the shallow-water and the hydrostatic pressure approximations (MÜNNICH; WÜEST; IMBODEN, 1992). This solution is presented in Appendix D.5.

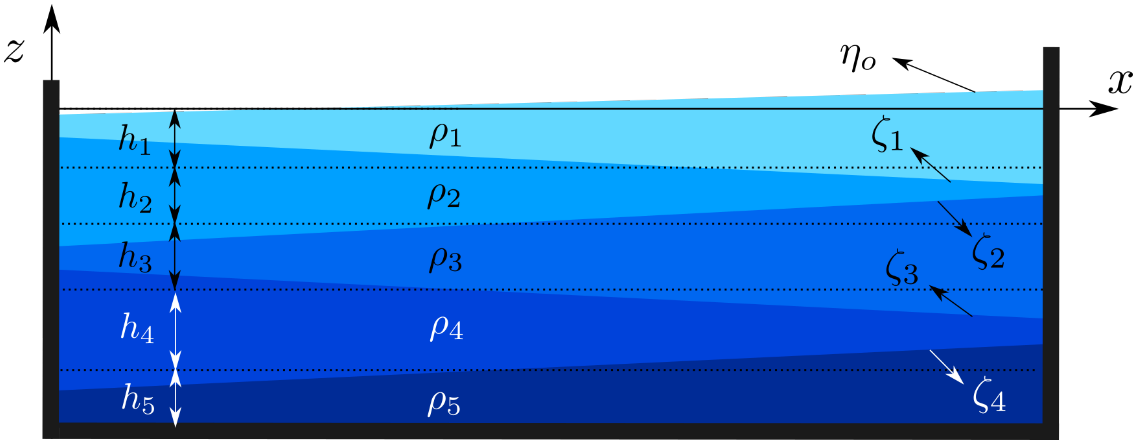

Figure 38 – Illustration of the modal structure of basin-scale (standing) internal waves in an idealized (rectangular) basin. Vertical density stratification is approximated by five vertical layers,(different shades of blue), each having a constant density ρ and thickness (at equilibrium position h). The equilibrium position of the layer interfaces is shown as black dashed lines. The blue shading illustrates the layer displacement (ζ) of a horizontal mode 1 and vertical mode four wave (V4H1). η_0 denotes the displacement of the water surface.

In large basins and at high latitudes, internal waves can be affected by Coriolis force (LEMMIN; MORTIMER; BÄUERLE, 2005; BERNHARDT; KIRILLIN, 2013). The potential effect is described by the Burger number, which represents the squared ratio of the internal Rossby radius of deformation ($R_D = c/\overline{\omega_o}$, where c is the internal seiche phase speed, $\overline{\omega_o}$ is the Coriolis frequency) and the basin length L:

$$Bu = \left(\frac{R_D}{L} \right)^2 . \tag{5.1}$$

For a Burger number larger than unity, gravity force dominates and the modal model described above is fully applicable. For Burger numbers smaller than unity, the internal waves are affected by Earth's rotation and the mathematical formulation of the multi-layer system has to be extended (SUTHERLAND, 2010).

5.2.2 Wave generation and mixing

The stability of stratified shear flows is described by the dimensionless Richardson number (Ri), which relates buoyancy to shear forces. For small Ri (< 1), the system is susceptible to mixing since work against buoyancy force is small compared to the production turbulent kinetic energy. Large values of Ri indicate that the flow is more stable, and consequently less susceptible to vertical mixing. Depending on the scale and the type of flow, Ri can be expressed in a variety of different formulations. When it is related to the wind stress applied at the surface of a water column with two layers of constant density (epilimnion and hypolimnion), it is expressed as the bulk (mixed layer) Richardson number as:

$$Ri_{V1} = \frac{g' h_e}{\kappa_v u_*^2}, \tag{5.2}$$

in which h_e is the epilimnion thickness, u_* is the friction velocity of the wind, and $\kappa_v \approx 0.4$ is the Von Kármán constant. $g' = g\Delta\rho/\rho_h$ is the reduced gravity, where g is the acceleration of gravity, ρ_h is the hypolimnion water density, and $\Delta\rho$ is the density difference between the hypolimnion and epilimnion. The bulk Richardson number has been found to be a good indicator of baroclinic activity in stratified lakes and reservoirs (SPIGEL; IMBERGER, 1980; SHINTANI et al., 2010; BUENO et al., 2020).

Based on the Richardson number, Thompson (1980) proposed a normalization to account for the finite longitudinal dimension of the basin. The normalization was named the Wedderburn number and is expressed as

$$W_{V1} = Ri_{V1} \, \frac{h_e}{L}, \tag{5.3}$$

in which h_e is the epilimnion thickness and L is the basin length that is aligned with the wind direction. The Wedderburn number represents the ratio between the wind stress and horizontal pressure gradients due to vertical displacement of the thermocline (i.e., the interface between the two layers of constant density). It is related to the longitudinal tilt of the thermocline in response to wind shear.

The Wedderburn number formed the basis of a classification scheme of lake dynamics in terms of four different regimes (SPIGEL; IMBERGER, 1980): strong mixing, steep tilt of the thermocline followed by mixing, higher amplitude internal waves dominance, and buoyancy dominance (Figure 39). When $W_{V1} < h_e/L$ (strong mixing regime, $Ri_{V1} < 1$), mixing occurs faster than the time required for the formation of billows. However, observations in different lakes have identified complete mixing events even when $W_{V1} > h_e/L$ (steep thermocline tilt followed by mixing) (MORTIMER, 1952; MORTIMER, 1955a; THORPE, 1978). In this intermediate regime, although the mixing does not occur instantaneously, vertical displacement is accompanied by billows and interfacial shear that eventually leads to complete mixing of the system. This

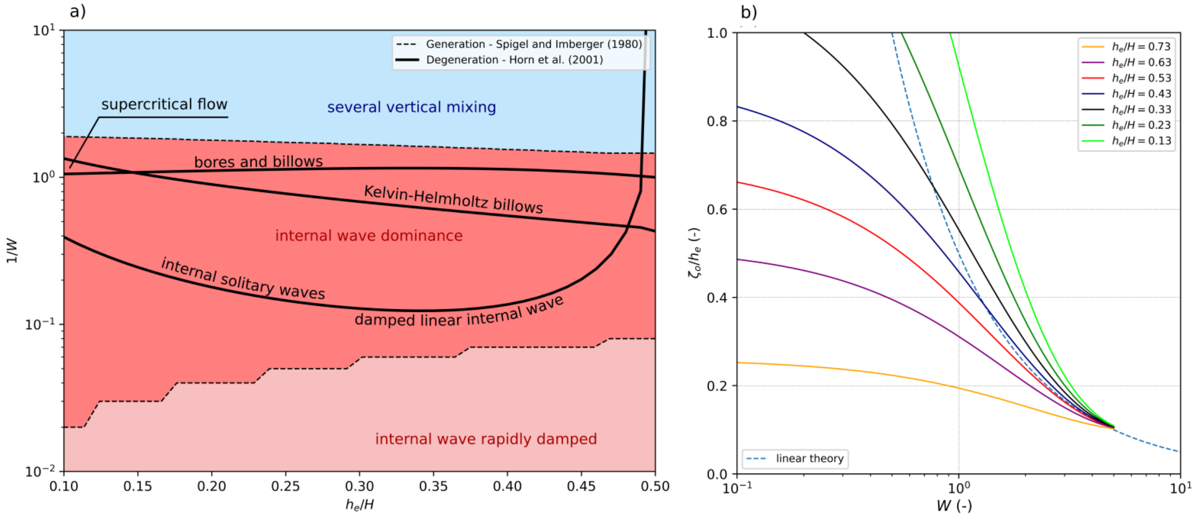

Figure 39 – a) Regime diagram for generation and degeneration of internal waves for a hypothetical reservoir with a basin length of $L = 4$ km. Different colors separate three mixing regimes based on Wedderburn number W_{V1} and the epilimnion thickness (h_e) normalized by the lake depth H. The two regimes proposed by Spigel and Imberger (1980), which result in complete vertical mixing are combined in the *severe vertical mixing*. Dashed lines show regime boundaries according to Spigel and Imberger (1980). Solid lines separate regimes of wave degeneration, as proposed by Horn, Imberger and Ivey (2001). b) The theoretical relationship between W_{V1} and the vertical displacement of the thermocline ζ_o normalized by the epilimnion thickness (h_e). Solid lines show theoretical results from Spigel and Imberger (1980) and the dashed line shows the empirical formulation proposed by Bueno et al. (2020). The latter takes an additional contribution of the epilimnion thickness and the interaction of the internal seiche with the lake boundaries into account.

regime persists until $W_{V1} < 0.5\ \sqrt{H/h_h}$. For larger values of W_{V1}, the lake remains stably stratified despite the formation of basin-scale internal waves. In the buoyancy dominated regime, i.e. if:

$$W_{V1} > \frac{L\ H}{4\ h_e\ h_h}, \tag{5.4}$$

the density stratification is too strong to support larger vertical displacement of the thermocline, and only small amplitude internal waves are susceptible to be excited. Observations have identified that high amplitude internal seiches are often generated between $W_{V1} = 1$ and 20 (STEVENS et al., 1996; ROGET et al., 1993; HEAPS; RAMSBOTTOM, 1966; STEVENS; LAWRENCE, 1997; MÜNNICH; WÜEST; IMBODEN, 1992).

The Wedderburn number has also be used to characterize the degeneration of internal seiches (HORN; IMBERGER; IVEY, 1998; HORN; IMBERGER; IVEY, 2001; BOEGMAN; IVEY; IMBERGER, 2005a; DOROSTKAR; BOEGMAN, 2013). The disintegration of basin-scale internal waves can be classified into five different regimes: damped linear wave, degeneration into propagating solitary internal waves, Kelvin-Helmholtz instabilities, bores and billows, and super flow (Figure 39). Each regime is based on the analysis of timescales. If the amplitude of an internal seiche is too small for strong shear instability and supercritical regime, it is damped by viscosity or by nonlinear effects including wave steepening, which can result into the generation of propagating solitary internal waves. The transition from damped linear waves to the formation of solitary internal waves regimes occurs when the dissipative timescale is proportional to the steepening timescale, which gives that

$$\frac{\zeta_o}{h_e} = \frac{\nu T_{\mathrm{V1H1}}}{3H}\left(\frac{\sqrt{\pi/(\nu T_{\mathrm{V1H1}})(1-h_e/H)^2 + 1/\Delta h}}{h_e/H(1-2h_e/H)}\right), \tag{5.5}$$

in which ζ_o is the initial wave amplitude, h_e is the epilimnion thickness, ν is the kinematic viscosity, T_{V1H1} is the fundamental internal seiche period, H is the total water depth, and Δh is the metalimnion thickness.

If the amplitude of the basin-scale internal wave is large and its period long compared to the timescale of supercritical flow, the flow may become supercritical, with Froude number $Fr > 1$. The transition is characterized by hydraulic jumps (bores), which are accompanied by strong vertical mixing. The formation of supercritical flows, that degenerate the basin-scale internal waves into bores, occurs if

$$\frac{\zeta_o}{h_e} > \sqrt{\frac{(1 - h_e/H)^2}{(h_e/H)^3 + (1 - h_e/H)^3}}. \tag{5.6}$$

Large-amplitude internal waves, for which the instability timescale is smaller than the internal wave period, the shear across the thermocline may generate Kelvin-Helmholtz billows, if the local Ri is lower than 0.25. The ratio of the stability timescale to the internal wave period can be expressed as:

$$\frac{\zeta_o}{h_e} > 2\sqrt{\frac{\Delta h}{H}\left(\frac{H}{h_e} - 1\right)}. \tag{5.7}$$

If equations 5.6 and 5.7 are satisfied, both degeneration mechanisms can occur simultaneously, which leads to formation of bores and Kelvin-Helmholtz billows (Figure 39).

Based on field observations, laboratory experiments, numerical and theoretical models, the Wedderburn number has been related for predicting the initial vertical displacement of the thermocline in a two-layer system exposed to a steady wind (THOMPSON, 1980):

$$\zeta_o = k_o \, \frac{h_e}{W}, \tag{5.8}$$

in which $k_o = \mathcal{O}(1)$ is a constant, where often $k_o = 0.5$ (STEVENS; LAWRENCE, 1997).

The amplitude of the basin-scale internal wave (ζ_o, Eq. 5.8), which corresponds to the maximum displacement of the thermocline is related to the maximum displacement of the water surface (initial surface seiche amplitude, η_o, Figure 38):

$$\eta_o = \zeta_o \frac{\Delta\rho}{\rho_h}, \tag{5.9}$$

where $\Delta\rho = \rho_h - \rho_e$, is the difference between the density of the epilimnion (ρ_e) and the density in the hypolimnion (ρ_h).

Eq. 5.8 has been extended to account for total water depth and the effects of the lake boundaries (lake bottom and water surface) (BUENO et al., 2020):

$$\frac{\zeta_o}{h_e} = k_1 \; \exp\left(-\frac{(W_{V1} - k_2)^2}{2f^2}\right), \tag{5.10}$$

in which $k_1 = 0.1$ and $k_2 = 6$ are empirical constants and f is a non-dimensional function of the total water depth H, and epilimnion and hypolimnion thickness (BUENO et al., 2020):

$$f(h_e/H) = g(h_e/H) \; \exp\left\{\frac{h_e/H^2}{0.125}\right\}, \tag{5.11}$$

where $g = -12 \; h_e/H^3 - 15.7 \; h_e/H^2 + 2.8 \; h_e/H + 2.1$ and was determined empirically. The extended equation improves the parameterization of the basin-scale internal waves in cases of $W_{V1} < 5$ (Figure 39b).

Resonance effects can play an important role on the amplitudes of internal seiches if the period of a basin-scale interval wave is similar to that of a periodic wind forcing, e.g. daily variations in wind velocity. Resonance with wind forcing have been also suggested as a facilitator to generate higher amplitude waves and higher vertical modes (MÜNNICH; WÜEST; IMBODEN, 1992; ANTENUCCI; IMBERGER, 2003; BOEGMAN; IVEY, 2012). These effects, however are not accounted for in the above parameterizations.

A parameter that characterizes the vertical mixing events in measured temperature profiles with fast-response thermistors is the Thorpe displacement length D_T (THORPE, 1977):

$$D_T = z_i - z_j, \tag{5.12}$$

in which z_i is the depth of the monotonically decreasing vertical temperature profile and z_j is the depth of the measured water temperature.

It provides indication of periods larger-scale vertical overturns, as they occur in strong billows. Although small-scale temperature inversions resulting from overturning motions are difficult to be resolved due to slow response time of thermistors, their absolute measurement accuracy (critical for most temperature loggers), and coarse vertical distribution of sensors, the Thorpe scale can provide information about the convective mixing observed near the water surface (BRAINERD; GREGG, 1995).

5.3 Methods

5.3.1 Input data processing

The water density is calculated from user-provided time series of water temperature measured at fixed depths using the equation of state for freshwater (CHEN; MILLERO, 1986). The contribution of salinity, suspended particles, and pressure on water density are neglected. This simplification has been used in many studies investigating internal wave activity in thermally stratified lakes and reservoirs (MORTIMER, 1979; VIDAL; RUEDA; CASAMITJANA, 2007; BERNHARDT; KIRILLIN, 2013; GUYENNON et al., 2014).

Based on the vertical profile of mean density, the software divides the water column into different layers. For a two-layer internal wave model, the water column is divided into two layers of constant density, in which the density gradient at the interface between both layers is defined as the thermocline. The thermocline depth is calculated by weighting the magnitudes of the difference between the maximum calculated density change and the adjacent measurements. This method has been described in detailed by Read et al. (2011) and significantly improves the initial guess that the thermocline is located in the middle between of the two sampling depth with the largest density difference. Similarly, based on the temperature gradients between two neighboring thermistors, the program estimates the metalimnion thickness to divide the water column into three distinct layers. These procedures are described in detail in Appendix D.2. For analysis with more than 3 layers, the density profile is divided based on nodes found by the mode decomposition model. For more details see Appendix D.6. The maximum number of layers is corresponds to the number of sampling depths divided by two. For each layer, the average water density is calculated.

Internal seiche period is calculated by solving the modal multi-layer model. The model is presented in details in Appendix D.5. The Interwave Analyzer provides solutions for different vertical and horizontal modes, considering different division of the vertical density profile. Interwave Analyzer also provides a sensitivity analysis to evaluate how the internal wave periods are changing due to the variation of the thickness and water density in the layers during the measured time series. The algorithm computes the deviation of internal wave periods considering variations of $\sqrt{\rho_h/(\rho_h - \rho_e)} = \pm 4$ and $h_e \dot{h}_h / H = \pm 0.1$. Interwave Analyzer also indicates the maximum and minimum variability of layer thickness and water density considering the analyzed data. In addition, the program provides a sensitivity analysis for the user-provided value of metalimnion threshold. This parameter is used to specify the minimum density gradient to define the metalimnion boundaries, used to estimate the three-layer system. Appendix D.6 provides a schematic representation of the metalimnion threshold parameter. The sensitivity analysis of this parameter provides an indication on how this parameter may influence the period of the second vertical mode.

Interwave Analyzer uses two methods of spectral-analysis (Fourier and wavelet transforms) to identify internal wave periods in temperature time series and in time series of isothermal depths. Isothermal depths are determined for specified temperatures by linear interpolation of temperature signals measured at different depths. Power spectral density is estimated using Welch's method (THOMSON; EMERY, 2014). Prior to Fourier analysis and spectral averaging, segments of the time series are weighted by a window function (Hamming, Hanning, Blackman, or Flattop window functions). The segment size can be specified by the user, but can also be calculated automatically according to the fundamental internal wave period estimated by the internal wave model. In this case, the program considers a segment length corresponding to 10 times the V1H1 period for Fourier analysis. This automatic analysis is just recommended to detect internal seiches of the first vertical mode. The overlap percentage between neighbouring segments is defined as 50 % for all window functions. The significance of the spectral peaks is estimated by comparing their amplitude to the mean red noise spectrum estimated from the time series through a qui-square test, with 95% confidence interval (BERNHARDT; KIRILLIN, 2013).

Interwave Analyzer also offers methods to detect coherence and phase shifts of isotherm displacements (cross spectral density of two selected isotherms), which facilitates the identification of higher vertical modes and internal wave resonance with the wind (PANNARD et al., 2011; ANTENUCCI; IMBERGER; SAGGIO, 2000; VIDAL et al., 2005; SAGGIO; IMBERGER, 1998).

A band-pass filter is used in the program to isolate frequency components of variations in isothermal depth. A fourth order Butterworth filter is implemented as a series of second-order filters with transpose direct-form II (SMITH, 2007). The cutoff-frequencies, which define the frequency bandwidth of interest, must be specified by the user. The program also identifies the most energetic fluctuation of the analyzed isotherms. However, depending on the specified isotherms and measurement location, the amplitude provided by the program can be strongly underestimated.

The wavelet transform is used to facilitate analyses of isothermal depth and temperature time series in the time and the frequency domain simultaneously. The procedure is applied according to techniques described by Torrence and Compo (1998). Three options of mother wavelet functions are implemented: Morlet, Paul, and DOG. More details about the calculation procedures used to identify internal waves through spectral and wavelet analysis is presented in Appendix D.7.

Since the period of internal seiche is fetch-dependent, and wind fetch may also vary according to the wind direction, Interwave Analyzer calculates the wind fetch as time-series based on the wind direction and the basin length along this direction. The program calculates the mean wind direction and, based on a user-specified range of directions around this mean value, it identifies the variability of wind fetch for the analyzed period. The maximum and minimum values of the wind-fetch are used to compute a range of internal wave periods.

To facilitate the identification and analyses if internal seiches, all physical indices described in section 5.2.2 are calculated. The Wedderburn number (W, Eq. 5.3) is considered wind fetch-dependent and described as a mean value as well as time series. Previous studies showed, that the consistency of wind direction and speed are crucial for describing the formation of internal seiche (STEVENS; IMBERGER, 1996; VALERIO et al., 2017; GAUDARD et al., 2017). Observations have suggested that the Wedderburn number is underestimated to describe the formation of internal seiche because of variations in wind direction. The program includes a filter for the identification of homogeneous wind events. The filtered values of W implemented in the Interwave Analyzer takes into account the calculated periods of consecutive wind events. Based on wind direction contribution, the software indicates periods of constant wind events, which could be a potential period for internal seiche activity. The Interwave Analyzer identifies wind events based on the wind tolerance angle specified by users. To avoid an influence of temporal resolution of wind measurements, the homogeneous wind events are computed through an convolution based on the internal seiche period (1/8 T_{V1H1}). Based in the same principle, the program also estimates an effective Wedderburn number, which takes into account the wind direction of the wind event (W_{efe}) (GAUDARD et al., 2017):

$$W_{\text{efe}} = \frac{W}{f_{\text{dur}}^2}, \tag{5.13}$$

in which $f_{\text{dur}}^2 = 4T_{\text{wind}}/T_{V1H1}$ is the duration factor. T_{wind} is the duration of homogeneous wind events, T_{V1H1} the fundamental internal wave period, L is the basin length that is aligned with the wind direction, h_e is the epilimnion thickness, and W_{V1} is the non filtered Wedderburn number.

The internal seiche amplitudes are estimated following Bueno et al. (2020) and Spigel and Imberger (1980), the corresponding surface seiche amplitude is computed (Eq. 5.9). Thorpe scales are calculated according to (Eq. 5.12). The most important calculations provided by the Interwave Analyzer are summarized in Table 1.

Output variables	Reference
Mean wind direction	Eq. D.8
Wind stress	Eq. D.2
Friction velocity of the wind	Eq. D.1
Water density	Eq. D.9
Thermocline depth	Eq. D.3
Metalimnion boundaries	Eqs. D.6-D.7
Richardson number	Eq. 5.2
Wedderburn number	Eq. 5.3
Effective Wedderburn number	Eq.5.13
Thorpe scale	Eq.5.12
Burger number	Eq.5.1
Internal wave periods	Eq.D.14
Surface wave amplitude	Eq. 5.9
Internal wave amplitude^1	Eq. 5.10
Internal wave amplitude^2	Eq. 5.8
Regimes of internal wave degeneration	Eqs. 5.5, 5.6, and 5.7
Power spectral density of time-series	Eq. D.17
Coherence analysis	Eq. D.18

Output variables	Reference
Phase lag	Eq. D.19

Table 1 – Output parameters provided by Interwave Analyzer.

5.3.2 Input data and configuration

The Interwave analyzer requires a minimum of four input files, including time-series of water temperature (.tem), wind direction and wind speed (.met). Water surface elevation can be defined as a fixed value or provided as an input file containing a time series of surface elevation, in which a reference level (altitude) must be defined by the user (default value is zero). The temporal resolution of all input parameters are linearly interpolated to match the timing and temporal resolution of the temperature measurements.

The user has the options to define a fixed basin length, or to provide a file with the basin length for a range of directions (.fet). Wind direction is specified as the angle measured relative to true North (positive clockwise) and refers to the direction from which wind is coming from.

The depth of each water temperature sensor is defined in a separate text file (.sen). The program allows users to choose if sensors were anchored at the lake bottom (then depth will be defined as the distance between the sensor and the lake bottom) or if it was attached to a floating buoy (then the depth is defined as the distance between the sensor and the water surface).

All input data files must be tab-delimited ASCII files with a single header line, which must be also tab-delimited with the same number of columns of the file. For more details about the input formats, see the Interwave Analyzer's User Manual (BUENO; LORKE; BLENINGER, 2020).

Additional parameters must be defined by the user in a graphical user interface (GUI). These include the height of the wind measurements (to compute the wind stress, see appendix D.1), basin latitude (to analyze the contribution of Earth rotation on the internal seiche evolution, Eqs. 5.1), and the reference altitude of the basin bottom (a parameter just used for plotting purposes, e.g. to facilitate referencing the water level to sea-level height). In addition, the metalimnion threshold must be specified to define the criterion to divide the system into three distinct layers.

User-adjustable parameters for filtering and spectral analysis include cutoff frequencies for band pass filters (default value is the maximum and minimum internal wave frequency obtained by the multi-layer model considering the fundamental internal seiche), Fourier window function (default window is Hamming) and size (default value is 3 days), as well as the Wavelet mother function (default function is Morlet). An analysis of how these parameters may influence results of the internal wave analysis is provided in section 5.4.1.2.

The setting defined in the GUI can be saved to a file (.set), and be imported for a new run with similar parameter definitions. See the Interwave Analyzer's User Manual for more details (BUENO; LORKE; BLENINGER, 2020).

5.3.3 Overview and program structure

Interwave analyzer is an open-source software investigate the occurrence of internal waves and mixing regimes in thermal-stratified basins implemented in Python. It calculates the physical indices listed in Table

1 ans plots several graphical results.

The program is structured into seven modules (Table 2) including a graphical user interface (GUI). All information provided by the user are transferred to the main module (interwave_analyzer.py), where physical parameters are calculated and analyzed.

Subprogram	Brief Description
GUI_executer.py	Graphic interface
input_package.py	Read the inputs
internal_module.py	Contain all functions
wavelib.py	Wavelet transform definition
modeling_internalwave.py	Internal wave model
graph_package.py	Output layout
warnings.py	Diagnosis warnings

Table 2 – Description of Interwave Analyzer subprograms (modules).

The modeling_internalwave.py module contains a multi-layer hydrostatic linear model with free surface and shallow water assumption, in which it solve problems to the first three vertical modes. In addition, the subprogram also provides a the correction of internal wave periods caused by the Coriolis effect for low-frequency internal waves. All results are passed over to the graph package (graph_package.py), that provides graphical output.

Output is provided as graphs and as text files containing the parameters listed in 1. In addition, the program also provides the *Interwave Analyzer's report*, a document (.pdf) that contains an overview on physical indices and most important graphs. Examples of the Interwave Analyzer's report are presented in the section 5.4 and a full documentation can be found in the Interwave Analyzer's website.

The complete source code of the Interwave Analyzer is available in the repository on GitHub[2], and distributed under MIT license. The executable version (available only for Windows operating system) can be downloaded in the Interwave analyzer website [3].

5.4 Results and discussions

5.4.1 Case Studies

5.4.1.1 Rectangular-shaped box

To demonstrate the capabilities of the Interwave Analyzer in describing the hydrodynamics of thermally stratified water bodies forced by wind, a numerical simulation of an idealized, rectangular shaped basin (4.0 km long, 450 m wide and 15 m deep) was performed with the 3D hydrodynamic model Delft3D-FLOW, which solves the shallow water momentum equations using the hydrostatic assumption (HYDRAULICS, 2003). Delft3D model has been successfully used to describe internal seiche in thermally-stratified lakes (DISSANAYAKE; HOFMANN; PEETERS, 2019), even though, due to the Reynolds-averaged Navier–Stokes

---

[2] *https://github.com/buenorc/interwaveanalyzer*

[3] *https://sites.google.com/view/interwaveanalyzer/interwave-analyzer*

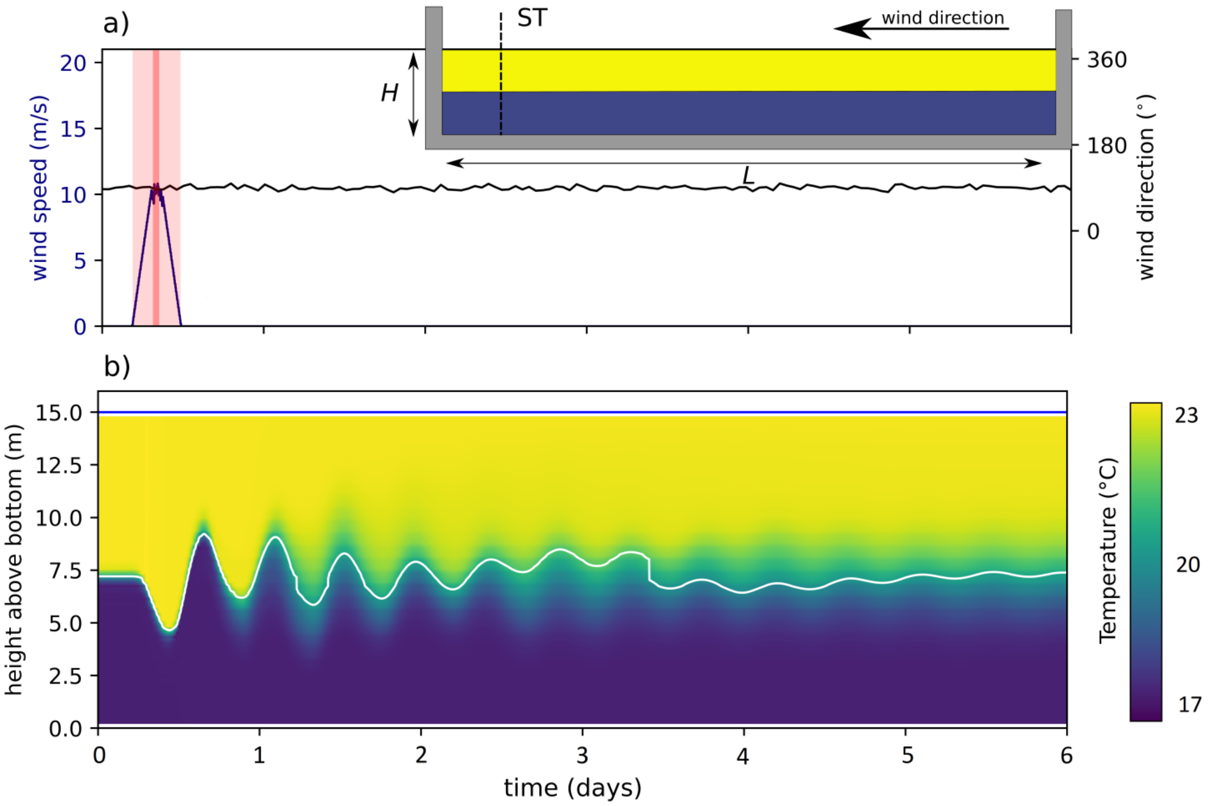

Figure 40 – Results of the numerical simulation of water temperature in an idealized (rectangular) basin in response to a single wind event. a) Time series of wind speed (blue solid line) and wind direction (gray solid line). The dark and light vertical red box indicates the period of maximum and the total duration of the wind event, respectively. The inset figure shows a sketch of the two-layer rectangular tank of $H = 15$ m and $L = 4.5$ km with the initial temperature distribution. ST is the location where temperature time series were analyzed. b) Contour plot of water temperature at station ST. The solid blue and white line represent the water level ($H = 15$ m) and the thermocline, respectively.

approach and the hydrostatic approximation, the model fails to reproduce internal wave breaking and propagating nonlinear internal waves.

The implemented model operated in a horizontal Cartesian grid cells of 30 m × 30 m and 50 fixed vertical layers. Eddy diffusivity and eddy viscosity were calculated using the κ-ε turbulence closure model. The coefficients of background vertical and horizontal viscosity and diffusivity were considered as calibration coefficients and were kept fixed during the simulation. Heat flux at the water surface was neglected. A time step of 0.1 minutes was used to simulate a period of 6 days.

The water level was kept constant along the entire basin with a two-layer temperature stratification as initial condition (23 °C in the epilimnion and 17 °C at hypolimnion). The thermocline was set located at mid depth (Figure 40b). We applied a wind event with a maximum speed of 10 m/s blowing from east to west direction during the first hours of simulation (inset figure from Figure 40a). The wind event lasted for 7 h, and was kept 1.5 h blowing with maximum speed (Figure 40a). The wind event started with zero wind speed and increased linearly with a rate of 3.6 m/s per hour during 2.75 h, and decreasing afterwards with the same rate, simulating a smooth variation of the wind.

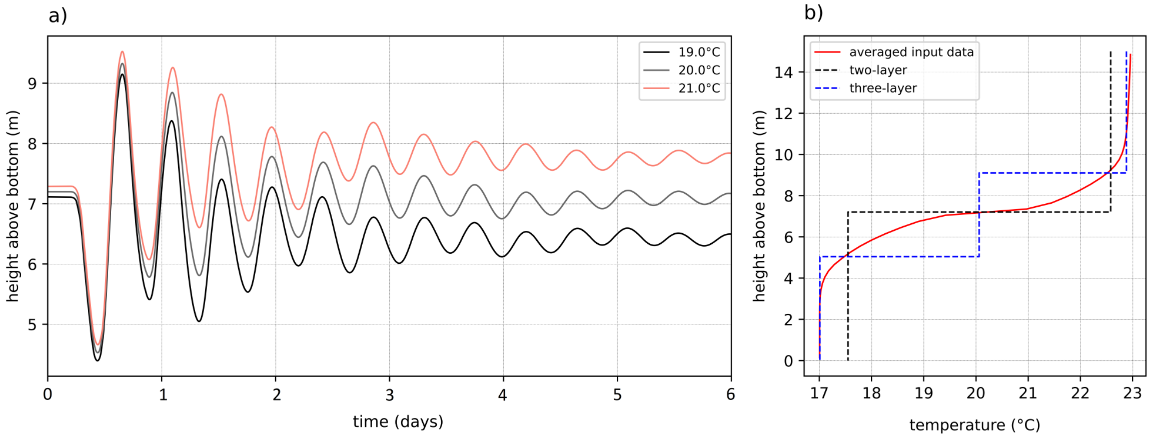

Figure 41 – a) Time series of selected isothermal depths at the sampling point ST in the numerical simulations. b) Temporarily averaged vertical temperature profiles /red line) and the two (black line) and three-layer (blue line) approximation of the temperature profiles used for modal internal wave analysis.

At the analyzed location (ST, Figure 40), the thermocline was displaced downward during the wind event with a maximum vertical displacement of approximately 2.5 m (Fig 40a). As soon as the wind stopped, the thermocline relaxed and periodical vertical displacements with decreasing amplitude were observed during the entire period of the simulation (Fig 40). The temperature oscillation observed over the water column (Figure 40b) are analyzed in terms of the temporal dynamics of isotherms. The vertical displacement of the 20 °C isotherm, which was initially located at mid depth of the reservoir, had an initial amplitude of $\approx$ 2.5 m just after the wind event (Figure 41a). The increased spreading of isotherms, i.e. the increasing thickness of the metalimnion, indicates turbulent diffusion (Figure 41a). The temporarily averaged temperature profile showed substantial deviations from both the two-ayer and three-layer approximations that are used for internal wave analysis (Figure 41b).

Power spectral density of isotherms showed maximum spectral energy at a frequency of 2.72 10^{-5} Hz (10.21 h). The spectral peak is higher than the mean red noise spectrum for the time series at a 95% confidence level, indicating a significant peak (Figure 42a).

The temporal averaged layered profile (Figure 41b) was used to estimate the theoretical periods of different internal wave modes using the multi-layered hydrostatic model for different vertical and horizontal modes, presented in section 5.2.1. The energetic peak observed in the power spectra was close (within 7%) to the theoretical period calculated for the fundamental basin-scale internal wave in a two-layer water column (V1H1, 11 h ± 0.6 h). The estimated variability of the wave period corresponds to the variability in the basin length based on the direction of wind event.

The theoretical estimates of the internal wave periods are based on the temporarily averaged vertical temperature profile approximated by a multilayer structure (Figure 41 b). The actual vertical temperature structure varies over time, which causes variations in internal wave periods. The sensitivity of the multi-layer model to variation in water density and layer thicknesses is illustrated in Figure 42b. The discrepancy of 7% between observed and predicted internal wave period may be explained by the variability of thermal stratification. Since the density difference between the layers is lower for the averaged two-layer structure, the period of the internal wave is overestimated (Figure 42b). Thus, for periods in which thermal stratification changes constantly, the sensitivity analysis may help to identify deviation of theoretical periods of internal

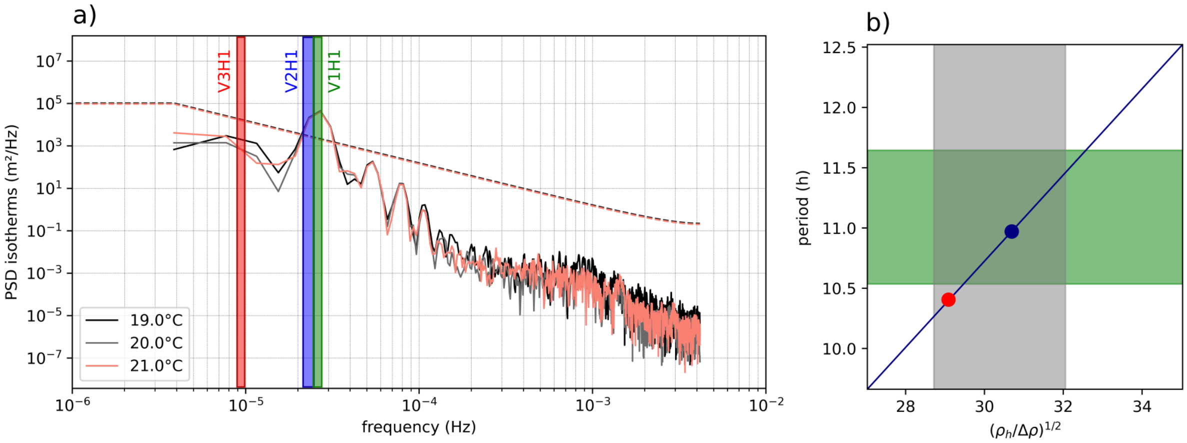

Figure 42 – a) Power spectral density (PSD) of isotherm displacements for the three isotherms shown in Figure 41a. The vertical red, green, and blue bars in the spectrum mark the frequencies of basin-scale internal waves estimated by the multi-layer model for first, second, third vertical mode, respectively. The width of the colored boxes indicate the variability of the estimated internal wave periods based on variations of the basin length that was aligned with the mean wind direction. The dashed lines indicate the mean red noise spectrum for the time series at a 95% confidence level. b) Sensitivity analysis of the multi-layer hydrostatic model to variations in density stratification. ρ_1 and ρ_2 are the mean density in the hypolimnion and epilimnion, respectively, whereas $\Delta\rho = \rho_2 - \rho_1$. The green horizontal bar corresponds to the width of the green bare in a) (caused by variability of wind direction). The gray vertical bar indicates the variability of the density gradient during the analyzed period. Blue and red dots show the average internal wave periods predicted by the internal wave model and estimated from spectral analysis, respectively.

waves.

Based on the Wedderburn number (Eq. 5.3), the program provides a classification according to the thermal stratification conditions of lakes, and indicates periods at which basin-scale internal seiches are more susceptible to be excited. During the analyzed wind event, the Wedderburn number decreased to a minimum value of 1.83 (when the wind is maximal), indicating a regime of high amplitude internal wave activity (Figure 43).

Based on Wedderburn number, layer thickness, and Eq. 5.10, the maximum vertical displacement associated with the wind event was estimated to be around 3.6 m. This theoretical result is slightly higher than the vertical displacement observed in isotherms time-series (Figure 41 and 43b), which has a vertical displacement of approximately 2.2 m. The internal seiche amplitude can be underestimated depending on the longitudinal location of the sampling point, as the maximum amplitudes occur only at the boundaries in a horizontal mode one wave.

The theoretically estimated amplitude of the surface seiche (Eq. 5.9) was 1.60 mm and agree well with amplitudes estimated by the numerical model (1.65 mm). Although the numerical model did not completely resolve the degeneration processes of the basin-scale internal wave, the degeneration regime analysis showed that the internal wave was within two regimes of degeneration: viscous and nonlinear regime (Figure 43b). This analysis indicates that internal waves could be damped by viscosity or degenerate into a train of internal solitary waves.

Based on the analysis of temperature observations made at a single location in the simulated basin, we may conclude that baroclinic effects were responsible for the observed large-scale water motion and that

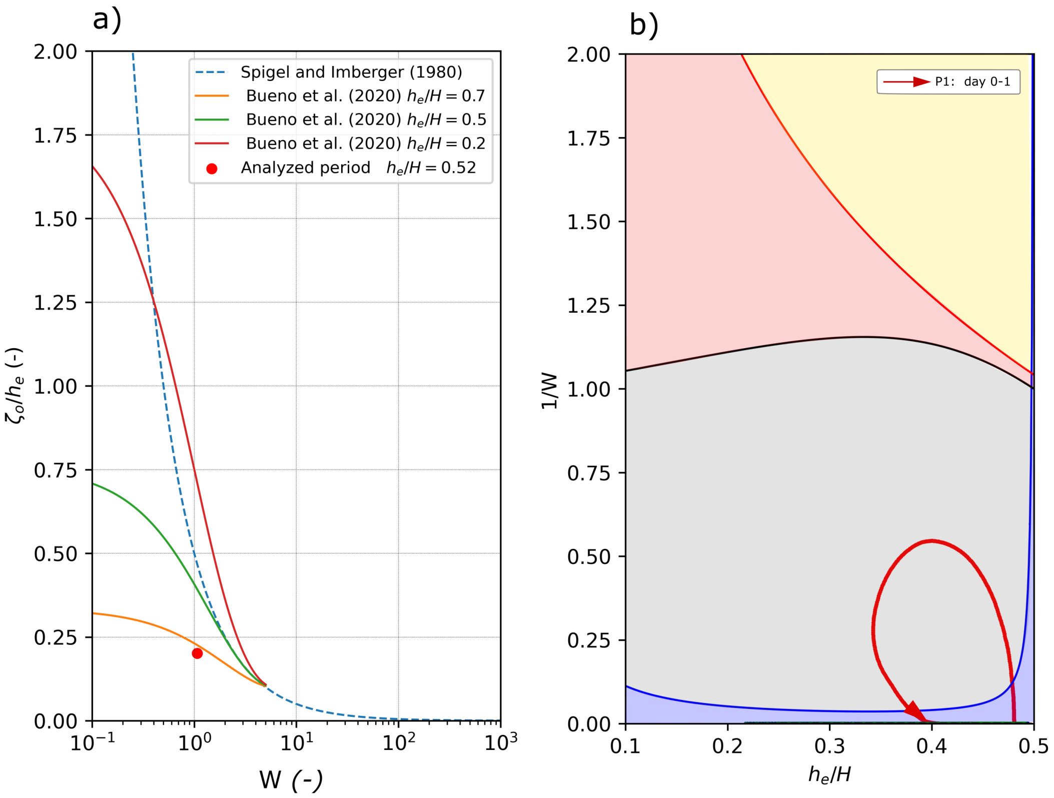

Figure 43 – a) Normalized internal wave amplitude (normalized by the epilimnion thickness (ζ_o/h_e)) versus Wedderburn number W. The blue solid line represents the theoretical formulation defined by Spigel and Imberger (1980), whilst green and yellow represent the empirical parameterization described by equation 5.10. The red dot indicates the maximum observed for the modeled wind event. b) Regime diagram characterizing the degeneration of basin-scale internal waves according to the theoretical classification (HORN; IMBERGER; IVEY, 2001). The variability of h_e/H and W marked by the red arrow refers to the first two days of simulation, which may characterize the degeneration regime of internal wave. The blue region indicates conditions when internal seiche are more susceptible to be damped by viscosity. The range colored in gray indicates a regime where internal waves degenerate into a propagating waves. The red and yellow region characterize regime of degeneration with formation of supercritical flow, and bore and billows, respectively.

a fundamental mode internal seiche was excited during the wind event. This conclusion is confirmed by the spatially-resolved thermal structure provided by the three-dimensional numerical model (Figure 44). The shear stress exerted by the wind pushed the water surface toward the leeward shore, resulting in a surface displacement. Due to the increase of the horizontal pressure, the hypolimnion was accelerated toward the upwind direction, characterizing a out-of-phase response between the thermocline and the water surface. The following oscillatory motion matches with theoretical periods identified by the Interwave Analyzer (Figure 44).

Other variables and physical indices calculated by the Interwave Analyzer are available in the final report. It should be noted, that the numerical model (Delft3D) is based on Reynolds averaged Navier-Stokes equations and cannot accurately describe turbulent fluctuations and individual overturns, as they are estimated by the Thorpe scale analysis.

The hypothetical reservoir simulated in this case study was located near the equator (latitude of 5° N), where internal waves are only marginally affected by Earth's rotation (Burger number $Bu = 11 \gg 1$).

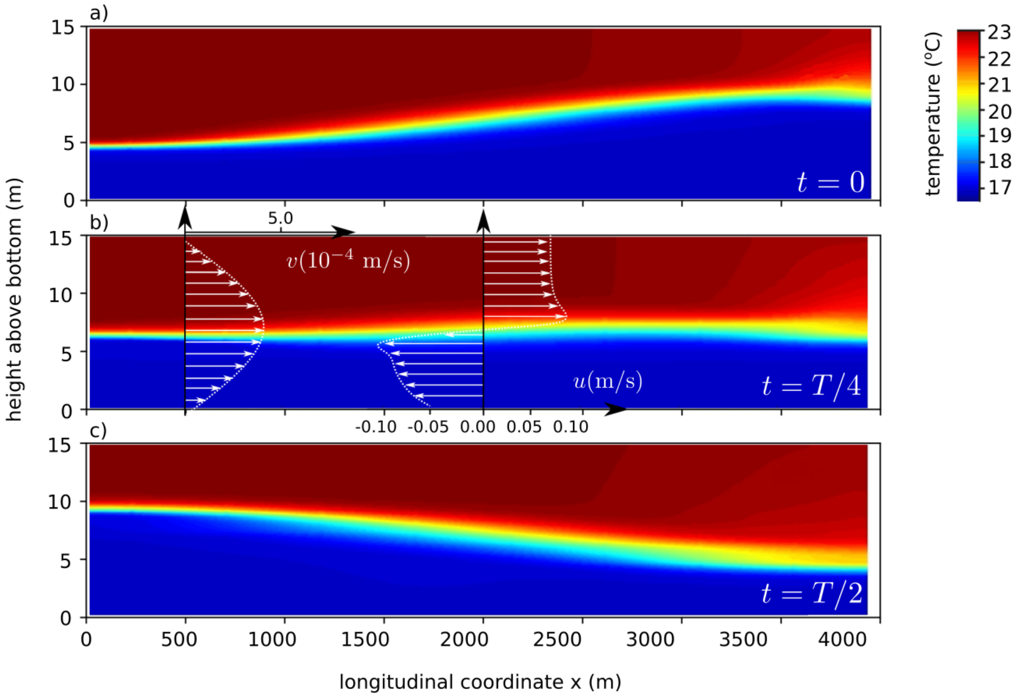

Figure 44 – Overview of the water temperature distribution along the centerline of the rectangular basin for three selected times: a) right after the wind event (t=0), b) $t = T_{V1H1}/4$, and c) $t = T_{V1H1}/2$, in which T_{V1H1} is the theoretical period of the fundamental basin-scale internal wave. The vertical (v) and horizontal (u) velocity profiles are shown at different locations near the basin shore and in the center of the reservoir ($x \approx 2000$ m), respectively.

Considering similar stratification and geometrical conditions, we tested at which latitude the Interwave Analyzer would indicate that Earth rotation would start to play an important role on the simulated internal wave activity. Internal waves would start to be influenced by Earth rotation just for latitude higher than 70° N or lower than $-70°$ S, where $Bu \approx 1$. Note that this is valid only for the specific conditions considered here. For a smaller density gradient, the period of the internal seiche would be higher, and the Earth rotation effect would become important already at lower latitudes.

5.4.1.2 Vossoroca Reservoir

In this section we apply the Interwave Analyzer to observations in a subtropical reservoir. The main goal is to demonstrate additional feature and to describe the influence of additional parameters, that have not been presented in the previous case study.

Vossoroca reservoir is a monomictic reservoir with an irregular, dendritic shape, located in south Brazil (25° 49' 31" S, 49° 3' 60" W). It has a maximum depth of 17 m and a volume of 35.7 10^6 m^3 (See (BUENO, 2019) for additional details). Water temperature was recorded every 15 min during April 2013 in the deepest region of the reservoir using seven thermistors (accuracy: ±0.1 °C). The sensors were deployed at water depths of 1, 3, 5, 7, 9, and 11 m. An additional sensor was anchored 1 m above the reservoir bottom (Figure 45b). Wind speed and direction were measured with a Young wind monitor (accuracy: ±2° and ±0.3 m/s) (Figure 45a). The meteorological station was positioned 10 m above the water surface and data was recorded at 30 min intervals. Water level was sampled every 15 min.

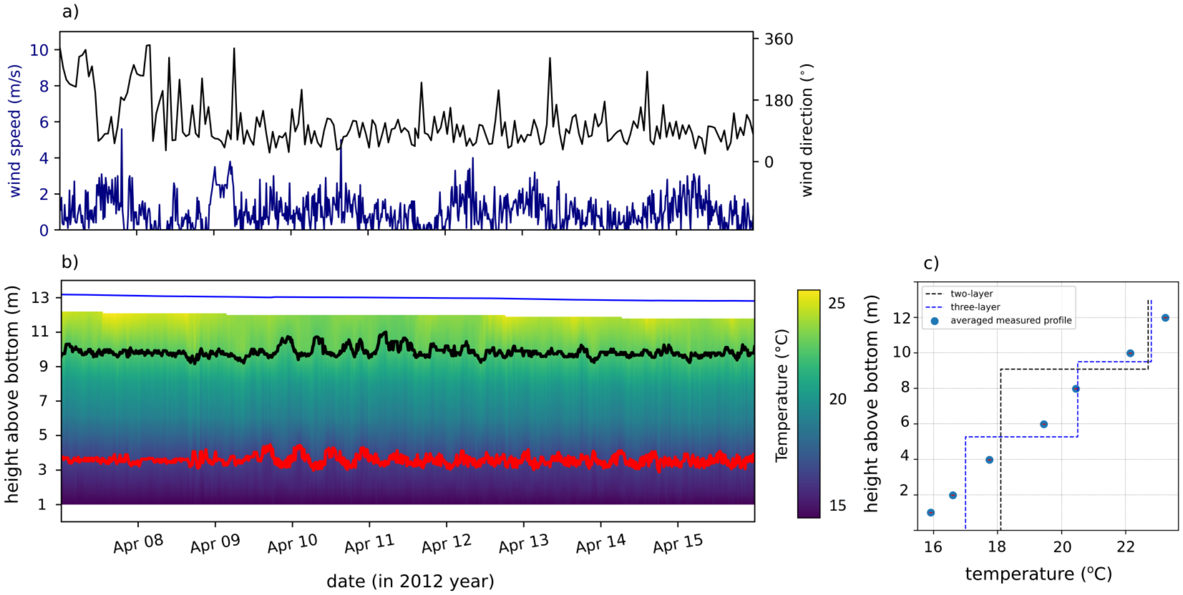

Figure 45 – Measurements at Vossoroca reservoir: a) Wind speed and direction. b) Water temperature measured by a thermistor chain. The solid blue line represents the water surface. black and red lines represent the isotherms of 22 °C and 17.5 °C, respectively. The altitude of reference for reservoir bottom is 799 m. c) Temperature profile estimated by the software for a two- and three-layer approximations. The blue dots show the mean temperature measured by the 7 thermistors deployed in the reservoir.

In contrast to the hypothetical case analyzed in section 5.4.1.1, where a two-layer system was forced by a single wind event, in real data it is difficult to distinguish individual wind events and to relate them to internal wave activity. To overcome the difficulty to classify wind events that could favor the excitation of internal seiche, the analysis based on Wedderburn number is useful to identify periods of potential baroclinic activity (Figure 46). Although the classification of Spigel and Imberger (1980) indicate many periods of potential internal wave activity, homogeneous wind events with $W_{V1} < 20$ were mainly observed on a single day (April 9, Figure 46).

The differences between homogeneous wind events (Figure 46 illustrate the influence of the wind direction contribution parameter on the identification of such events. The parameter must be defined by the user (Default is ± 20 °C) and indicates the deviation of mean wind direction that may contribute to excite internal seiches. The wind speed is just added into a homogeneous wind event, if the criteria of internal wave formation proposed by Spigel and Imberger (1980) is satisfied. The increase of wind direction contribution leads to longer homogeneous wind events. The choice of the value for the wind direction contribution also affects the calculation of the Wedderburn number, since it influences the lake length that is aligned with the wind directions. Varying the angle of the wind direction contribution from ± 5° to ± 40°, we observed an average lake length of 2625 m ± 81 m, corresponding to a variation of the mean Wedderburn number (that falls into the internal wave regime) between 46 and 47. Compared to variations of W_{V1} between wind events, it represents a small difference, since W_{V1} can be reduced more than 10 times after a strong wind event. The period of internal wave excitation during the beginning of April 9 reduced W_{V1} by 97 %, a variation much larger than the change associated with the uncertainty of the longitudinal extend of the basin.

Since the wind direction contribution parameter also influences the computed wind-fetch, the internal wave period estimated by the hydrostatic internal seiche model also may present variation of the wave periods

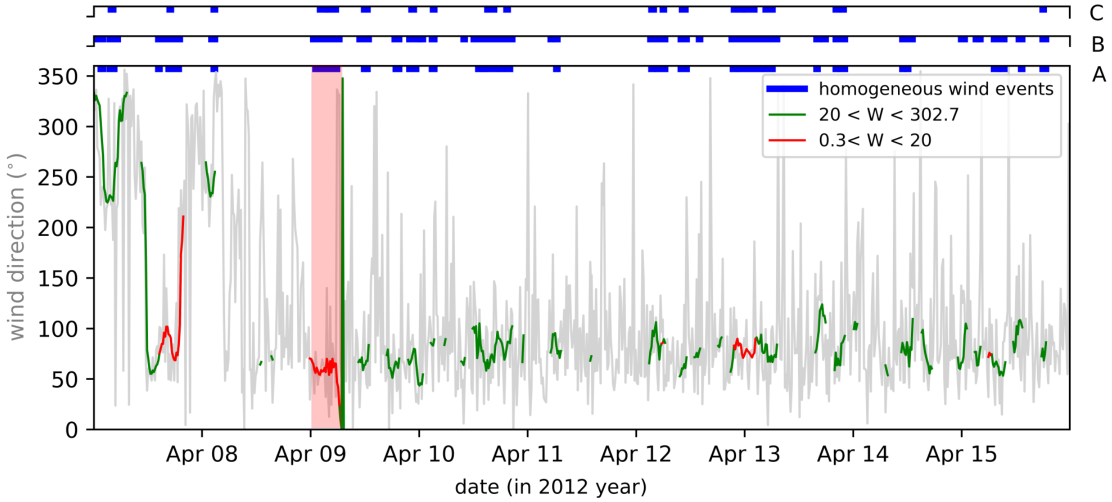

Figure 46 – Time series of wind direction at Vossoroca reservoir (grey line). The blue bars above the graph indicates periods of constant wind directions according to three different angles of wind direction contribution: A: ± 20°, B: ± 40°, and C: ± 5°. Periods marked by green and red color correspond to criteria suggesting internal wave generation. The green line represents the more flexible criteria often described by mathematical results from Spigel and Imberger (1980). The red line indicates a more restrictive result, which fall into regime of internal wave described by Spigel and Imberger (1980) and often observed from field data reported in the wide literature. The value of W_{V1} displayed in the label indicates an average for the entire period, and just illustrates the mean value of the adopted criteria. The vertical red bar indicates the period in which the internal wave was generated.

due to the wind-fetch dependency (Fig. 47).

The power spectrum of the isotherms showed significant peaks at frequencies corresponding to period of 10.28 h. The analysis was been conducted with two different Fourier window functions: Flattop (Fig. 47a) and Hamming (Fig. 47b and c). Although the Flattop has a broader shape, both windows presented a reliable estimation of the oscillatory response of isotherms with exception of Fig. 47c, which has poor frequency and spectral resolution due to the length of the window size chosen. To analyze the influence of window size on spectral results, we applied window size of 3 (Fig. 47a and b) and 1 (Fig. 47c), corresponding to frequency resolutions of 2.77 10^{-3} and 1.38 10^{-3} 1.16 10^{-5} Hz, respectively.

To analyze more in detail high-frequency spectral variance, users can reduce the window size to average more numbers of segments. Note that this could lead to an energy loss in low-frequency band depending on data length (Fig. 47c). In general, a sufficient spectral resolution may be obtained with a window size of at least 7 times the analyzed oscillatory response. The window can be choose according to the expected internal wave frequencies excited in the system, however, if the wave characteristics are not known, a first candidate can be the Hanning window function, which has good balance between spectral energy and frequency accuracy.

The results from the Interwave Analyzer suggest that the predominant response of the reservoir to variable wind forcing is the excitation of an internal wave of the second vertical mode (V2H1) (Fig. 47). To better analyze the isotherm displacements associated with higher vertical modes, Interwave analyzer provides analysis of coherence and phase-shift between specified isotherms (Fig. 48). The coherence analysis between 20 °C and 17.5 °C isotherms indicates high coherence (0.6) near the period of the internal wave, with a phase difference of 147 °. The small deviation from the executed phase difference of 180 ° could be

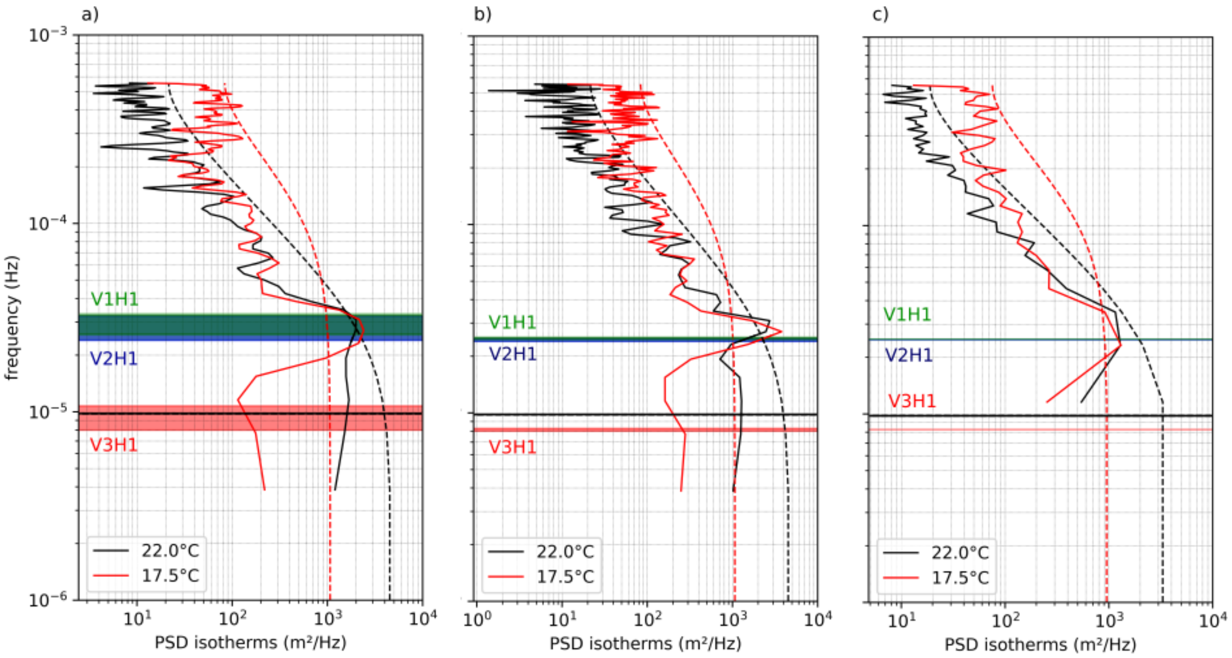

Figure 47 – Power spectral density (PSD) of isotherm displacements for three different segment sizes for the Fourier transform: a) 4 days (Flattop window function), b) 4 days (Hamming window function), and c) 1.5 days (Hamming window function). The theoretical period of internal waves are marked by horizontal bars: mode V1H1 (green), V2H1 (red), and V3H1 (blue). The theoretical period threshold (height of the horizontal bars) are plotted for three different wind direction contribution parameter, which are estimated through the maximum and minimum length of the lake that is aligned with the wind direction: a) ± 40°, b) ± 20°, and c) ± 10°. The black horizontal solid lines indicate the inertial frequency and the dashed lines shows the mean red noise spectrum for each time series at a 95% confidence level.

related to the coarse spectral resolution resulting from the short period of baroclinic activity. The counter-cyclic displacement of the two isotherms, which is indicative of an internal wave of higher vertical mode, is illustrated in Fig. 48.

Based on the temperature profiles, the Interwave Analyzer approximated the vertical temperature profile by two- and three-layers (Fig. 48b) to obtain the internal wave periods associated with different modes. Based on Spigel and Imberger (1980), the Interwave Analyzer indicates that the reservoir is under two regimes of lake mixing during the period of analysis: periods of internal seiche dominance is interspersed with periods of strong stability, which may not support large vertical displacement of isotherms. Based on Horn, Imberger and Ivey (1998), the program also indicates that the excited internal seiche is more susceptible to be degenerated into a train of solitary internal waves. The relatively long sampling interval of thermistors (15 min) did not allow for resolving high-frequency internal waves, thus the suggested degeneration mechanism could not be confirmed for this data set. The Thorpe scale analysis did not identify temperature inversion, except for near the water surface during convective mixing. The lack of vertical overturns associated with internal wave breaking, however,could be related to the coarse vertical and temporal resolution of the thermistors. The final report generated by the Interwave Analyzer for the analyzed period is provided in additional material.

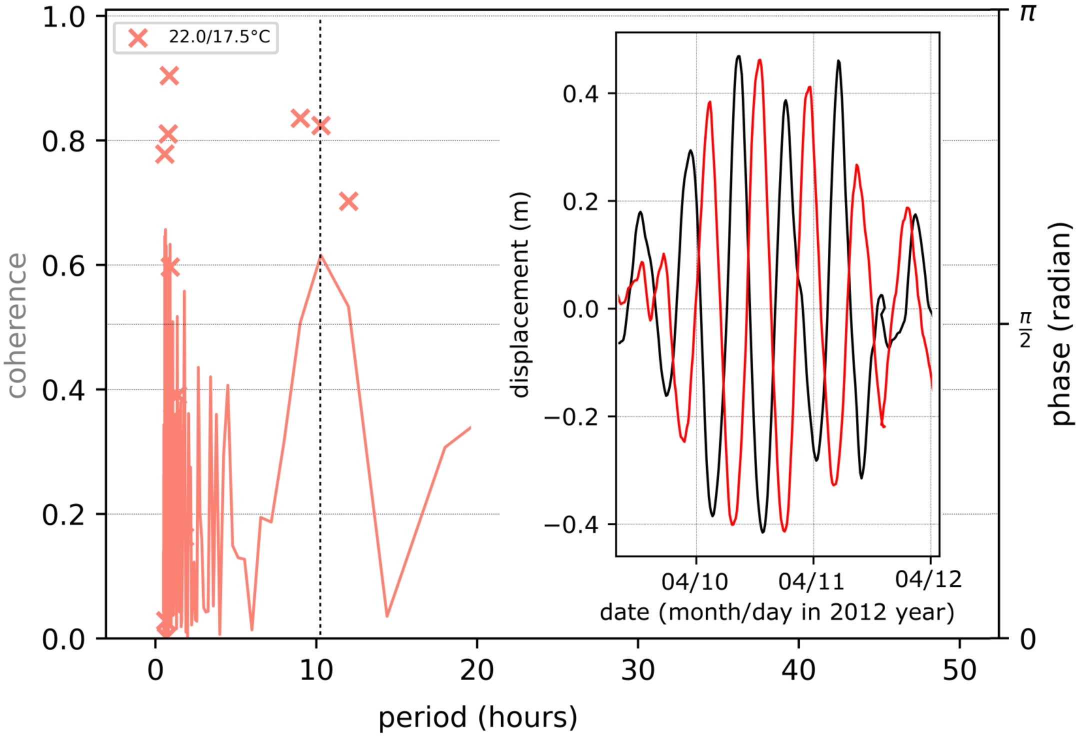

Figure 48 – Coherence (solid line) and phase-shift (cross symbols) of two selected isotherms (17.5 °C and 21 °C) during the period April 9 to 12 (2012).The vertical black dashed line indicates the period of the internal wave detected by spectral analysis (Fig 47). The embedded graph shows the opposing displacement of both isotherms in response to a wind event. The time series of isothermal depth were band-pass filtered with cutoff frequencies of 1/10 and 1/9 h^{-1}.

5.4.2 Software availability and performance

The Interwave Analyzer is free to download [4] under the MIT General Public Licence. The algorithm has been implemented in Python scripting language, and is available in our repository[5]. A executable version of the code is available for Windows operating systems, which requires 0.72 GB of disk space and does not require installation of additional packages. This version may be downloaded in Interwave Analyzer's website. To run the python scripts, the algorithm requires a minimum version number of Python 3.7 and the packages: Numpy 1.16.3, Datetime 4.0.1, Reportlab 3.5.19, Scipy 1.2.1, Nitime 0.7, Matplotlib 3.1.0, and tk (tkinter) 8.6.8, or compatibles versions. For anaconda users (Anaconda Software Distribution, 2016), the only packages that need to be installed are Nitime and Reportlab. In Appendix E, we provide a step-by-step guide on how to install Interwave Analyzer. The pre-compiled version can be obtained in the Interwave Analyzer website.

The Interwave Analyzer for the case studies were ran on an Intel(R) Core(TM) i7-1065G7 CPU 1.30 GHz Processor with 32 GB of RAM. We used a version number of Python 3.7.6 bundled with Anaconda 3.0 (running the program in the Ipython console version 7.16.1). The analysis of the rectangular-shaped basin, presented in section 5.4.1.1, analyzed 5 days of simulation with a temporal resolution of 1 min and 50 layers, and took 5 min to analyze and generate the output data.

---

[4] https://sites.google.com/view/interwaveanalyzer/interwave-analyzer

[5] https://github.com/buenorc/interwaveanalyzer

For field data from Vossoroca reservoir, the program took a total of 4 min to analyze a period of 9 days with 15 min time resolution. The program loaded 16 MB of data, including the time-series files (.tem, .met, .niv, .sen). The program provided 16 MB of results including graphs/figures and one report. Initially we ran the script directly in the Anaconda distribution, the processing took less than 2 min. For the same configuration, we also tested the executable version, which took approximately 1 min to complete. Other tests were ran to identify the program performance for larger data sets. For an analysis of two and three months of data recorded from Vossoroca reservoir, the program took ≈ 27 min and ≈ 1 h45 min, respectively.

5.5 Conclusion

A open software tool with an intuitive graphical user interface for investigating internal waves in lakes and reservoir has been presented. The Interwave Analyzer provides a set of tools for estimating physical indices from time series of water temperature and wind velocity. The analysis reveals information about internal seiche formation, including higher vertical modes, wind-wave resonance, internal wave amplitude, internal seiche degeneration, lake mixing, Wedderburn number, including an effective Wedderburn number, which is filtered by the wind direction. Users without access to a Python interpreter can also use the software through a pre-compiled version (.exe), which requires only the input files for the analysis. We demonstrated potential applications of the Interwave Analyzer as a post-processing tool for numerical simulations and for analyzing field measurements. The Interwave Analyzer has been designed to increase the accessibility to state of the art theoretical and empirical knowledge on physical limnology. The analysis results can make important contributions to interdisciplinary studies, analyzing linkages between internal wave dynamics and water quality or biogeochemical cycling in aquatic ecosystems.

6 Discussion

To answer the proposed research question, five mechanisms that could contribute to inhibiting or accelerating the dissipation of basin-scale internal waves in thermally stratified lakes were investigated using numerical models and field measurements: (1) the mixing mechanism generated at the wave crest due to the destabilization of miscible layers (Fig. 49a), (2) the increase in turbulence rates due to the interaction between internal waves and reservoir bends (Fig. 49d), (3) the energy dissipation due to the slope bottom (Fig. 49 e), (4) the influence on the energy transference between the wind and the internal wave due to the stratification profile (Fig. 49c), and (5) the increase of turbulence rates due to the interaction of internal seiche with the surface boundary layer (Fig. 49b).

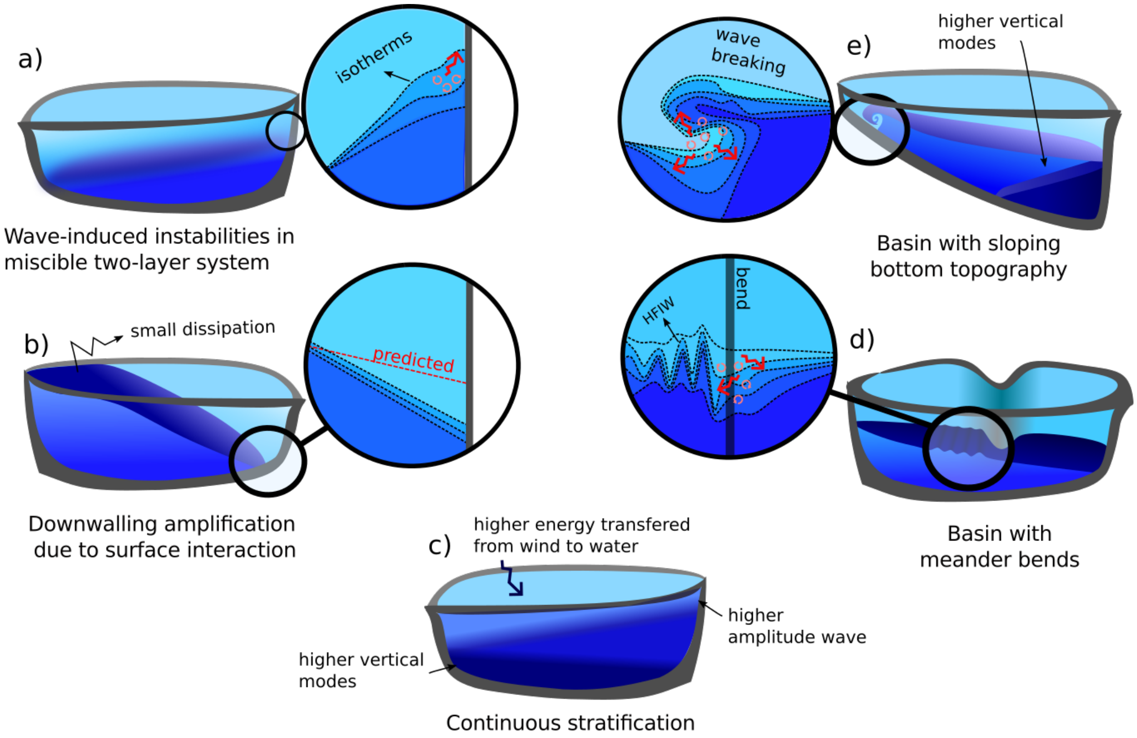
a)
isotherms
Wave-induced instabilities in miscible two-layer system
wave breaking
e)
higher vertical modes
Basin with sloping bottom topography
b)
small dissipation
predicted
Downwalling amplification due to surface interaction
HFIW
bend
d)
Basin with meander bends
c)
higher energy transfered from wind to water
higher amplitude wave
higher vertical modes
Continuous stratification

Figure 49 – Summary of the main findings related to the mechanism of wave dissipation observed during upwelling events and internal seiche activity. Explanations are provided in the text.

This chapter brings together all the findings of individual manuscripts, presenting their contributions to reject or retain the hypotheses raised in chapter 1.1. Furthermore, we speculate on the significance and biogeochemical implications of each analyzed mechanism, highlighting the shortcomings of the study and how to overcome them in future analysis.

6.1 Internal seiche generation and detection

This thesis shows that 1.0 to 3.0% of the wind energy that crosses the water surface is responsible for the excitation of basin-scale internal waves (Chapter 4). Wind introduces kinetic energy to the water surface, and momentum transference pushes a volume of water to the leeward shore, resulting in surface displacement. If the wind event persists for a sufficient time, part of the energy crosses the surface boundary layer and is responsible for generating upwelling events in the interior of the stratified layers. Upwelling triggers the evolution of internal seiche, which is often detected by combining spectral analysis, mathematical models, and derived indices to describe and characterize the excitation of internal waves and lake-mixing regimes.

For the internal waves generated and analyzed in the chapters 3 and 4, the main modes of internal waves have been detected using the *Interwave Analyzer* software, a tool developed to facilitate a consistent methodology for the analysis of internal waves in thermally stratified lakes and reservoirs (Chapter 5). The *Interwave Analyzer* has been developed to identify internal waves with different vertical modes, providing Fourier and wavelet spectral analysis of different isotherms. The software also provides theoretical wave periods for different internal seiche modes estimated by multilayer models (MÜNNICH, 1996). Combined with these analyses, the software also provides theoretical values, such as the Wedderburn number (STEVENS; LAWRENCE, 1997; SHINTANI et al., 2010) and the Richardson number (SPIGEL; IMBERGER, 1980), which are dimensionless numbers derived from the governing equations of motion often used to describe lake mixing regimes (SPIGEL; IMBERGER, 1980) and internal seiche degeneration (HORN; IMBERGER; IVEY, 1998).

Interwave Analyzer facilitates the costly and time-consuming effort to process and analyze internal waves, combining a consistent and universal technique with theoretical results from the wide literature. The tool helps to draw links between internal seiche motion and biogeochemical cycle, even for those without special knowledge in fluid dynamics. In this study, software was used to investigate the wind-induced thermal response of three different thermally stratified basins (Vossoroca reservoir, Harp Lake, and Passaúna reservoir) and of all simulated scenarios. Although internal seiche are susceptible to persist for a long time even after the wind stops, many dissipative mechanisms can contribute to its dissipation, and a couple of them have been investigated in this study (Fig. 2).

6.1.1 Internal seiche destabilization due to wave interaction on slopping boundaries

Interactions of internal waves on gentle sloping boundaries increase the dissipation of turbulent energy at the bottom boundary layer during upwelling events (Fig. 49e), contributing to inhibit the generation of internal seiche or strongly accelerating the decay of wave energy in reservoirs and lakes with a gentle sloping bed. Our observation suggests that this interaction is the dominant contributor to inhibiting internal seiche generation in the Passaúna reservoir (Chapter 4), supporting our hypothesis (**H.1**). According to our results, wind-induced upwelling events in the Passaúna reservoir are damped after the first interaction with the sloping bed, favoring the formation of a hot spot of vertical mixing near the lakeshore.

Numerical simulations and theoretical values from the Passaúna reservoir suggest two possible mechanisms to explain the strong internal seiche damping due to the interaction with the sloped bed, in which all are related to the gentle sloped bottom of the Passaúna reservoir (0.095°): (1) internal wave breaking mechanisms due to the destabilization of the bottom boundary layer (LORKE, 2007; COSSU; WELLS, 2013); and (2) subcritical topography that favors the formation of internal wave attractors, contributing to wave dissipation near the lakeshore (PILLET; MAAS; DAUXOIS, 2019). Although the generation of wave attractors can lead to an increase in dissipative rates, this mechanism is often triggered by forcing frequencies (HENDERSON; DEEMER, 2012). More studies are needed to investigate separately the contribution of energy dissipation due to internal wave breaking and wave attractors in thermally stratified lakes and reservoirs.

Although our study reveals that the slope boundary is the main mechanism to inhibit internal seiche formation in the Passaúna reservoir and the results are expected to be representative of most shallow small to medium reservoirs and lakes with a sloped bed around 0.1°, more studies are needed to investigate this effect more thoroughly in a systematic way, analyzing how internal seiche dissipation occurs for different sloping beds.

Higher dissipation rates near a gentle slope boundary can affect the biogeochemical cycle, enhancing vertical and horizontal fluxes of nutrients contained in sediment and promoting chlorophyll growth near the littoral zone (IMBERGER; PATTERSON, 1989; MACINTYRE et al., 1999). Furthermore, mixing conditions can promote mussel growth (CHOWDHURY; WELLS; HOWELL, 2016), green algae, and diatoms (LOFTON et al., 2019) in thermally stratified lakes. Although this hot spot of vertical mixing has not been investigated through field measurements in the Passaúna reservoir, other studies have observed higher levels of turbulence due to destabilization of upwelling events (LORKE, 2007; COSSU; WELLS, 2013). Further studies should conduct field measurements in the Passaúna reservoir to investigate dissipation rates along the littoral zone, correlating wave energy and turbulent energy dissipation to prove the existence of a hot spot of vertical mixing near the lakeshore induced by upwelling and downwelling events and the influence on the biogeochemical cycle (COSSU; WELLS, 2013; LORKE; UMLAUF; MOHRHOLZ, 2008; LORRAI et al., 2011).

6.1.2 Self-induced mixing during upwelling event

Even in a rectangular shaped-box tank, numerical simulations in a miscible multilayer system show surprisingly a decrease in the magnitude of the upwelling, especially when $W < 2$ (Chapter 3). Unlike the strong energy dissipation observed due to the interaction of internal waves on a gentle lake bottom slope (Chapter 4), this mixing mechanism occurs due to shear velocity as a source of turbulent kinetic energy available for mixing during upwelling events, which attenuates slightly the internal seiche amplitude (Fig. 49a). The linear W-based classification (SPIGEL; IMBERGER, 1980) overestimated the initial internal seiche amplitude for all simulations performed in rectangular shaped-box tanks with $W < 2$ (Sections 3, 5, and 4).

Although this study demonstrated that this effect reduces the amplitude of internal waves (Chapter 3), the vertical mixing mechanism is too weak to inhibit the generation of basin-scale internal waves in lakes and reservoirs (Fig. 25, chapter 3) compared to the increase of dissipation rates due to the gentle sloping bottom (Chapter 4). The damping effect due to shear instabilities should be observed in most lakes and reservoirs, except for those with a gentle slope bottom, in which the mechanism of bottom boundary layer destabilization due to the sloped bed should overcome the effects of shear instabilities for a period of $W \lesssim 3$.

This source of turbulent kinetic energy available for mixing attenuates the wave amplitude due to the increase of vertical mixing near steep slopes (Chapter 3), but may have a minor influence on biogeochemical cycling in reservoirs with very gentle slope gradients, where we would expect dominance of vertical mixing promoted by the interaction of internal seiche with sloping boundaries (Chapter 4). Unlike a gentle lake bottom slope, in steep bottom topography, the flow reflects in the boundary without a significant increase of dissipation rate, and consequently, the lake-scale circulations may have a stronger influence on the biogeochemical cycle near the lakeshore. Vertical displacement induced by internal seiches can promote strong vertical variability of temperature (Chapter 3), leading to pronounced spatio-temporal oxycline dynamics (CORMAN et al., 2010) with major implications for processes at the sediment–water interface (VALERIO et al., 2019). In Lake Iseo, the internal waves induced fluctuations in oxygen concentration between 0 and 3 mg/l, leading to 4 days of oxygen depletion in surface waters (VALERIO et al., 2019). Furthermore, observations indicate that wave-induced vertical movements can cause a steep displacement in phytoplankton communities (HINGSAMER; PEETERS; HOFMANN, 2014), and also influence light availability for photosynthetic microorganisms (EVANS; MACINTYRE; KLING, 2008).

6.1.3 Internal wave disintegration due to reservoir bends

Morphology has been identified as a secondary mechanism that contributes to internal seiche damping (Chapter 4). This study suggests that interactions between the internal seiche and reservoir boundaries promote shear instability along the meander bends and accelerate energy transference from basin-scale internal wave to higher frequency flow variations, generating high-frequency internal waves from reservoir bends (Fig. 49d), corroborating our hypothesis (**H.2**).

We observed that lateral shear is significantly lower than the increase in dissipation rates caused by the interaction between internal waves and lake bathymetry (sloping bottom) in the Passaúna reservoir, but it is still an important mechanism for extracting energy from basin-scale flows by promoting local mixing and high-frequency internal waves.

Although a significant part of the energy of high-frequency internal waves can be driven to the lakeshore (LORKE, 2007), propagating internal waves are susceptible to dissipate their energy within the layer interior due to shear instabilities (BOEGMAN et al., 2003). High-frequency internal waves lead to a significant increase in turbulence and mixing around the metalimnion in the offshore zones (PREUSSE; PEETERS; LORKE, 2010), which may induce vertical fluxes in the lake interior, driving nutrients to the epilimnion layer and improving the generation of plankton patchiness (MACKAS; DENMAN; ABBOTT, 1985). Furthermore, since part of the energy is dissipated into the stratified lake interior, less energy is available to generate mixing near littoral zones and a lower basin-scale internal wave amplitude could be expected.

Although we have observed that morphology acts as a secondary mechanism to dissipate internal seiches in the Passaúna reservoir (half of the dissipation observed in the case with a gentle sloping bed), a systematic study is needed to describe how different morphologies can contribute to the generation of higher-frequency flow variations and how this can influence the magnitude of upwelling events and vertical mixing near the lake shore. Although the actual numbers presented in this study are site-specific, we suggest that, regardless of the reservoir bends, bathymetry is the main contributor to inhibiting internal seiche generation because stronger reservoir bends could favor internal seiche formation with higher horizontal modes, in which each side arm could support its generation (IMAM et al., 2020).

6.1.4 Effects of stratification profile on the internal seiche generation

Surprisingly, contradicting the initial hypothesis (**H.4**), this study suggests that stratification profiles are not responsible for inhibiting the occurrence of internal seiches in thermally stratified lakes. The results show that the nearly linear stratification of the Passaúna reservoir was not responsible for preventing the generation of internal seiches, but it facilitates the transfer of energy from the wind to the water, promoting the amplitude of internal seiches and the formation of internal seiches with higher vertical modes (Fig. 49c). Numerical simulations indicate that a higher amount of energy is transferred from the wind to the internal seiche for an increasing deviation of the stratification from a two-layer structure (30% higher), which may be caused by attenuation of the wind energy lost in the surface boundary layer.

The study showed that the W-based classification is suitable for application for non-ideal stratification in order to predict the occurrence of internal seiches, although the generation of higher vertical modes (Chapter 4) and the wave amplitude (Chapter 3) cannot be revealed. In the case of the higher vertical mode, the biogeochemical cycle will be altered in a different way compared to the evolution of the fundamental internal seiche and the parameterization proposed in chapter 3 could not be applied to estimate the wave amplitude, only to predict the occurrence of internal seiche.

6.1.5 Effect of the interaction between internal seiche and water surface on internal seiche generation

Internal waves formed in lakes with shallow epilimnion are susceptible to strong surface temperature drops due to the thermocline breaking the surface, in which the hypolimnion water may occupy a large portion of the lake surface (Fig. 49b). On the opposite side of the lake, the downwelling mechanism erodes the thermocline, shortening the effective internal seiche fetch. The additional thermocline erosion is proportional to the horizontal distance that the hypolimnetic volume occupies the water surface, refuting the initial hypothesis (**H.5**) that the interaction between the thermocline and the turbulent surface boundary layer could promote higher turbulence rates that could inhibit or reduce the magnitude of internal waves.

This study showed that due to interaction with the surface of the water, internal waves can erode the thermocline to much deeper regions than the magnitude predicted by the W-based classification (Chapter 3, Fig. 24b). This effect may transport oxygen-rich surface water to the deeper part of the water column, amplifying the biogeochemical effects described above as a result of the upwelling and downwelling mechanisms.

6.2 Research Limitation and recommendation for future investigations

All simulations were performed with a hydrostatic model based on the Reynolds-averaged Navier-Stokes equations (RANS) concept, which averages all flow fluctuations and model the influence of turbulent fluctuation on mean flow by a turbulence model. In simulated scenarios with measured data, such as those presented in Chapter 4, a manual calibration procedure was adopted by adjusting the numerical parameters mentioned in the Appendix K to reduce the mean absolute error of the water temperature (ISHIKAWA et al., 2021). A similar procedure was used for hypothetical scenarios created in the rectangular-shaped box tank carried out in Chapter 3. However, unlike the calibration performed in the simulations of the Passaúna reservoir, only the bottom friction was adjusted to generate turbulent dissipation rates comparable to those found in lakes of similar size.

Although RANS simulations have been extensively applied to investigate the hydrodynamics of stratified lakes (ISHIKAWA et al., 2021; DISSANAYAKE; HOFMANN; PEETERS, 2019), including the largest majority of studies involving internal waves in lakes and reservoirs (BOCANIOV et al., 2014; MARTI; IMBERGER, 2006; BRUCE et al., 2008b; HODGES et al., 2000; DISSANAYAKE; HOFMANN; PEETERS, 2019; CIMATORIBUS et al., 2018), RANS assumes that the eddy diffusivity is linearly related to the eddy viscosity by the constant Prandtl number or Schmidt number, which governs the ratio of the momentum diffusivity to the thermal diffusivity or the mass diffusivity, respectively (ULLOA et al., 2019). An alternative approach to RANS is the large-eddy simulation (LES), which, unlike RANS, can resolve most of the important eddies in the flow, not only the largest ones. In LES, the method involves filtering out the larger eddies and directly resolving them using the governing equations, while the smaller turbulence length scales are modeled similarly to the RANS technique. In other words, while the LES method still requires a refined temporal and spatial grid to capture certain turbulence-length scales, the smaller scales can be effectively modeled, reducing computational requirements compared to Direct Numerical Simulations. The LES method strikes a balance between accuracy and computational efficiency, which is an option for future investigations. However,

In our application, we have used a κ-ε model, which is a second-order turbulence closure scheme that is based on the balance between dissipation and the production of turbulent energy. Investigations have shown that the κ-ε turbulence closure model provides good applicability to detect internal seiches in stratified lakes (GOUDSMIT et al., 2002) and capture the initial nonlinear steepening of internal waves(WADZUK; HODGES, 2009), but cannot simulate the subsequent degeneration into a high-frequency internal wave train and vertical mixing induced by shear and break of high-frequency internal waves (HYDRAULICS, 2003).

Due to numerical diffusion and dissipation (HODGES; LAVAL; WADZUK, 2006) and the inability of hydrodynamic models to deal with nonlinear and nonhydrostatic mechanisms, energy fluxes must be carefully investigated (SHIMIZU; IMBERGER, 2008). Although we have observed the initial mixing induced by nonlinear steepening and the generation of propagating internal waves (λ = 280 m) induced by the interaction between mean flow and reservoir meander bends (Chapter 4), the reader should be aware of the limitation when comparing the simulated results with the measured data. As observed in chapter 4 (Fig. 59 c), the spectral variance of the simulated velocities decreased strongly for frequencies exceeding 8×10^{-4} Hz, indicating that the energy of these waves could be underestimated. In our simulations, the turbulence rates induced by initial nonlinear steepening are much higher than the energy transferred to high-frequency internal waves in real lakes, supporting our hypothesis that most of the energy is dissipated due to the interaction between the internal seiche and a gently sloping bed, even considering results from a hydrostatic model. However, the systematic study proposed in this chapter for future investigations should be carried out with a nonhydrostatic model to overcome this limitation and guarantee a fair comparison with data from real lakes.

Simulations have been performed in the absence of Coriolis effects, which neglects the formation of internal Kelvin and Poincaré waves (BOUFFARD; LEMMIN, 2013; BOUFFARD; BOEGMAN; RAO, 2012), resulting in waves with different periods and forms. Since internal waves influenced by Earth's rotation generate a completely different flow, the findings from this study cannot be applied to large lakes and at high latitudes. The potential effect of Earth's rotation on internal seiche should be evaluated carefully by the Burger number before any conclusions could be made from this study.

Furthermore, in all simulations, we applied only one single wind event to generate internal waves. However, the winds that excite internal seiches in lakes and reservoirs are not always characterized by singular events. Continuous winds with frequency close to the fundamental internal seiche period may induce resonant amplifications, which may increase the nonlinear and dispersive energy flux (BOEGMAN; IVEY, 2012). Our findings may not satisfactorily explain the internal seiche dissipation in lakes with strong periodic winds (e.g. diurnal and semi-diurnal winds), especially when the wind forcing frequency is equal or higher than the wave period. Further research could explore wave dissipation and how these mechanisms act in lakes with strong periodic winds. This analysis could also contribute to understanding the contribution of wave attractors and wave breaking to wave dissipation.

Another point of interest for further investigation is related to the distribution of energy to higher vertical modes. Our analysis is essentially based on wave energy and does not distinguish the contribution from different vertical modes. Although we have suggested that the gently sloping bed favors the formation of internal seiches with higher vertical modes (Chapter 4; Fig. 54), we were unable to infer any conclusion about how the sloping bed may influence the energy distribution in different modes. A mode decomposition (SHIMIZU, 2019; SHIMIZU, 2011; BOEHRER, 2000) could help this analysis for future studies. Note that in a constantly sloping reservoir, the boundary conditions of no vertical flow are not (neither nearly) conserved. Therefore, the flow along the bottom of the lake has the vertical speed given by the average slope through the lake. Hence if the horizontal velocities at the bottom are about the same as in the rest of the hypolimnion, the vertical velocity at the boundary is about the same as in the thermocline. As a result, the application of a mode decomposition model for subcritical slopes is strongly recommended for future studies (e.g. Shimizu (2019))

Finally, although many results have been guided by a simplified W-based classification, which is based on a stratified, straight, flat bottom two-layer basin, many recent studies still consider the simplified model to be a reasonable predictor of upwelling events and subsequent energy relaxation (VALBUENA et al., 2022; ROBERTS et al., 2021).

Although many studies predict upwelling events and internal seiche activity using the Lake Number, an integral form of the Wedderburn number, which incorporates lake bathymetry and the effects of continuous stratification into the Wedderburn number (IMBERGER; PATTERSON, 1989; STEVENS; IMBERGER, 1996), the difference between them is typically smaller by one order of magnitude or less in gently sloped boundaries (RUEDA; COWEN, 2005; MACINTYRE et al., 1999). Observations in steep-sloped lakes (e.g. Brenda Mines Pit Lake) did not show differences between the Wedderburn number and the Lake number (STEVENS; LAWRENCE, 1997; DOROSTKAR; BOEGMAN, 2013).

The difference observed in reservoirs with gentle sloping beds is not associated with any of the mechanisms mentioned in this thesis (e.g., breaking events induced by the interaction between internal seiches and sloping beds). Instead, it arises solely from the variation in the distance between the centroid and the center of mass of the lake. In the hypothetical cases presented in this thesis, the variation between both numbers would result in a difference between the Wedderburn number and the Lake number that is less than one order of magnitude (e.g. 1 to 4). Such a difference would not be sufficient to inhibit the occurrence of internal seiche activity, as observed in the cases demonstrated here.

This study serves as a starting point to propose a new classification, highlighting which simplification should be avoided to obtain a more accurate classification while maintaining the simplicity of the analytical solution.

7 Conclusion

This thesis advances our understanding of internal seiches in thermally stratified lakes and reservoirs and contributes to increase the accessibility to state-of-the-art on physical limnology, helping interdisciplinary studies analyze links between internal wave dynamics and water quality in aquatic ecosystems. To answer the proposed research question, five mechanisms that could contribute to inhibiting or accelerating the dissipation of basin-scale internal waves in thermally stratified lakes were investigated using numerical models and field measurements: (1) The study reveals the existence of a mixing mechanism generated during internal seiche events due to the destabilization of miscible layers even in rectangular tanks with vertical boundary walls. Although the mechanism is weak in inhibiting the generation of internal seiche, the mixing event is susceptible to attenuate the wave amplitude especially during periods of low Wedderburn number; (2) the study underlines the importance of lake morphology on the energy transference from basin-scale internal seiche to higher frequency internal waves. This mechanism slightly accelerates wave dissipation by promoting faster internal wave degeneration through the formation of high-frequency internal waves, acting as a secondary factor in inhibiting internal seiches; (3) this study suggests that the primary contributor to inhibiting internal seiches is the sloping lake bottom, which may promote strong vertical mixing events near the lakeshore.

Contradicting the initial hypothesis, the results of this work remarkably indicate that two mechanisms listed in the hypothesis do not act as a limiting factor on internal seiche generation: (4) the study reveals that more energy is transferred from wind to basin-scale internal wave when the stratification profile deviates from the two-layer structure. Although more energy should be observed in the internal seiche field, the amount of energy dissipated at the sloping bottom and reservoir bends is much greater than the gain due to the stratification profile; (5) the study underlines the importance of shallow thermoclines in the amplification of downwelling events. The interaction of the internal seiche with surface water induces a shortening of the effective internal seiche fetch, not inhibiting its formation, but promoting higher thermocline erosion than predicted by W-based classification.

The outcome of this study may be of great interest and relevance to those investigating the cycling of nutrients and other elements in thermally stratified lakes, as each investigated mechanism may influence the biogeochemical cycle differently. To increase accessibility to state-of-the-art physical limnology and facilitate the correlation between internal seiche mechanisms and biogeochemical cycle, an internal wave analyzer for thermally stratified lakes and reservoirs, the Interwave Analyzer, has been developed.

References

Anaconda Software Distribution. *Computer software. Vers. 2-2.4.0. Anaconda.* 2016. Https://www.anaconda.com/.

ANTENUCCI, J. P.; IMBERGER, J. Energetics of long internal gravity waves in large lakes. *Limnology and Oceanography*, Wiley Online Library, v. 46, n. 7, p. 1760–1773, 2001. https://doi.org/10.1080/15715124.2003.9635214.

ANTENUCCI, J. P.; IMBERGER, J. On internal waves near the high-frequency limit in an enclosed basin. *Journal of Geophysical Research: Oceans*, Wiley Online Library, v. 106, n. C10, p. 22465–22474, 2001. https://doi.org/10.1029/2000JC000465.

ANTENUCCI, J. P.; IMBERGER, J. The seasonal evolution of wind/internal wave resonance in Lake Kinneret. *Limnology and oceanography*, Wiley Online Library, v. 48, n. 5, p. 2055–2061, 2003. https://doi.org/10.4319/lo.2003.48.5.2055.

ANTENUCCI, J. P.; IMBERGER, J.; SAGGIO, A. Seasonal evolution of the basin-scale internal wave field in a large stratified lake. *Limnology and oceanography*, Wiley Online Library, v. 45, n. 7, p. 1621–1638, 2000. https://doi.org/10.4319/lo.2000.45.7.1621.

APPT, J.; IMBERGER, J.; KOBUS, H. Basin-scale motion in stratified Upper Lake Constance. *Limnol. Oceanogr.*, Wiley Online Library, v. 49, n. 4, p. 919–933, 2004.

ARAKAWA, A.; LAMB, V. R. Computational design of the basic dynamical processes of the UCLA general circulation model. *General circulation models of the atmosphere*, Methods in computational Physics, v. 17, n. Supplement C, p. 173–265, 1977. https://doi.org/10.1016/B978-0-12-460817-7.50009-4.

ARNON, A.; BRENNER, S.; SELKER, J. S.; GERTMAN, I.; LENSKY, N. G. Seasonal dynamics of internal waves governed by stratification stability and wind: Analysis of high-resolution observations from the Dead Sea. *Limnology and Oceanography*, Wiley Online Library, 2019. https://doi.org/10.5194/os-13-145-2017.

BARACCHINI, T.; HUMMEL, S.; VERLAAN, M.; CIMATORIBUS, A.; WÜEST, A.; BOUFFARD, D. An automated calibration framework and open source tools for 3D lake hydrodynamic models. *Environmental Modelling \& Software*, Elsevier, v. 134, p. 104787, 2020. https://doi.org/10.1016/j.envsoft.2020.104787.

BERNHARDT, J.; KIRILLIN, G. Seasonal pattern of rotation-affected internal seiches in a small temperate lake. *Limnology and oceanography*, Wiley Online Library, v. 58, n. 4, p. 1344–1360, 2013. https://doi.org/10.4319/lo.2013.58.4.1344.

BOCANIOV, S. A.; ULLMANN, C.; RINKE, K.; LAMB, K. G.; BOEHRER, B. Internal waves and mixing in a stratified reservoir: Insights from three-dimensional modeling. *Limnologica*, Elsevier, v. 49, p. 52–67, 2014. https://doi.org/10.1016/j.limno.2014.08.004.

BOEGMAN, L. Currents in stratified water bodies 2: Internal waves. *Encyclopedia of inland waters*, Academic Press, v. 1, p. 539–558, 2009. https://doi.org/10.1016/B978-012370626-3.00081-8.

BOEGMAN, L.; IMBERGER, J.; IVEY, G. N.; ANTENUCCI, J. P. High-frequency internal waves in large stratified lakes. *Limnology and oceanography*, Wiley Online Library, v. 48, n. 2, p. 895–919, 2003. https://doi.org/10.4319/lo.2003.48.2.0895.

BOEGMAN, L.; IVEY, G. N. The dynamics of internal wave resonance in periodically forced narrow basins. *Journal of Geophysical Research: Oceans*, Wiley Online Library, v. 117, n. C11, 2012. https://doi.org/10.1029/2012JC008134.

BOEGMAN, L.; IVEY, G. N.; IMBERGER, J. The degeneration of internal waves in lakes with sloping topography. *Limnology and oceanography*, Wiley Online Library, v. 50, n. 5, p. 1620–1637, 2005. https://doi.org/10.4319/lo.2005.50.5.1620.

BOEGMAN, L.; IVEY, G. N.; IMBERGER, J. The energetics of large-scale internal wave degeneration in lakes. *J Fluid Mech*, Cambridge University Press, v. 531, p. 159–180, 2005. https://doi.org/10.1017/S0022112005003915.

BOEGMAN, L.; STASTNA, M. Sediment resuspension and transport by internal solitary waves. *Annual review of fluid mechanics*, Annual Reviews, v. 51, p. 129–154, 2019. https://doi.org/10.1146/annurev-fluid-122316-045049.

BOEHRER, B. Modal response of a deep stratified lake: western Lake Constance. *Journal of Geophysical Research: Oceans*, Wiley Online Library, v. 105, n. C12, p. 28837–28845, 2000. https://doi.org/10.1029/2000JC900125.

BOEHRER, B.; ILMBERGER, J.; MÜNNICH, K. O. Vertical structure of currents in western Lake Constance. *Journal of Geophysical Research: Oceans*, Wiley Online Library, v. 105, n. C12, p. 28823–28835, 2000. https://doi.org/10.1029/2000JC900139.

BOEHRER, B.; SCHULTZE, M. Stratification of lakes. *Reviews of Geophysics*, Wiley Online Library, v. 46, n. 2, 2008. https://doi.org/10.1029/2006RG000210.

BOGUCKI, D.; DICKEY, T.; REDEKOPP, L. G. Sediment resuspension and mixing by resonantly generated internal solitary waves. *Journal of Physical Oceanography*, v. 27, n. 7, p. 1181–1196, 1997.

BOUFFARD, D.; ACKERMAN, J. D.; BOEGMAN, L. Factors affecting the development and dynamics of hypoxia in a large shallow stratified lake: hourly to seasonal patterns. *Water Resour Res*, Wiley Online Library, v. 49, n. 5, p. 2380–2394, 2013. https://doi.org/10.1002/wrcr.20241.

BOUFFARD, D.; BOEGMAN, L. Basin-scale internal waves. In: *Encyclopedia of lakes and Reservoirs*. [S.l.]: Springer, 2012. p. 102–107.

BOUFFARD, D.; BOEGMAN, L.; RAO, Y. R. Poincaré wave–induced mixing in a large lake. *Limnology and oceanography*, Wiley Online Library, v. 57, n. 4, p. 1201–1216, 2012. https://doi.org/10.4319/lo.2012.57.4.1201.

BOUFFARD, D.; LEMMIN, U. Kelvin waves in lake geneva. *Journal of Great Lakes Research*, Elsevier, v. 39, n. 4, p. 637–645, 2013. https://doi.org/10.1016/j.jglr.2013.09.005.

BOUFFARD, D.; WUEST, A. Mixing in Stratified Lakes and Reservoirs. In: *Mixing and Dispersion in Flows Dominated by Rotation and Buoyancy*. Springer, 2018. p. 61–88. https://doi.org/10.1007/978-3-319-66887-1_3.

BOUFFARD, D.; WÜEST, A. Convection in lakes. *Annual Review of Fluid Mechanics*, Annual Reviews, v. 51, p. 189–215, 2019. https://doi.org/10.1146/annurev-fluid-010518-040506.

BOUFFARD, D.; ZDOROVENNOV, R. E.; ZDOROVENNOVA, G. E.; PASCHE, N.; WÜEST, A.; TERZHEVIK, A. Y. Ice-covered Lake Onega: effects of radiation on convection and internal waves. *Hydrobiologia*, Springer, v. 780, n. 1, p. 21–36, 2016. https://doi.org/10.1007/s10750-016-2915-3.

BRAINERD, K. E.; GREGG, M. C. Surface mixed and mixing layer depths. *Deep Sea Research-Part I-Oceanographic Research Papers*, Oxford [England]; Tarrytown, NY: Pergamon Press, c1992-, v. 42, n. 9, p. 1521–1544, 1995. https://doi.org/10.1016/0967-0637(95)00068-H.

BRENNER, S. D.; LAVAL, B. E. Seiche modes in multi-armed lakes. *Limnology and Oceanography*, Wiley Online Library, v. 63, n. 6, p. 2717–2726, 2018. https://doi.org/10.1002/lno.11001.

BRUCE, L. C.; JELLISON, R.; IMBERGER, J.; MELACK, J. M. Effect of benthic boundary layer transport on the productivity of Mono Lake, California. *Saline Syst.*, BioMed Central, v. 4, n. 1, p. 11, 2008. https://doi.org/10.1186/1746-1448-4-11.

BRUCE, L. C.; JELLISON, R.; IMBERGER, J.; MELACK, J. M. Effect of benthic boundary layer transport on the productivity of Mono Lake, California. *Saline Systems*, v. 4, n. 1, 2008. ISSN 17461448.

BUENO, R.; BLENINGER, T. Lake dynamic during thermal stratified periods: internal seiche formation. In: *XXIII Simpósio Brasileiro de Recursos Hídricos*. Foz do Iguaçu-PR, Brazil: [s.n.], 2019.

BUENO, R. de C. *Wind-induced internal waves in closed basins: A laboratory experiment and field study.* (Doctoral dissertation) — Graduate Program in Environmental Engineering of the Federal University of Paraná., 2019. https://doi.org/10.13140/RG.2.2.35265.20328.

BUENO, R. de C.; BLENINGER, T. Wind-induced internal seiches in vossoroca reservoir, PR, Brazil. *Revista Brasileira de Recursos Hidricos*, v. 23, 2018. ISSN 23180331.

BUENO, R. de C.; BLENINGER, T.; YAO, H.; RUSAK, J. A. An empirical parametrization of internal seiche amplitude including secondary effects. *Environmental Fluid Mechanics*, Springer, 2020. https://doi.org/10.1007/s10652-020-09767-1.

BUENO, R. de C.; LORKE, A.; BLENINGER, T. *Interwave Analyzer: User Manual.* 2020.

CARMACK, E. C.; WIEGAND, R. C.; DALEY, R. J.; GRAY, C. B. J.; JASPER, S.; PHARO, C. H. Mechanisms influencing the circulation and distribution of water mass in a medium residence-time lake. *Limnology and oceanography*, Wiley Online Library, v. 31, n. 2, p. 249–265, 1986. https://doi.org/10.4319/lo.1986.31.2.0249.

CARR, M.; DAVIES, P. A. The motion of an internal solitary wave of depression over a fixed bottom boundary in a shallow, two-layer fluid. *Physics of Fluids*, AIP, v. 18, n. 1, p. 16601, 2006. https://doi.org/10.1063/1.2162033.

CHEN, C.-T. A.; MILLERO, F. J. Thermodynamic properties for natural waters covering only the limnological range 1. *Limnology and Oceanography*, Wiley Online Library, v. 31, n. 3, p. 657–662, 1986. https://doi.org/10.4319/lo.1986.31.3.0657.

CHOWDHURY, M. R.; WELLS, M. G.; HOWELL, T. Movements of the thermocline lead to high variability in benthic mixing in the nearshore of a large lake. *Water Resources Research*, v. 52, n. 4, p. 3019–3039, 4 2016. ISSN 00431397.

CHU, C. K.; CHOU, R. L. Solitons induced by boundary conditions. *Advances in applied mechanics*, Academic Press New York, v. 27, p. 283–302, 1990. https://doi.org/10.1016/S0065-2156(08)70198-4.

CIMATORIBUS, A. A.; LEMMIN, U.; BOUFFARD, D.; BARRY, D. A. Nonlinear Dynamics of the Nearshore Boundary Layer of a Large Lake (Lake Geneva). *Journal of Geophysical Research: Oceans*, Blackwell Publishing Ltd, v. 123, n. 2, p. 1016–1031, 2 2018. ISSN 21699291.

CORMAN, J. R.; MCINTYRE, P. B.; KUBOJA, B.; MBEMBA, W.; FINK, D.; WHEELER, C. W.; GANS, C.; MICHEL, E.; FLECKER, A. S. Upwelling couples chemical and biological dynamics across the littoral and pelagic zones of Lake Tanganyika, East Africa. *Limnology and Oceanography*, v. 55, n. 1, p. 214–224, 1 2010. ISSN 00243590.

COSSU, R.; RIDGWAY, M. S.; LI, J. Z.; CHOWDHURY, M. R.; WELLS, M. G. Wash-zone dynamics of the thermocline in Lake Simcoe, Ontario. *Journal of Great Lakes Research*, Elsevier, v. 43, n. 4, p. 689–699, 2017.

COSSU, R.; WELLS, M. G. The interaction of large amplitude internal seiches with a shallow sloping lakebed: observations of benthic turbulence in Lake Simcoe, Ontario, Canada. *PloS one*, Public Library of Science, v. 8, n. 3, p. e57444, 2013. https://doi.org/10.1371/journal.pone.0057444.

CUYPERS, Y.; VINÇON-LEITE, B.; GROLEAU, A.; TASSIN, B.; HUMBERT, J.-F. Impact of internal waves on the spatial distribution of Planktothrix rubescens (cyanobacteria) in an alpine lake. *The ISME journal*, Nature Publishing Group, v. 5, n. 4, p. 580, 2011.

Deltares. *Simulation of multi-dimensional hydrodynamic flows and transport phenomena, including sediments.* [S.l.: s.n.], 2014.

DILLON, T. M. Vertical overturns: A comparison of Thorpe and Ozmidov length scales. *Journal of Geophysical Research: Oceans*, Wiley Online Library, v. 87, n. C12, p. 9601–9613, 1982. https://doi.org/10.1029/JC087iC12p09601.

DILLON, T. M. The energetics of overturning structures: Implications for the theory of fossil turbulence. *Journal of physical oceanography*, v. 14, n. 3, p. 541–549, 1984. https://doi.org/10.1175/1520-0485(1984)014%3C0541:TEOOSI%3E2.0.CO;2.

DILLON, T. M.; PARK, M. M. The available potential energy of overturns as an indicator of mixing in the seasonal thermocline. *Journal of Geophysical Research*, v. 92, n. C5, p. 5345, 1987. ISSN 0148-0227.

DISSANAYAKE, P.; HOFMANN, H.; PEETERS, F. Comparison of results from two 3D hydrodynamic models with field data: Internal seiches and horizontal currents. *Inland waters*, Taylor \& Francis, v. 9, n. 2, p. 239–260, 2019. https://doi.org/10.1080/20442041.2019.1580079.

DONELAN, M. A. Air-water exchange processes. *Coastal and Estuarine Studies*, AGU AMERICAN GEOPHYSICAL UNION, p. 19–36, 1998. https://doi.org/10.1029/CE054p0019.

DOROSTKAR, A.; BOEGMAN, L. Internal hydraulic jumps in a long narrow lake. *Limnology and oceanography*, Wiley Online Library, v. 58, n. 1, p. 153–172, 2013. https://doi.org/10.4319/lo.2013.58.1.0153.

ETEMAD-SHAHIDI, A.; IMBERGER, J. Diapycnal mixing in the thermocline of lakes: estimations by different methods. *Environmental Fluid Mechanics*, Springer, v. 6, n. 3, p. 227–240, 2006. https://doi.org/10.1007/s10652-005-4480-6.

EVANS, M. A.; MACINTYRE, S.; KLING, G. W. Internal wave effects on photosynthesis: Experiments, theory, and modeling. *Limnol. Oceanogr.*, Wiley Online Library, v. 53, n. 1, p. 339–353, 2008. https://doi.org/10.4319/lo.2008.53.1.0339.

FARMER, D.; ARMI, L. The generation and trapping of solitary waves over topography. *Science*, American Association for the Advancement of Science, v. 283, n. 5399, p. 188–190, 1999. https://doi.org/10.1126/science.283.5399.188.

FLOOD, B.; WELLS, M.; DUNLOP, E.; YOUNG, J. Internal waves pump waters in and out of a deep coastal embayment of a large lake. *Limnology and Oceanography*, Wiley Online Library, v. 65, n. 2, p. 205–223, 2020.

FLOOD, B.; WELLS, M.; MIDWOOD, J. D.; BROOKS, J.; KUAI, Y.; LI, J. Intense variability of dissolved oxygen and temperature in the internal swash zone of Hamilton Harbour, Lake Ontario. *Inland Waters*, Taylor \& Francis, p. 1–18, 2021. https://doi.org/10.1080/20442041.2020.1843930.

FOREL, F. A. *Le Léman: monographie limnologique.* [S.l.]: F. Rouge, 1892. v. 1.

FORSYTHE, K. W.; MARVIN, C. H. Analyzing the spatial distribution of sediment contamination in the lower Great Lakes. *Water Quality Research Journal*, IWA Publishing, v. 40, n. 4, p. 389–401, 2005. https://doi.org/10.2166/wqrj.2005.043.

FRICKER, P. D.; NEPF, H. M. Bathymetry, stratification, and internal seiche structure. *Journal of Geophysical Research: Oceans*, Wiley Online Library, v. 105, n. C6, p. 14237–14251, 2000. https://doi.org/10.1029/2000JC900060.

FRINDTE, K.; ECKERT, W.; ATTERMEYER, K.; GROSSART, H.-P. Internal wave-induced redox shifts affect biogeochemistry and microbial activity in sediments: a simulation experiment. *Biogeochemistry*, Springer, v. 113, n. 1-3, p. 423–434, 2013. https://doi.org/10.1007/s10533-012-9769-1.

GARRETT, C. Internal tides and ocean mixing. *Science*, American Association for the Advancement of Science, v. 301, n. 5641, p. 1858–1859, 2003. https://doi.org/10.1126/science.1090002.

GARRETT, C.; MUNK, W. Space-time scales of internal waves. *Geophysical \& Astrophysical Fluid Dynamics*, Taylor \& Francis, v. 3, n. 1, p. 225–264, 1972. https://doi.org/10.1080/03091927208236082.

GAUDARD, A.; SCHWEFEL, R.; VINNÅ, L. R.; SCHMID, M.; WÜEST, A.; BOUFFARD, D. Optimizing the parameterization of deep mixing and internal seiches in one-dimensional hydrodynamic models: a case study with Simstrat v1. 3. *Geoscientific Model Development*, Copernicus GmbH, v. 10, n. 9, p. 3411–3423, 2017. https://doi.org/10.5194/gmd-10-3411-2017.

GIBSON, C. H. Internal waves, fossil turbulence, and composite ocean microstructure spectra. *Journal of fluid mechanics*, Cambridge University Press, v. 168, p. 89–117, 1986. https://doi.org/10.1017/S0022112086000307.

GILL, A. E. *Atmosphere—ocean dynamics.* [S.l.]: Elsevier, 2016.

GLOOR, M.; WÜEST, A.; IMBODEN, D. M. Dynamics of mixed bottom boundary layers and its implications for diapycnal transport in a stratified, natural water basin. *Journal of Geophysical Research: Oceans*, Wiley Online Library, v. 105, n. C4, p. 8629–8646, 2000.

GÓMEZ-GIRALDO, A.; IMBERGER, J.; ANTENUCCI, J. P. Spatial structure of the dominant basin-scale internal waves in Lake Kinneret. *Limnology and Oceanography*, v. 51, n. 1, p. 229–246, 2006. https://aslopubs.onlinelibrary.wiley.com/doi/abs/10.4319/lo.2006.51.1.0229.

GOUDSMIT, G. H.; BURCHARD, H.; PEETERS, F.; WÜEST, A. Application of k-ϵ turbulence models to enclosed basins: The role of internal seiches. *Journal of Geophysical Research C: Oceans*, v. 107, n. 12, p. 23–1, 12 2002. ISSN 01480227.

GOUDSMIT, G.-H.; PEETERS, F.; GLOOR, M.; WÜEST, A. Boundary versus internal diapycnal mixing in stratified natural waters. *Journal of Geophysical Research: Oceans*, Wiley Online Library, v. 102, n. C13, p. 27903–27914, 1997. https://doi.org/10.1029/97JC01861.

GRANGE, S. Averaging wind speeds and directions. *no. October*, p. 12, 2014. https://doi.org/10.13140/RG.2.1.3349.2006.

GUSEVA, S.; CASPER, P.; SACHS, T.; SPANK, U.; LORKE, A. Energy Flux Paths in Lakes and Reservoirs. *Water*, Multidisciplinary Digital Publishing Institute, v. 13, n. 22, p. 3270, 2021. https://doi.org/10.3390/w13223270.

GUYENNON, N.; VALERIO, G.; SALERNO, F.; PILOTTI, M.; TARTARI, G.; COPETTI, D. Internal wave weather heterogeneity in a deep multi-basin subalpine lake resulting from wavelet transform and numerical analysis. *Advances in water resources*, Elsevier, v. 71, p. 149–161, 2014. https://doi.org/10.1016/j.advwatres.2014.06.013.

HAREN, H. van; DIJKSTRA, H. A. Convection under internal waves in an alpine lake. *Environmental Fluid Mechanics*, v. 21, n. 2, p. 305–316, 4 2021. ISSN 1567-7419.

HEAPS, N. S.; RAMSBOTTOM, A. E. Wind effects on the water in a narrow two-layered lake. Part I. Theoretical analysis. Part II. Analysis of observations from Windermere. Part III. Application of the theory to Windermere. *Phil. Trans. R. Soc. Lond. A*, The Royal Society, v. 259, n. 1102, p. 391–430, 1966. https://doi.org/10.1098/rsta.1966.0021.

HEINZEL, G.; RÜDIGER, A.; SCHILLING, R. Spectrum and spectral density estimation by the Discrete Fourier transform (DFT), including a comprehensive list of window functions and some new at-top windows. *Max Plank Inst.*, 2002. https://doi.org/10.22027/395068.

HELFRICH, K. R. Internal solitary wave breaking and run-up on a uniform slope. *Journal of Fluid Mechanics*, Cambridge University Press, v. 243, p. 133–154, 1992. https://doi.org/10.1017/S0022112092002660.

HENDERSON, S. M.; DEEMER, B. R. Vertical propagation of lakewide internal waves. *Geophysical Research Letters*, v. 39, n. 6, p. n/a–n/a, 3 2012. ISSN 00948276.

HINGSAMER, P.; PEETERS, F.; HOFMANN, H. The consequences of internal waves for phytoplankton focusing on the distribution and production of Planktothrix rubescens. *PloS one*, Public Library of Science, v. 9, n. 8, p. e104359, 2014. https://doi.org/10.1371/journal.pone.0104359.

HODGES, B. R.; IMBERGER, J.; SAGGIO, A.; WINTERS, K. B. Modeling basin-scale internal waves in a stratified lake. *Limnology and oceanography*, Wiley Online Library, v. 45, n. 7, p. 1603–1620, 2000. https://doi.org/10.4319/lo.2000.45.7.1603.

HODGES, B. R.; LAVAL, B.; WADZUK, B. M. Numerical error assessment and a temporal horizon for internal waves in a hydrostatic model. *Ocean Modelling*, Elsevier, v. 13, n. 1, p. 44–64, 1 2006. ISSN 14635003.

HOLLOWAY, G. Theoretical approaches to interactions among internal waves, turbulence and finestructure. In: AIP. *AIP Conference Proceedings*. 1981. v. 76, n. 1, p. 47–77. https://doi.org/10.1063/1.33197.

HOMMA, H.; NAGAI, T.; SHIMIZU, K.; YAMAZAKI, H. Early-winter mixing event associated with baroclinic motions in weakly stratified Lake Biwa. *Inland Waters*, Taylor \& Francis, v. 6, n. 3, p. 364–378, 2016.

HORN, D. A.; IMBERGER, J.; IVEY, G. N. The degeneration of basin-scale internal waves in lakes. In: *Thirteenth Australasian Fluid Mechanics Conference*. Monash University: [s.n.], 1998. p. 863–866.

HORN, D. A.; IMBERGER, J.; IVEY, G. N. The degeneration of large-scale interfacial gravity waves in lakes. *Journal of Fluid Mechanics*, Cambridge University Press, v. 434, p. 181–207, 2001. https://doi.org/10.1017/S0022112001003536.

HUANG, A.; RAO, Y. R.; LU, Y. Evaluation of a 3-D hydrodynamic model and atmospheric forecast forcing using observations in Lake Ontario. *Journal of Geophysical Research: Oceans*, Wiley Online Library, v. 115, n. C2, 2010. https://doi.org/10.1029/2009JC005601.

HUBER, A. M. R.; PEETERS, F.; LORKE, A. Active and passive vertical motion of zooplankton in a lake. *Limnology and Oceanography*, Wiley Online Library, v. 56, n. 2, p. 695–706, 2011. https://doi.org/10.4319/lo.2011.56.2.0695.

HUTTER, K. *Nonlinear internal waves in lakes.* [S.l.]: Springer Science \& Business Media, 2011.

HUTTER, K.; FILATOV, N.; MADERICH, V.; NIKISHOV, V.; PELINOVSKY, E.; VLASENKO, V. *Strongly nonlinear internal waves in lakes: Generation, transformation, meromixis.* [S.l.], 2007.

HUTTER, K.; WANG, Y.; CHUBARENKO, I. P. *Physics of Lakes, volume 2: lakes as oscillators. Advances in geophysical and environmental mechanics and mathematics.* Springer, 2011. https://doi.org/10.1007/978-3-642-19112-1.

HYDRAULICS, W. L. D. *User Manual of Delft3D-FLOW—Simulation of Multi-dimensional Hydrodynamic Flows and Transport Phenomena, Including Sediments.* 2003.

IMAM, Y. E.; LAVAL, B.; PIETERS, R.; LAWRENCE, G. The baroclinic response to wind in a multiarm multibasin reservoir. *Limnology and Oceanography*, Wiley Online Library, v. 65, n. 3, p. 582–600, 2020. https://doi.org/10.1002/lno.11328.

IMBERGER, J. The diurnal mixed layer. *Limnology and oceanography*, Wiley Online Library, v. 30, n. 4, p. 737–770, 1985. https://doi.org/10.4319/lo.1985.30.4.0737.

IMBERGER, J. *Physical processes in lakes and oceans.* American Geophysical Union, 1998. v. 54. https://doi.org/10.1029/CE054.

IMBERGER, J. *Flux Paths in a Stratified Lake.* American Geophysical Union (AGU), 2013. 1–17 p. https://agupubs.onlinelibrary.wiley.com/doi/abs/10.1029/CE054p0001.

IMBERGER, J.; PATTERSON, J. C. Physical limnology. In: *Advances in applied mechanics.* Elsevier, 1989. v. 27, p. 303–475. https://doi.org/10.1016/S0065-2156(08)70199-6.

IMBODEN, D. M. The motion of lake waters. *The Lakes Handbook: Limnology and Limnetic Ecology*, Wiley Online Library, p. 115–152, 2003. https://doi.org/10.1002/9780470999271.ch6.

IMBODEN, D. M.; WÜEST, A. Mixing mechanisms in lakes. In: *Physics and chemistry of lakes*. Springer, 1995. p. 83–138. https://doi.org/10.1007/978-3-642-85132-2_4.

Intergovernmental Oceanographic Commission; others. *The International thermodynamic equation of seawater–2010: calculation and use of thermodynamic properties. Corrections – 2015*. [S.l.]: Unesco, 2015.

ISHIKAWA, M.; BLENINGER, T.; LORKE, A. Hydrodynamics and mixing mechanisms in a subtropical reservoir. *Inland Waters*, 2021. ISSN 2044205X.

ISHIKAWA, M.; GONZALEZ, W.; GOLYJESWSKI, O.; SALES, G.; RIGOTTI, J. A.; BLENINGER, T.; MANNICH, M.; LORKE, A. *Effects of dimensionality on the performance of hydrodynamic models*. Copernicus GmbH, 2021. 1–34 p. https://doi.org/10.5194/gmd-2021-250.

IVEY, G. N.; IMBERGER, J.; KOSEFF, J. R. Buoyancy fluxes in a stratified fluid. *Coastal and Estuarine Studies*, AGU AMERICAN GEOPHYSICAL UNION, p. 377–388, 1998. https://doi.org/10.1029/CE054p0377.

IVEY, G. N.; WINTERS, K. B.; SILVA, I. P. D. D. Turbulent mixing in a sloping benthic boundary layer energized by internal waves. *Journal of Fluid Mechanics*, Cambridge University Press, v. 418, p. 59–76, 2000. https://doi.org/10.1017/S0022112000008788.

KRANENBURG, W.; TIESSEN, M.; VEENSTRA, J.; GRAAFF, R. de; UITTENBOGAARD, R.; BOUFFARD, D.; SAKINDI, G.; UMUTONI, A.; WALLE, J. de; THIERY, W.; others. 3D-modelling of Lake Kivu: Horizontal and vertical flow and temperature structure under spatially variable atmospheric forcing. *Journal of Great Lakes Research*, Elsevier, v. 46, n. 4, p. 947–960, 2020. https://doi.org/10.1016/j.jglr.2020.05.012.

LANE, A. The heat balance of the North Sea. Proudman Oceanographic Laboratory, 1989.

LAVAL, B.; IMBERGER, J.; HODGES, B. R.; STOCKER, R. Modeling circulation in lakes: Spatial and temporal variations. *Limnology and Oceanography*, v. 48, n. 3, p. 983–994, 2003. ISSN 00243590. https://aslopubs.onlinelibrary.wiley.com/doi/abs/10.4319/lo.2003.48.3.0983.

LAVAL, B. E.; IMBERGER, J.; FINDIKAKIS, A. N. Dynamics of a large tropical lake: Lake Maracaibo. *Aquatic sciences*, Springer, v. 67, n. 3, p. 337–349, 2005. https://doi.org/10.1007/s00027-005-0778-1.

LAZERTE, B. D. The dominating higher order vertical modes of the internal seiche in a small lake. *Limnology and Oceanography*, Wiley Online Library, 1980.

LEMCKERT, C.; IMBERGER, J. Turbulent benthic boundary layer mixing events in fresh water lakes. *Physical processes in lakes and oceans*, Wiley Online Library, v. 54, p. 503–516, 1998. https://doi.org/10.1029/CE054p0503.

LEMMIN, U. The structure and dynamics of internal waves in Baldeggersee. *Limnol. Oceanogr.*, Wiley Online Library, v. 32, n. 1, p. 43–61, 1987. https://doi.org/10.4319/lo.1987.32.1.0043.

LEMMIN, U.; MORTIMER, C. H. Tests of an extension to internal seiches of Defant's procedure for determination of surface seiche characteristics in real lakes. *Limnology and oceanography*, Wiley Online Library, v. 31, n. 6, p. 1207–1231, 1986. https://doi.org/10.4319/lo.1986.31.6.1207.

LEMMIN, U.; MORTIMER, C. H.; BÄUERLE, E. Internal seiche dynamics in Lake Geneva. *Limnology and Oceanography*, Wiley Online Library, v. 50, n. 1, p. 207–216, 2005. https://doi.org/10.4319/lo.2005.50.1.0207.

LEÓN, L. F.; IMBERGER, J.; SMITH, R. E. H.; HECKY, R. E.; LAM, D. C. L.; SCHERTZER, W. M. Modeling as a tool for nutrient management in Lake Erie: A hydrodynamics study. *Journal of Great Lakes Research*, Elsevier, v. 31, p. 309–318, 2005. https://doi.org/10.1016/S0380-1330(05)70323-3.

LIN, S.; BOEGMAN, L.; RAO, Y. R. Characterizing spatial and temporal distributions of turbulent mixing and dissipation in Lake Erie. *Journal of Great Lakes Research*, Elsevier, v. 47, n. 1, p. 168–179, 2021. https://doi.org/10.1016/j.jglr.2020.11.014.

LINDEN, P. F. The deepening of a mixed layer in a stratified fluid. *Journal of Fluid Mechanics*, Cambridge University Press, v. 71, n. 2, p. 385–405, 1975. https://doi.org/10.1017/S0022112075002637.

LOFTON, M.; MCCLURE, R.; CHEN, S.; LITTLE, J.; CAREY, C. Whole-Ecosystem Experiments Reveal Varying Responses of Phytoplankton Functional Groups to Epilimnetic Mixing in a Eutrophic Reservoir. *Water*, v. 11, n. 2, p. 222, 1 2019. ISSN 2073-4441.

LORKE, A. Boundary mixing in the thermocline of a large lake. *Journal of Geophysical Research: Oceans*, Wiley Online Library, v. 112, n. C9, 2007. https://doi.org/10.1029/2006JC004008.

LORKE, A.; MÜLLER, B.; MAERKI, M.; WÜEST, A. Breathing sediments: The control of diffusive transport across the sediment—water interface by periodic boundary-layer turbulence. *Limnology and Oceanography*, Wiley Online Library, v. 48, n. 6, p. 2077–2085, 2003. https://doi.org/10.4319/lo.2003.48.6.2077.

LORKE, A.; PEETERS, F.; BÄUERLE, E. High-frequency internal waves in the littoral zone of a large lake. *Limnology and oceanography*, Wiley Online Library, v. 51, n. 4, p. 1935–1939, 2006. https://doi.org/10.4319/lo.2006.51.4.1935.

LORKE, A.; PEETERS, F.; WÜEST, A. Shear-induced convective mixing in bottom boundary layers on slopes. *Limnology and Oceanography*, Wiley Online Library, v. 50, n. 5, p. 1612–1619, 2005. https://doi.org/10.4319/lo.2005.50.5.1612.

LORKE, A.; UMLAUF, L.; JONAS, T.; WÜEST, A. Dynamics of turbulence in low-speed oscillating bottom-boundary layers of stratified basins. *Environmental Fluid Mechanics*, Springer, v. 2, n. 4, p. 291–313, 2002. https://doi.org/10.1023/A:1020450729821.

LORKE, A.; UMLAUF, L.; MOHRHOLZ, V. Stratification and mixing on sloping boundaries. *Geophysical Research Letters*, v. 35, n. 14, 7 2008. ISSN 00948276.

LORKE, A.; WÜEST, A. Application of coherent ADCP for turbulence measurements in the bottom boundary layer. *Journal of Atmospheric and Oceanic Technology*, v. 22, n. 11, p. 1821–1828, 2005. https://doi.org/10.1175/JTECH1813.1.

LORRAI, C.; UMLAUF, L.; BECHERER, J. K.; LORKE, A.; WÜEST, A. Boundary mixing in lakes: 2. Combined effects of shear-and convectively induced turbulence on basin-scale mixing. *Journal of Geophysical Research: Oceans*, Blackwell Publishing Ltd, v. 116, n. 10, 2011. ISSN 21699291.

LOZOVATSKY, I.; ROGET, E.; FERNADO, H. J. S. Mixing in shallow waters: Measurements, processing, and applications. *Journal of Ocean University of China*, Springer, v. 4, n. 4, p. 293–305, 2005. https://doi.org/10.1007/s11802-005-0050-2.

MAAS, L. R. M.; BENIELLI, D.; SOMMERIA, J.; LAM, F.-P. A. Observation of an internal wave attractor in a confined, stably stratified fluid. *Nature*, v. 388, n. 6642, p. 557–561, 8 1997. ISSN 0028-0836.

MACDONALD, R. H. *Hypolimnetic withdrawl from a shallow, eutrophic lake.* (Doctoral dissertation) — University of British Columbia, 1995.

MACINTYRE, S.; CLARK, J. F.; JELLISON, R.; FRAM, J. P. Turbulent mixing induced by nonlinear internal waves in Mono Lake, California. *Limnology and Oceanography*, Wiley Online Library, v. 54, n. 6, p. 2255–2272, 2009. https://doi.org/10.4319/lo.2009.54.6.2255.

MACINTYRE, S.; FLYNN, K. M.; JELLISON, R.; ROMERO, J. R. Boundary mixing and nutrient fluxes in Mono Lake, California. *Limnology and Oceanography*, Wiley Online Library, v. 44, n. 3, p. 512–529, 1999. https://doi.org/10.4319/lo.1999.44.3.0512.

MACINTYRE, S.; JELLISON, R. *Nutrient fluxes from upwelling and enhanced turbulence at the top of the pycnocline in Mono Lake, California.* [S.l.]: Springer, 2001. 13–29 p.

MACKAS, D.; DENMAN, K.; ABBOTT, M. Plankton patchiness: biology in the physical vernacular. *Bulletin of Marine Science*, 1985.

MAKAREWICZ, J. C.; LEWIS, T. W.; PENNUTO, C. M.; ATKINSON, J. F.; EDWARDS, W. J.; BOYER, G. L.; HOWELL, E. T.; THOMAS, G. Physical and chemical characteristics of the nearshore zone of Lake Ontario. *Journal of Great Lakes Research*, Elsevier, v. 38, p. 21–31, 2012.

MARTI, C. L.; IMBERGER, J. Dynamics of the benthic boundary layer in a strongly forced stratified lake. *Hydrobiologia*, v. 568, n. 1, p. 217–233, 9 2006. ISSN 00188158.

MAXWORTHY, T.; IMBERGER, J.; SAGGIO, A. A Laboratory Demonstration of a Mechanism for the Production of Secondary, Internal Gravity-Waves in a Stratified Fluid. *Physical processes in lakes and oceans*, Wiley Online Library, v. 54, p. 261–270, 1998. https://doi.org/10.1029/CE054p0261.

MAXWORTHY, T.; MONISMITH, S. G. Differential mixing in a stratified fluid. *Journal of Fluid Mechanics*, Cambridge University Press, v. 189, p. 571–598, 1988. https://doi.org/10.1017/S0022112088001156.

MICHALLET, H.; IVEY, G. N. Experiments on mixing due to internal solitary waves breaking on uniform slopes. *Journal of Geophysical Research: Oceans*, Wiley Online Library, v. 104, n. C6, p. 13467–13477, 1999. https://doi.org/10.1029/1999JC900037.

MORTIMER, C. H. Water movements in lakes during summer stratification; evidence from the distribution of temperature in Windermere. *Philosophical Transactions of the Royal Society of London B: Biological Sciences*, The Royal Society, v. 236, n. 635, p. 355–398, 1952. https://doi.org/10.1098/rstb.1952.0005.

MORTIMER, C. H. The resonant response of stratified lakes to wind. *Schweizerische Zeitschrift für Hydrologie*, Springer, v. 15, n. 1, p. 94–151, 1953. https://doi.org/10.1007/BF02486219.

MORTIMER, C. H. *Some effects of the earth's rotation on water movements in stratified lakes.* [S.l.: s.n.], 1955.

MORTIMER, C. H. The dynamics of the autumn overturn in a lake. *Gen. Ass. Int. Geod*, v. 3, p. 15–21, 1955.

MORTIMER, C. H. Large-scale oscillatory motions and seasonal temperature changes in Lake Michigan and Lake Ontario. 1971.

MORTIMER, C. H. Lake hydrodynamics. *SIL Communications, 1953-1996*, Taylor and Francis, v. 20, n. 1, p. 124–197, 1974. https://doi.org/10.1080/05384680.1974.11923886.

MORTIMER, C. H. Strategies for coupling data collection and analysis with dynamic modelling of lake motions. *Developments in Water Science*, Elsevier, v. 11, p. 183–222, 1979. https://doi.org/10.1016/S0167-5648(08)70395-2.

MORTIMER, C. H.; HORN, W. Internal wave dynamics and their implications for plankton biology in the Lake of Zurich. *Vier. Natur. Gesell. Zurich*, v. 127, p. 299–318, 1982.

MÜNNICH, M. The influence of bottom topography on internal seiches in stratified media. *Dynamics of Atmospheres and Oceans*, Elsevier, v. 23, n. 1-4, p. 257–266, 1996. https://doi.org/10.1016/0377-0265(95)00439-4.

MÜNNICH, M.; WÜEST, A.; IMBODEN, D. M. Observations of the second vertical mode of the internal seiche in an alpine lake. *Limnology and oceanography*, Wiley Online Library, v. 37, n. 8, p. 1705–1719, 1992. https://doi.org/10.4319/lo.1992.37.8.1705.

MURAKAMI, M.; OONISHI, Y.; KUNISHI, H. A numerical simulation of the distribution of water temperature and salinity in the Seto Inland Sea. *Journal of the oceanographical society of Japan*, Springer, v. 41, n. 4, p. 213–224, 1985. https://doi.org/10.1007/BF02109271.

OKELY, P.; IMBERGER, J. Horizontal transport induced by upwelling in a canyon-shaped reservoir. *Hydrobiologia*, Springer, v. 586, n. 1, p. 343–355, 2007. https://doi.org/10.1007/s10750-007-0706-6.

OSBORNE, P. L. *Tropical ecosystems and ecological concepts.* [S.l.]: Cambridge University Press, 2000.

OSTROVSKY, L. A.; KAZAKOV, V. I.; MATUSOV, P. A.; ZABORSKIKH, D. V. Experimental study of the internal wave damping on small-scale turbulence. *Journal of physical oceanography*, v. 26, n. 3, p. 398–405, 1996. https://doi.org/10.1175/1520-0485(1996)026%3C0398:ESOTIW%3E2.0.CO;2.

OTTOLENGHI, L.; ADDUCE, C.; ROMAN, F.; FORGIA, G. la. Large eddy simulations of solitons colliding with intrusions. *Physics of Fluids*, v. 32, n. 9, p. 096606, 9 2020. ISSN 1070-6631.

PANNARD, A.; BEISNER, B. E.; BIRD, D. F.; BRAUN, J.; PLANAS, D.; BORMANS, M. Recurrent internal waves in a small lake: Potential ecological consequences for metalimnetic phytoplankton populations. *Limnology and Oceanography: Fluids and Environments*, Wiley Online Library, v. 1, n. 1, p. 91–109, 2011. https://doi.org/10.1215/21573698-1303296.

PANNARD, A.; BORMANS, M.; LAGADEUC, Y. Phytoplankton species turnover controlled by physical forcing at different time scales. *Can. J. Fish. Aquat. Sci.*, NRC Research Press, v. 65, n. 1, p. 47–60, 2008. https://doi.org/10.1139/f07-149.

PATTERSON, J. C.; HAMBLIN, P. F.; IMBERGER, J. Classification and dynamic simulation of the vertical density structure of lakes 1. *Limnology and oceanography*, Wiley Online Library, v. 29, n. 4, p. 845–861, 1984. https://doi.org/10.4319/lo.1984.29.4.0845.

PETERS, H.; GREGG, M. C.; TOOLE, J. M. On the parameterization of equatorial turbulence. *Journal of Geophysical Research: Oceans*, Wiley Online Library, v. 93, n. C2, p. 1199–1218, 1988. https://doi.org/10.1029/JC093iC02p01199.

PILLET, G.; MAAS, L. R.; DAUXOIS, T. Internal wave attractors in 3D geometries : A dynamical systems approach. *European Journal of Mechanics - B/Fluids*, Elsevier Masson, v. 77, p. 1–16, 9 2019. ISSN 0997-7546.

POLLI, B. A.; BLENINGER, T. Comparison of 1D and 3D reservoir heat transport models and temperature effects on mass transport. *RBRH*, SciELO Brasil, v. 24, 2019. https://doi.org/10.1590/2318-0331.241920190023.

PRANDTL, L. Verhandlungen des dritten internationalen Mathematiker-Kongresses. *Heidelberg, Leipeizig*, p. 484–491, 1904.

PREUSSE, M.; PEETERS, F.; LORKE, A. Internal waves and the generation of turbulence in the thermocline of a large lake. *Limnology and oceanography*, Wiley Online Library, v. 55, n. 6, p. 2353–2365, 2010. https://doi.org/10.4319/lo.2010.55.6.2353.

RABINOVICH, A. B. *Seiches and harbor oscillations, Handbook of Coastal and Ocean Engineering, 193-236, edited by Y. C. Kim.* World Scientific Publ., Singapore, 2009. https://doi.org/10.1142/9789812819307_0009.

RAVENS, T. M.; KOCSIS, O.; WÜEST, A.; GRANIN, N. Small-scale turbulence and vertical mixing in Lake Baikal. *Limnology and oceanography*, Wiley Online Library, v. 45, n. 1, p. 159–173, 2000. https://doi.org/10.4319/lo.2000.45.1.0159.

READ, J. S.; HAMILTON, D. P.; JONES, I. D.; MURAOKA, K.; WINSLOW, L. A.; KROISS, R.; WU, C. H.; GAISER, E. Derivation of lake mixing and stratification indices from high-resolution lake buoy data. *Environmental Modelling \& Software*, Elsevier, v. 26, n. 11, p. 1325–1336, 2011. https://doi.org/10.1016/j.envsoft.2011.05.006.

RINKE, K.; HÜBNER, I.; PETZOLDT, T.; ROLINSKI, S.; KÖNIG-RINKE, M.; POST, J.; LORKE, A.; BENNDORF, J. How internal waves influence the vertical distribution of zooplankton. *Freshwater Biology*, Wiley Online Library, v. 52, n. 1, p. 137–144, 2007. https://doi.org/10.1111/j.1365-2427.2006.01687.x.

ROBERTS, D. C.; EGAN, G. C.; FORREST, A. L.; LARGIER, J. L.; BOMBARDELLI, F. A.; LAVAL, B. E.; MONISMITH, S. G.; SCHLADOW, G. The setup and relaxation of spring upwelling in a deep, rotationally influenced lake. *Limnology and Oceanography*, v. 66, n. 4, p. 1168–1189, 4 2021. ISSN 0024-3590. https://onlinelibrary.wiley.com/doi/10.1002/lno.11673.

RODI, W. *Turbulence models and their application in hydraulics.* [S.l.]: Routledge, 2017. ISBN 9789054101505.

ROGET, E.; KHIMCHENKO, E.; FORCAT, F.; ZAVIALOV, P. The internal seiche field in the changing South Aral Sea (2006-2013). *Hydrol Earth Syst Sci*, Copernicus GmbH, v. 21, n. 2, p. 1093, 2017. https://doi.org/10.5194/hess-21-1093-2017.

ROGET, E.; SALVADÉ, G.; ZAMBONI, F. Internal seiche climatology in a small lake where transversal and second vertical modes are usually observed. *Limnol. Oceanogr.*, Wiley Online Library, v. 42, n. 4, p. 663–673, 1997. https://doi.org/10.4319/lo.1997.42.4.0663.

ROGET, E.; SALVADÉ, G.; ZAMBONI, F.; LLEBOT, J. E. Internal waves in a small lake with a thick metalimnion. *Internationale Vereinigung für theoretische und angewandte Limnologie: Verhandlungen*, Taylor \& Francis, v. 25, n. 1, p. 91–99, 1993. https://doi.org/10.1080/03680770.1992.11900066.

ROHR, J. J.; ITSWEIRE, E. C.; HELLAND, K. N.; ATTA, C. W. V. Growth and decay of turbulence in a stably stratified shear flow. *Journal of Fluid Mechanics*, Cambridge University Press, v. 195, p. 77–111, 1988. https://doi.org/10.1017/S0022112088002332.

RUDNICK, D. L.; BOYD, T. J.; BRAINARD, R. E.; CARTER, G. S.; EGBERT, G. D.; GREGG, M. C.; HOLLOWAY, P. E.; KLYMAK, J. M.; KUNZE, E.; LEE, C. M.; others. From tides to mixing along the Hawaiian Ridge. *science*, American Association for the Advancement of Science, v. 301, n. 5631, p. 355–357, 2003. https://doi.org/10.1126/science.1085837.

RUEDA, F. J.; COWEN, E. A. Exchange between a freshwater embayment and a large lake through a long, shallow channel. *Limnology and Oceanography*, v. 50, n. 1, p. 169–183, 1 2005. ISSN 00243590.

SAGGIO, A.; IMBERGER, J. Internal wave weather in a stratified lake. *Limnology and oceanography*, Wiley Online Library, v. 43, n. 8, p. 1780–1795, 1998. https://doi.org/10.4319/lo.1998.43.8.1780.

SAKAI, Y.; MURASE, J.; SUGIMOTO, A.; OKUBO, K.; NAKAYAMA, E. Resuspension of bottom sediment by an internal wave in Lake Biwa. *Lakes \& Reservoirs: Research \& Management*, Wiley Online Library, v. 7, n. 4, p. 339–344, 2002. https://doi.org/10.1046/j.1440-1770.2002.00200.x.

SCHWEFEL, R.; GAUDARD, A.; WÜEST, A.; BOUFFARD, D. Effects of climate change on deepwater oxygen and winter mixing in a deep lake (Lake Geneva): Comparing observational findings and modeling. *Water Resour Res*, Wiley Online Library, v. 52, n. 11, p. 8811–8826, 2016. https://doi.org/10.1002/2016WR019194.

SERRA, T.; VIDAL, J.; CASAMITJANA, X.; SOLER, M.; COLOMER, J. The role of surface vertical mixing in phytoplankton distribution in a stratified reservoir. *Limnology and Oceanography*, Wiley Online Library, v. 52, n. 2, p. 620–634, 2007. https://doi.org/10.4319/lo.2007.52.2.0620.

SHIMIZU, K. A Theory of Vertical Modes in Multilayer Stratified Fluids. *Journal of Physical Oceanography*, v. 41, n. 9, p. 1694–1707, 9 2011. ISSN 0022-3670.

SHIMIZU, K. Fully nonlinear simple internal waves over subcritical slopes in continuously stratified fluids: Theoretical development. *Physics of Fluids*, v. 31, n. 1, p. 016601, 1 2019. ISSN 1070-6631.

SHIMIZU, K.; IMBERGER, J. Energetics and damping of basin-scale internal waves in a strongly stratified lake. *Limnol. Oceanogr.*, Wiley Online Library, v. 53, n. 4, p. 1574–1588, 2008.

SHINTANI, T.; FUENTE, A. D. L.; NIÑO, Y.; IMBERGER, J. Generalizations of the wedderburn number: Parameterizing upwelling in stratified lakes. *Limnology and Oceanography*, American Society of Limnology and Oceanography Inc., v. 55, n. 3, p. 1377–1389, 2010. ISSN 00243590.

SILVA, J. C. da; BUIJSMAN, M. C.; MAGALHAES, J. M. Internal waves on the upstream side of a large sill of the Mascarene Ridge: a comprehensive view of their generation mechanisms and evolution. *Deep Sea Research Part I: Oceanographic Research Papers*, Pergamon, v. 99, p. 87–104, 5 2015. ISSN 0967-0637.

SIMON, A. *Turbulent mixing in the upper layer of lakes.* [S.l.]: Erdgenössische Technische Höchschule., No. 12272, Zürich„ Switzerland, 1997.

SIMPSON, J. H.; WILES, P. J.; LINCOLN, B. J. Internal seiche modes and bottom boundary-layer dissipation in a temperate lake from acoustic measurements. *Limnology and oceanography*, Wiley Online Library, v. 56, n. 5, p. 1893–1906, 2011. https://doi.org/10.4319/lo.2011.56.5.1893.

SIMPSON, J. H.; WILES, P. J.; LINCOLN, B. J. Internal seiche modes and bottom boundary-layer dissipation in a temperate lake from acoustic measurements. *Limnology and Oceanography*, v. 56, n. 5, p. 1893–1906, 9 2011. ISSN 00243590.

SMITH, G. D.; SMITH, G. D.; SMITH, G. D. S. *Numerical solution of partial differential equations: finite difference methods.* [S.l.]: Oxford university press, 1985.

SMITH, J. O. *Introduction to digital filters: with audio applications.* [S.l.]: Julius Smith, 2007. v. 2.

SMYTH, W. D.; MOUM, J. N. Anisotropy of turbulence in stably stratified mixing layers. *Physics of Fluids*, v. 12, n. 6, p. 1343–1362, 6 2000. ISSN 1070-6631.

SPIGEL, R. H.; IMBERGER, J. The classification of mixed-layer dynamics of lakes of small to medium size. *Journal of physical oceanography*, v. 10, n. 7, p. 1104–1121, 1980. https://doi.org/10.1175/1520-0485(1980)010%3C1104:TCOMLD%3E2.0.CO;2.

STASTNA, M.; LAMB, K. G. Sediment resuspension mechanisms associated with internal waves in coastal waters. *Journal of Geophysical Research: Oceans*, Wiley Online Library, v. 113, n. C10, 2008. https://doi.org/10.1029/2007JC004711.

STELLING, G. S.; DUINMEIJER, S. P. A. A staggered conservative scheme for every Froude number in rapidly varied shallow water flows. *International journal for numerical methods in fluids*, Wiley Online Library, v. 43, n. 12, p. 1329–1354, 2003. https://doi.org/10.1002/fld.537.

STEPANENKO, V.; MAMMARELLA, I.; OJALA, A. K.; MIETTINEN, H. M.; LYKOSOV, V. N.; VESALA, T. V.; others. LAKE 2.0: a model for temperature, methane, carbon dioxide and oxygen dynamics in lakes. *Geoscientific Model Development*, 2016. https://doi.org/10.5194/gmd-9-1977-2016.

STEVENS, C.; IMBERGER, J. The initial response of a stratified lake to a surface shear stress. *Journal of Fluid Mechanics*, Cambridge University Press, v. 312, p. 39–66, 1996. https://doi.org/10.1017/S0022112096001917.

STEVENS, C.; LAWRENCE, G.; HAMBLIN, P.; CARMACK, E. Wind forcing of internal waves in a long narrow stratified lake. *Dynamics of atmospheres and oceans*, Elsevier, v. 24, n. 1-4, p. 41–50, 1996. https://doi.org/10.1016/0377-0265(95)00409-2.

STEVENS, C. L. Internal waves in a small reservoir. *J Geophys Res Oceans*, Wiley Online Library, v. 104, n. C7, p. 15777–15788, 1999. https://doi.org/10.1029/1999JC900098.

STEVENS, C. L.; LAWRENCE, G. A. Estimation of wind-forced internal seiche amplitudes in lakes and reservoirs, with data from British Columbia, Canada. *Aquatic Sciences*, Springer, v. 59, n. 2, p. 115–134, 1997. https://doi.org/10.1007/BF02523176.

SUTHERLAND, B. R. *Internal gravity waves.* Cambridge University Press, 2010. https://doi.org/10.1017/CBO9780511780318.

SUTHERLAND, B. R. Internal Waves in the Atmosphere and Ocean: Instability Mechanisms. In: *Fluid Mechanics of Planets and Stars.* Springer, 2020. p. 71–89. https://doi.org/10.1007/978-3-030-22074-7%5C_3.

THOMPSON, R. Response of a numerical model of a stratified lake to wind stress. In: *Proc. Second Int. Symp. Stratified Flows, IAHR, 1980.* [S.l.: s.n.], 1980.

THOMSON, R. E.; EMERY, W. J. *Data analysis methods in physical oceanography.* [S.l.]: Newnes, 2014.

THORPE, S. A. Turbulence and mixing in a Scottish loch. *Philosophical Transactions of the Royal Society of London. Series A, Mathematical and Physical Sciences*, The Royal Society London, v. 286, n. 1334, p. 125–181, 1977. https://doi/abs/10.1098/rsta.1977.0112.

THORPE, S. A. The near-surface ocean mixing layer in stable heating conditions. *Journal of Geophysical Research: Oceans*, Wiley Online Library, v. 83, n. C6, p. 2875–2885, 1978. https://doi.org/10.1029/JC083iC06p02875.

THORPE, S. A. On the interactions of internal waves reflecting from slopes. *Journal of physical oceanography*, v. 27, n. 9, p. 2072–2078, 1997. https://doi.org/10.1175/1520-0485(1997)027%3C2072:OTIOIW%3E2.0.CO;2.

THORPE, S. A. *The turbulent ocean.* [S.l.]: Cambridge University Press, 2005.

THORPE, S. A.; HALL, A.; CROFTS, I. The internal surge in Loch Ness. *Nature*, Nature Publishing Group, v. 237, n. 5350, p. 96, 1972. https://doi.org/10.1038/237096b0.

THORPE, S. A.; KEEN, J. M.; JIANG, R.; LEMMIN, U. High-frequency internal waves in Lake Geneva. *Phil. Trans. R. Soc. Lond. A*, The Royal Society, v. 354, n. 1705, p. 237–257, 1996. https://doi.org/10.1098/rsta.1996.0008.

TORRENCE, C.; COMPO, G. P. A practical guide to wavelet analysis. *Bulletin of the American Meteorological society*, v. 79, n. 1, p. 61–78, 1998. https://doi.org/10.1175/1520-0477(1998)079%3C0061:APGTWA%3E2.0.CO;2.

TOWNSEND, A. A. Natural convection in water over an ice surface. *Quarterly Journal of the Royal Meteorological Society*, Wiley Online Library, v. 90, n. 385, p. 248–259, 1964. https://doi.org/10.1002/qj.49709038503.

TROY, C. D.; KOSEFF, J. R. The viscous decay of progressive interfacial waves. *Physics of Fluids*, AIP, v. 18, n. 2, p. 26602, 2006. https://doi.org/10.1063/1.2166849.

UITTENBOGAARD, R. E.; KESTER, J. V.; STELLING, G. S. Implementation of three turbulence models in 3D-TRISULA for rectangular grids. *Report Z81, Delft Hydraulics*, 1992.

ULLOA, H. N.; CONSTANTINESCU, G.; CHANG, K.; HORNA-MUNOZ, D.; STEINER, O. S.; BOUFFARD, D.; WÜEST, A. Hydrodynamics of a periodically wind-forced small and narrow stratified basin: a large-eddy simulation experiment. *Environmental Fluid Mechanics*, v. 19, n. 3, p. 667–698, 6 2019. ISSN 1567-7419.

UMLAUF, L.; LEMMIN, U. Interbasin exchange and mixing in the hypolimnion of a large lake: The role of long internal waves. *Limnol. Oceanogr.*, Wiley Online Library, v. 50, n. 5, p. 1601–1611, 2005. https://doi.org/10.4319/lo.2005.50.5.1601.

VALBUENA, S. A.; BOMBARDELLI, F. A.; CORTÉS, A.; LARGIER, J. L.; ROBERTS, D. C.; FORREST, A. L.; SCHLADOW, S. G. 3D Flow Structures During Upwelling Events in Lakes of Moderate Size. *Water Resources Research*, v. 58, n. 3, 3 2022. ISSN 0043-1397. https://onlinelibrary.wiley.com/doi/10.1029/2021WR030666.

VALERIO, G.; CANTELLI, A.; MONTI, P.; LEUZZI, G. A modeling approach to identify the effective forcing exerted by wind on a prealpine lake surrounded by a complex topography. *Water Resources Research*, Wiley Online Library, v. 53, n. 5, p. 4036–4052, 2017. https://doi.org/10.1002/2016WR020335.

VALERIO, G.; PILOTTI, M.; LAU, M. P.; HUPFER, M. Oxycline oscillations induced by internal waves in deep Lake Iseo. *Hydrology and Earth System Sciences*, v. 23, n. 3, p. 1763–1777, 4 2019. ISSN 1607-7938.

VALERIO, G.; PILOTTI, M.; MARTI, C. L.; IMBERGER, J. r. The structure of basin-scale internal waves in a stratified lake in response to lake bathymetry and wind spatial and temporal distribution: Lake Iseo, Italy. *Limnology and Oceanography*, Wiley Online Library, v. 57, n. 3, p. 772–786, 2012. https://doi.org/10.4319/lo.2012.57.3.0772.

VIDAL, J.; CASAMITJANA, X. Forced resonant oscillations as a response to periodic winds in a stratified reservoir. *Journal of Hydraulic Engineering*, American Society of Civil Engineers, v. 134, n. 4, p. 416–425, 2008. https://doi.org/10.1061/(ASCE)0733-9429(2008)134:4(416).

VIDAL, J.; CASAMITJANA, X.; COLOMER, J.; SERRA, T. The internal wave field in Sau reservoir: Observation and modeling of a third vertical mode. *Limnol. Oceanogr.*, Wiley Online Library, v. 50, n. 4, p. 1326–1333, 2005. https://doi.org/10.4319/lo.2005.50.4.1326.

VIDAL, J.; MACINTYRE, S.; MCPHEE-SHAW, E. E.; SHAW, W. J.; MONISMITH, S. G. Temporal and spatial variability of the internal wave field in a lake with complex morphometry. *Limnology and Oceanography*, v. 58, n. 5, p. 1557–1580, 9 2013. ISSN 00243590.

VIDAL, J.; RUEDA, F. J.; CASAMITJANA, X. The seasonal evolution of high vertical-mode internal waves in a deep reservoir. *Limnology and oceanography*, Wiley Online Library, v. 52, n. 6, p. 2656–2667, 2007. https://doi.org/10.4319/lo.2007.52.6.2656.

WADZUK, B. M.; HODGES, B. R. Hydrostatic versus nonhydrostatic Euler-equation modeling of nonlinear internal waves. *Journal of engineering mechanics*, American Society of Civil Engineers, v. 135, n. 10, p. 1069–1080, 2009. https://doi.org/10.1061/(ASCE)0733-9399(2009)135:10(1069).

WANG, Y.; HUTTER, K.; BÄUERLE, E. Wind-induced baroclinic response of Lake Constance. In: SPRINGER. *Annales Geophysicae*. 2000. v. 18, n. 11, p. 1488–14501. https://doi.org/10.1007/s00585-000-1488-6.

WATSON, E. R. Internal oscillation in the waters of Loch Ness. *Nature*, v. 69, p. 174, 1903. https://doi.org/10.1038/069174a0.

WATSON, E. R. Movements of the waters of Loch Ness, as indicated by temperature observations. *The Geographical Journal*, JSTOR, v. 24, n. 4, p. 430–437, 1904.

WEDDERBURN, E. M. Temperature Observations in Loch Earn; with a further Contribution to the Hydrodynamical Theory of the Temperature Seiche. *Earth and Environmental Science Transactions of The Royal Society of Edinburgh*, Royal Society of Edinburgh Scotland Foundation, v. 48, n. 3, p. 629–695, 1912. https://doi.org/10.1017/S0080456800015842.

WELCH, P. The use of fast Fourier transform for the estimation of power spectra: a method based on time averaging over short, modified periodograms. *IEEE Transactions on audio and electroacoustics*, IEEE, v. 15, n. 2, p. 70–73, 1967. https://doi.org/10.1109/TAU.1967.1161901.

WELLS, A. Variations in sea surface temperature due to near surface straining flow. Citeseer, 2007. https://doi.org/10.1175/2009JPO3980.1.

WETZEL, R. G. *Limnology: lake and river ecosystems.* [S.l.]: Gulf Professional Publishing, 2001.

WHITE, B. L.; HELFRICH, K. R. Gravity currents and internal waves in a stratified fluid. *Journal of Fluid Mechanics*, Cambridge University Press, v. 616, p. 327–356, 2008. https://doi.org/10.1017/S0022112008003984.

WHITHAM, G. B.; FOWLER, R. G. Linear and nonlinear waves. *Physics Today*, v. 28, p. 55, 1975.

WILES, P. J.; RIPPETH, T. P.; SIMPSON, J. H.; HENDRICKS, P. J. A novel technique for measuring the rate of turbulent dissipation in the marine environment. *Geophysical Research Letters*, Wiley Online Library, v. 33, n. 21, 2006. https://doi.org/10.1029/2006GL027050.

WU, J. The sea surface is aerodynamically rough even under light winds. *Boundary-Layer Meteorology*, Springer, v. 69, n. 1-2, p. 149–158, 1994. https://doi.org/10.1007/BF00713300.

WÜEST, A.; LORKE, A. Small-scale hydrodynamics in lakes. *Annual Review of fluid mechanics*, Annual Reviews 4139 El Camino Way, PO Box 10139, Palo Alto, CA 94303-0139, USA, v. 35, n. 1, p. 373–412, 2003. https://doi.org/10.1146/annurev.fluid.35.101101.161220.

WÜEST, A.; LORKE, A. Small-scale turbulence and mixing: Energy fluxes in stratified lakes. *Encyclopedia of inland waters*, Elsevier, v. 1, n. BOOK_CHAP, p. 628–635, 2009. https://doi.org/10.1016/B978-012370626-3.00084-3.

WÜEST, A.; PIEPKE, G.; SENDEN, D. C. V. Turbulent kinetic energy balance as a tool for estimating vertical diffusivity in wind-forced stratified waters. *Limnology and Oceanography*, Wiley Online Library, v. 45, n. 6, p. 1388–1400, 2000. https://doi.org/10.4319/lo.2000.45.6.1388.

YAN, N.; PAWSON, T. Changes in the crustacean zooplankton community of Harp Lake, Canada, following invasion by Bythotrephes cederstroemi. *Freshw. Biol.*, Wiley Online Library, v. 37, n. 2, p. 409–425, 1997. https://doi.org/10.1046/j.1365-2427.1997.00172.x.

YAN, N. D.; STRUS, R. Crustacean zooplankton communities of acidic, metal-contaminated lakes near Sudbury, Ontario. *Can. J. Fish. Aquat. Sci.*, NRC Research Press, v. 37, n. 12, p. 2282–2293, 1980. https://doi.org/10.1139/f80-275.

YEATES, P. S.; GÓMEZ-GIRALDO, A.; IMBERGER, J. Observed relationships between microstructure patches and the gradient Richardson number in a thermally stratified lake. *Environmental Fluid Mechanics*, v. 13, n. 3, p. 205–226, 6 2013. ISSN 1567-7419.

YOUNG, J. D.; LOEW, E. R.; YAN, N. D. Examination of direct daytime predation by Coregonus artedi on Bythotrephes longimanus in Harp Lake, Ontario, Canada: no evidence for the refuge hypothesis. *Can. J. Fish. Aquat. Sci.*, NRC Research Press, v. 66, n. 3, p. 449–459, 2009. https://doi.org/10.1139/F09-006.

APPENDIX A – Linearization

The linearization procedure adopted in section 2.2.1 for both internal wave models results not only in a linear solution, but also in a solution valid for small-amplitude waves only. It is intuitive to think that the linearization procedure neglects non-linear terms, and as a consequence, the solution found just describes linear waves. But the reason why a linear solution leads to small-amplitude wave can be reveled through a the dimension analysis. This technique can be applied for all linearization procedure adopted in section 2.2.1, but we demonstrate it just for the mass conservation equation:

$$\frac{\partial \rho}{\partial t} + u_i \frac{\partial \rho}{\partial x_i} = -w \frac{\partial \overline{\rho}}{\partial z}, \tag{A.1}$$

in which ρ is the water density and $\overline{\rho}$ is the mean component of density.

Firstly, equation A.1 can be presented in a non-dimensional form using the following transformation variables:

$$\rho = \widetilde{\rho}\ \rho^* \qquad\qquad \overline{\rho} = \rho_o\ \overline{\rho}^*, \tag{A.2a}$$

$$u_i = a/T\ u_i^* \qquad\qquad x_i = \lambda x_i^* \qquad\qquad t = Tt^*, \tag{A.2b}$$

in which T is the wave period, a is the wave amplitude, λ is the wavelength, and ρ_o and $\widetilde{\rho}$ are the unperturbed and perturbed fluid density modulated by the dimensionless form, respectively. Variable denoted by * has no dimension.

Substitution of equations A.2 into A.1, gives us

$$\frac{\widetilde{\rho}}{T} \frac{\partial \rho^*}{\partial t^*} + \frac{a\ \widetilde{\rho}}{T\lambda} u_i^* \frac{\partial \rho^*}{\partial x_i^*} = -\frac{a\rho_o}{T\lambda} w^* \frac{\partial \overline{\rho}^*}{\partial z^*},$$

$$\frac{\partial \rho^*}{\partial t^*} + \cancelto{a \ll \lambda}{\frac{a}{\lambda}} u_i^* \frac{\partial \rho^*}{\partial x_i^*} = -\frac{a\ \rho_o}{\lambda\ \widetilde{\rho}} w^* \frac{\partial \overline{\rho}^*}{\partial z^*},$$

$$\frac{\partial \rho^*}{\partial t^*} + \frac{a}{\lambda} u_i^* \frac{\partial \rho^*}{\partial x_i^*} = -\frac{a\ \rho_o}{\lambda\ \widetilde{\rho}} w^* \frac{\partial \overline{\rho}^*}{\partial z^*}, \tag{A.3}$$

in which terms with order $\mathcal{O}(a/\lambda)$ can be neglected for small-amplitude waves ($a \ll \lambda$). Note that we cannot neglect the last term of equation A.3 because even though $a \ll \lambda$, the therm is counterbalanced by $\rho_o/\widetilde{\rho}$.

Considering the linearization procedure and rewriting equation A.3 in terms of dimensional variables, we obtain

$$\frac{\partial \rho}{\partial t} = -w \frac{\partial \overline{\rho}}{\partial z}, \tag{A.4}$$

which is exactly the same equation if we neglect directly the non-linear term from equation A.1.

APPENDIX B – Rectangular shaped-box simulations

This appendix contains detailed parameters used to simulate the evolution of basin-scale internal waves in Delft3D. Tables 3 and 4 present general data and processed results from all 32 simulated cases, including general parameters of boundary conditions, theoretical results for vertical displacement and degeneration regime.

We used the three-dimensional hydrodynamic model Delft3D-FLOW, which solves the shallow water equations using the hydrostatic assumption (HYDRAULICS, 2003). Although Delft3D model may fails to reproduce the internal wave breaking and most of degeneration regimes, it has already been used to describe internal seiche in real lakes and reservoir (DISSANAYAKE; HOFMANN; PEETERS, 2019).

Simulation	h_e	h_e/H	$E_{\text{dissipation}}$	ζ_o	$Ri_{\min}\ h_e/L$	$Ri_{\max}\ h_e/L$	$Ri\ h_e/L$	ζ_o/h_e
1	7	0.47	-	-	0.685	171.163	0.305	-
2	7	0.47	62.3%	3.360	0.685	171.163	0.939	0.4800
3	7	0.47	76.9%	2.415	0.685	171.163	1.605	0.3450
4	7	0.47	84.6%	1.735	0.685	171.163	2.333	0.2479
5	7	0.47	67.4%	1.205	0.685	171.163	3.119	0.1721
6	7	0.47	57.4%	0.850	0.685	171.163	3.950	0.1214
7	6	0.40	-	-	0.645	143.444	0.242	-
8	6	0.40	54.4%	3.575	0.645	143.444	0.764	0.5958
9	6	0.40	73.0%	2.725	0.645	143.444	1.285	0.4542
10	6	0.40	80.3%	1.965	0.645	143.444	1.849	0.3275
11	6	0.40	80.4%	1.425	0.645	143.444	2.455	0.2375
12	6	0.40	64.7%	0.980	0.645	143.444	3.106	0.1633
13	4	0.27	-	-	0.584	106.159	0.102	-
14	4	0.27	49.8%	4.960	0.584	106.159	0.447	1.2400
15	4	0.27	38.0%	3.270	0.584	106.159	0.702	0.8175
16	4	0.27	43.5%	2.310	0.584	106.159	0.972	0.5775
17	4	0.27	63.0%	1.940	0.584	106.159	1.259	0.4850
18	4	0.27	80.6%	1.680	0.584	106.159	1.562	0.4200
19	2	0.13	-	-	0.537	82.629	0.049	-
20	2	0.13	-	-	0.537	82.629	0.239	-
21	2	0.13	-	-	0.537	82.629	0.432	-
22	2	0.13	-	-	0.537	82.629	0.547	-
23	2	0.13	43.1%	2.655	0.537	82.629	0.658	1.3275
24	2	0.13	45.5%	2.400	0.537	82.629	0.772	1.2000
25	9	0.60	88.5%	4.270	0.791	263.523	1.290	0.4744
26	9	0.60	68.1%	4.135	0.791	263.523	0.192	0.4594
27	9	0.60	34.9%	3.540	0.791	263.523	0.095	0.3933

Simulation	h_e	h_e/H	$E_{\text{dissipation}}$	ζ_o	$Ri_{\min}\ h_e/L$	$Ri_{\max}\ h_e/L$	$Ri\ h_e/L$	ζ_o/h_e
28	9	0.60	75.9%	4.300	0.791	263.523	0.153	0.4778
29	11	0.73	62.2%	2.622	0.968	484.123	0.126	0.2384
30	11	0.73	72.6%	2.676	0.968	484.123	0.232	0.2432
31	11	0.73	109.5%	2.880	0.968	484.123	1.400	0.2618
32	11	0.73	69.5%	2.390	0.968	484.123	0.295	0.2173

Table 3 – Summary of collected data from simulated cases. h_e and H indicate the epilimnion and total water depth, respectively. $E_{\text{dissipation}}$ represents the internal wave energy that is dissipated in the first wave cycle. ζ_o is the measured initial vertical displacement.$Ri_{\min}\ h_e/L$ and $Ri_{\max}\ h_e/L$ are the minimum and maximum values from theoretical results in which internal wave activity should be dominant in the lake interior, respectively. $Ri\ h_e/L$ was obtained from numerical results.

The implemented model operated in a horizontal Cartesian grid cells of 90 m × 90 m and 50 fixed layers, with no heat flux at water surface. For the turbulence closure scheme, vertical eddy diffusivity and viscosity was calculated using the $k - \epsilon$ model. The coefficients of background vertical and horizontal viscosity and diffusivity were considered as calibration coefficients and were kept fixed during the simulation. Considering the stability condition, specified by the Courant-Friedrichs number, we used a time step of 1 minutes to simulate approximately 10 days.

Although Delft3D fails to describe most of the degeneration process of BSIW, Figure 50 highlights the evolution of the internal bore generated after the degeneration of the basin-scale internal wave detected in simulation 23 (Figure 24b). The degeneration regime evidenced in the simulation matches with theoretical results (HORN; IMBERGER; IVEY, 1998; HORN; IMBERGER; IVEY, 2001).

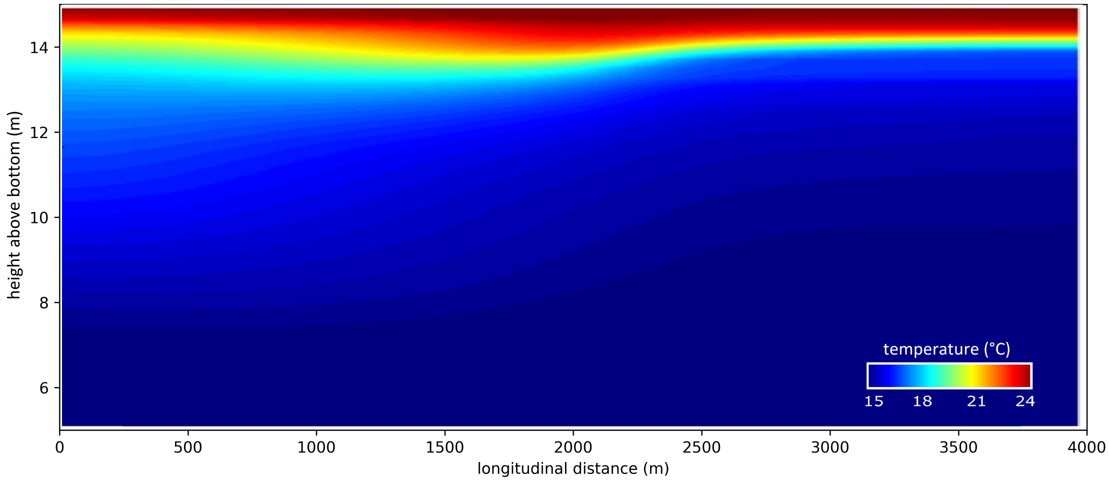

Figure 50 – Internal bore generated as a result of the degeneration process of basin-scale internal wave (Simulation: Run 23)

Simulation	ζ_o/h_e			Obs. regime	Degeneration
	linear theory	parametrization (Eq. 3.8)			
		$g(h_e/H)_{\text{lin}}$	$g(h_e/H)_{\text{pol}}$		
1	-	-	-	mixing	supercritical and billows

Simulation	ζ_o/h_e linear theory	ζ_o/h_e parametrization (Eq. 3.8)		Obs. regime	Degeneration
		$g(h_e/H)_{\text{lin}}$	$g(h_e/H)_{\text{pol}}$		
2	0.5322	0.4128	0.4463	BSIW	K-H billows
3	0.3115	0.2913	0.3090	BSIW	solitary waves
4	0.2143	0.2105	0.2193	BSIW	solitary waves
5	0.1603	0.1583	0.1624	BSIW	solitary waves
6	0.1266	0.1262	0.1278	BSIW	solitary waves
7	-	-	-	mixing	supercritical and billows
8	0.6547	0.5993	0.5627	BSIW	supercritical and billows
9	0.3893	0.4272	0.4059	BSIW	K-H billows
10	0.2704	0.3080	0.2961	BSIW	solitary waves
11	0.2037	0.2272	0.2208	BSIW	solitary waves
12	0.1610	0.1728	0.1695	BSIW	solitary waves
13	-	-	-	mixing	supercritical and billows
14	1.1197	1.2412	0.9802	BSIW	supercritical and billows
15	0.7118	0.9893	0.7981	BSIW	supercritical and billows
16	0.5144	0.7882	0.6495	BSIW	solitary waves
17	0.3971	0.6269	0.5278	BSIW	solitary waves
18	0.3201	0.4995	0.4296	BSIW	solitary waves
19	-	-	-	mixing	supercritical and billows
20	-	-	-	mixing	supercritical and billows
21	-	-	-	mixing	supercritical and billows
22	-	-	-	mixing	supercritical and billows
23	0.7601	1.1174	1.2520	BSIW	Supercritical
24	0.6479	1.0092	1.1253	BSIW	Supercritical
25	0.3876	0.2345	0.2949	BSIW	solitary waves
26	2.6042	0.3654	0.5177	BSIW	supercritical and billows
27	5.2632	0.3817	0.5472	BSIW	supercritical and billows
28	3.2680	0.3718	0.5293	BSIW	supercritical and billows
29	3.9683	0.3137	0.2433	BSIW	supercritical and billows
30	2.1552	0.3011	0.2357	BSIW	supercritical and billows
31	0.3571	0.2016	0.1725	BSIW	solitary waves
32	1.6949	0.3539	0.4080	BSIW	supercritical and billows

Table 4 – Summary of processed results from simulated cases. Linear theory indicates the ζ_o/h_e obtained from linear theory (SPIGEL; IMBERGER, 1980). $g(h_e/H)_{\text{lin}}$ and $g(h_e/H)_{\text{pol}}$ represents the ζ_o/h_e estimated by the parametrized equation (Eq. 3.8) using the linear and polynomial expression of g-function, respectively. *Obs. regime* indicates the observed regime of lake mixing, whilst the *Degeneration* describes, according to theoretical results derived from Horn, Imberger and Ivey (1998), the regimes for internal seiches degeneration.

APPENDIX C – Harp Lake

For time being this appendix highlights only one period of basin-scale internal wave activity in Harp Lake. For Harp Lake, the basin-scale internal waves were excited in summer and spring in the North Hemisphere. The highlighted sub-period is comprised between September 16 and October 20, 2013.

We selected the period from 25th of September to 4th of October since it presented low Ri due to the strong wind events, with mean wind speed > 3.5 m/s and peaks that reached almost 6 m/s. Homogeneous wind events presented duration of approximately 11 h blowing 169 ° North. The thermal stratification was constant during the period, $\Delta\tau \approx 15$ °C. The strong wind events decreased the Ri from 10^6 to 10^3, which lead to the formation of basin-scale internal waves. According to the criteria established by Spigel and Imberger (1980), the reduction of Ri value leads to a lake regime of internal seiche dominance. Although it is not a full proof of their existence, this theory gives indication of their generation.

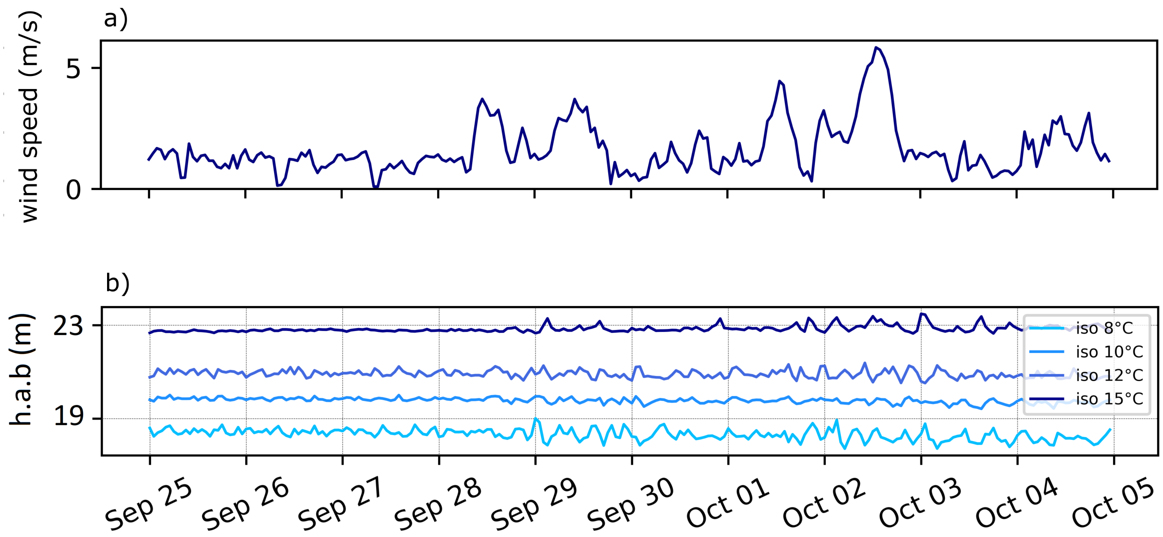

Figure 51 – Thermal and wind speed condition in Harp Lake. a) Wind speed time series (Harp Lake; 25/09 – 04/10). b) Isotherms time-series in height above the bottom (h.a.b.)

Considering the analyzed period, oscillatory motion was observed mainly in the 8 °C isotherm, located approximately 1 m below the mean thermocline depth (≈ 7 m above the water surface). The first event occurred between September 28 and 30, whilst the second and stronger one was detected in the last five days of the analyzed sub-period, from 1st to 5th of October, 2013. The first one presents mean wind intensity of 2.7 m/s, whereas the second one a mean wind speed of 3.5 m/s (Figure 51a). Both periods present low Ri and, according to Spigel and Imberger (1980), were susceptible to internal seiche formations. Although the Ri does not account the wind direction to analyze the excitation of internal waves, the period presents homogeneous wind events, with mean wind direction to 120° and 270° North, respectively. Stronger wind events provided higher oscillations, with vertical displacement reaching 1.2 m, whilst the first period presented maximum vertical displacement of 0.6 m.

Figure 52a shows results of the multi-layer hydrostatic linear model with free surface and the power spectral density of isotherms time series. The power spectral density of 8 °C isotherm shows two prominent peaks (Figure 52a). Peak (I) and (II) are above the mean red noise spectrum, presenting period of 5 h 30 and 4 h 30, respectively. Both periods are close and compatible with the first two vertical modes. Both modes showed similar results since the thermal structure of Harp Lake during this period of analysis is characterized by a thin metalimnion (Figure 52c).

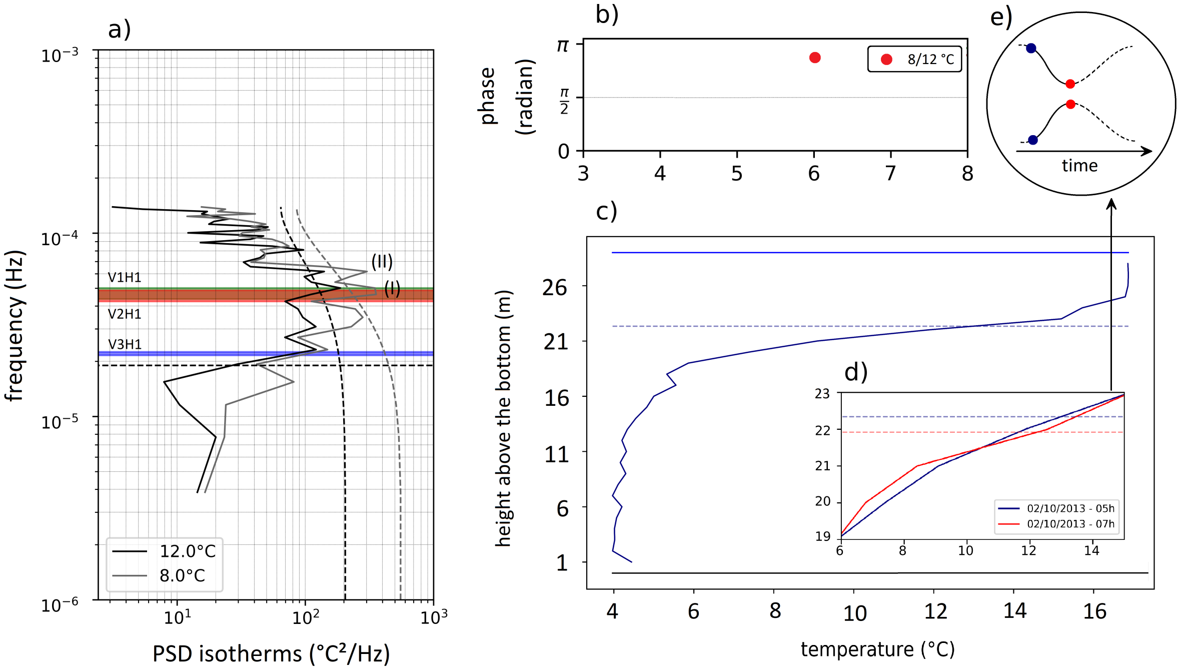

Figure 52 – a) Power spectral density of the isotherms of 12 °C and 8 °C. Dashed lines show the mean red noise spectrum for the time series, indicating significant peaks at a 95% confidence level. b) spectral phase analyses considering just coherence higher than 80% (Harp Lake; 25/09 – 05/10), c) Vertical temperature profile obtained from Harp Lake in 2nd of October 2013 at 5 a.m., d) Zoom-in view of the temperature profile with a second profile 2 h late, which is approximately half of the internal seiche period. At 22 m above the bottom the water becomes warmer, which leads to an erosion of the 12 °C isotherm due to internal seiche passage. However, 2 m bellow that point, the water becomes colder due to the elevation of the 8 °C isotherm, that was caused by the oscillation of the second interface, clearly out-of-phase with the 12 °C isotherm. e) a sketch of the V2 mode that is presented in item (d).

The 4 h 30 peak (Figure 52a; peak I), has lower spectral energy compared to the peak (II), that has periodicity of 5 h 30. It indicates that the 4 h 30 fluctuation occurred between September 28 and 30 due to wind event of 2.7 m/s. The phase analysis indicates that the 8 °C and 12 °C isotherms propagates out-of-phase (Figure 52b), suggesting the occurrence of a higher baroclinic internal wave. The out-of-phase structure may also be observed through Figure 51b from 1st to 5th of October. However, the detection of the out-of-phase structure is harder for the first period, since the internal seiche amplitude is lower. In both periods the V2H1 mode was more pronounced below the thermocline, in the 8 °C isotherm, and barely detectable at the 10 °C isotherm.

The second vertical mode affects the vertical temperature profile as shown in Figure 52d, generating vertical displacement in opposite directions. This motion occurs repeatedly, as illustrated schematically in Figure 52e, until the complete internal seiche dissipation.

APPENDIX D – Additional calculation

D.1 wind parameters

The friction velocity of the wind is computed as in Read et al. (2011):

$$u_* = \sqrt{\frac{\sigma_{\text{wind}}}{\rho_e}}, \tag{D.1}$$

in which the ρ_e is the mean water density in the epilimnion (kg/m^3) and σ_{wind} is the wind shear stress (N/m^2). The shear stress can be estimated from bulk atmospheric scaling as (WÜEST; LORKE, 2003):

$$\sigma_{\text{wind}} = C_D \rho_{\text{atm}} U_{10}^2, \tag{D.2}$$

in which $\rho_{\text{atm}} = 1.225$ kg/m^3 is the density of air, U_{10} is the wind speed measured at 10 m above the water surface, and C_D is the surface drag coefficient (-):

$$\begin{aligned} C_D &= 1.0\ 10^{-3} \quad \text{for} \quad U_{10} < 5 \text{ m/s} \\ C_D &= 1.5\ 10^{-3} \quad \text{for} \quad U_{10} \geq 5 \text{ m/s} \end{aligned}$$

D.2 Thermocline depth and metalimnion boundaries

The thermocline depth (Z_τ) is estimated using a similar procedure as described by Read et al. (2011), which is based on the vertical derivative of measured temperature profiles:

$$Z_\tau = z_{j+1}\left(\frac{\gamma'}{\gamma' + \gamma''}\right) + z_j\left(\frac{\gamma''}{\gamma' + \gamma''}\right), \tag{D.3}$$

in which

$$\gamma' = \frac{z_j - z_{j+2}}{2\left(\frac{\rho_{j+1}-\rho_j}{z_j - z_{j+1}} - \frac{\rho_{j+2}-\rho_{j+1}}{z_{j+1}-z_{j+2}}\right)} \tag{D.4}$$

and

$$\gamma'' = \frac{z_{j-1} - z_{j+1}}{2\left(\frac{\rho_{j+1}-\rho_j}{z_j - z_{j+1}} - \frac{\rho_j-\rho_{j-1}}{z_{j-1}-z_j}\right)}, \tag{D.5}$$

where the index j-index refers to that position of discrete measurements along the vertical profile for which the maximum density gradient was observed between j and $j+1$. ρ_j and z_j indicate the density and depth of discrete measurements, respectively.

As an initial guess, the upper boundary of the metalimnion is defined as the depth at which the observed density gradients fall below the metalimnion threshold value ($\delta_{\min}$) for the first time (starting from the thermocline depth upward). The value is subsequently refined by taking the density gradients at the upper and lower boundaries into account:

$$Z_{\mathrm{e}} = \frac{z_i + z_{i-1}}{2} + 0.5\left(\delta_{\min} - \hat{\varrho}\right)\frac{z_{i-1} + z_{i+1}}{\Delta\hat{\varrho}_e}, \tag{D.6}$$

in which

$$\Delta\hat{\varrho}_e = \hat{\varrho} - \frac{\rho_{i+1} - \rho_i}{z_{i+1} - z_i},$$

and

$$\hat{\varrho} = \frac{\rho_i - \rho_{i-1}}{z_i - z_{i-1}}.$$

Similarly, the lower boundary of the metalimnion is defined by the same procedure as for the upper boundary, except that the first occurrence of density gradients below the metalimnion threshold is estimated from the thermocline depth downward:

$$Z_{\mathrm{h}} = \frac{z_{i-1} + z_{i-2}}{2} + 0.5\left(\delta_{min} + \Delta\hat{\varrho_h} - \hat{\varrho}\right)\frac{z_i - z_{i-2}}{\Delta\hat{\varrho_h}}, \tag{D.7}$$

in which $\hat{\varrho_h}$ is given as

$$\Delta\hat{\varrho_h} = \hat{\varrho} - \frac{\rho_{i-1} - \rho_{i-2}}{z_{i-1} - z_{i-2}}$$

D.3 Mean wind direction

The wind direction is averaged following Grange (2014). Firstly, the wind vector components is calculated by

$$\langle u\rangle_t = -\langle u\ \sin\theta\rangle_t,$$

$$\langle v\rangle_t = -\langle u\ \sin\theta\rangle_t,$$

in which u is the wind speed, θ is the wind direction adjusted from the Nautical coordination (radians), and $\langle\rangle_t$ indicates the time average.

The mean wind direction $\bar{\theta}$ is obtained as:

$$\bar{\theta} = \arctan\left(\frac{\vec{u}}{\vec{v}}\right) + Y, \tag{D.8}$$

in which $Y = 180$ when the first argument of equation D.8 is lower than 180, whilst $Y = -180$ when the first argument is grater than 180.

D.4 Equation of state

Water density is calculated according to Chen and Millero (1986), assuming negligible contributions of pressure and solutes:

$$\rho(\tau) = a_0 + a_1\tau - a_2\tau^2 + a_3\tau^3 - a_4\tau^4 + a_5\tau^5, \tag{D.9}$$

in which ρ is the water density expressed in kg/m^3, τ is the water temperature in °C, and

$$\begin{aligned}
a_0 &= 999.84\ \mathrm{kg/m^3},\\
a_1 &= 6.794\ \mathrm{kg/m^3/^\circ C},\\
a_2 &= 9.095\ \mathrm{kg/m^3/^\circ C^2},\\
a_3 &= 1.002\ \mathrm{kg/m^3/^\circ C^3},\\
a_4 &= 1.120\ \mathrm{kg/m^3/^\circ C^4},\\
a_5 &= 6.536\ \mathrm{kg/m^3/^\circ C^5}.
\end{aligned}$$

D.5 Multi-layer internal wave model

The inviscid, linearized, one-dimensional momentum equation for layer i is given by

$$\frac{\partial u_i}{\partial t} + \frac{1}{\rho_i}\frac{\partial p_i}{\partial x} = 0, \tag{D.10}$$

in which ρ is the water density, p is the hydrostatic pressure, and the subscript i varies between 1 and N, where N is the maximum layer number.

The linearized equation describing mass-conservation in layer i is obtained through the expansion the non-dimensional mass-conservation equation in a Taylor series, considering $a_i \ll \lambda$, where a is the wave amplitude and λ is the wave length:

$$(-1)^{j+1}\frac{\partial}{\partial t}\Bigg(\zeta_i - \zeta_{i+1}\Bigg) + H_i\frac{\partial u_i}{\partial x} = 0, \tag{D.11}$$

in which ζ is the interfacial displacement, and H_i and u_i are the thickness and long velocity of layer i, respectively. The subscript j is used to account the contribution of other layers on layer $-i$.

Combining equations D.10 and D.11 to eliminate u, gives:

$$\frac{\partial^2}{\partial t^2}(\zeta_i - \zeta_{i+1}) - gH_i\sum_{j=1}^{N}\left(\frac{\rho_{i,j}}{\rho_i}\right)\frac{\partial^2}{\partial x^2}(\zeta_i - \zeta_{i+1}) = 0, \tag{D.12}$$

where $\rho_{i,j}$ is the density of the layer i when $j \geq i$ whilst for $j < i$, the $\rho_{i,j} = \rho_j$.

The wave equation D.12 is a second order partial differential equation system. By simplification, the equation reduces to a second-order linear ordinary differential equation, which is a classical Sturm-Liouville eigenvalue problem. Combining the horizontal eigenvalue problem with the phase speed yields the dispersion relation

$$\omega_{n,m}^2 = c^2\frac{4\pi^2}{\lambda_m^2}, \tag{D.13}$$

where ω is the angular frequency of the wave, $c^2 = g\ \beta_n$ is the phase speed of vertical mode n, and the λ_m is the wave length of horizontal mode m.

Considering the lateral boundary condition of a basin, the dispersion relation, equation D.13, in terms of the internal wave period $T_{n,m}$, becomes

$$T_{n,m} = \frac{\lambda}{c} = \frac{2L}{m\sqrt{g\beta_n}}, \tag{D.14}$$

in which L is the basin length that is aligned with the wind direction and $\lambda = 2\ L/m$ is the wave length, obtained from the vertical boundaries conditions. Each solution of equation D.14 represents a different vertical n and horizontal m mode. Interwave Analyzer just presents solutions for the first three vertical baroclinic modes, considering the system division explained in section D.2 and D.6.

D.6 Decomposition model

The model decomposition is used to define the thermal structure for higher vertical modes ($> V2$). The solution is obtained through the linear internal wave equation:

$$\frac{\partial^2 \phi}{\partial z^2} + k^2 \frac{N^2(z) - \omega^2}{\omega^2} \phi = 0, \tag{D.15}$$

in which ϕ is the potential velocity, N is the buoyancy frequency, k is the wavenumber and ω is the wave frequency.

Equation D.15 is solved considering the rigid-lid boundary conditions, in which $\phi = 0$ at vertical boundaries.The discretized version can be write with a tri-diagonal matrix (D):

$$\vec{D}\phi = c^2 \phi, \tag{D.16}$$

where c is the eigenvalues to be determined. The solution provides theoretical velocity structure for basin-scale internal wave modes. Based on vertical nodes ($v = 0$), the program calculates the thickness of each layer. The number of internal seiche modes is limited by the number of sensor deployed in the thermistor chain.

D.7 Spectral analysis

Interwave analyzer estimates the power spectral density based on Welch's method (WELCH, 1967), which computes an estimate of the PSD by dividing the time-series into overlapping segments. The PSD can be obtained though the ratio of sampling frequency and the mean-square power spectrum of each segment, which is obtained though the Fourier transform of the auto-covariance function,

$$\phi_{ff}(\omega) = \phi^*_{ff} \times T_s \equiv \frac{T_s}{M} |\mathscr{F}\{f(n)\}|^2. \tag{D.17}$$

in which $\phi_{ff}(\omega)$ is the PSD of the function $f(n)$, ϕ^*_{ff} is mean-square power spectrum of the function $f(n)$, T_s is the sampling period, and M is the signal length.

To obtain the PSD, the $\phi_{ff}(\omega)$ is averaged, powered by two, and normalized by the frequency bandwidth to obtain the power spectral density of the signal.

The coherence and phase lag between two signals can be obtained using the mean-square power spectrum of each signal and the cross power spectrum, ϕ^*_{fg}. Considering two signals f and g, the coherence is given as

$$C_{fg}(\omega) = \left| \frac{\phi^*_{fg}(\omega)}{\sqrt{\phi^*_{ff}(\omega)\ \phi^*_{gg}(\omega)}} \right|^2 \quad \in [0, 1], \tag{D.18}$$

in which ϕ_{fg} is the cross-power spectral density (CPSD) of signal $f(n)$ and $g(n)$, and ϕ^*_{ff} and ϕ^*_{gg} are the mean-square power spectrum of functions $f(n)$ and $g(n)$, respectively.

The phase lag between two signals (f and g) in radians for each frequency is estimated by the cross power spectrum, ϕ^*_{fg}:

$$P_{fg}(\omega) = \frac{\mathrm{Re}\left\{\phi^*_{fg}\right\}}{\mathrm{Im}\left\{\phi^*_{fg}\right\}} \qquad \in [\pi, -\pi]. \tag{D.19}$$

APPENDIX E – Running Interwave Analyzer in a python interpreter

The steps below describes the installation instruction for Anaconda's users. We recommend the use of the Anaconda distribution since it automatically installs almost all required additional Python packages. Interwave Analyzer also can be ran through other Python interpreters, but additional packages must be installed. For more details and other ways to install and run Interwave Analyzer, see the Interwave Analyzer user manual (BUENO; LORKE; BLENINGER, 2020).

To run Interwave Analyzer's scripts directly in Anaconda interpreter, first download the Anaconda distribution for Python 3.x.

- Go to Anaconda website (https://www.anaconda.com/) and find the option for **Anaconda distribution**;
- choose the Python 3.x graphical installer version (note that there are three options for operating system: Windows, macOS, and Linux);
- Install the Anaconda interpreter;
- After the installation, open the Anaconda Prompt (as administrator) and install the following packages that are used by Interwave Analyzer and are not available in Anaconda:

  Nitime (0.7 or compatible):

  ```
  conda install -c conda-forge nitime
  ```

  Reportlab (3.5 or compatible):

  ```
  conda install -c anaconda reportlab
  ```

Attention: If you already have anaconda installed in your computer, make sure that the above packages are installed and the anaconda version has Python 3.x. If you use another interpreter, make sure that the following packages are installed in the your python interpreter: Numpy 1.16.3, Datetime 4.0.1, Reportlab 3.5.19, Scipy 1.2.1, Nitime 0.7, Matplotlib 3.1.0, and tk (tkinter) 8.6.8, or compatibles versions.

- After the installation, go to Interwave Analyzer website and click on **Code repository**, or access directly our repository [1];
- Download all files .py available to download, **including the raster-graphics file-format 0interwave.png and interwave.ico**;
- Put everything in the same folder and run the script called GUIexecuter.py;
- A graphical user interface (GUI) should be launched in seconds;

---

[1] https://github.com/buenorc/interwaveanalyzer

- We recommend you to download the example files [2] used in this publication, to have a first hands-on experience in use Interwave Analyzer. For a detailed tutorial for run Interwave Analyzer with these files, see the Interwave Analyzer‘s User Manual.

---

[2] available at https://sites.google.com/view/interwaveanalyzer/interwave-analyzer on the *download example*

APPENDIX F – Longitudinal cross sections

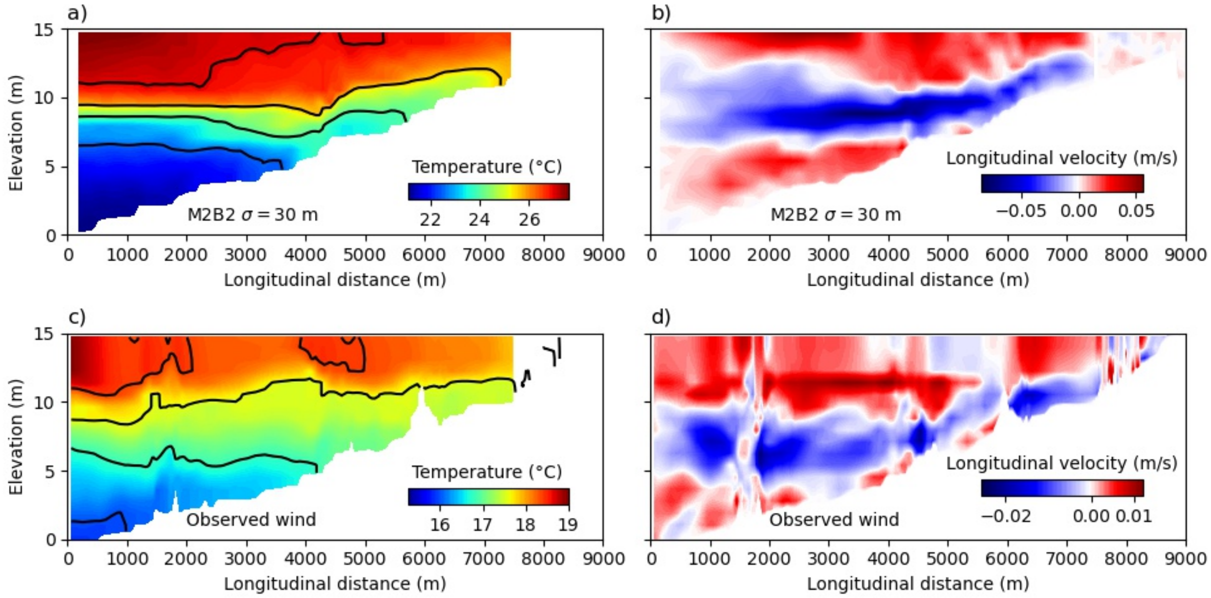

Figure 53 – Longitudinal sections of water temperature and horizontal flow velocity in Passauna Reservoir in response to an idealized 8-h wind episode (scenario M2B2) and with observed wind forcing. a) Water temperature and b) longitudinal flow velocity for scenario M2B2. c) Water temperature and d) longitudinal flow velocity simulated with observed wind dynamics and measured initial water temperature profile. The temperature distribution was obtained at the end of the wind episode, which was at $t = 8$ h in a), while for the measured data the end of the wind episode was characterized by the end of a strong wind event measured on 29 June at 21 h 20 min (cf. Fig. 31 in the main text). The horizontal velocities are shown at the end of the wind event, during the initial seiche excitation. The solid black lines in a) and c) mark isothermal depth with 1.0 °C increment.

APPENDIX G – Hydrodynamic characterization (Period P1)

No significant peaks that could be related to internal seiche activity were present in the power spectra of horizontal flow velocity in the lake interior (Fig. 54b and c). The low-frequency peaks (with period of 24 h and 12 h) identified in the power spectral density are more energetic near the water surface, indicating that the observed oscillatory response is related to the diurnal and semidiurnal components of the wind forcing that accelerate the water surface periodically.

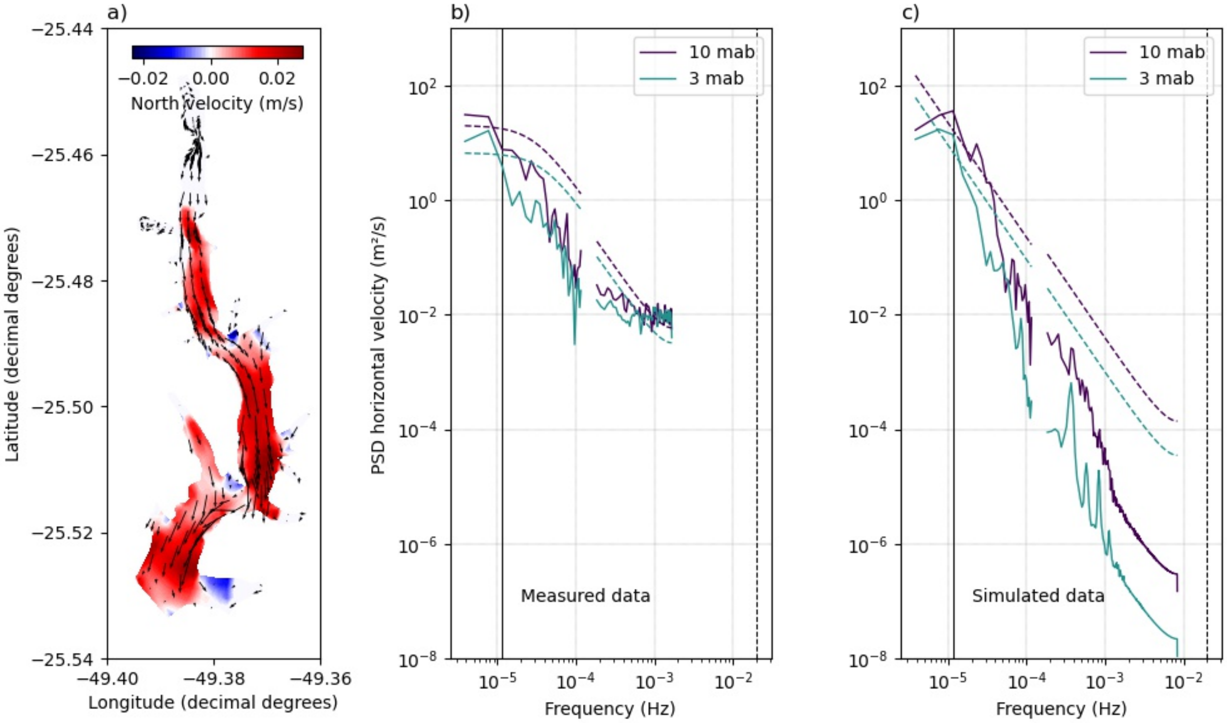

Figure 54 – Hydrodynamic characterization of the analyzed period P1. a) Simulated horizontal flow velocity during the upwelling event on June 29 (2018) at 17 : 00 h. The black arrows illustrate the horizontal velocity direction and magnitude near the water surface (2 m depth). The color scaling shows opposing (northward) flow in the hypolimnion (8 m above the deepest part of the reservoir). Power spectral density of b) observed, and c) simulated time series of horizontal flow velocity at two different depths at the monitoring station (red dot in Fig. 29a in the main text). For low-frequencies (10^{-6} to 10^{-4} Hz), the spectra were calculated with a window size of 3 d, while in the high-frequency range (up to 10^{-4} Hz), we used a window size of 12 h. The dashed lines show the 95% confidence limit of the mean red noise spectrum estimated for each time series. The vertical black dashed line marks the buoyancy frequency ($N = 0.02$ Hz), and the vertical solid black line shows a 24-h period.

Particularly near the water surface, the spectra of the simulated horizontal velocity indicates the presence of oscillatory flows at a frequency of 4×10^{-4} Hz (Fig. 54c). Since the model is not capable of resolving high-frequency (propagating) internal waves due to its coarse spatial resolution, the peak can likely be assigned to surface (baroclinic) seiches of different horizontal modes, which were hidden by other unresolved motions in the measured data. The theoretical period of the fundamental surface seiche in Passauna reservoir, assuming a reservoir-shaped basin (RABINOVICH, 2009), is around 42 min, which matches the frequency of the spectral peak at 3.8×10^{-4} Hz, corresponding to period of 43 min (Fig. 54c).

APPENDIX H – Downwelling at sloping bottom

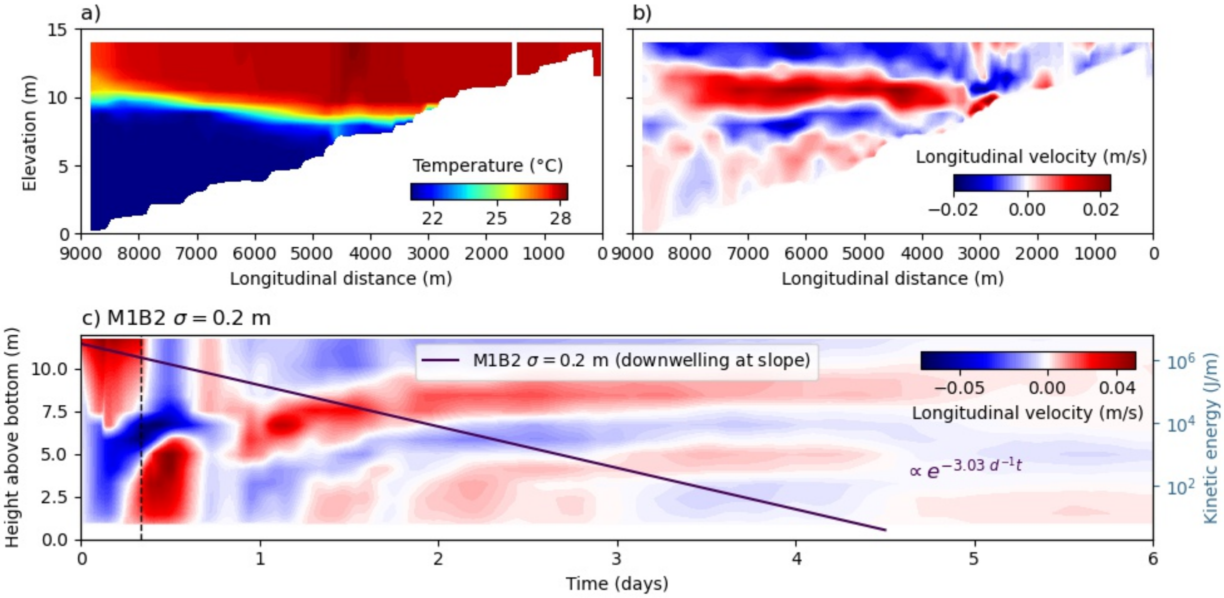

Figure 55 – The influence of bathymetry on internal seiches analyzed in scenario M1B2 (straight channel with sloping water depth) for nearly two-layer stratification (σ = 0.2 m) in response to a wind event from southern direction (from the left towards the dam). a) Temperature distribution along the longitudinal cross section of the reservoir during the wind set-up ($t = 0.3$ d) and b) the longitudinal flow velocity distribution at $t \approx 38.5$ h. c) Time series of horizontal velocity profiles at the basin center. The solid lines illustrate the exponential wave energy decay (see labels for decay rates, in which t is defined in days).

APPENDIX I – Horizontal flow velocity of hypothetical scenarios

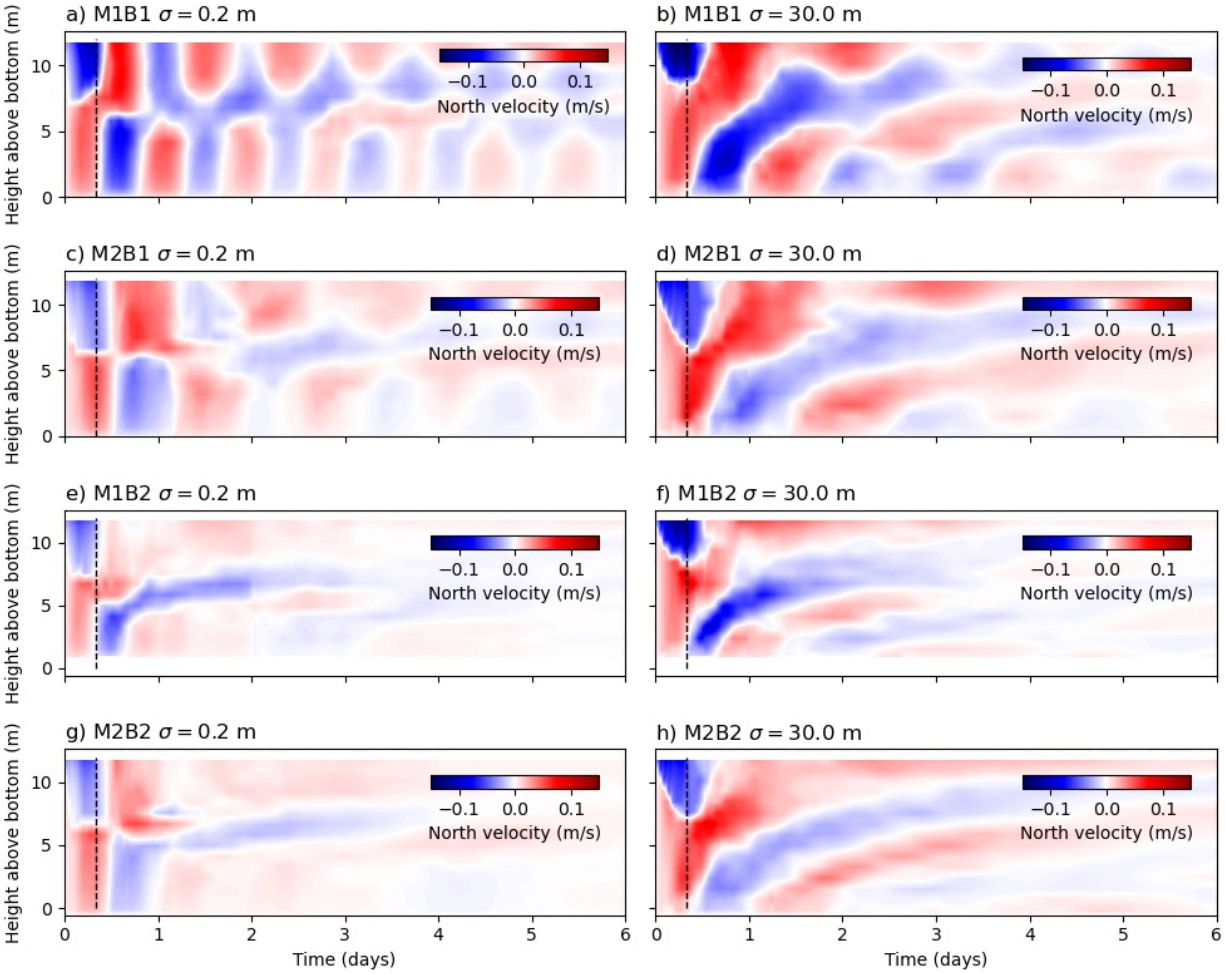

Figure 56 – Temporal dynamics of the vertical profiles of horizontal flow velocities near the center of the reservoir (station S1, velocity indicated by color) for scenario a) M1B1 $\sigma = 0.2$ m, b) M1B1 $\sigma = 30$ m, c) M2B1 $\sigma = 0.2$ m, d) M2B1 $\sigma = 30$ m, e) M1B2 $\sigma = 0.2$ m, f) M1B2 $\sigma = 30$ m, g) M2B2 $\sigma = 0.2$ m, and h) M2B2 $\sigma = 30$ m. The vertical black dashed lines mark the end of the wind event.

APPENDIX J – Effects of sloping boundary

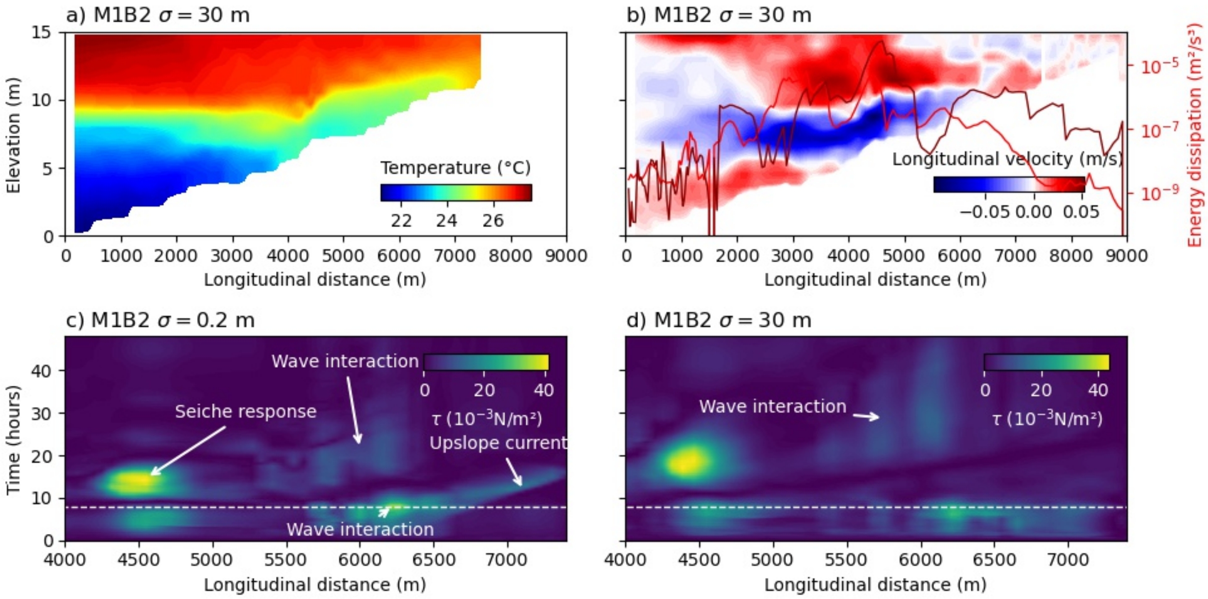

Figure 57 – Simulated water temperature, horizontal flow velocity, bed shear stress, and depth-integrated energy dissipation rates at the center line of Passaúna reservoir for scenario M1B2. a) Longitudinal cross section of water temperature (at t = 7 h 12 min) and b) horizontal velocity (at t = 7 h 12 min). Light and dark red lines show time series of integrated turbulent energy dissipation rates during the first interaction with the lakeshore for scenario M1B1 with σ = 0.2 m and σ = 30 m, respectively. Bed shear stress for c) σ = 0.2 m and d) σ = 30 m at the center line of Passaúna reservoir. High shear stress observed after the wind event (above the dashed white line) at the center of the basin (4500 m from the dam) indicates the response of internal seiche, since higher horizontal velocity are observed near the wave node (seiche response). Right after the end of the wind event high shear stress is observed near the shore, where the current shear across the density interface interacts with the bottom slope, at 6200 m from the dam (wave interaction). This occurs due to the acceleration of the flow near the sloping bottom, causing a up sloping current. This event persists for more wave periods (wave interaction) but promoting lower shear stresses since most part of the energy has been dissipated during the first interaction.

APPENDIX K – Numerical parameters

This appendix serves to provide a list of physical and numerical parameters that have been used in the numerical simulations. All input data to support the findings presented here are available at our repository[1] (DOI: 10.5281/zenodo.5708040).

Parameters	Value
Latitude	-25 °C
Number of layers	20 (equally spaced)
Days of simulation	10 days*
Time step of numerical computation	0.1 min
Results - temporal resolution	1.0 min
Gravity	9.81 m s^{-2}
Water density (reference)	1000 kg m^{-3}
Air density (reference)	1 kg m^{-3}
Salinity (reference)	0 ppt
Wind drag coefficient (wind speed: 0.00 m s^{-1})	0
Wind drag coefficient (wind speed: 1.25 m s^{-1})	0.0025
Wind drag coefficient (wind speed: 3.00 m s^{-1})	0.0018
Bottom roughness	Manning - uniform value: n=0.035
Wall roughness	Slip condition: Free
Model for 3D turbulence	$\kappa - \epsilon$ model
Background horizontal eddy diffusivity	0 m^2 s^{-1}
Drying and flooding check at	Grid centers and faces
Depth at grid cell faces	Minimum
Threshold depth	0.1 m
Marginal depth	Not applied
Smoothing time	60 min
Advection scheme for momentum	Cyclic
Advection scheme for transport	Cyclic
Vertical grid system	Cartesian coordinate system (Z-model)
Maximum depth in the model (lower boundary)	-16.949524 m
Maximum water level in the model	0.3 m
Heat flux model	Ocean (with solar radiation) **
Secchi depth	2 m**
Dalton number	0.0013**
Stanton number	0.0013**

---

[1] https://github.com/buenorc/wepaper.git

Table 5 – List of physical and numerical parameters used in numerical simulations of the baseline and hypothetical scenarios with Delft3D. *10 days have been simulated for baseline and hypothetical scenarios, however, for baseline simulations (validation simulations) the first 4 days have been used for model spin-up and were discarded from further analysis. **Heat flux model has been applied only for the baseline scenario, and neglected for hypothetical scenarios.

APPENDIX L – Damping Coefficients

Simulation	σ (m)	Damping Coefficient (d^{-1})
M1B1	0.2	0.85
M1B1	3	0.94
M1B1	10	0.99
M1B1	30	1.01
M2B1	0.2	1.05
M2B1	3	1.15
M2B1	10	1.23
M2B1	30	1.31
M1B2	0.2	3.05
M1B2	3	1.96
M1B2	10	1.76
M1B2	30	1.71

Table 6 – Damping coefficients for all hypothetical scenarios. σ is the standard deviation describing the Gaussian form of the buoyancy-frequency profile, in which $\sigma = 0.2$ m indicates that the basin approximates to a two-layer stratification and $\sigma = 30$ m indicates that the basin presents a linear stratification condition from surface to bottom.

APPENDIX M – Model validation

To evaluate the model's ability to reproduce the thermal stratification, modeled and measured temperature profiles were compared by their root mean square difference. The observed horizontal flow velocities were compared with simulations using the mean normalized velocity difference (HUANG; RAO; LU, 2010; DISSANAYAKE; HOFMANN; PEETERS, 2019):

$$\overline{D} = \sqrt{\frac{(u_m - u_s)^2}{u_m^2}}, \tag{M.1}$$

where $\overline{D}$ is the mean normalized difference, and u_m and u_s are the measured and simulated horizontal velocity components aligned to the wind direction, respectively.

To investigate the influence of the grid size on model performance, a similar simulation was run for a cell size of 200 m and a rectangular grid, thus, being 150% coarser than the standard grid used in the baseline scenario.

The simulation results obtained from the three-dimensional hydrodynamic model were compared to measured data for the analysis periods P1 and P2 at the location of the monitoring station (Fig. 58). In general, the simulated temperature profiles were in good agreement with the observations, with a relatively small root mean square difference (0.64 °C ± 0.40 °C). The simulation slightly overestimated the water temperature during both analysis periods. During period P1, the root mean square difference was highest in the top 3 m (0.30 °C ± 0.20 °C). During summer (period P2), larger differences between measurements and simulations occurred near the reservoir bottom (1.2 °C).

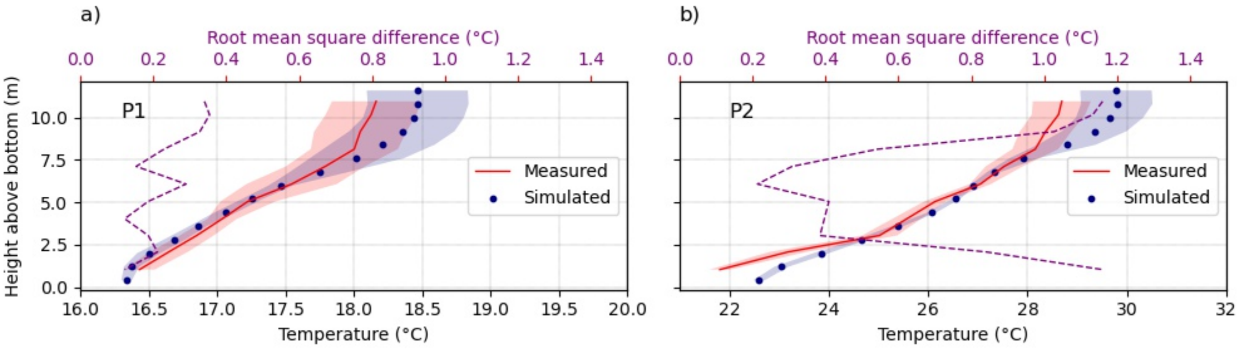

Figure 58 – Vertical stratification during the analysis periods at the sampling site near the intake station (Fig. 29a in the main text): a) P1 (from June 28 to July 04, 2018) and b) P2 (from January 29 to February 04, 2019). Both panels show the mean vertical profiles of simulated (blue dots) and measured (red solid line) temperature, with their standard deviations marked by the blue and red shaded areas. The purple dashed lines show the root mean square difference between simulations and observations.

The normalized root mean square difference (NRMSD) between the measured and simulated horizontal flow velocities (Eq. M.1) was larger for small velocities, particularly for horizontal velocities smaller than 0.005 m s^{-1} (Fig. 59a). The median of the NRMSD significantly decreased for larger velocities. The comparison also showed larger deviations at small velocities during period P2, when the density stratification was stronger (Fig. 59a).

For flow velocities exceeding 0.005 m s^{-1}, the differences between simulations and observations were generally small and without systematic differences between both periods.

The comparison of the directional components of the horizontal velocity between simulated and measured data also indicate decreasing deviations as the velocity increases, which is characterized by the increase of phase agreement in Fig. 59b.

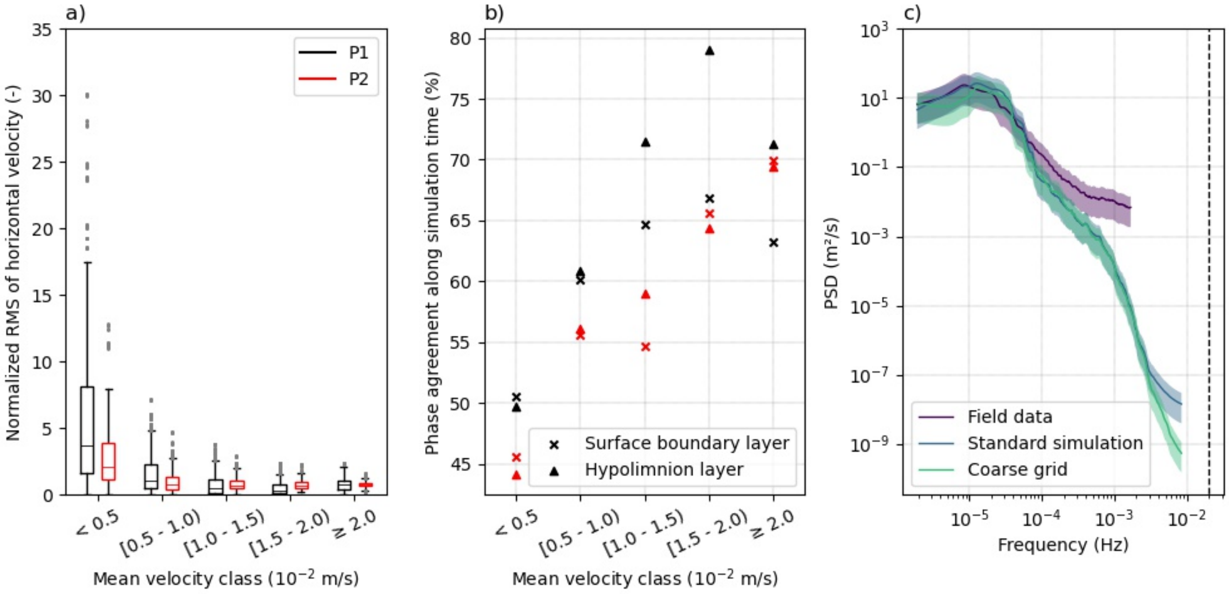

Figure 59 – Comparison of measured and simulated horizontal flow velocities for period P1 (weaker stratification) and P2 (stronger stratification). a) Normalized root mean square difference (NRMSD) of the horizontal velocity difference between measured and simulated data for different velocity classes for period P1 (black) and P2 (red). The boxes extend over the 25th and 75th quartiles, whilst the horizontal line indicates the median value. The whiskers extend to the minimum and maximum values neglecting outliers, which are represented by gray dots. b) Period of time (in percentage) that the direction of simulated horizontal velocities agreed with measured data for both periods and for different velocity classes. Crosses and triangles represent data from near the reservoir bottom (2.5 m above the bottom) and near the water surface (9 m above the bottom), respectively. c) Power spectral density of horizontal velocity variations at approximately 2.5 m above the bottom for measured (purple) and two simulations (blue and green). The solid blue line represents the spectral density of simulations using the standard grid size of our scenario analyses, whilst the solid green line represents PSD obtained from a coarser numerical grid. The colored shaded area shows the 95% confidence interval.

Fig. 32 in the main text provides an exemplary comparison of simulated and observed flow dynamics at the monitoring station, indicating that the model was able to capture the hydrodynamics of Passaúna reservoir reasonably well. Even though the simulated horizontal velocity components were slightly lower than the measurements, the dynamics and vertical distribution of larger-scale flow structures were well reproduced by the model (Fig. 32b and c in the main text), in which discrepancies were small, especially for horizontal velocity larger than 5×10^{-3} m s^{-1} (Fig. 59a).

Finally, we compared the power spectral density of measured and simulated horizontal velocity variations (Fig. 59c). The spectra show good agreement for low-frequency variability, but the spectral variance of the simulated velocities decreased strongly for frequencies exceeding 8×10^{-4} Hz (corresponding to a period of 21 min). The sharp drop-off in the spectra of simulated velocities can be caused by the spatial discretization of the numerical model, or by other unresolved motions.

To evaluate the influence of grid size on the spectrum, we analyzed simulations using a 150% coarser numerical grid. Low frequency variations and the general drop-off of power spectral are not affected by the increase in grid size (Fig. 59c). The spectra deviated only in the highest frequency bands, near the buoyancy frequency (2×10^{-2} Hz), suggesting large-scale motions can be well captured by the model even increasing the grid size at the point of interest from approximately 62 m to 200 m. For extremely coarse grids, we may also expect a stronger influence on large-scale motions due to the poor description of the longitudinal variability in reservoir topography and flow conditions.

APPENDIX N – Lake classification

The Wedderburn W number represents the force balance between wind shear at the water surface and the horizontal pressure gradients resulting from the vertical displacement of the thermocline (THOMPSON, 1980). It can be obtained by integration of the hydrostatic momentum equation in a rectangular basin with constant width and depth with two layers of an immiscible fluid subjected to a constant shear stress at the water surface as (THOMPSON, 1980):

$$W = \frac{\Delta\rho\ g\ h^2}{\rho_o\ u_*^2\ L}, \tag{N.1}$$

where $\Delta\rho$ is the density difference between the two layers (epilimnion and hypolimnion), ρ_o is the mean density, g is the gravitational acceleration, h is the thickness of the upper layer, u_* is the wind shear velocity, and L is the length of the basin. W is a dimensionless physical quantity, which can be derived from readily available bulk characteristics of a stratified lake or reservoir, including mean wind speed, length and depth, along with a measure of vertical density stratification. It is often used as a parameter to describe lake and reservoir hydrodynamics, including the potential of internal seiche generation (SPIGEL; IMBERGER, 1980; STEVENS; LAWRENCE, 1997).

The classification scheme for the mixing dynamics in stratified lakes and reservoirs is derived from characteristic time-scales of the relevant processes, including the wave damping, and the time required for thermocline erosion due to mixing (entrainment). Four different regimes of how a stratified basin responds to wind forcing, can be distinguished as a function of the Wedderburn number and the epilimnion thickness normalized by the total water depth (h/L, Fig. 60).

The dominance of basin scale internal wave is expected for a range:

$$\frac{1}{2}\sqrt{\frac{H}{H-h}} < W < \frac{L}{4\ h}\left(\frac{H}{H-h}\right), \tag{N.2}$$

This criterion is based on time scale of entrainment, derived by integrating the one dimensional turbulent kinetic energy budget over the upper layer, and the time scale for upwelling, which was defined based on the period of the fundamental (first horizontal and first vertical) mode of internal seiche in a rectangular-shaped box and a two layer stratification, as it is described by the Merian formula (WATSON, 1904):

$$T_{\mathrm{V1}} = 2\ L\ \sqrt{\frac{\rho_o\ H}{g\ \Delta\rho\ h\ (H-h)}}, \tag{N.3}$$

where H is the total water depth (considering a rectangular-shaped basin).

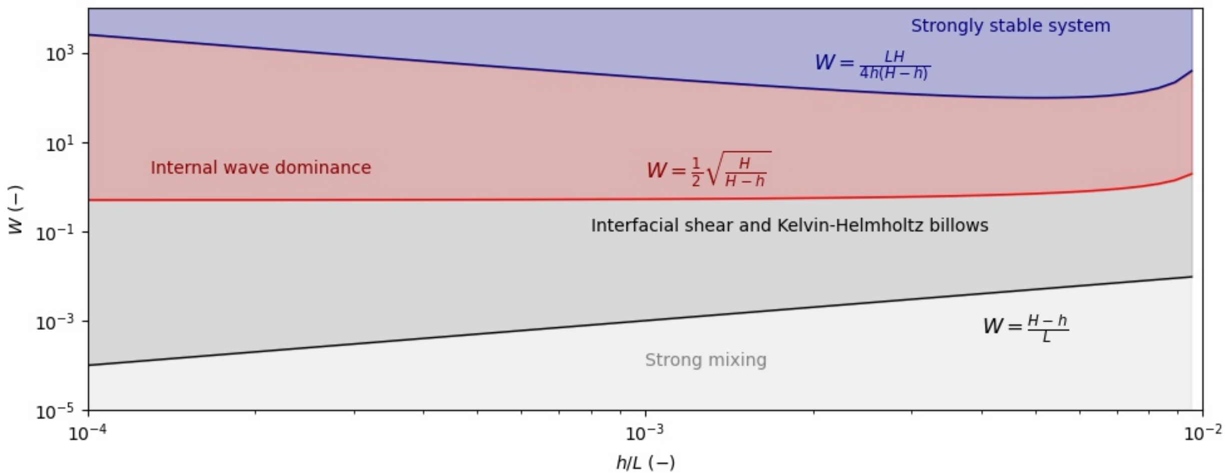

Figure 60 – Regime diagram for the classification of mixing dynamics in a stratified basin in response to wind forcing. Different color separate four mixing regimes based on the Wedderburn number (W) and the epilimnion thickness (h) normalized by the total water depth H (considering a rectangular-shaped basin). Solid lines shows regime boundaries according to the classification scheme of Spigel and Imberger (1980), text labels show the respective equations. The diagram presented here assumes $H/L = 0.01$, but even for other value the variation is relatively small, keeping the same order of magnitude of W.

APPENDIX O – Internal wave energy

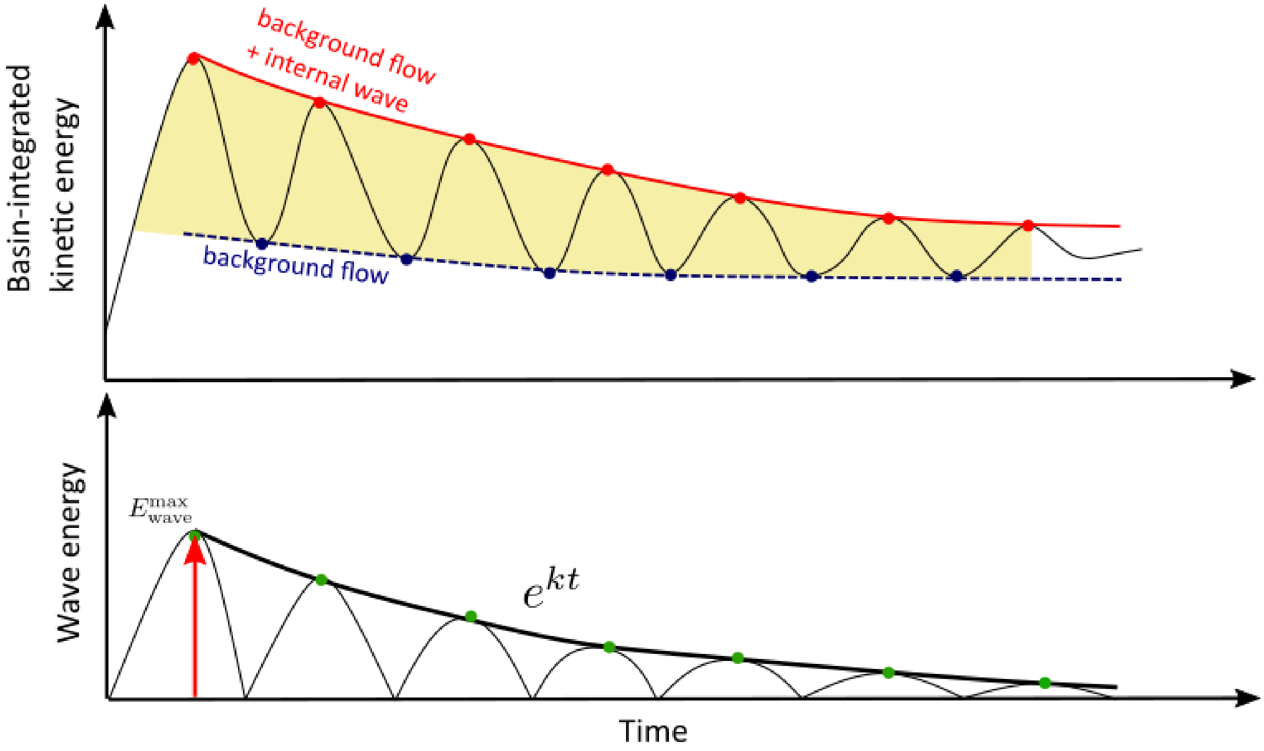
Basin-integrated kinetic energy
background flow + internal wave
background flow
Wave energy
$E_{\text{wave}}^{\text{max}}$
e^{kt}
Time

Figure 61 – Time-series of internal wave energy (E_{wave}) and the procedure to remove the background flow from the basin-integrated kinetic energy (Eq. 4.2 in the main text). Red and blue dots represent the identified maximum and minimum values from the time-series of basin-integrated kinetic energy, respectively. Red solid and blue dashed lines represent the total energy decay and the background flow decay, respectively. Green blue dot is the internal wave energy obtained from the difference between the basin-integrated kinetic energy (red dots) and the function of the background flow energy (blue dashed line), in which the first green dot (red arrow) describes the initial energy of the internal wave ($E_{\text{wave}}^{\text{max}}$). k is the internal wave damping coefficient (Eq. 4.3 in the main text).

ANNEX A – Author contributions

This thesis is based on three original research articles provided in chapters 3-5 which were conceived by all of the authors. I am the lead author of all articles and the contributions of all authors are explained in the following:

A.1 Internal seiche parameterization

The manuscript available in chapter 3 is published in *Environmental Fluid Mechanics* under the title **An empirical parametrization of internal seiche amplitude including secondary effects** by de Carvalho Bueno, Bleninger, Yao, and Rusak. (2020) https://doi.org/10.1007/s10652-020-09767-1

Conceptualization: R. de Carvalho Bueno, T. B. Bleninger **Data acquisition:** H. Yao and J. A. Rusak **Methodology:** R. de Carvalho Bueno, T. B. Bleninger **Model design:** R. de Carvalho Bueno **Formal analysis:** R. de Carvalho Bueno, T. B. Bleninger **Writing the manuscript:** R. de Carvalho Bueno **Revising the manuscript:** R. de Carvalho Bueno, T. B. Bleninger, H. Yao and J. A. Rusak

A.2 Physical mechanisms of internal seiche attenuation

The manuscript available in chapter 4 is published in *Environmental Fluid Mechanics* under the title **Physical mechanisms of internal seiche attenuation for non-ideal stratification and basin topography** by de Carvalho Bueno, Bleninger, Boehrer, and lorke. (2023) 10.1007/s10652-023-09928-y

Conceptualization: R. de Carvalho Bueno, A. Lorke, and T. B. Bleninger **Data acquisition:** A. Lorke **Methodology:** R. de Carvalho Bueno, A. Lorke, and T. B. Bleninger **Model design:** R. de Carvalho Bueno **Formal analysis:** R. de Carvalho Bueno, A. Lorke, T. B. Bleninger, and B. Boehrer **Writing the manuscript:** R. de Carvalho Bueno **Revising the manuscript:** R. de Carvalho Bueno, A. Lorke, T. B. Bleninger, and B. Boehrer

A.3 Internal wave analyzer

The manuscript available in chapter 5 is published in *Environmental Modelling and Software* under the title **Internal wave analyzer for thermally stratified lakes** by de Carvalho Bueno, Bleninger, and Lorke. (2021) 10.1016/j.envsoft.2020.104950

Conceptualization: R. de Carvalho Bueno, and T. B. Bleninger **Software development:** R. de Carvalho Bueno **Methodology:** R. de Carvalho Bueno, A. Lorke, and T. B. Bleninger **Case studies:** R. de Carvalho Bueno and A. Lorke **Writing the manuscript:** R. de Carvalho Bueno **Revising the manuscript:** R. de Carvalho Bueno, A. Lorke, and T. B. Bleninger

RAFAEL DE CARVALHO BUENO

I am a Ph.D. student in Environmental Engineering at the Federal University of Paraná
and in Natural Science at the University of Koblenz-Landau
My research interests are in physical limnology
and dynamic of stratified flows.

CONTACT

Nationality: Brazil

decarvalhobueno@gmail.com
+55 999 553598
Av. São José 700 (36D), Curitiba-PR Brazil
https://buenorc.github.io/

@buenorc
Rafael Bueno
0000-0003-4205-2119
Lattes: Rafael de Carvalho Bueno

SKILLS

Scientific competences

Internal waves	●●●●●
Gravity currents	●●●●●
Physical limnology	●●●●○
Numerical modelling	●●●●○
Software development	●●●○○
Sensor development	●●●○○

Programming skills

Python	●●●●●
C++	●●●●○
Arduino	●●●●○
Fortran	●●●○○
Matlab	●○○○○

general skills

LaTeX	●●●●●
Microsoft Office Skills	●●●●●
Microcontroller	●●●●○

Languages

Portuguese	●●●●●
English	●●●●○
Spanish	●●●○○

ABOUT ME

I am a Ph.D. student in Environmental Engineering at the Federal University of Paraná (Brazil) and in the Environmental Physics group at the University of Koblenz-Landau (Germany). I am a member of the Research Group of Environmental Monitoring, Modeling and Management of Reservoirs, Estuaries, and Catchments (REMARE). B.Eng and M.Eng in Environmental Engineering from Federal University of Paraná with a long term in Institute of Technology Tralee (Ireland). My research interests are in physical limnology and dynamic of stratified flows.

EDUCATION

Atual
University of Koblez-Landau, Germany
Natural and Environmental Sciences
Ph.D., Natural Science

Atual
Federal University of Paraná, Brazil
GPA 3.9/4.0 (98%)
Ph.D., Environmental Engineering

2019
Federal University of Paraná, Brazil
GPA 3.8/4.0 (96%)
MEng., Environmental Engineering

2016
Federal University of Paraná, Brazil
Institute of Technology Tralee, Ireland
BEng., Environmental Engineering

COMPLEMENTARY COURSES

2020
Heidelberg University, Germany
Helmholtz Centre for Env. Research
Physical Limnology Course

2019
University of Freiburg, Germany
University computing centre
Research Data Management

EXPERIENCE

01/2017 - Actual
Federal University of Paraná, Brazil
Teaching assistant

Teaching assistant in the Environmental Engineering Department and the Graduate Program of Environmental Engineering (PPGEA) at UFPR for the following courses: Fluid Mechanics, Applied Mathematics to Environmental Engineering (undergraduate level) and Hydrodynamics of Environmental Aquatic System (Graduate level).

02/2020 - 10/2020
University of Koblenz-Landau, Germany
Guest scientist

Visiting PhD student in the physical limnology research group at the University of Koblenz-Landau under the orientation of professor Dr. Andreas Lorke. Research focus on environmental fluid mechanics, physical limnology, numerical modelling and sensor development.

02/2015 - 12/2016
Federal University of Paraná
Internationalization Scholarship

Apoio em traduções de artigos científicos e material institucional da UFPR, promovendo a melhoria da visibilidade e internacionalização da produção científica da Universidade Federal do Paraná.

02/2012 - 12/2014
LACTEC institutes
Intern
Desenvolvimento de projetos e estudos hidrológicos, geoprocessamento, de-senvolvimento de modelos numéricos relacionados aos fenômenos ambientais(hidrológicos e topográficos).

02/2011 - 12/2012
Department of Computer Science (UFPR)
Program of Initiation to Teaching
Support for the following courses: programming language (C++).

COURSES TAUGHT

2021
GRACE, Technical Courses, Germany
Teacher
Hydrodynamic modelling with Delft3D

2021
FLUXNET-ECN Spring Workshop 2021
Teacher
Python Course

2020
KIT (Karlsruhe), Germany
Professor's Assistant
Hydrodynamic modelling

2019
Federal University of Paraná, Brazil
Professor's Assistant
Hydrodynamics of aquatic ecosystems

2019
Federal University of Paraná, Brazil
Professor's Assistant
Applied Mathematics I

2018 - 2019
Federal University of Paraná, Brazil
Professor's Assistant
Environmental Fluid Mechanics I

2018 - 2019
Federal University of Paraná, Brazil
Professor's Assistant
Environmental Fluid Mechanics II

RESEARCH INTERESTS

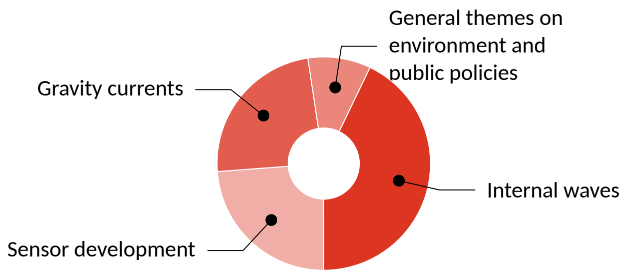

ONGOING SCIENTIFIC PROJECTS

Sensors development for environmental monitoring

This project is a group of studies focused on the development of low-cost sensors to control continuously the environmental conditions, which is a key parameter to establish circumstances in which human activities carry the risk of harmful effects on the natural environment.

Dynamic of lakes and reservoirs

This project is a group of studies investigating the hydrodynamic of lakes and reservoirs, including the effect of internal waves and gravity current on the biogeochemical fluxes, sediment resuspension, and greenhouse gases emissions in lakes and reservoirs.

REFERENCES

Dr.-Ing. Tobias Bleninger
Env. Engineering Department (UFPR)
Tel: +55(41) 98497 5685
Email: tobias.bleninger@gmail.com
Advisor

Dr. Michael Mannich
Env. Engineering Department (UFPR)
Tel: +55(41) 3361 3030
Email: mmannich@gmail.com
Collaborating researcher

Dr. Andreas Lorke
Head of Env. Physics Group (UKL)
Tel: +49 06341 28031317
Email: lorke@uni-landau.de
Advisor

PEER-REVIEWED JOURNAL ARTICLES

Physical mechanisms of internal seiche attenuation for non-ideal stratification and basin topography

👥 **de Carvalho Bueno, R.**; R., Bleninger, T.; Bertram, B.; Lorke, A.

📅 2022 📖 Limnol. Oceanogr. Submitted

Internal wave analyzer for thermally stratified lakes

👥 **de Carvalho Bueno, R.**; R., Bleninger, T.; Lorke, A.

📅 2021 📖 Environ. Model. Softw. DOI

An empirical parametrization of internal seiche amplitude including secondary effects

👥 **de Carvalho Bueno, R.**; Bleninger, T.; Yao, H.; Rusak, J.

📅 2021 📖 Environ. Fluid Mech. DOI

Wind-induced internal seiches in Vossoroca reservoir, PR, Brazil

👥 **de Carvalho Bueno, R.**; Bleninger, T.

📅 2018 📖 Revista Brasileira de Recursos Hídricos, Scielo Brasil DOI

CONFERENCE PRESENTATIONS AND TALKS

An IoT based low-cost turbidity probe and the influence of color light emitter and microcontroler resolution

👥 **de Carvalho Bueno, R.**; Morales, F.; Diniz, A.; Bleninger, T.

📅 2022 📖 XXX Congreso Latinoamericano de Hidraulica, Foz do Iguaçu (Brazil)

Dynamic: Automatic dye tracing software applied to gravity currents

👥 **Silva, N. S.**; de Carvalho Bueno, R.; Diniz, A.; Bleninger, T.

📅 2021 📖 XXIV Simpósio Brasileiro de Recursos Hídricos, Belo Horizonte (Brazil)

Dinâmica de lagos em período de estratificação térmica: Ocorrência de Seichas Internas

👥 **de Carvalho Bueno, R.**; Bleninger, T.

📅 2020 📖 XIII Simpósio Brasileirade Recursos Hídricos, Foz do Iguaçu (Brazil)

Desenvolvimento de um sensor de turbidez da água de baixo custo utilizando um Arduino

👥 **de Carvalho Bueno, R.**; Diniz, A.; Ribeiro, C.; Bleninger, T.

📅 2020 📖 XIII Simpósio Brasileirade Recursos Hídricos, Foz do Iguaçu (Brazil)

Experimental analysis of gravity currents on smooth and rough bottom and in an unstratified and stratified ambient

👥 **de Carvalho Bueno, R.**; Hoeltgebaum, L.; Colombo, G.; Mannich, M.; Bleninger, T.

📅 2019 📖 AHR World Congress, Panama City (Panama)

Avaliação e detecção de ondas internas em lagos

👥 **de Carvalho Bueno, R.**; Bleninger, T.

📅 2018 📖 I Encontro de Pesquisa e Desenvolvimento Tecnológico da UFPR

Análise experimental da formação de ondas internas gravitacionais a partir de correntes de gravidade

👥 **de Carvalho Bueno, R.**; Hoeltgebaum, L.; Colombo, G.; Mannich, M.; Bleninger, T.

📅 2018 📖 II Encontro Sul Brasileiro de Engenharia Ambiental e Sanitária, Foz doIguaçu-PR (Brazil)

Análise experimental da estratificação causada por correntes de gravidade sobre fundo liso e rugoso.

👥 **Hoeltgebaum, L.**; Colombo, G.; de Carvalho Bueno, R.; Bleninger, T.; Mannich, M.

📅 2018 📖 II Encontro Sul Brasileiro de Engenharia Ambiental e Sanitária, Foz doIguaçu-PR (Brazil)

Gravity currents produced by lock-exchange and intrusion.

👥 **de Carvalho Bueno, R.**; Marcon, L.; Wosiacki, L.; Romero, M.; Bleninger, T.; Mannich, M.

📅 2017 📖 XXII Simpósio Brasileira deRecursos Hídricos, Florianópolis-SC (Brazil)

Avaliação experimental da dispersão da pluma de um jato denso.

👥 **Romero, M.**; Marcon, L.; de Carvalho Bueno, R.; Wosiacki, L.; Mannich, M.; Bleninger, T.

📅 2017 📖 XXII Simpósio Brasileira deRecursos Hídricos, Florianópolis-SC (Brazil)

Verificação da ocorrência de ondas internas no reservatóriodo Vossoroca.

de Carvalho Bueno, R.; Bleninger, T.

2017 XXII Simpósio Brasileira deRecursos Hídricos, Florianópolis-SC (Brazil)